

# Computational Investigations of Streamers

*From Input Cross Sections to Evolution of  
Plasma Species*

Andy Martinez Nieto



# Computational Investigations of Streamers

*From Input Cross Sections to Evolution of Plasma  
Species*

PROEFSCHRIFT

ter verkrijging van de graad van doctor aan de Technische Universiteit  
Eindhoven, op gezag van de rector magnificus prof.dr.ir. F.P.T. Baaijens,  
voor een commissie aangewezen door het College voor Promoties, in het  
openbaar te verdedigen op vrijdag 18 februari 2022 om 13:30 uur

door

Andy Martinez Nieto

geboren te Antwerpen, België

---

Dit proefschrift is goedgekeurd door de promotoren en de samenstelling van de promotiecommissie is als volgt:

<b>Voorzitter</b>		prof.dr.ir. G.M.W. Kroesen	
<b>Promotores</b>	1 <sup>e</sup> Promotor	prof.dr. U.M. Ebert	
	2 <sup>e</sup> Promotor	dr. S. Nijdam	
	Copromotor	dr. H.J. Teunissen	Centrum Wiskunde & Informatica
<b>Leden</b>		prof.dr. O. Scholten	Rijksuniversiteit Groningen
		dr. J. van Dijk	
		prof.dr. G.J. van Rooij	Universiteit Maastricht

*Het onderzoek of ontwerp dat in dit proefschrift wordt beschreven is uitgevoerd in overeenstemming met de TU/e Gedragscode Wetenschapsbeoefening.*



Centrum Wiskunde & Informatica



Technische Universiteit  
Eindhoven  
University of Technology

The research in this thesis was funded by European Union's Horizon 2020 research and innovation program under project ID 722337 (<https://www.saint-h2020.eu/>), CWI, and TUE.

Cover Design: Illustration created using <https://app.wombo.art/>. Editing, layout, and typesetting done by Marie Missoorten.;

Printing: Ipskamp Printing

A catalogue record is available from the Eindhoven University of Technology Library.

ISBN: 978-90-386-5451-5

This thesis was typeset using  $\text{\LaTeX}$  starting from the template of Mandar Chandorkar (with permission) found at <https://github.com/mandar2812/phd-thesis>.

Copyright © 2021 Andy Martinez Nieto

All rights reserved. No part of the material protected by this copyright notice may be reproduced or utilised in any form or by any means, electronic or mechanical, including photocopying, recording or by any information storage and retrieval system, without written permission from the copyright owner.



# Summary

## Computational Investigations of Streamers

*From Input Cross Sections to Evolution of Plasma Species*

The subject of this thesis was streamer discharges. Streamer discharges are a type of transient discharge characterized by a finger-like structure and an EEDF where at STP air (gas temperature of 300 K, and gas pressure of 1 bar) most electrons have an energy of  $<10$  eV, but some can reach energies above 100 eV. Because of their curved charged front there is an enhancement of the electric field at the front of the streamer. This gives streamers the ability to produce these high-energy electrons at room temperature and to allow “hot” chemical reactions to happen without needing to have a hot gas and thus equipment that can handle this hot gas. This property makes streamer discharges attractive for applications in for example plasma medicine, gas processing, and surface treatment.

The investigation of streamer discharges was done using simulation software based on different modelling methods. Particle simulations track individual particles and their collisions while they are accelerated by an electric field. These simulations are the most computationally intensive and so are limited to short timescales (tens of nanoseconds). Fluid models evolve for each plasma species a continuous density, instead of discrete particles as in the particle simulations. These simulations are computationally less intensive, due to approximations made, and thus allow for longer timescales (hundreds of nanoseconds). Depending on the research question a less detailed, but computationally less intensive fluid simulation can be adequate.

Streamers have several important properties which make them difficult or expensive to simulate:

- 
1. Transient on a short timescale: Streamers propagate on a nanosecond timescale (at STP air) which means that any modelling effort needs to evolve with picosecond timesteps to capture the streamer and its effects. The necessity of using such a small timestep forces us to simulate a large amount of timesteps to reach timescales which are of interest for applications or for comparison with experiment.
  2. Localized: Streamers are a type of discharge that does not extend throughout the entire (or even a large part) of any vessel in which they are produced. Simulating single streamers thus comes with the added complexity that only a small region of space contains “interesting” physics, while the rest will be normal gas. A square computational domain will thus result in a lot of “wasted” computational effort if no special care is taken on how this domain is split up into computational grid points.
  3. Curved charged front: A streamer has a curved and thin charged layer at the front. This charged layer is responsible for the production of the electric field necessary to develop the streamer further and should thus be resolved as best as possible. Because the charged layer is thin, a small mesh-size for the computational grid is necessary. Combining the requirement of a small mesh-size and the localized nature of the streamer this is a recipe for high computational workload and has to be dealt with appropriately in the modelling software.

In this thesis several modelling methods are used to simulate streamers or properties of the species within a streamer. Topics spanning the fundamental input for the simulation models to the long time behaviour of plasma species within a streamer are investigated. The thesis is structured as follows:

First, an addition to electron collision cross sections with methane was made in chapter 2. Specifically, neutral dissociation cross sections were calculated using analytical formulas which use dissociative ionization cross sections as input. These ionization cross sections have been thoroughly investigated and reviewed in the past. The resulting neutral dissociation cross sections were added to a comprehensively reviewed set of cross sections to obtain a complete set of cross sections which retrieve experimentally measured transport parameters when used in a Boltzmann equation solver.

---

Second, an extensive comparison was made in chapter 3 between freely available Boltzmann equation solvers for transport parameters since these are crucial components of a fluid model. Model gases, both analytical and fabricated to test a specific part of the solver, were compared using these solvers. Besides model gases, also Argon, Nitrogen, and Oxygen gas were compared where care was taken to choose cross sections for each gas which do not favor any specific (type of) solver. The results of the real gases were compared to experimentally measured transport parameters. The resulting comparison showed that the used solvers agree to within a couple percent of each-other and that the biggest differences are found in user-friendliness and performance. This chapter should be viewed more as a “community service” instead of a chapter where novel and unexpected results were obtained. The testing and comparison of modelling software used within the community is necessary to increase confidence in results produced by different research groups.

Third, the inception phase of the streamer was investigated in chapter 4. This was done in close collaboration with experiment. The time delay between application of the voltage and light emission from the streamer in experiment was compared to the time delay of streamer development in a particle simulation. A histogram of the experimental delays showed a bias at three distinct timescales. Using particle simulations an explanation was postulated for each of the three timescales.

Lastly, the evolution of streamers has been investigated in chapter 5 using a fluid simulation where a double voltage pulse is applied to a rod electrode within a vessel filled with low pressure synthetic air. The time between the voltage pulses was varied to investigate a different development of the second pulse streamer as has been shown experimentally in literature. Since long timescales of no applied voltage were simulated, an extended set of chemical reactions for air was used. The set contains over 300 reactions and more than 30 plasma species. Additionally, the effects of gas heating on the gas dynamics were investigated. Due to the relative short duration of the voltage pulses and only applying two pulses the heating was limited to a few Kelvin so had negligible effects on the gas dynamics, and reaction rates.

---

# Acknowledgements

Here, I can finally thank all the people in my life who are directly responsible for making this thesis happen. This acknowledgement is all about thanking the people that I love, who love me, and express my gratitude to them and acknowledge how lucky I am.

Obviously, it all started with my parents and my sister. I am incredibly lucky to be raised in such a warm and loving family. Mom and dad, I know that I did not always make your lives the easiest, as I also had to explain and apologize for in the acknowledgements of my master thesis :), but you were always there to help and support me no matter what foul mood I was in. For this I cannot thank you enough and I will continue to show my love and appreciation for you until the end of time. Sis, you are one of the most important people in my life, you showed me that it is perfectly fine (and even preferable) to be different and choose your own path. The path that I chose was one that led to this thesis and even though it came with a lot of hardships I am glad that I followed it. Throughout the PhD I got to experience the addition of two new members to the family, my nephews Arlo and Ilio. Whenever I had a bad work-week I only had to spend one day playing with you guys and all was fine in the world. Without you two rascals knowing it you have helped me through some very difficult times. I will always be there for you, you will always be able to count on me. Mom, dad, sis, and nephews, I love you all so much and thank you for everything that you have done!

Every day I count my lucky stars to have such a large, diverse, and genuine group of friends. You all do not realize how much you have helped me get

---

through this entire PhD. One of the toughest parts of the PhD was living relatively far away from you guys. Luckily, all I had to do was send one text and most of you were prepared to spend the evening with me playing video games, and laughing on Discord. I have learned that there is no job offer that is worth it to move such a distance away from you all. Friends, thank you for everything. I love you all, and you will never get rid of me !

I would also like to express my gratitude for several teachers I had throughout my life. The first and foremost is my high school physics teacher Hilde Verheijen. All this and previous work that I have done would have never happened if it wasn't for you. You were one of the best, if not the best, teacher I have ever had. The curiosity and passion you had for even the simplest physics concepts is something that I admire and hope I will continue to have as well. Besides physics, you are a very caring and joyful teacher, someone who is always ready to help students in whichever way you can. I was lucky to experience this during the time I didn't join my classmates on a school trip to Italy. You took me under your wings and I was allowed to join and help you during physics classes that you had to give to other students. This seemingly small gesture for you was an amazingly big one for me. You have directly made my life into what it is today. Thank you sincerely.

At university I had the pleasure and privilege to be supervised by Bart Partoens for both a bachelor and my master thesis. Bart, you had the task of steering my passion and enthusiasm for any and all subjects into a single thesis on a single subject. This was not a simple feat, but you did this effortlessly. You allowed me to explore my ideas and help me with whatever problems I stumbled upon without pushing me in the exact direction that you personally wanted to take. This type of supervision was exactly what I needed and I haven't had it ever since. Because of the projects we had done my love for physics and research only grew more. If life didn't take me away from Belgium I would have surely tried my best to continue working with you. Thank you Bart for the guidance! Hopefully someday our research paths cross and I can work with you again.

The final teacher I want to thank is Nick van Remortel. During my bache-

---

lor thesis you gave me an opportunity to work on an ESA student project which opened so many doors for me. Not only did you give me that opportunity, you were also always prepared to write recommendation letters for internships and even this PhD. Many of the opportunities that I got in my physics career were made possible because of you and for that I am so grateful. I realise I am very lucky to have received these opportunities. Thank you for all that you have done, I will never forget this and I will try to pay it forward in whichever way I can.

Throughout this PhD I met some wonderful fellow PhD students! These people know exactly what you are going through and allow you to vent all your frustration over a beer at the end of the working week. With some students I had a closer relationship with than others and I would like to thank them here. Of course the first one I would like to thank is Shahriar Mirpour. Agh agh agh, I will forever remember our trips and talks together! I know that you will do great things in life and I will try to help you in whichever way I can. I do not have any doubt that you will do the same. I cannot wait for the time that we can eat and have drinks together again! Next I would like to thank Behnaz Bagheri. I spent many afternoons in your office being distracted from work and talking about random other stuff. I loved every minute of it and it helped me relax in the office environment. You have taught me many of the inner workings of academia which have helped me make choices even after you have left the research group to start your tenure track. I also have many great memories of our trips together, I will forever cherish them. Hani Francisco, I am really happy that you joined me in the PhD. Your honesty and directness was a breath of fresh air that I needed. I knew that you would not bullshit me and I could always ask you if I was imagining things or if things were really that weird. I had so many great laughs and drinking nights with you and even though I might not completely remember them that clearly, I know that they were amazing. Dennis Bouwman and Hema(ditya) Malla, you were the new fresh guys that I had so much fun teaching things to. Of course it didn't take long until I had nothing left to tell you guys and you were teaching me things, but it was fun while it lasted. I loved our board game nights, they were a much needed break from the monotony of work-life. Although we didn't get to experience as many trips, our first trip to Italy was

---

still one of the best trips I had. Good luck with your PhD. you will do great!

I also want to sincerely thank the supporting staff at both CWI and TUE. Specifically I want to thank Nada Mitrovic and Anita Peeters. Nada, you eliminated all of the stress that came with any sort of administrative task we had to do. I hope you realize just how much you lessen our burden by taking care of all of these things in the calm and joyful way that you do. Since my final PhD year was done at TUE, I got in touch with Anita. We don't know each other for too long, but you have already helped me a tremendous amount in all parts of the finalization process of the PhD. Now that I continue working at TUE, I feel at ease knowing that, just like with Nada, much of the stress for administrative tasks will be taken care of by you. Thank you both so much! Your impact on our lives and on the research cannot be stressed enough!

Lastly, I want to thank the supervisors that I had throughout my PhD. Sander Nijdam, during the time that I spent at TUE for a project with your student Shahriar we had many brainstorming sessions. You never gave me the feeling that I was lesser or knew less than you (even though obviously you know so much more than me). Brainstorming sessions with you were so much fun and they reminded me of the sessions I had with a previous supervisor Bart Partoens (which is a compliment!). I hope that I can work with you more throughout my career! Jannis Teunissen, you arrived in the group at the perfect time for me. When things didn't go that well for me you were always ready to have a good, open, and relaxed conversation with me. I hope you realize how much these talks helped me get through the PhD. You are obviously a good researcher, but I think your skills and qualities at being a supervisor for students are the most important. We will surely stay in touch! Lastly, I would like to thank my direct supervisor Ute Ebert. Thank you for the opportunity that you gave me. You were always ready and eager to discuss new ideas, which I appreciate. Besides the research, you have allowed me to see so many different places of the world and talk to so many different people. Thank you for this PhD. adventure!

# Contents

<b>1</b>	<b>Introduction</b>	<b>1</b>
1.1	Particle Collisions . . . . .	2
1.1.1	Production of Charged Particles . . . . .	2
1.1.1.1	Direct-Impact Ionization . . . . .	2
1.1.1.2	Photo-Ionization . . . . .	2
1.1.1.3	Penning Ionization . . . . .	3
1.1.2	Removal or Conversion of Charged Particles . . . . .	3
1.1.2.1	Attachment . . . . .	3
1.1.2.2	Detachment . . . . .	4
1.1.2.3	Recombination . . . . .	4
1.1.2.4	Ion-Conversion . . . . .	4
1.1.3	Swarm Parameters . . . . .	5
1.1.4	Cross Sections . . . . .	5
1.2	Streamers . . . . .	6
1.2.1	Positive Streamers . . . . .	8
1.2.1.1	Propagation . . . . .	8
1.2.1.2	Photo-ionization . . . . .	10
1.2.2	Applications . . . . .	10
1.3	Discharge Modelling . . . . .	11
1.3.1	Electron Boltzmann Solver . . . . .	11
1.3.2	Particle Model . . . . .	12
1.3.2.1	Particle Movement . . . . .	13
1.3.2.2	Particle Collisions . . . . .	13
1.3.2.3	Particle Weighting . . . . .	14
1.3.2.4	Necessity of super-particles . . . . .	15
1.3.3	Fluid Model . . . . .	15
1.3.3.1	Evolving Particle Densities . . . . .	16

1.3.4	Calculating the Electric Field . . . . .	17
1.4	Research Questions . . . . .	18
1.4.1	Chapter 2: Neutral Dissociation Cross Sections of CH <sub>4</sub> . . . . .	18
1.4.2	Chapter 3: Extensive Comparison of Available Electron Boltzmann Solvers . . . . .	19
1.4.3	Chapter 4: Investigation of Streamer Inception in Air . . . . .	20
1.4.4	Chapter 5: Repetitive Pulsed Streamer Discharges in Air . . . . .	20
1.4.5	Internship at Plasma Matters b.v. . . . .	21
<b>2</b>	<b>Methane Dissociation Cross Sections</b>	<b>23</b>
2.1	Introduction . . . . .	25
2.1.1	Methane-containing plasmas . . . . .	25
2.1.2	Demands on cross sections . . . . .	25
2.1.3	Goal of the paper . . . . .	26
2.1.4	Relation to earlier work . . . . .	27
2.2	Compilation of unfitted cross sections for neutral dissociation of CH <sub>4</sub> . . . . .	28
2.2.1	Neutral dissociation of CH <sub>4</sub> . . . . .	29
2.2.2	Our proposed cross sections . . . . .	33
2.3	Comparison of calculated and measured swarm parameters . . . . .	38
2.4	Production rates for hydrogen radicals . . . . .	42
2.5	Summary and Outlook . . . . .	44
2.5.1	Summary . . . . .	44
2.5.2	Outlook . . . . .	45
<b>Appendices</b>		<b>47</b>
2.A	Fitting functions and parameters for used and reported cross sections . . . . .	47
2.A.1	Basis functions . . . . .	47
2.A.2	Dissociative Ionization . . . . .	48
2.A.3	Dissociative Electron Attachment . . . . .	48
2.A.4	Total Dissociation . . . . .	49
2.A.5	Neutral Dissociation to CH <sub>2</sub> . . . . .	50
2.B	Tabulated cross sections for neutral dissociation to CH <sub>3</sub> , CH, and C . . . . .	52

---

<b>3</b>	<b>Comparison of Six Electron Boltzmann Solvers</b>	<b>57</b>
3.1	Introduction . . . . .	58
3.2	Boltzmann Solvers . . . . .	60
3.2.1	BOLSIG+ . . . . .	60
3.2.2	BOLOS . . . . .	61
3.2.3	particle_swarm . . . . .	61
3.2.4	METHES . . . . .	61
3.2.5	LoKI-B . . . . .	62
3.2.6	MultiBolt . . . . .	62
3.3	Methodology . . . . .	62
3.3.1	Inter- and Extrapolation of Input Cross Sections . . . . .	62
3.3.2	Compared Swarm Parameters . . . . .	63
3.3.3	Configuration Parameters . . . . .	64
3.3.4	Convergence Criteria . . . . .	65
3.3.5	Comparison with BOLSIG+ . . . . .	66
3.4	Model Gas Comparisons . . . . .	66
3.4.1	Maxwell Model . . . . .	66
3.4.2	Reid Ramp Model . . . . .	68
3.4.3	Lucas-Salee gas . . . . .	71
3.4.3.1	Non-Ionizing: $F = 0$ . . . . .	71
3.4.3.2	Ionizing: $F = 1$ . . . . .	72
3.4.4	Discussion . . . . .	76
3.5	Real gas comparison . . . . .	80
3.5.1	Ar . . . . .	81
3.5.2	$N_2$ . . . . .	81
3.5.3	$O_2$ . . . . .	84
3.5.4	Discussion . . . . .	87
3.6	Performance . . . . .	91
3.7	User-experience . . . . .	92
3.8	Conclusion . . . . .	94
<b>4</b>	<b>Distribution of Inception Times</b>	<b>97</b>
4.1	Introduction . . . . .	99
4.2	Experimental Setup . . . . .	103
4.2.1	Experimental conditions . . . . .	103
4.2.2	Measuring inception time $t_{inc}$ . . . . .	103

---

CONTENTS

---

4.2.3	ICCD imaging of streamers . . . . .	104
4.3	Estimate of initial conditions . . . . .	107
4.4	Simulation Model . . . . .	109
4.4.1	Particle model . . . . .	109
4.4.2	Electric field . . . . .	113
4.4.3	Inception time $t_{inc}$ . . . . .	113
4.4.4	Drift and reaction times . . . . .	115
4.5	Results and Discussion . . . . .	118
4.5.1	Baseline Experiment . . . . .	118
4.5.2	Baseline theory . . . . .	118
4.5.3	The first peak . . . . .	122
4.5.3.1	Hypothesis: electrons detaching from $O_2^-$ in the active zone as the source of the first peak	123
4.5.4	The second peak . . . . .	125
4.5.4.1	Experimental evaluation . . . . .	125
4.5.4.2	Hypothesis . . . . .	128
4.5.5	The third peak . . . . .	129
4.5.5.1	Source of Electrons . . . . .	129
4.5.5.2	Hypothesis: Drift time of $O_2^-$ as the char- acteristic time of the third peak . . . . .	129
4.5.5.3	Producing the Third Peak . . . . .	132
4.5.5.4	Increasing duration between LV and HV pulse	134
4.5.5.5	Increasing LV Pulse Duration . . . . .	136
4.5.6	Streamer inception under different conditions . . . . .	136
4.6	Summary and open questions . . . . .	140
<b>Appendices</b>		<b>143</b>
4.A	Analytic estimate for inception probability . . . . .	143
<b>5 Simulations of Repetitive Pulsed Streamer Discharges in Syn- thetic Air</b>		<b>145</b>
5.1	Introduction . . . . .	147
5.2	Model . . . . .	148
5.2.1	Equations . . . . .	148
5.2.2	Geometry . . . . .	150
5.2.3	Reaction Set . . . . .	150
5.2.4	Simulation conditions . . . . .	153

---

5.2.4.1	Gas . . . . .	153
5.2.4.2	Applied Voltage. . . . .	153
5.3	Results and Discussion . . . . .	154
5.3.1	Velocity . . . . .	157
5.3.2	Conductivity of the Channel . . . . .	157
5.3.2.1	Interpulse time . . . . .	159
5.3.2.2	End of Constant Voltage Interval . . . . .	159
5.3.3	Dominant Species . . . . .	162
5.3.3.1	Interpulse time . . . . .	162
5.3.3.2	End of Constant Voltage Interval . . . . .	165
5.3.4	Dominant Reactions . . . . .	167
5.3.4.1	Interpulse time . . . . .	167
Streamers	Head . . . . .	167
Streamers	Channel . . . . .	167
Streamers	Back/Near Electrode . . . . .	170
5.3.4.2	End of Constant Voltage Interval . . . . .	170
Streamers	Head . . . . .	170
Streamers	Channel . . . . .	170
Streamers	Back/Near Electrode . . . . .	173
5.4	Gas Heating and Dynamics . . . . .	176
5.4.1	Equations . . . . .	176
5.4.2	Gas heating model . . . . .	177
5.4.3	Gas Temperature, and Density . . . . .	180
5.5	Conclusion . . . . .	183
<b>6</b>	<b>Conclusions and Outlook</b>	<b>185</b>
6.1	Chapter 2: Neutral Dissociation Cross Sections of CH <sub>4</sub> . . . . .	185
6.2	Chapter 3: Extensive Comparison of Available Electron Boltzmann Solvers . . . . .	187
6.3	Chapter 4: Investigation of Streamer Inception in Air . . . . .	188
6.4	Chapter 5: Repetitive Pulsed Streamer Discharges in Air . . . . .	190
6.5	Outlook . . . . .	192
6.5.1	Discharge Inception . . . . .	192
6.5.2	Repetitive Pulses . . . . .	192
6.5.3	Boltzmann Solvers and Other Scientific Software . . . . .	193
	<b>Curriculum Vitae</b>	<b>225</b>

---



# Chapter 1

## Introduction

Plasma is the most common state of ordinary matter in the universe. It is a gas-like state, in that it has no definite shape or volume, composed of electrons, ions, and possibly neutral molecules. It is the state of matter of stars and it is used to drive nuclear fusion reactors. It occurs on earth as lightning and can be used in fabrication of semiconductor devices. This large variation of natural occurrences and technological applications shows the variety of environments in which the plasma state-of-matter can exist. An important parameter distinguishing these types of plasmas is the degree of ionization i.e. the fraction of all particles which are electrically charged.

In this thesis we discuss plasmas with a degree of ionization up to  $10^{-4}$  [134, 158]. This means that the charged particles within the plasma will predominantly collide with neutral particles rather than with each other. The interaction between charged particles happens essentially through the electric field produced by them. This assumption lies at the foundation of the computational modelling done in this thesis. We will introduce the reader to particle collisions (and how they are included within a computational model), streamer discharges (including some applications), and computational methods for modelling streamers (and other types of discharges and plasmas).

## 1.1 Particle Collisions

As mentioned, the degree of ionization for the plasmas discussed in this thesis is relatively low (up to  $10^{-4}$ ) which means that charged particles will predominantly collide with neutral particles rather than with each other. In this section we will discuss the most important types of particle collisions which are included in the computational models in this thesis. Examples for each collision type are given for the case of an  $N_2/O_2$  mixture like air. Additionally, average quantities of swarms of particles resulting from these collisions are discussed. Finally, the discussion ends on the necessary input data for including these particle collisions in the computational models.

### 1.1.1 Production of Charged Particles

#### 1.1.1.1 Direct-Impact Ionization

A particle (e.g. an electron) collides with an atom or molecule. If the particle imparts more energy than the binding energy of an electron to the atom or molecule then this electron can be liberated. The binding energy of an electron is more commonly called the ionization energy.

The main ionization reactions in air are:



The ionization energies of  $O_2$  and  $N_2$  are 12.07 eV [73] and 15.58 eV [72] respectively.

#### 1.1.1.2 Photo-Ionization

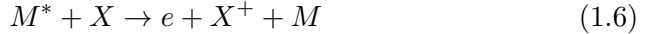
Photons with more energy than the ionization energy can free an electron from an atom or molecule upon absorption. The process of photo-ionization in air goes in three steps [213]:



where  $\gamma$  denotes a photon. As mentioned in (1.1), this photon needs to have an energy of at least 12.07 eV i.e. a wavelength of 102.7 nm (UV).

### 1.1.1.3 Penning Ionization

Excited atoms or molecules which collide with a target atom or molecule can de-excite by transferring potential energy to the target causing the target to be excited to an unstable state. This unstable state will de-excite by emitting an electron. This process only happens if the excitation energy of the initial atom or molecule is higher than the ionization energy of the target. This looks like the following reaction [115]:



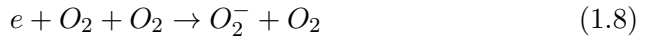
A variation on this is associative Penning ionization. In this process ionization occurs due to a bond that forms between the colliding atoms/molecules. This bonding energy contributes to the release of an electron. An example of an associative Penning ionization reaction in nitrogen is [59]:



## 1.1.2 Removal or Conversion of Charged Particles

### 1.1.2.1 Attachment

A free electron can become bound to another atom or molecule and create a negative ion. The three-body reaction with oxygen is an important attachment reaction in air [28, 138]. This reaction does not have a threshold energy and occurs at thermal energies:



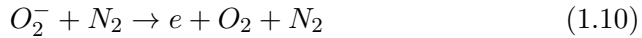
A variation on this is the dissociative attachment process. This process requires the free electron to have enough energy to break the bond of a molecule. An important reaction in air is:



This dissociative ionization reaction has a threshold energy of 4.8 eV [73].

### 1.1.2.2 Detachment

Negative ions have one or more extra electrons bound to them. These electrons can be detached by collisions with other atoms or molecules. An example of a detachment reaction in air is [89]:

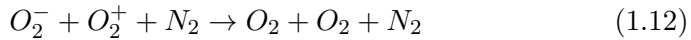


### 1.1.2.3 Recombination

Charge carriers can recombine to form neutral particles and thus reduce the conductivity of the channel. Recombination can be divided into electron-positive-ion recombination and negative-positive-ion recombination. An important electron-positive-ion recombination reaction in air is [89]:

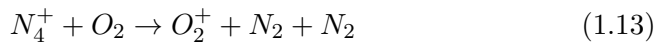


For negative-positive-ion recombination, an example of a reaction in air is [89]:

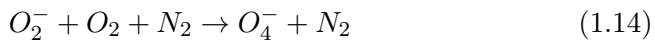


### 1.1.2.4 Ion-Conversion

Positive and negative ions can collide with other neutral targets and convert into a different positive and negative ion respectively. Because the mass of the converted ion can be different from the initial ion mass the conductivity can be affected by this. An example of a positive-ion conversion reaction in air is [89]:



An example of a negative-ion conversion reaction in air is [89]:



### 1.1.3 Swarm Parameters

A group or “swarm” of charged particles which undergoes acceleration by a constant and uniform electric field and collides with a background neutral gas (through collisions shown in the previous section) will relax towards a stationary velocity distribution. From this velocity distribution average properties of the swarm can be calculated, e.g., velocity, diffusion, energy, etc. These average properties are called swarm parameters [145].

Swarm parameters are easier to measure in experiment since individual particle collisions do not need to be resolved, only the collective behaviour of a swarm of particles is of importance. Swarm parameters are obtained for a specific electric field, gas mixture, and pressure, i.e., for a specific set of particle collisions.

As will be seen in future sections, when modelling a plasma where resolving individual collisions is computationally too expensive, models relying on swarm parameters can offer a viable alternative to gain insights on the overall plasma behaviour.

### 1.1.4 Cross Sections

After identifying the (important) collisions that can occur for the specific gas and conditions under investigation a quantity related to the likelihood of a specific collision occurring is necessary. The quantity which gives this measure is called the cross section. The cross section has units of area and is dependent on the relative velocity between colliding particles. The cross section can be thought of as the area in which two colliding particles should meet for that collision/interaction to take place. In general, cross sections are dependent on the scattering angle of the incident particle after the collisions. Cross sections dependent on scattering angle are called differential cross sections. When the differential cross sections are integrated over all scattering angles we obtain the total or integrated cross sections.

The cross section of a collision is the most important input parameter of any plasma modelling endeavour. Much care goes into choosing the “right” cross sections. Cross sections can be measured experimentally e.g. [88,

126], calculated theoretically e.g. [20, 214], or obtained by educated guess using the aforementioned swarm parameters i.e. swarm derived e.g. [6, 146]. Discussing the experimental and theoretical methods for obtaining cross sections goes far beyond the scope of this thesis, however the method of swarm derived cross sections is an important and conceptually straightforward one.

Swarm derived cross sections are obtained by inputting both known and guessed cross sections into a plasma model, calculating swarm parameters within this model, and then comparing the calculated swarm parameters to the measured swarm parameters [146]. The guessed cross sections are adapted until the calculated and measured swarm parameters (mostly the electron mobility and the ionization coefficient) are within a couple % of each other. This method is very effective at providing cross sections for processes which are important, but too difficult to investigate experimentally/theoretically. Also, this method provides a way to extend existing cross sections to an energy where measurements/calculations do not exist yet. The downside of this method is that calculated swarm parameters do not uniquely determine the input cross section set. Cross sections for similar collision processes can be adapted in different ways while still resulting in similar swarm parameters. For this reason good knowledge of the processes for which we are guessing cross sections is necessary making this a conceptually easy method, but practically difficult one to do correctly. Different models can be used to calculate swarm parameters starting from a set of input cross sections, these will be discussed in chapter 3.

## 1.2 Streamers

Discharges are electrically conductive paths created by a high enough electric field within a non-conductive medium. There are many different types of discharges which can be characterised in different ways including morphology, current, propagation mechanism, heating, being transient or stationary, and generation mechanism (e.g. microwaves or fast DC pulses). This thesis revolves around a specific type of discharge: streamers.

The streamer discharge mechanism was first proposed in [105], [113] and

[157] to explain shortcomings of the Townsend discharge mechanism prevalent at the time. The Townsend discharge can be divided into a transient non-self-sustaining and a stationary self-sustaining discharge. The transient non-self-sustaining Townsend discharge goes as follows: electrons are accelerated in an applied electric field and gain enough energy to ionize neutral gas molecules. These liberated electrons will also accelerate within this electric field and also ionize neutral gas molecules. This process repeats resulting in an exponentially growing group of electrons. This type of Townsend discharge is more commonly referred to now as an electron avalanche. When this electron avalanche reaches the cathode, the discharge stops unless a source of new electrons is provided. This source of electrons can be provided by the discharge itself through secondary emission of electrons caused by ions impacting the electrode surface. The electric field at which the secondary emission from the electrode surfaces can sustain the discharge, and thus when the transition towards the self-sustaining Townsend discharge happens, is called the breakdown field.

Experiments showed that the Townsend discharge mechanism only seemed to be valid for relatively small products of pressures  $p$  and gap lengths  $d$  with  $pd < 100 - 200$  mmHg·cm in air [158]. For larger  $pd$  values the breakdown happens at much faster timescales than the travel times of ions towards an electrode i.e. the secondary emission from the electrodes seemed to not be necessary anymore to sustain the discharge; it became electrode-material independent.

Streamers initiate in a similar way; free electrons producing electron avalanches. The major difference between the streamer discharge and that of the Townsend discharge mechanism is that the applied electric field becomes considerably distorted by the size of the electron avalanches in the streamer discharge mechanism. The large net charge layer at the front of the streamer is called the “space charge”. Additionally, the space charge layer is curved due to the non-linearity of the ionization reactions, electron drift, and the space charge itself. This curvature enhances the electric field ahead of the space charge layer. The electric field produced by the space charge is large enough to enable electrons within this field to produce electron avalanches. Streamers can therefore be defined as space charge dominated discharges.

The breakdown field is now defined more precisely as the field at which more free electrons are produced (through ionization and detachment) than lost (through attachment).

The polarity of the space charge strongly influences the properties and development of the streamer. In this thesis streamers with a positive space charge (i.e. positive streamers) were the main subject because they (at least in air) initiate easier and propagate faster and further than negative streamers as discussed in a recent and extensive review on streamer discharges [134]. This makes them preferable for comparison with experiments and for technological applications. Negative streamers were not investigated in this thesis, but they have been modelled [109] and experimentally investigated [85] before.

## 1.2.1 Positive Streamers

The discharges modelled in this thesis are streamers with a positive space charge i.e. positive streamers. Because positive streamers were only modelled in air within this thesis (both in chapter 4 and 5) we will not go into too much detail about positive streamers in other gases.

### 1.2.1.1 Propagation

The positive space charge consists of positive ions leftover after ionization events. Positive ions move about several hundred times slower than electrons and can be approximated as stationary in many cases when discussing/modeling streamers. Besides the negligible movement of the positive ions contained within the space charge at the front, electrons will move in the opposite direction of the propagation direction of the positive streamer. So how does a positive streamer propagate if the electrons move in the opposite direction and the positive ions do not move ?

The propagation of a positive streamer is best described in a couple of clearly distinct steps:

1. A positively charged electrode produces a (local) electric field above

breakdown.

2. An electron in this field will be accelerated and ionize gas molecules on its path through direct-impact ionization.
3. This avalanche of electrons propagates towards the positive electrode and leaves positive ions behind.
4. Besides direct-impact ionization, the electrons also excite gas molecules which can de-excite by emitting a photon. Dependent on the gas mixture this photon can ionize a gas molecule through photo-ionization [213].
5. The photons are emitted isotropically and so will also propagate counter the direction of the electrons. These photons can ionize gas molecules ahead of the positive ion layer left behind by the electron avalanches.
6. As the electrons leave behind a net positive space charge layer an electric field is produced by these positive ions. Due to avalanche morphology the positive space charge layer will also be curved enhancing the electric field produced by the space charge.
7. The electrons produced by photo-ionization ahead of the positive space charge layer will be accelerated by the strongly enhanced electric field of this layer and (if the field is above breakdown) trigger electron avalanches.
8. Since many electrons are produced by photo-ionization around the space charge layer, many electron avalanches develop and propagate towards the positive space charge layer.
9. These newly developed electron avalanches will neutralize the positive space charge layer.
10. Just like before, as these electrons move towards the positive space charge layer they leave behind a new net positive space charge layer.
11. The positive space charge layer has now “propagated” forward even though the positive ions were approximated to be immobile.

Remark that electron avalanches are moving inwards toward the positive space charge layer. This inward movement makes it so that the positive space charge layer does not lose its curvature. By keeping the curvature, the electric field stays enhanced and will be easier to keep above breakdown. Experiments and models have also shown that positive streamers are easier to start and can propagate faster and further than negative streamers [109].

### 1.2.1.2 Photo-ionization

When discussing the way in which positive streamers propagate, the crucial ingredient is the availability of free electrons ahead of the positive streamer so that they can be accelerated and produce avalanches towards the positive streamer tip. These avalanches leave behind a new positively charged layer which corresponds to the “movement” of the positive streamer.

These free electrons were described as being produced by photo-ionization. They can also be produced by using an ionizing laser [130, 133], or radioactive sample [132]. Photo-ionization requires photons to be of higher energy than the ionization energy of the target molecule. In air these photons are predominantly produced by the de-excitation of  $N_2$  molecules which then ionize  $O_2$  molecules as described in section 1.1.1.2.

When comparing modelling results to experiments, great care must be taken to understand what gas mixture is present in experiment. Even a small admixture to otherwise ‘pure’ gases can change the photo-ionization process drastically and thus change how to model the experiment. An example of this is pure  $N_2$  where a process exists for photo-ionization but adding only 1% of  $O_2$  to the gas makes the dominant photo-ionization process the aforementioned photo-ionization process in air [141].

## 1.2.2 Applications

Due to the strongly enhanced electric field at the streamer tip, electrons can reach energies of several eV in gases at room temperature. These high energy electrons can initiate chemical reactions at room temperature which are normally not possible. This allows streamers to be used to initiate hot chemical reactions in an environment that cannot produce or sustain these

high temperatures. Streamers are therefore used in a wide variety of applications ranging from medicine [48, 57, 98], surface disinfection [84], and ozone production [65] to propulsion [90, 99] and plasma-assisted combustion [150, 184].

## 1.3 Discharge Modelling

This section will introduce the most common methods for modelling discharges. Most of these methods are used in a specific chapter in the thesis and for more details on the details of the used model we refer to those chapters.

The choice of modelling method can be made on the basis of: required physical results, computational cost (time, memory, or storage), required level of detail, validity of the model for the research question or discharge type at hand, and of course the availability of modelling software.

### 1.3.1 Electron Boltzmann Solver

The particle distribution function describes all properties of a plasma. This function gives the density of particles within a volume in phase space, and it fulfills the Boltzmann equation [27]:

$$\frac{\partial f}{\partial t} + \mathbf{v} \cdot \nabla f + \mathbf{F} \cdot \frac{\partial f}{\partial \mathbf{p}} = \left( \frac{\partial f}{\partial t} \right)_C, \quad (1.15)$$

where  $f$  is the particle distribution function in phase space,  $\mathbf{p}$  and  $m$  are the particle momentum and mass respectively,  $\mathbf{F}$  is the force acting on the particles, and  $\left( \frac{\partial f}{\partial t} \right)_C$  represents the rate of change of  $f$  due to particle collisions. For the discharges important in this thesis we are mainly interested in the electron distribution function  $f_e$ , for which equation (1.15) is written as [61]:

$$\frac{\partial f_e}{\partial t} + \mathbf{v} \cdot \nabla f_e - \frac{e}{m_e} \mathbf{E} \cdot \nabla_{\mathbf{v}} f_e = \left( \frac{\partial f_e}{\partial t} \right)_C, \quad (1.16)$$

where  $\mathbf{v}$  is the velocity,  $e$  the elementary charge,  $m_e$  the electron mass, and  $\mathbf{E}$  the electric field. Note that magnetic effects are not included, as they

play a negligible role for the discharges considered in this thesis.

After solving equation (1.16) for  $f_e$ , typically under simplified conditions, electron swarm parameters and reaction rates can be computed from  $f_e$ . These swarm parameters are used as input for fluid models, to be discussed in section 1.3.3. Common methods and software for solving equation (1.16) are discussed and compared in detail in chapter 3.

### 1.3.2 Particle Model

For modelling plasmas, the particle model is conceptually simple: you start with some initial charged particles, an electric field, and you evolve the particles by solving Newton's second law of motion. Complexity is added when collisions and the electric field produced by the charged particles themselves are included. Note that depending on the ionization degree of the plasma, collisions between charged particles themselves can be neglected and only collisions with the neutral background gas molecules should be included. This is the case for the discharges worked on in this thesis, i.e., for streamers.

The basic algorithm of the particle model used in this thesis goes as follows:

1. Interpolate the electric field, computed on a numerical grid, to particle positions.
2. Particle movement (Newton's second law of motion).
3. Collide particle with neutral background gas molecules.
4. Compute particle densities on the numerical grid.
5. Calculate a new electric field.

This method where particles move in continuous space, but quantities like particle densities and electric fields are calculated only on discrete grid-points is called the particle-in-cell (PIC) method [68]. Although conceptually the model is simple to understand, each step comes with its own complexities.

### 1.3.2.1 Particle Movement

There are many algorithms available for advancing the particle coordinates in time, which differ in their accuracy, computation time, memory requirements, and in their energy conserving (phase space volume conserving) properties. Since many particles have to be evolved at every timestep computation time is an important factor. In this thesis, the common velocity Verlet algorithm is used [190]. It is second order accurate ( $\mathcal{O}(\Delta t^2)$ ) in the position and velocity and follows the following steps:

1. Update the position:  $\mathbf{x}(t + \Delta t) = \mathbf{x}(t) + \mathbf{v}(t)\Delta t + 0.5\mathbf{a}(t)\Delta t^2$ .
2. Calculate  $\mathbf{a}(t + \Delta t)$  based on the new particle positions  $\mathbf{x}(t + \Delta t)$  i.e.  $\mathbf{a}(t + \Delta t) = \frac{q\mathbf{E}(t+\Delta t)}{m}$  with  $\mathbf{E}$  the electric field, and  $q$  and  $m$  the charge and mass of the particle we are moving respectively.
3. Update the velocity:  $\mathbf{v}(t + \Delta t) = \mathbf{v}(t) + 0.5(\mathbf{a}(t) + \mathbf{a}(t + \Delta t))$ .

Note that we assume that the force on the particle can be calculated from the positions alone. In this thesis streamers are investigated only under influence of an applied electric field and no magnetic field. Additionally, streamers themselves do not produce a significant magnetic field [134].

### 1.3.2.2 Particle Collisions

While a particle moves it can collide with a gas molecule. In simulation we need to decide not only if a collision occurs, but also which collision occurs. In this thesis, the commonly used null-collision method [91] is used for this purpose. A first question is when a moving particle will collide with a gas molecule. To answer this question, it is convenient to define collision frequencies:

$$\nu_j(\epsilon) = \sqrt{\frac{2\epsilon}{m}}\sigma_j(\epsilon)N_j, \quad (1.17)$$

where  $\epsilon$  is the particle energy,  $\nu_j(\epsilon)$  is the collision frequency of process  $j$ ,  $m$  is the mass of the colliding particle,  $\sigma_j(\epsilon)$  is the cross section for process  $j$ , and  $N_j$  is the number density of the collision partner (gas molecule) of process  $j$ . The total collision frequency  $\nu_{tot}(\epsilon)$  is:

$$\nu_{tot}(\epsilon) = \sum_j \nu_j(\epsilon). \quad (1.18)$$

Note that equation (1.17) only takes into account the colliding particles energy/velocity. The implicit assumption made is that the velocity of the collision partner (gas molecule) is so small compared to the colliding particles velocity that it can be ignored. For low-energy processes this is no longer the case and the velocity of the collision partner needs to be taken into account. The following discussion will assume negligible gas molecule velocity however it was taken into account for the particle models used in chapter 2 and 3.

The total collision frequency depends on the particles' energy. This makes it complicated to sample a future collision time, because the particle's energy will change while it is moving. The null-collision method resolves this by adding a fictitious collision process, such that the total collision frequency is constant

$$\nu_{null}(\epsilon) = \nu_{max} - \nu_{tot}(\epsilon), \quad (1.19)$$

where  $\nu_{max} = \max(\nu_{tot}(\epsilon))$ . This fictitious collision process is called the null collision and does not change any particle properties. Because the total collision frequency (including the null collision frequency) is now constant, the time between collisions  $\Delta t_{coll}$  is exponentially distributed with a rate  $\nu_{max}$ . Samples of  $\Delta t_{coll}$  can be obtained via inverse transform sampling [38] as

$$\Delta t_{coll} = -\frac{\ln(1-U)}{\nu_{max}} = \Delta t, \quad (1.20)$$

where  $U$  is a uniform  $[0, 1)$  random number. Afterwards, the type of collision has to be determined, which depends on the collision rates  $\nu_j$  at the time of collision. The probability of the  $j^{\text{th}}$  collision occurring is given by  $\nu_j/\nu_{max}$ . Inverse transform sampling can then again be used, by comparing a uniform  $[0, 1)$  random number to the cumulative probabilities, see e.g. [191].

### 1.3.2.3 Particle Weighting

The PIC approach requires a method to map particles to densities on a numerical grid. The zeroth order approach would be to deposit the particle completely on the nearest grid point, the so-called NGP scheme [68]. This scheme is computationally cheap, but it leads to increased fluctuations.

When a particle moves closer to another grid point a sudden jump in the density of the new nearest grid point (and a fall in the density of the previous nearest grid point) is observable. The particle model used in this thesis therefore employs the common cloud-in-cell (CIC) scheme [68]. This scheme is based on linear interpolation (bilinear in 2D, trilinear in 3D), so that each particle is deposited on the nearest  $2^D$  grid points, where  $D$  is the problem dimension. The contribution to each grid point depends on the location of the particle, i.e., closer grid points receive a larger contribution.

#### 1.3.2.4 Necessity of super-particles

When all physical particles are individually evolved, memory requirements become prohibitive quickly for most realistic simulations. At a minimum, for each particle (in 3D) nine numbers need to be stored, three for the position, velocity, and acceleration coordinates. Because of accuracy demands these numbers will be stored as a 64-bit floating point number. Each individual particle will therefore require at least 576 bits or 72 bytes of memory. Now take for example the streamer simulations of chapter 5, in 80 mbar air and a 15 cm discharge gap. These streamers have a diameter of about 4 cm and an electron density of around  $10^{10} \text{ cm}^{-3}$ . A 15 cm long streamer would have a volume of about  $190 \text{ cm}^3$  thus contain around  $2 \cdot 10^{12}$  electrons. Only storing the position, velocities, and acceleration of each electron would thus require 140 Terabytes of memory.

To reduce the number of simulation particles, so-called super-particles are used. Super-particles are particles which represent more than one real particle. Combining particles which are close to each other in phase space into one super-particle can drastically reduce the memory requirements, making realistic simulations a practical possibility, see e.g. [193, 204].

#### 1.3.3 Fluid Model

In a fluid model particle densities are evolved in time on a numerical grid. Because individual particles are not resolved, the computational cost of fluid models is usually lower than that of particle models (both in memory usage and computation time). Below, we will discuss the equations that are solved, and some of the difficulties in simulating streamers with a fluid model.

### 1.3.3.1 Evolving Particle Densities

A key equation for fluid models is the continuity equation [173]:

$$\frac{\partial n}{\partial t} + \nabla \cdot \mathbf{\Gamma} = S, \quad (1.21)$$

where  $n$  is the density,  $\mathbf{\Gamma}$  is the flux, and  $S$  is a source (and sink) term. This equation states that changes in density over time are due to in- and outflows ( $\nabla \cdot \mathbf{\Gamma}$ ) and due to source terms ( $S$ ).

The streamer discharges simulated in this thesis develop on nanosecond time scales. It is often a good approximation to only consider the flux of electrons, as ions have a much larger mass and would barely move. The electron flux is commonly described as the sum of a drift and a diffusion term

$$\mathbf{\Gamma}_e = -\mu_e \mathbf{E} n_e - D_e \nabla n_e, \quad (1.22)$$

where  $\mu_e$  is electron mobility,  $D_e$  is the electron diffusion coefficient and  $\mathbf{E}$  the electric field. Note that the average drift velocity  $\mathbf{v}_e$  is given by  $\mathbf{v}_e = -\mu_e \mathbf{E}$ . The electron source term  $S$  in equation (1.21) can for example be written as

$$S = \bar{\alpha} \mu_e |\mathbf{E}| n_e + S_\gamma, \quad (1.23)$$

where  $S_\gamma$  is a photo-ionization source term and  $\bar{\alpha}$  is the net ionization coefficient  $\bar{\alpha} = \alpha - \eta$ . Here  $\alpha$  and  $\eta$  are the ionization and attachment coefficients, respectively, with inverse length units, which represent the number of electrons produced/lost by ionization/attachment processes per unit length traveled through the gas.

Putting equations (1.22) and (1.23) into equation (1.21) gives the following equation for the electron density

$$\frac{\partial n_e}{\partial t} = \nabla \cdot (\mu_e \mathbf{E} n_e + D_e \nabla n_e) + \bar{\alpha} \mu_e |\mathbf{E}| n_e + S_\gamma. \quad (1.24)$$

The electron coefficients  $\mu_e$ ,  $D_e$ , and  $\bar{\alpha}$  are examples of swarm parameters, as discussed in section 1.1.3. These swarm parameters can be calculated with an electron Boltzmann equation solver, see section 1.3.1. For the simulations performed in this thesis, it is assumed these swarm parameters

depend only on the local electric field strength, which is known as the local field approximation (LFA)[58, 82].

### 1.3.4 Calculating the Electric Field

Both fluid and particle models require the calculation of the electric field. The electrostatic approximation is used within this thesis which is a valid approximation as long as: there is no large (tens of Tesla) externally applied magnetic field [112], and the induced magnetic field of the streamer remains small (which it does within this thesis [134]). These negligible magnetic fields result in a negligible contribution of the magnetic field to the fourth Maxwell equation  $\nabla \times \mathbf{E} = -\frac{\partial \mathbf{B}}{\partial t}$ .

Using the electrostatic approximation allows us to solve for the electric field using Poisson's equation:

$$\mathbf{E} = -\nabla\phi, \tag{1.25}$$

where  $\phi$  is the electrostatic potential, which can be obtained by solving Poisson's equation:

$$\nabla^2\phi = -\frac{\rho}{\epsilon_0}, \tag{1.26}$$

where  $\rho$  is the charge density, and  $\epsilon_0$  is the dielectric permittivity. Solving Poisson's equation can be a thesis subject on its own. There are many different methods that can be used depending on boundary conditions, accuracy, grid type (structured/unstructured), and scaling with number of grid points.

In this thesis Poisson's equation was solved on structured grids with either Dirichlet (fixed potential) or Neumann (fixed electric field) boundary conditions. One of the fastest algorithms to solve Poisson's equation for these conditions is the multigrid method, which has ideal linear scaling ( $\mathcal{O}(N)$ , with  $N$  the number of grid points). Only the basic idea of the multigrid method will be explained here, for an introduction to multigrid see e.g. [21].

At the heart of the Multigrid method lie basic iterative schemes for finding a

solution to a set of linear equations like the Jacobi or Gauss-Seidel method. These iterative schemes can very quickly reduce the short-wavelength components of the error of the solution, but need significantly more iterations to reduce longer wavelength components. The Multigrid method will restrict (or downsample) the error of a fine grid to a coarser grid. The long wavelength components of the error on the fine grid correspond to shorter wavelengths on the coarse grid, due to the reduction in grid points. A basic iterative scheme is run on this coarse grid solution again to quickly reduce these short wavelength components of the error. This is the core of the Multigrid method: Restriction of the error on a fine grid to progressively coarser grids and using a simple iterative scheme to quickly reduce the short wavelength components of this error. After a sufficiently coarse grid has been reached, corrections are interpolated to the finer grids, after which the whole process can start again until a user-defined convergence criteria is met.

The models used in this thesis made use of an implementation of the multigrid method for solving Poisson's equation as described in [192].

## 1.4 Research Questions

The central theme of this thesis remained generic i.e. streamer modelling. However, a varied set of plasma models were used to answer specific questions within the field of streamer discharges. In this section we will summarize the research topics and questions addressed in this thesis.

### 1.4.1 Chapter 2: Neutral Dissociation Cross Sections of CH<sub>4</sub>

Streamers in CH<sub>4</sub> are investigated for their application in, among other things, plasma-assisted combustion [150, 184]. As previously mentioned, cross sections are the most important input data for any streamer modelling endeavour. The two most important/complete cross section sets for CH<sub>4</sub> were: the IST-Lisbon set [6], and the set gathered by Song *et al.* [180].

These cross sections differ in the way they are compiled. The IST-Lisbon set is a swarm derived set (see 1.1.4) i.e. cross sections are adjusted in a clever way as to make the electron swarm parameters derived from the

solutions of a particular electron Boltzmann solver match with those measured in experiment. The Song set is compiled through extensive literature review and is mainly comprised out of experimentally measured cross sections.

Being a swarm derived set the IST-Lisbon set produced electron swarm parameters (and thus an ionization coefficient) matching with experiments. Using the IST-Lisbon set for plasma modelling would give you the correct average behavior of the plasma electrons. However, several questions arise when working with a swarm derived set: “Is a swarm derived set suited for particle models where individual collision types have to be resolved?”, and “How correct will the rates of individual collision processes be, knowing that a swarm derived set is not unique?”.

The Song cross section set on the other hand is compiled from mainly measurements. The cross sections are not altered to match any measured swarm parameters. They are as accurate as the experiments could measure them. The problem with this set is that the resulting ionization coefficient is much higher than is the case in reality. Since streamers (any discharge) relies heavily on ionization, this makes the resulting streamer simulations not realistic. The questions we aimed to solve were: “Which processes are missing from this set and why could they not be included?”, and “Is there a way, without resorting to the swarm derived approach, to calculate/produce cross sections for these missing processes?”.

### **1.4.2 Chapter 3: Extensive Comparison of Available Electron Boltzmann Solvers**

Electron Boltzmann solvers are an essential tool within the plasma modelling community. They provide researchers with fast and easy access to swarm parameters for any gas mixture, pressure, temperature, and electric field as long as a set of cross sections can be provided.

Many researchers and research groups have developed their own solvers based on different approximations and mathematical methods. Often times these solvers are made available to other researchers through providing bi-

aries for download or uploading the source code to Gitlab/Github.

In this thesis we compared the most widely used solvers for a large collection of model gases. It is crucial to know if all these different solvers produce the same output given the same input. By defining a large and clear set of model gases, through which many aspects of the solver can be tested, more confidence in modelling results and solver quality can be obtained.

### **1.4.3 Chapter 4: Investigation of Streamer Inception in Air**

Explaining the development of a streamer always starts from an electron which produces an avalanche. In this thesis we have tried to shed more light on the origin of these streamer-initiating electrons in air. Measurements of the time between the onset of the voltage and the initiation of a streamer (detection of light using a photomultiplier tube) were compared with a particle model. We wanted to investigate if there was a preferential time after the onset of the voltage when the streamer would initiate. And if there was, why this time existed and which species or processes caused it.

Additionally, we explored the possibility of delaying or speeding up streamer inception. Being able to delay the inception of a streamer could be beneficial in applications with a pulsed power source. If the onset of a streamer discharge can be delayed to a time that would fall outside of the voltage pulse, then streamer inception can be prevented indefinitely.

This work was done in close collaboration with Dr. Shariar Mirpour who was responsible for all experimental work and measurements, while I developed simulations and understanding.

### **1.4.4 Chapter 5: Repetitive Pulsed Streamer Discharges in Air**

It is common for experiments on streamer discharges to make use of a repetitively pulsed power source. It has been observed in experiments [101, 129] that streamers can be influenced by the streamer produced in a previous pulse. In this thesis we have investigated how the plasma species produced by a positive streamer in air evolve temporally and spatially during the time

between voltage pulses. We wanted to understand which charged species remained in the discharge gap over long periods of time when no voltage pulse was applied and how these species would influence the streamer produced by the subsequent voltage pulse.

The time between voltage pulses (i.e. the interpulse time) is a major determining factor as to which species are present in the discharge gap when the subsequent voltage pulse is applied. We investigated at which interpulse times the streamer of the subsequent voltage pulse could continue (practically unhindered) from the plasma species leftover by the discharge of the previous voltage pulse.

Additionally, we investigated how gas temperature (and resulting gas dynamics) changes based on the interpulse time. If a large amount of gas heating is produced then this can have effects on plasma-chemical reaction rates and thus influence the development of subsequent streamers.

### **1.4.5 Internship at Plasma Matters b.v.**

During a 5 month period I had the pleasure to do an internship at Plasma Matters b.v. under supervision of Dr. Diana Mihailova. This internship was part of the European Training Network agreement within the SAINT project.

The main question during this internship was: How can we couple a fluid and a particle model spatially i.e. spatial hybridization and implement it into the commercial software PLASIMO. The goal was to have a predefined area of the modelling domain where a particle model should be used. This could be in close proximity to a wall to simulate the sheath region where fluid models can have problems due to the high electric field produced in a very small region (causing a very small timestep and driving the simulation to a halt/crash).

Although the implementation was not finalized during this internship, a couple of important steps were made. Added to the code is the possibility to define region of space where the software would only use the particle model. Additionally, at the boundary of these regions, the fluid model and

the particle model have to be connected. When particle cross the boundary they are added to the fluid density, but the other direction is not so trivial. Particles from the fluid should be introduced into the particle model cells, but from what energy distribution should they be sampled?

The internship at Plasma Matters b.v. did not lead to a publication, but did lead to experience in a scientific software company and in practical skills related to scientific software development.

## Chapter 2

# Neutral dissociation of methane by electron impact and a complete and consistent cross section set

We present cross sections for the neutral dissociation of methane, in a large part obtained through analytical approximations. With these cross sections the work of Song *et al.* [J. Phys. Chem. Ref. Data, **44**, 023101, (2015)] can be extended which results in a complete and consistent set of cross sections for the collision of electrons with up to 100 eV energy with methane molecules. Notably, the resulting cross section set does not require any data fitting to produce bulk swarm parameters that match with experiments. Therefore consistency can be considered an inherent trait of the set, since swarm parameters are used exclusively for validation of the cross sections. Neutral dissociation of methane is essential to include (1) because it is a crucial electron energy sink in methane plasma, and (2) because it largely contributes to the production of hydrogen radicals that can be vital for plasma-chemical processes. Finally, we compare the production rates of hydrogen species for a swarm-fitted data set with ours. The two consistent cross section sets predict different production rates, with differences of 45% (at 100 Td) and 125% (at 50 Td) for production of H<sub>2</sub> and a similar trend for production of H. With this comparison we underline that the swarm-fitting procedure, used to

## CHAPTER 2. METHANE DISSOCIATION CROSS SECTIONS

---

ensure consistency of the electron swarm parameters, can possibly deteriorate the accuracy with which chemical production rates are estimated. This is of particular importance for applications with an emphasis on plasma-chemical activation of the gas.



This chapter is largely based on the published article:

Dennis Bouwman *et al.* 2021 *Plasma Sources Sci. Technol.* **30** 075012

The current author was responsible for the calculations of cross sections, and the majority of comparisons of resulting swarm parameters with experimental measurements.

## 2.1 Introduction

### 2.1.1 Methane-containing plasmas

There are many types of plasma that contain methane ( $\text{CH}_4$ ). Proper models of their properties require cross sections for the collisions of electrons with methane molecules. The present study was particularly motivated by applications such as plasma-assisted combustion of air-methane mixtures, where electron impact dissociation accounts for most of the plasma-produced radicals during the discharge phase [185, 186]. Another combustion-related application is the production of hydrogen fuel through electron impact dissociation, referred to as low-temperature methane conversion [135]. Furthermore, methane plasmas are found in a variety of thin film applications, such as diamond synthesis by plasma-assisted vapour deposition [80]. Other applications range from modelling lightning in methane-containing atmospheres (such as Titan [86, 209]) to studies of carbon-impurities inside a tokamak [69].

### 2.1.2 Demands on cross sections

Theoretical and computational studies that underlie and enable the aforementioned applications all require a set of cross sections of electron collisions as model input. Although the requirements that are placed on a cross section data set can vary between applications, in general a set is required to be complete and consistent. Within the framework of low-temperature plasma modelling these properties are often defined according to [148] as:

- *Complete* cross section sets accurately represent all electron energy and momentum losses as well as the electron number changing processes such as ionization and attachment.
- *Consistent* cross section sets are able to reproduce measured values of swarm parameters within an order of ten percent, when used as an input to evaluate the electron energy distribution function from a Boltzmann solver.

Note that these definitions only apply to the behaviour of electron swarms. Other important demands on cross sections, such as the correct approximation of the production rates for chemical species, are not addressed.

When compiling a data set it is often found that experimental data alone is insufficient to ensure completeness and consistency, as data for crucial processes might be missing or measurements from different studies might disagree. The existence of such gaps in the literature can typically be attributed to the challenging nature of measurements for scattering processes such as: rotational and electronic excitation, dissociative attachment and, most notably, neutral dissociation [23]. Although theoretical cross section calculations can be used to supplement the experiments, such results are often constrained to specific energy ranges and are limited to simple molecules with low atom numbers. Within the framework of low-temperature plasma modelling a common method to overcome the limitations imposed by missing data is to fit presumably incorrect cross sections in order to have better agreement with measured swarm parameters [146], c.f. the IST-Lisbon data set [6]. Such data-fitting techniques are immensely enabling for their ability to produce consistent data sets in the absence of reliable measurements. However by fitting cross section data the scope of applicability of a data set is limited to describing the electron swarm behaviour of a plasma, as the rates of individual processes may have been altered significantly and the resulting cross section set can be non-unique [146, 181, 196]. In other words, plasma models using such *swarm-fitted* data sets are not guaranteed to predict production rates of individual chemical species with a high degree of accuracy.

With an eye on accurately predicting the production of reactive species, it would be a highly attractive property for a cross section set to reproduce swarm parameters without the need for any fitting procedures. For such a set consistency is an inherent trait, i.e. independent of the limitations imposed by the swarm-fitting procedure. This would be especially attractive for applications that focus on the plasma-chemical activation of the gas, since the absence of a fitting procedure gives greater confidence that the individual cross sections are close to their ‘true’ value. Moreover, an unfitted and consistent cross section set could be used in any plasma-modelling approach (e.g. hydrodynamic, multi-term Boltzmann or Monte-Carlo/PIC).

### 2.1.3 Goal of the paper

The goal of this paper is to derive cross sections for the neutral dissociation of the ground state of  $\text{CH}_4$  by electron impact. Secondly, we want to

show that these cross sections in combination with data on other relevant scattering processes in  $\text{CH}_4$  produces a complete and consistent data set without the need for any data fitting. Our efforts are documented in two parts: in section 2.2, we will review experimental and theoretical literature on the electron collision cross sections of  $\text{CH}_4$ . We highlight a gap in the literature corresponding to the neutral dissociation processes. In order to fill in this gap we propose a blend of empirical and analytical cross sections for the neutral dissociation processes in the energy range up to 100 eV. In section 2.3 we show that the addition of our cross sections to the recommendations of [180] produces a complete and consistent data set *without* the need for any data-fitting techniques. By performing a Boltzmann analysis in pure methane we show that the agreement between calculated and measured swarm parameters is within error margins.

Finally, in section 2.4 we compare the production of hydrogen species as given by our cross section set and the IST-Lisbon data set [6]. The observed differences underline the issue regarding the non-uniqueness of swarm-fitted cross section sets.

#### 2.1.4 Relation to earlier work

An extensive data evaluation regarding electron scattering with  $\text{CH}_4$  was published by [180]. In their work they recommend cross section values for most of the electron-neutral collisions: momentum-transfer [5, 43, 46, 96, 168], vibrational excitation [96], ionization [103] and dissociative electron attachment [160]. However, recommendations for the neutral dissociation processes have explicitly not been made due to inconsistencies in the available data. In section 2.3 we demonstrate, by performing a Boltzmann analysis in pure methane, that simply neglecting these processes results in an ionization rate that is a factor ten larger than experimentally observed (This behaviour has also been documented in [51]). The reason for this is that neutral dissociation processes are an important sink of electron energy that must be incorporated.

Approximations for the missing cross sections of the electron impact dissociation processes are also presented by [51]. In essence, they employ a variation of the approximation technique formulated by [44, 45]. The latter is also thoroughly discussed and evaluated in this study. The variant that [51] have used contains more fitting parameters in their low-energy

approximation. Also by reordering the formulae, their variant requires the total (neutral and ionizing) cross sections into  $\text{CH}_3$  as an input parameter (which they have obtained from [123]) instead of the total neutral dissociation. To avoid having to discuss two variants of the same approximation technique we have chosen to only include the original approximation technique formulated by [44, 45] in our analysis.

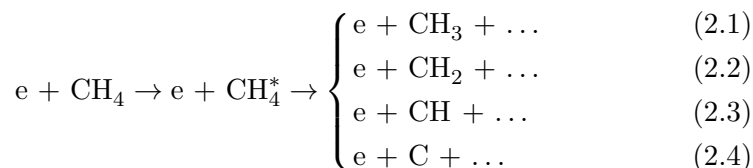
Data for a wider range of hydrocarbon collision processes in a near-wall fusion plasma have been assembled by [75, 163]. The interest in that work is the complete breakdown chain of methane, ethane and propane, so including neutral and charged dissociation cross sections for electron impact on  $\text{C}_x\text{H}_y$  with  $1 \leq x \leq 3$  and  $1 \leq y \leq 2x + 2$ . Because of the paucity of data the emphasis in the work of Janev and Reiter, especially in the more recent work [163] for the case of neutral dissociation, is on the development of physically plausible functional forms for the cross sections for all target hydrocarbons. The data in [75, 163] are valuable and widely used for simulations of fusion plasma with carbon-based wall material where collisions involving many distinct hydrocarbon radical fragments are important. For our application to collisions with  $\text{CH}_4$  alone the data in [75, 163] are lacking validation and uncertainty estimates, so for us the starting point is [180] which we supplement with neutral dissociation cross sections validated to swarm data.

## 2.2 Compilation of unfitted cross sections for neutral dissociation of $\text{CH}_4$

We will start by evaluating the literature regarding neutral dissociation. We address the same inconsistencies as were found by [180], but for energies as high as 100 eV. We then proceed by formulating our approximation for the cross sections of this process. We will lay an emphasis on the energy range of up to 100 eV, relevant for low temperature plasmas. Note that some of our proposed cross sections extend up to 500 eV, however such high energies are not shown because they have a negligible contribution on the computation of swarm parameters in numerical swarm experiments, which we will use to evaluate these approximations in section 2.3.

### 2.2.1 Neutral dissociation of CH<sub>4</sub>

The dissociation processes of methane generally occur through electronic excitation of the molecule to an intermediate state[214]. All of the electronically excited states of methane are short-lived (Mostly between 5-10 fs, none longer than 20 fs[214]. In comparison, typical collision times at 1 bar are 400 fs) and are dissociative or subject to auto-ionization, hence the intermediate electronic excited state can generally be omitted from consideration [180]. For the excitations that lead to neutral dissociation several channels have to be considered:



The cross sections of these neutral dissociation processes are denoted by  $\sigma_i$  with  $i$  representing the particular dissociated methane fragment: CH<sub>3</sub>, CH<sub>2</sub>, etc.

The body of literature regarding the neutral dissociation cross sections is sparse. For instance, no direct measurements below 100 eV exist for  $\sigma_{\text{CH}}$  and  $\sigma_{\text{C}}$ . However, cross sections for the neutral dissociation into specific excited states, e.g. CH( $A^2\Delta$ ) and CH( $B^2\Sigma^-$ ), have been determined by [170]. For the remaining dissociation processes, the experimental observations are in disagreement and theoretical results are only available for a narrow energy range of 10 eV to 16.5 eV. In figure 2.1 we have shown a selection of the experimental results evaluated by [181] of  $\sigma_{\text{CH}_3}$  and  $\sigma_{\text{CH}_2}$  for electron energies up to 100 eV. The relative overall (combination of statistical and systematic uncertainties) experimental uncertainty accompanying these measurements are  $\pm 100\%$  for [125, 126],  $\pm 30\%$  for [123] and  $\pm 20\%$  for [111]. In this figure we have also supplied the fitted cross sections from the IST-Lisbon data set [6], our recommendations which are derived at the end of this section, and the isolated measurements of [114] for  $\sigma_{\text{CH}_3}$ ,  $\sigma_{\text{CH}_2}$  and  $\sigma_{\text{CH}}$  at 100 eV. No measure of uncertainty was supplied for the measurements by Melton and Rudolph.

In figure 2.2 we zoom in and compare the values of  $\sigma_{\text{CH}_3}$  up to 40 eV from the experimental observations mentioned above with the results from

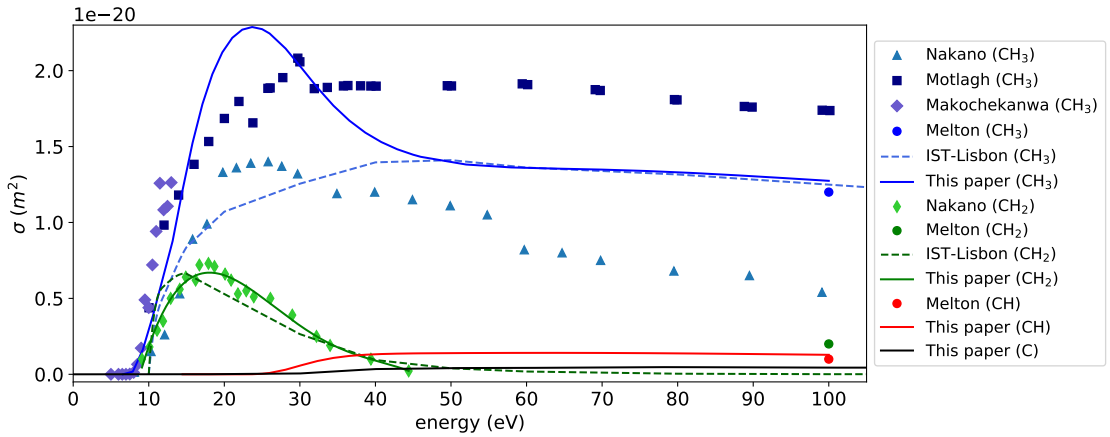


Figure 2.1: An overview of experimental values for neutral dissociation cross sections of each channel together with the fitted values from IST-Lisbon [6] and our proposed values, within the considered energy range up to 100 eV. The shown measurements are from: [125, 126], [123], [111], and [114]. Note that these measurements do not agree with each other.

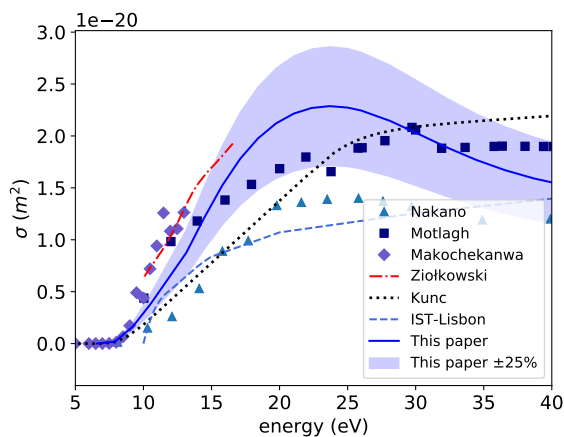


Figure 2.2: A zoom on the low-energy range of the cross sections of neutral dissociation into  $\text{CH}_3$  together with our recommendations (including a  $\pm 25\%$  deviation). The shown values are obtained *experimentally*: [125, 126], [123], and [111], *theoretically*: [214], by *semi-empirical approximations*: [44, 45] or by *swarm fitting*: IST-Lisbon [6]. Note the agreement between Ziolkowski and Makochekanwa.

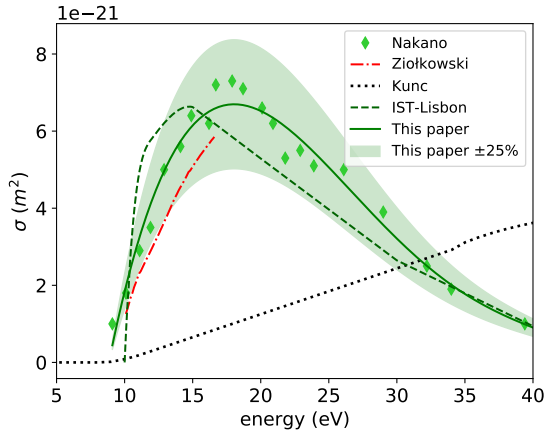


Figure 2.3: A zoom on the low-energy range of the cross sections of neutral dissociation into  $\text{CH}_2$  together with our recommendations (including a  $\pm 25\%$  deviation). The shown values are obtained *experimentally*: [125, 126] *theoretically*: [214], by *semi-empirical approximations*: [44, 45] or by *swarm fitting*: IST-Lisbon [6]. Note the agreement between Ziolkowski and Nakano.

theoretical calculations by [214] and with the approximations from [44, 45]. Note the agreement between recent experimental and theoretical results from [111] and [214] which shows a sharp increasing cross section in the near-threshold region. Based on this agreement and the fundamental nature of their work, [214] conclude that their prediction and the measurements of [111] of  $\sigma_{\text{CH}_3}$  are more reliable than the results of [125, 126] and [44, 45]. Furthermore, [214] observe that within their considered energy range, 10 to 16.5 eV, their predictions match with [123]. However when transposing their measured relative cross sections to an absolute scale, Motlagh and Moore only considered neutral dissociation into  $\text{CH}_3$ . This means that the contributions due to  $\sigma_{\text{CH}_2}$ ,  $\sigma_{\text{CH}}$  and  $\sigma_{\text{C}}$  are neglected. Although these cross sections are not known exactly we estimate, based on the measurements of [125, 126], that the cross sections for  $\sigma_{\text{CH}_2}$  are considerable in the region between the threshold energy (which can be estimated to lie around 7.5 eV) and 20 eV. For this reason we do not use the measured cross sections for neutral dissociation into  $\text{CH}_3$  from [123].

A zoomed-in view of  $\sigma_{\text{CH}_2}$  is shown in figure 2.3. In this case the only

experimental observation for energies below 40 eV are reported in [125, 126]. Contrary to their results for  $\sigma_{\text{CH}_3}$ , the values of  $\sigma_{\text{CH}_2}$  are in excellent agreement with the theoretical predictions from [214] in the near-threshold energy region. Moreover, the approximation by [44] deviates significantly from the aforementioned results, as it does not portray the sharp rise for low energies. This qualitative difference might be attributed to the absence of any data calibration, aside from fixing a threshold energy, of the low-energy ( $< 50$  eV) approximation of [44]. For these reasons, [214] conclude that their results and the measurements of [125, 126] for the dissociation into  $\text{CH}_2$  are more reliable.

### 2.2.2 Our proposed cross sections

In the previous section it was discussed, relying on the advancements regarding neutral dissociation cross sections in the low-energy regime [111, 214], that the only available measurements for dissociation into  $\text{CH}_3$  across a wide energy range (i.e. [123] and [125, 126]) are unsatisfactory.

For this reason we resort to an alternative method to obtain cross sections for neutral dissociation into  $\text{CH}_3$ , following [75] and [45] with support from measurements of [207]. [207] observed that for energies above 50 eV the total dissociation cross section is split equally between neutral and ionizing dissociation, suggesting a common mechanism. [75] describe the common mechanism as: “[...] excitation of a dissociative state which lies in the ionization continuum. Autoionization of this state leads to dissociative ionization, while its survival leads to dissociation to neutrals.” They conclude from this that cross section branching ratios within the neutral dissociation channel should match cross section branching ratios within the ionized dissociation channel. [45] treat these branching ratios in a similar manner. Therefore, consistent with [75] and with [45] we chose to employ for electron impact energies above the threshold for ionizing dissociation the following functional approximation for  $\sigma_{\text{CH}_3}$ :

$$\sigma_{\text{CH}_3} = \frac{\sigma_{\text{ND}}}{\sigma_{\text{ID}}} (\sigma_{[\text{CH}_3^+ + \text{H}]} + \sigma_{[\text{CH}_3 + \text{H}^+]}),$$

for  $\epsilon \geq \epsilon_c$ ,

(2.5)

with  $\sigma_{\text{ID}}$  the cross section for total ionizing dissociation,  $\sigma_{\text{ND}}$  the cross section for total neutral dissociation,  $\sigma_{[\text{CH}_3^+ + \text{H}]}$  and  $\sigma_{[\text{CH}_3 + \text{H}^+]}$  correspond

	$\epsilon_{\text{ND}}$ (eV)	$\epsilon_b$ (eV)	$\epsilon_c$ (eV)	$\sigma_i^{(2)}(\epsilon_c)$ (m <sup>2</sup> )	$a$ (m <sup>2</sup> )	$p$
$\sigma_{\text{CH}_3}$	7.5	10.5	13.16	$8.8 \cdot 10^{-21}$	$1.5 \cdot 10^{-20}$	1.5
$\sigma_{\text{CH}}$	15.5	18.5	22.37	$2.9 \cdot 10^{-27}$	$1.3 \cdot 10^{-26}$	1.6
$\sigma_{\text{C}}$	15.5	18.5	22.37	$6.8 \cdot 10^{-29}$	$3.1 \cdot 10^{-28}$	1.6

Table 2.1: The parameters used for the low-energy approximations of our proposed cross sections.

to cross sections of specific ionizing dissociation by electron impact and  $\epsilon_c$  is the lowest energy at which “reliable” experimental cross sections are available. For ionization processes we adopted the cross sections reported by [103], as is recommended in [180]. Furthermore, the value of  $\sigma_{\text{ND}}$  can be obtained by subtracting the total ionizing dissociation from the total dissociation:

$$\sigma_{\text{ND}} = \sigma_{\text{TD}} - \sigma_{\text{ID}}, \quad (2.6)$$

with  $\sigma_{\text{TD}}$  the cross section for the total dissociation reported by [207]. Fitting functions reported in [178] were used for  $\sigma_{\text{TD}}$ , all ionizing dissociation cross sections, and the dissociative electron attachment cross sections. More details on these fitting functions and their parameters can be found in 2.A. We can recover the initial observation of Winters by taking  $\sigma_{\text{ND}} = \sigma_{\text{ID}}$ , which generally holds for energies above 50 eV. Note that the approximation from equation 2.5 only holds for energies above the threshold energies of the corresponding ionizing dissociation reactions.

However, neutral dissociation reactions have a lower threshold energy than their respective ionizing reactions and therefore also occur at energies below the ionization threshold. Thus for energies below the respective ionizing dissociation thresholds we apply the low-energy approximation method of Erwin and Kunc. Here we only present the final result applied to  $\sigma_{\text{CH}_3}$  used in our work, for a detailed discussion we refer to the original work [44]. In this method the below-ionization energy range is divided in a near-threshold range,  $\epsilon_{\text{ND}} \leq \epsilon \leq \epsilon_b$ , and a linear-growth range  $\epsilon_b \leq \epsilon \leq \epsilon_c$ . Here  $\epsilon_{\text{ND}}$  represents the threshold energy for neutral dissociation,  $\epsilon_b$  represents the energy value separating the near-threshold range from the linear growth

range. Then the near-threshold cross section is given by:

$$\sigma_{\text{CH}_3} = a \left( \frac{\epsilon}{\epsilon_{\text{ND}}} - 1 \right)^p, \quad \text{for } \epsilon_{\text{ND}} \leq \epsilon \leq \epsilon_b, \quad (2.7)$$

with  $a$  and  $p$  positive constants. For the linear-growth range the cross section are blended with the relation from equation (2.7) as follows:

$$\sigma_{\text{CH}_3} = \sigma_{\text{CH}_3}^{(1)}(\epsilon_b) + \frac{\sigma_{\text{CH}_3}^{(2)}(\epsilon_c) - \sigma_{\text{CH}_3}^{(1)}(\epsilon_b)}{\epsilon_c - \epsilon_b} (\epsilon - \epsilon_b), \quad \text{for } \epsilon_b \leq \epsilon \leq \epsilon_c, \quad (2.8)$$

with blending-parameter  $\sigma_{\text{CH}_3}^{(1)}(\epsilon_b)$  representing the value of the cross section evaluated at  $\epsilon_b$  as calculated from equation (2.7), and  $\sigma_{\text{CH}_3}^{(2)}(\epsilon_c)$  the value of the experimentally-obtained cross section at corresponding energy  $\epsilon_c$  corresponding to equation (2.5). As can be seen, equations (2.5)-(2.8) determine the cross section for neutral dissociation into  $\text{CH}_3$  for the whole energy range.

The cross sections for the neutral dissociation into  $\text{CH}$  and  $\text{C}$  are obtained analogously. The values for the parameters  $\epsilon_{\text{ND}}$ ,  $\epsilon_b$ ,  $\epsilon_c$ ,  $\sigma_i^{(2)}(\epsilon_c)$ ,  $a$  and  $p$  used in our work are given in table 2.1. The parameters for  $\sigma_{\text{C}}$  are not covered by [44], but here they are obtained following the same reasoning for the parameters of  $\text{CH}$ .

Although the approximations defined in equations (2.5)-(2.8) can be used for any of the neutral dissociation channels, they are only used for  $\sigma_{\text{CH}_3}$ ,  $\sigma_{\text{CH}}$  and  $\sigma_{\text{C}}$ . For the remaining neutral dissociation process,  $\sigma_{\text{CH}_2}$ , relying on the experimental observations by [125, 126] is preferred over the application of a similar approximation, due to the agreement with theoretical predictions by [214]. Thus, in this study we take  $\sigma_{\text{CH}_2}$  to be given by a fourth-order polynomial fit through the measurements of Nakano *et al.*. We refer to 2.A for the fitting parameters.

Our proposed cross sections for the neutral dissociation processes are shown in figures 2.1-2.3. For  $\sigma_{\text{CH}_3}$  the qualitative trend of our proposed cross section is similar to the results from [111] and [214] in the near-threshold energy region, although it appears shifted to higher energies

by around 1.5 eV. Our proposed cross sections have a maximum value of  $2.29 \cdot 10^{-20} \text{ m}^2$  at 24 eV, which is higher than any of the experimental results. After attaining this maximum the value decays and eventually agrees with the isolated measurement of [114] at 100 eV. Note also that for energies above 50 eV our proposed value corresponds to the fitted values from the IST-Lisbon set [6]. Our proposed values for  $\sigma_{\text{CH}_2}$ , based on the measurements of [125, 126], vanish for energies above 45 eV. This contradicts with the measurements from [114], which suggest that the cross section should be around  $1.95 \cdot 10^{-21} \text{ m}^2$  at 100 eV. This difference is also recognized by [125, 126]. To the best of our knowledge, there is currently no straightforward method to reconcile these two observations. Moreover, our proposed cross sections agree (qualitatively) with the fitted counterparts from the IST-Lisbon set [6], although the latter appears to have shifted the peak to lower energies by approximately 4 eV. For  $\sigma_{\text{CH}}$  and  $\sigma_{\text{C}}$  there is little literature to compare with aside from observing that our approximation of  $\sigma_{\text{CH}}$  agrees with the isolated measurement of Melton and Rudolph at 100 eV. Furthermore, we can compare our values of  $\sigma_{\text{CH}}$  with the results for the neutral dissociation into the excited fragments  $\text{CH}(A^2\Delta)$  and  $\text{CH}(B^2\Sigma^-)$  which have been determined by [170]. It should hold that the dissociation into specific excited fragments is lower than  $\sigma_{\text{CH}}$ . As shown in figure 2.4 this behaviour generally holds. Only in the vicinity of the threshold, i.e. below 25 eV, do we observe that the cross sections for dissociation into excited fragments are higher than our proposed value. However, this discrepancy is small compared to the dominant inelastic scattering processes and will therefore be negligible within the context of the swarm experiments that are presented in the following sections.

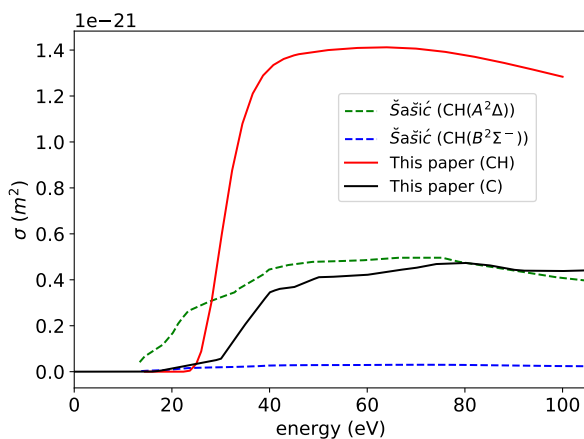


Figure 2.4: The cross sections  $\sigma_{\text{CH}}$  and  $\sigma_{\text{C}}$  used in our work alongside the experimentally-derived cross sections into specific excited fragments by [170]. The latter should always be smaller than  $\sigma_{\text{CH}}$ . This holds in general, aside from a small discrepancy in the vicinity of the threshold, i.e. below 25 eV.

## 2.3 Comparison of calculated and measured swarm parameters

Within the framework of low-temperature plasma modelling, a computation of swarm parameters is performed routinely, typically for reduced electric fields ( $E/N$ ) between 0.1 Td and 1000 Td, with  $E$  representing the electric field and  $N$  the number density of the gas. In a fluid description of electron swarms (e.g. [169] and references therein) the electrons are described by their density only and this density obeys a reaction-drift-diffusion equation governed by swarm parameters: diffusion coefficient  $D$ , mobility  $\mu$  and by coefficients for ionization  $\alpha$  and attachment  $\eta$ . Moreover, the characteristic energy  $D/\mu$ , reduced mobility  $\mu N$  and reduced Townsend ionization coefficient  $\alpha/N$  are functions of the reduced electric field  $E/N$  only (for a not too large electric fields). These swarm parameters can be obtained, given the gas composition and a cross section data set, by solving the Boltzmann equation [50].

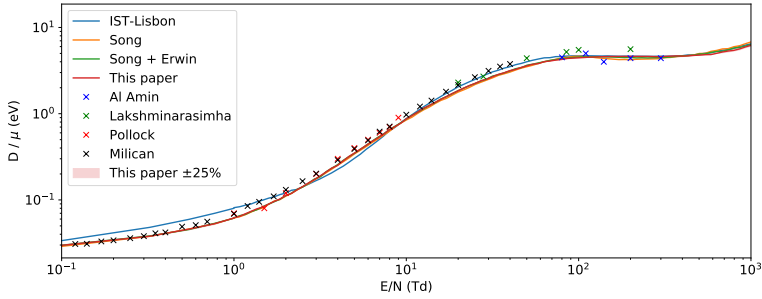
In this section we will use the difference between computed and measured swarm parameters as an implicit metric to evaluate the cross sections for neutral dissociation in conjunction with the recommendations from [180] (neglecting rotational excitations since these are already accounted for in the elastic momentum-transfer cross section). Note that explicit evaluation of the cross sections for neutral dissociation processes is not possible due to disagreement in the available literature, as was shown in section 2.2.1. On the other hand, the swarm parameters of a methane plasma are well-known, with the exception of the attachment coefficient. This can be seen from a compilation made in [6] of measurements containing observations for reduced mobility  $\mu N$ , characteristic energy  $D/\mu$ , and the reduced Townsend ionization coefficient  $\alpha/N$  [7, 32, 35, 37, 67, 70, 97, 102, 116, 149, 177]. Assuming that the recommendations by [180] have a sufficiently low error margin, any disagreement between calculated and measured swarm parameters must imply that the remaining cross sections, i.e. the neutral dissociation processes, are inaccurate. We will compare bulk swarm parameters as computed by the Monte-Carlo solver *particle\_swarm* [142] based on the modelling framework presented in [191]. The simulations are performed at standard temperature and pressure. We emphasize that we show the bulk coefficients and that the characteristic energy is based on the transversal

diffusion coefficient. The swarm parameters have been computed for four cross section data sets:

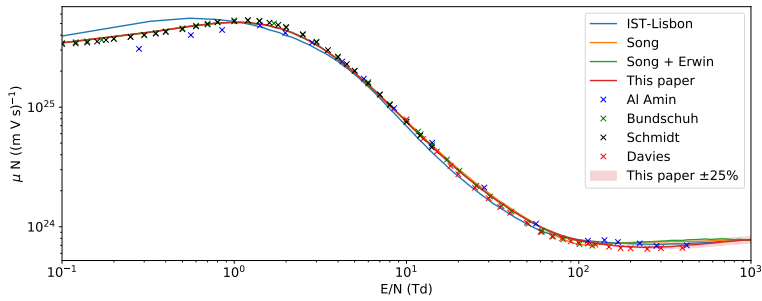
1. the *swarm-fitted* IST-Lisbon database [6],
2. the recommendations by [180] (lacking any neutral dissociation process),
3. the recommendations by Song *et al.* in conjunction with the original approximations by Erwin and Kunc [44, 45] for neutral dissociation,
4. the recommendations by Song *et al.* in conjunction with our approximations for neutral dissociation.

Moreover, for data set (4) we have included the effect of varying our proposed cross sections for neutral dissociation by  $\pm 25\%$ . This results in an upper and lower bound for the reproduced swarm parameters. These bounds define a range which we will refer to as the sensitivity interval. This interval is included to illustrate the effect that possible errors on the cross sections for neutral dissociation might impose on the computed swarm parameters.

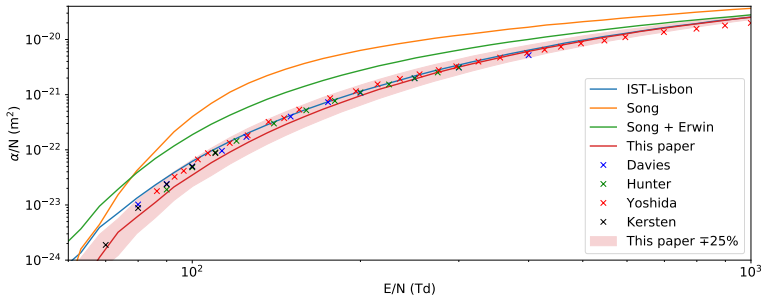
In figures 2.5a-2.5c we have respectively shown the characteristic energy, mobility and ionization from numerical and experimental studies on a double logarithmic scale. All of the considered data sets reproduce the characteristic energy within an error margin of 20% and the mobility within an error margin of 7.5%, as can be seen in figures 2.5a and 2.5b. One exception to this can be found at reduced electric fields below 10 Td. Where data set (1) exhibits deviations from the measured values (and the respective error margins) of the characteristic energy (25%) and the mobility (15% between 1 Td and 10 Td and 30% below 1 Td). On the other hand the ionization coefficient, in figure 6, varies strongly between different data sets. Data set (2) overshoots the measured values by as much as a factor of ten. Clearly the neutral dissociation of methane plays a vital role in determining the electron number changing processes and must be incorporated. Even though adding the cross sections for neutral dissociation from Erwin and Kunc reduces this discrepancy, the corresponding data set (3) still exhibits notable discrepancies with measured ionization coefficients. Given the high values of the ionization coefficient it appears that data sets (2) and (3) critically underestimate the sinks for electron energy. This can be explained



(a) characteristic energy  $D/\mu$



(b) reduced mobility  $\mu N$



(c) reduced Townsend ionization coefficient  $\alpha/N$

Figure 2.5: Measured and calculated values of the swarm parameters in pure methane. The shaded red region corresponds to the sensitivity interval, obtained by including a  $\pm 25\%$  deviation on the neutral dissociation processes. Overestimating the neutral dissociation leads to underestimating the ionization, and vice versa, hence the use of the ‘ $\mp$ ’ sign in 2.5c. Our cross section set reproduces swarm parameters within a few tens of percent.

by considering that the underestimation of energy losses means that an electron is more likely to obtain energies above the ionization potential and subsequently the rate of ionization increases. By inspecting figures 2.2 and 2.3, one can observe that for electron energies below 25 eV the values from Erwin and Kunc are lower than (most of) the other reported values. This behaviour is especially pronounced for dissociation into  $\text{CH}_2$ . For swarm experiments in general, the electrons in this energy regime play a dominant role in determining swarm parameters as the abundance of electrons typically reduces strongly for higher electron energies. Therefore the effect of omitting or underestimating the neutral dissociation processes as is done in data sets (2) and (3) can be expected to introduce large discrepancies in the computed ionization coefficient, as is also seen in figure 2.5c.

Such an overestimation of the ionization coefficient is not present for the other considered data sets. The swarm-fitted data set (1) reproduces the ionization coefficient with a maximum deviation of 25% in the region between 100 Td and 800 Td. However below 100 Td the deviations starts to increase. For instance, at 90 Td this deviation exceeds 40%. The large accuracy between 100 Td and 800 Td is to be expected from data sets which employ fitting procedures to ensure completeness and consistency. At 1000 Td the deviation is around 35%. The reproduction of the ionization coefficient is also observed for our approximations in conjunction with Song *et al.*, data set (4), with a maximum deviation up to 35% (at 100 Td). This is somewhat larger than observed for data set (1). For reduced electric fields below 100 Td our reduced Townsend ionization coefficient is closer to measurements than data set (1). Notably, up to 500 Td it can be observed that our reduced Townsend ionization coefficient is consistently lower than experimentally observed ionization coefficient. This indicates, if one assumes that the ionizing cross sections are sufficiently accurate, that the sum of all non-ionizing inelastic cross sections used here is probably an overestimation.

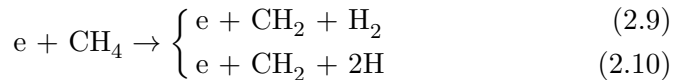
Furthermore, from the sensitivity interval corresponding to data set (4) we can conclude that the reproduction of characteristic energy and mobility is almost completely independent of the neutral dissociation processes. In contrast, the sensitivity interval for the ionization coefficient shows a significant spread. This again underlies that neutral dissociation processes are an important electron energy sink, at least within the context

of low-temperature plasmas. Moreover, the measured values of the reduced Townsend ionization coefficient lie within the sensitivity interval, indicating that a small adjustment ( $< 25\%$ ) of the proposed cross sections can account for the observed deviations regarding this swarm parameter.

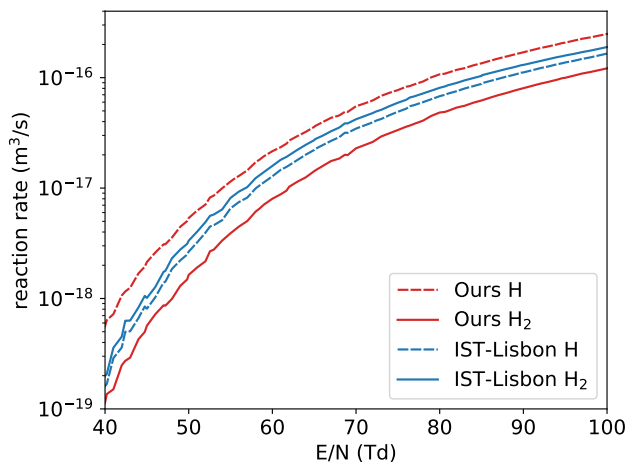
## 2.4 Production rates for hydrogen radicals

In the previous section we have introduced two consistent data sets: IST-Lisbon (1) and Ours (4). The fundamental difference between these two sets is that (4) is unfitted and consistent, whereas (1) employs a fitting procedure to ensure reproduction of swarm parameters. The use of such data-fitting techniques has already been discussed in section 2.1.2. Here we will illustrate how both data sets predict the production of atomic and molecular hydrogen by inspecting the sum of the reaction rates of hydrogen-producing electron collisions as calculated by a Monte-Carlo solver [142] based on the modelling framework presented in [191]. The simulations are performed at standard temperature and pressure.

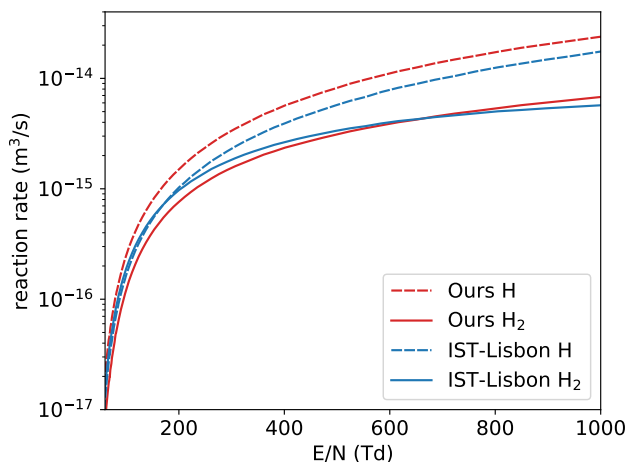
In order to make such a comparison we need ratios regarding the by-products of dissociative electron collisions. However, such data is virtually non-existent. For example: there are no cross sections which distinguish the neutral dissociation processes:



It is known that the dissociation energy of the relatively strong hydrogen bond is 4.52 eV, therefore it can be expected that due to this additional energy barrier the reaction rate of equation (2.10) will be lower than equation (2.9). However, without direct observations such arguments will always remain qualitative. For the current purpose of comparing the radical yields of the two data sets, we will assume that the composition of hydrogen products will always be in the lowest energy state. In other words, we assume that reactions like equation (2.10), which requires additional energy for dissociation, will not occur. The effect is that we will underestimate atomic hydrogen yield, and subsequently overestimate the production of molecular hydrogen.



(a) Low  $E/N$



(b) High  $E/N$

Figure 2.6: The predicted reaction rates for the production of the hydrogen species H and H<sub>2</sub> for the (swarm-fitted) IST-Lisbon set and Ours (unfitted). Although both cross section sets can be considered consistent (which refers to behaviour of electron swarms only), they exhibit clear differences in the prediction of hydrogen species production.

With this assumption, the reaction rates for hydrogen production have been calculated for both data sets; they are shown in figure 2.6. It can be seen that data set (1) predicts atomic hydrogen yields, approximately 35% lower than (4) above 100 Td. Similar deviations are also observed for the molecular hydrogen production. For instance, above 100 Td the maximum deviation is 45%. However, for reduced electric fields below 100 Td the deviations between the predictions of production rates for molecular hydrogen are increasing. For instance, at 50 Td data set (1) predicts a molecular hydrogen yield which is 125% higher than data set (4). For atomic hydrogen we find a difference around 50% at 50 Td.

These deviations between the production rates of chemical species of two consistent sets clearly illustrate the non-uniqueness of swarm-fitted data sets. Whether the errors on the production rates for chemical species introduced by relying on data-fitting are tolerable is always dependent on the application and the extent of adjustments performed. However, given the highly reactive nature of atomic hydrogen and the nonlinear nature of plasma-chemical applications, such deviations have to be treated with care.

## 2.5 Summary and Outlook

### 2.5.1 Summary

The main contribution of this article are the cross sections for the neutral dissociation of the ground state of  $\text{CH}_4$  by electron impact. Secondly, we have used these values to arrive at a complete and consistent cross sections for electron collisions with methane for reduced electric fields between 0.1 Td and 1000 Td, without relying on any data-fitting techniques. This data set is largely based on the recommendations of [180], with the addition of a blend of empirical and analytical cross sections for the remaining neutral dissociation processes.

Furthermore this work includes a Boltzmann analysis using a Monte-Carlo solver. We have shown that the presented set of cross sections reproduces measured swarm parameters with maximum deviations of: 35% for ionization, 7.5% for mobility and 20% for characteristic energy.

The presented cross section set distinguishes itself from other data sets by not relying on any data-fitting techniques to ensure consistency. This

feature makes our cross section set independent of the limitations imposed by the swarm-fitting procedure. This can be especially attractive for applications that focus on plasma-chemical activation of the gas, such as plasma-assisted vapour deposition, low-temperature methane reforming, etc. Moreover, the absence of any data fitting means that the presented cross section set can be used in a variety of plasma-modelling approaches (e.g. hydrodynamic, multi-term Boltzmann or Monte-Carlo/PIC).

## 2.5.2 Outlook

The validity of the cross sections proposed in this work has been considered by comparing measured and calculated swarm parameters. In principle this is an implicit metric, since the set of cross sections as a whole is considered as opposed to individual cross sections. However, in section 2.3 we have assumed that the recommendations of [180] have a sufficiently low error margin such that deviations in the reduced Townsend ionization coefficient can be primarily attributed to the proposed cross sections for neutral dissociation. Although this assumption enables much of the steps taken in this work, it does not give explicit certainty. One way to improve on this is by studying the swarm parameters of mixtures of methane with rare gases [146]. For example, the swarm parameters in Ar-CH<sub>4</sub> mixtures are studied by Sebastian and Wadehra [175]. Still, benchmark experiments for individual cross sections remain highly desirable if the difficulty of diagnosing neutral radical fragments can be overcome.

On the side of computation it would be very desirable to see work in the style of [214] (based on R-matrix calculations of electron excitation of methane followed by quasi-classical trajectory simulations with surface hopping) extended to higher electron collision energy than 17 eV. The work of [20] highlights some electronic structure issues with these computations and in particular they recommend a multi-reference configuration interaction approach to deal with the multiply-excited target states that are important at high impact energy. (However, the neutral dissociation cross section calculations in [20] are limited to electron impact energies below 15 eV and they do not supplant the results from [214]). Such R-matrix calculations and trajectory simulations would naturally predict branching ratios between 2H and H<sub>2</sub> channels as well, although an assessment of the importance of zero-point energy (quantized vibrational energy in molecular

fragments) should be made. However, there are tools (such as ring polymer Molecular Dynamics [60]) to incorporate this quantum effect into trajectory calculations.

## Acknowledgements

The authors would like to thank Grzegorz Karwasz and Jonathan Tennyson for their expertise and valuable feedback during correspondence.

## Availability of data

The data set will be made available on [www.lxcat.net](http://www.lxcat.net) [25]. Furthermore, cross sections obtained in this study are also available in analytical form and as tabulated data in 2.A and 2.B, respectively. The code for the Monte-Carlo Boltzmann solver can be found on [www.gitlab.com/MD-CWI-NL/particle\\_swarm](https://www.gitlab.com/MD-CWI-NL/particle_swarm) with the version used identified by the commit hash `e04a5644` made on 25th of May 2021.

# Appendix

## 2.A Fitting functions and parameters for used and reported cross sections

The cross sections for total neutral dissociation, all dissociative ionization processes, and dissociative electron attachment were obtained from fits through the data points reported in tables by [180]. The functions used were those reported in [178]. The fitting parameters were obtained again for this paper.

### 2.A.1 Basis functions

[178] used 3 basis functions from which the fitting functions were created:

$$f_1(x) = \sigma_0 a_1 \left( \frac{x}{\epsilon_R} \right)^{a_2}, \quad (2.11)$$

$$f_2(x) = \frac{f_1(x)}{\left[ 1 + \left( \frac{x}{a_3} \right)^{a_2+a_4} \right]}, \quad (2.12)$$

$$f_3(x) = \frac{f_1(x)}{\left[ 1 + \left( \frac{x}{a_3} \right)^{a_2+a_4} + \left( \frac{x}{a_5} \right)^{a_2+a_6} \right]}, \quad (2.13)$$

with  $\sigma_0 = 1 \cdot 10^{-20} \text{ m}^2$ ,  $\epsilon_R = 1.361 \cdot 10^{-2} \text{ keV}$  (Rydberg constant), and  $a_i$  the parameters which will be obtained for each specific reaction by fitting the data points.

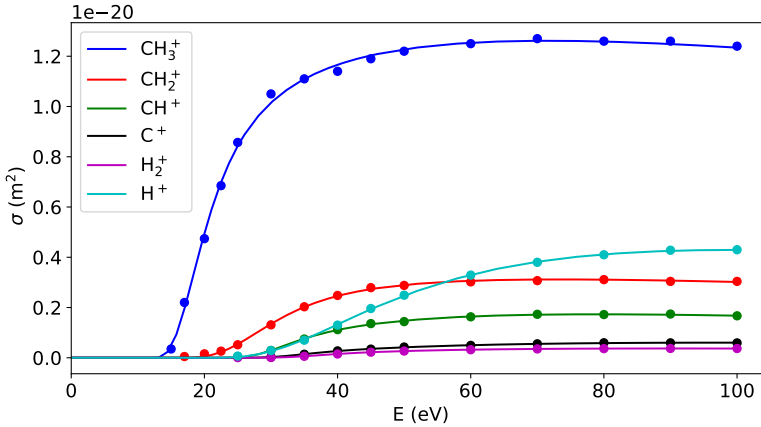


Figure 2.A.1: The cross sections of the dissociative ionization reactions of  $\text{CH}_4$ . The solid lines are the result of fitting equation (2.14) to the tabulated cross sections for these reactions from [180] which are represented by filled circles in the same color.

## 2.A.2 Dissociative Ionization

The fitting function reported by [178] to be used for the dissociative ionization reactions is the following:

$$\sigma_i(\epsilon) = f_3(\epsilon_1), \quad (2.14)$$

with  $\epsilon$  the incident electron energy in keV,  $\epsilon_1 = \epsilon - \epsilon_{th}$ , and  $\epsilon_{th}$  the threshold energy of the reaction in keV. Equation 2.14 was fitted through the tabulated cross sections and threshold energies for the dissociative ionization reactions reported in [180]. The used data points and resulting fits are shown up to 100 eV in figure 2.A.1. The fitting parameters are tabulated in table 2.A.1

## 2.A.3 Dissociative Electron Attachment

[178] use the same fitting function for dissociative ionization, equation (2.14), as for fitting the dissociative electron attachment cross sections (including the same definition for  $\epsilon_1$ ). We use this fitting function to fit the

	$\epsilon_{th}$ (eV)	$a_1$	$a_2$	$a_3$	$a_4$	$a_5$	$a_6$
CH <sub>3</sub> <sup>+</sup>	12.63	5.5333	2.7119	0.0071	-0.2619	0.0194	0.8917
CH <sub>2</sub> <sup>+</sup>	16.20	0.2575	2.9997	0.0141	-0.2828	0.0289	1.0172
CH <sup>+</sup>	22.20	0.295	3.4235	0.0207	0.9925	0.0100	-0.5789
C <sup>+</sup>	22.00	0.0392	4.6413	0.0243	1.1558	0.0125	-0.7372
H <sub>2</sub> <sup>+</sup>	22.30	0.0134	5.0600	0.0147	-0.7746	0.0242	1.0240
H <sup>+</sup>	21.10	0.0985	2.7831	0.0210	-0.6691	0.0403	1.0503

Table 2.A.1: Parameters obtained by fitting equation (2.14) to the tabulated cross sections of [180] for dissociative ionization reactions

	$\epsilon_{th}$ (eV)	$a_1$	$a_2$	$a_3$	$a_4$	$a_5$	$a_6$
H <sup>-</sup>	6.0	128.0817	5.0736	0.0024	0.1908	0.0041	10.1747
CH <sub>2</sub> <sup>-</sup>	6.0	1.5496	3.1405·10 <sup>-5</sup>	0.0012	4.8957	0.0164	-4.8826

Table 2.A.2: Parameters obtained by fitting equation (2.14) to the tabulated cross sections of [181] for dissociative electron attachment

tabulated cross sections for dissociative electron attachment reactions from [180]. The fits and corresponding data points are shown in figure 2.A.2 and the fitting parameters are reported in table 2.A.2.

## 2.A.4 Total Dissociation

The fitting function for the total dissociation used by [178] is given by:

$$\sigma_{TD}(\epsilon) = f_2(\epsilon_1) + a_5 \cdot f_2\left(\frac{\epsilon_1}{a_6}\right), \quad (2.15)$$

where  $\epsilon_1$  again has the same definition as for equation (2.14). The total dissociation cross section was measured by [207] and [143]. We have obtained data points for both measurements by extracting them from the published graphs using WebPlotDigitizer [166]. The fits and the data points for both measurements as well as equation (2.15) using the fitting parameters reported by [178] for total dissociation are shown in figure 2.A.3. Deviations up to 20% can arise due to different fitting parameters and fitted data points. These deviations in the total dissociation will propagate to the cross sections of the individual neutral dissociation reactions. Increasing

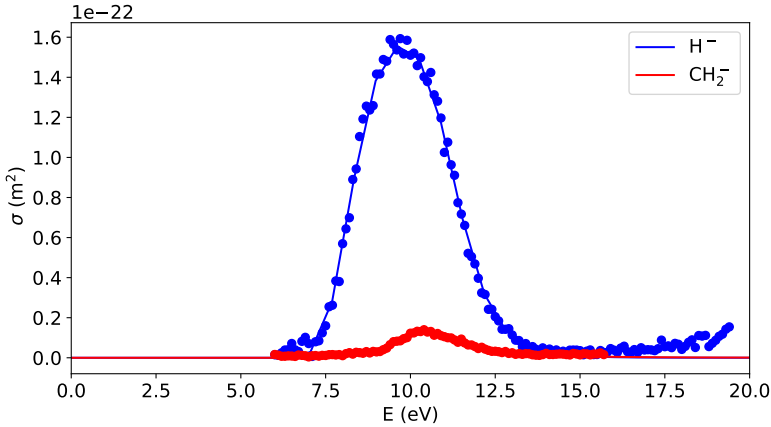


Figure 2.A.2: The cross sections of the dissociative electron attachment reactions of  $\text{CH}_4$ . The solid lines are the result of fitting equation (2.14) to the tabulated cross sections for these reactions from [180] which are represented as filled circles in the same color.

the cross section of the neutral dissociation cross sections has the effect of reducing the Townsend ionization coefficient  $\alpha$ . In this paper we have used the data points of [207] and the fitting parameters as reported in table 2.A.3.

### 2.A.5 Neutral Dissociation to $\text{CH}_2$

In this paper we have taken the measured cross sections for neutral dissociation into  $\text{CH}_2$  from [125, 126]. To smooth the data we have fitted a fourth order polynomial through the data points:

$$f(\epsilon) = a_0 + a_1\epsilon + a_2\epsilon^2 + a_3\epsilon^3 + a_4\epsilon^4, \quad (2.16)$$

with fitting parameters  $a_i$ , and  $\epsilon$  the incident electron energy in eV. Note that this function is only valid within the bounds of the measurement energies i.e.  $9.1 \text{ eV} \leq \epsilon \leq 44.4 \text{ eV}$ . The fit and the corresponding data points are shown in figure 2.A.4. The fitting parameters are reported in table 2.A.4.

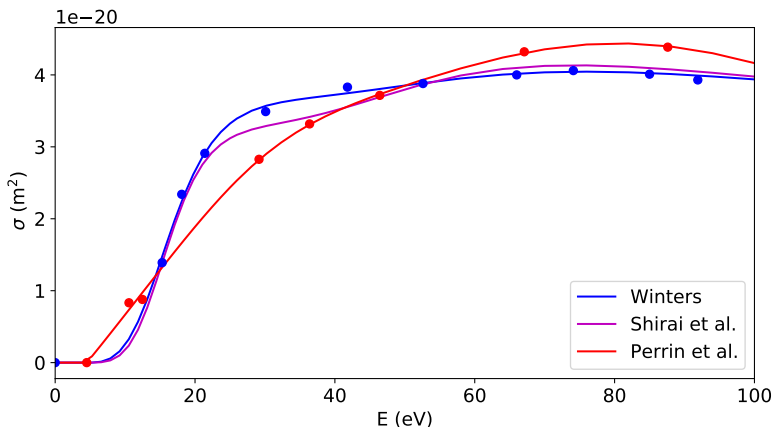


Figure 2.A.3: The total dissociation cross sections as measured by [207] (filled blue circles), and by [143] (filled red circles). The solid lines in the same colors as the measurement points are the fits done in this paper using equation (2.15). The solid line of [178] is obtained by using their reported fitting parameters with equation (2.15).

$\epsilon_{th}$ (eV)	4.51
$a_1$	4.1200
$a_2$	3.0594
$a_3$	0.0142
$a_4$	0.3606
$a_5$	0.4630
$a_6$	3.8830

Table 2.A.3: Parameters obtained by fitting equation (2.15) to the measured cross sections of [207] for total dissociation.

$a_0$	$-3.0203 \cdot 10^{-20}$
$a_1$	$5.4772 \cdot 10^{-21}$
$a_2$	$-2.8119 \cdot 10^{-22}$
$a_3$	$5.8213 \cdot 10^{-24}$
$a_4$	$-4.3221 \cdot 10^{-26}$

Table 2.A.4: Parameters obtained by fitting equation (2.16) to the measured cross sections of [125, 126] for neutral dissociation to  $\text{CH}_2$

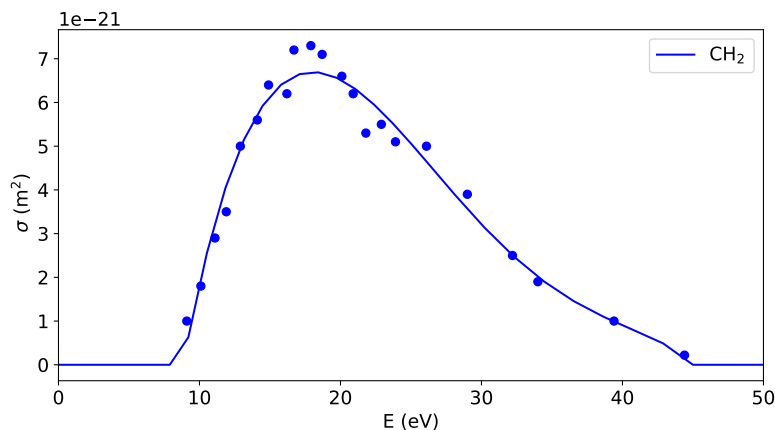


Figure 2.A.4: The cross sections for neutral dissociation to  $\text{CH}_2$  as measured by [125, 126] and the corresponding fit obtained by equation (2.16) combined with the fitting parameters in table 2.A.4

## 2.B Tabulated cross sections for neutral dissociation to $\text{CH}_3$ , $\text{CH}$ , and $\text{C}$

Calculated cross sections for neutral dissociation into  $\text{CH}_3$ ,  $\text{CH}$  and  $\text{C}$  are reported in table 2.B.2, 2.B.1, and 2.B.3, respectively.

$\epsilon$ (eV)	$\sigma_{\text{CH}}$ ( $\text{m}^2$ )	$\epsilon$ (eV)	$\sigma_{\text{CH}}$ ( $\text{m}^2$ )
15.79	$2.2169 \cdot 10^{-29}$	38.67	$1.2892 \cdot 10^{-21}$
17.11	$3.4360 \cdot 10^{-28}$	40.78	$1.3348 \cdot 10^{-21}$
18.42	$8.9545 \cdot 10^{-28}$	42.89	$1.3612 \cdot 10^{-21}$
19.74	$1.5509 \cdot 10^{-27}$	45.00	$1.3769 \cdot 10^{-21}$
21.05	$2.2067 \cdot 10^{-27}$	46.00	$1.3820 \cdot 10^{-21}$
22.37	$2.8625 \cdot 10^{-27}$	52.00	$1.3999 \cdot 10^{-21}$
23.68	$4.3996 \cdot 10^{-24}$	58.00	$1.4092 \cdot 10^{-21}$
25.00	$3.4406 \cdot 10^{-23}$	64.00	$1.4120 \cdot 10^{-21}$
26.00	$8.8330 \cdot 10^{-23}$	70.00	$1.4063 \cdot 10^{-21}$
28.11	$3.0330 \cdot 10^{-22}$	76.00	$1.3920 \cdot 10^{-21}$
30.22	$5.9931 \cdot 10^{-22}$	82.00	$1.3706 \cdot 10^{-21}$
32.33	$8.7592 \cdot 10^{-22}$	88.00	$1.3441 \cdot 10^{-21}$
34.44	$1.0797 \cdot 10^{-21}$	94.00	$1.3146 \cdot 10^{-21}$
36.56	$1.2107 \cdot 10^{-21}$	100.0	$1.2839 \cdot 10^{-21}$

Table 2.B.1: Calculated cross sections for neutral dissociation to CH. Threshold energy is 15.5 eV.

$\epsilon$ (eV)	$\sigma_{\text{CH}_3}$ (m <sup>2</sup> )	$\epsilon$ (eV)	$\sigma_{\text{CH}_3}$ (m <sup>2</sup> )
7.90	$1.7980 \cdot 10^{-22}$	32.33	$1.8871 \cdot 10^{-20}$
9.21	$1.6220 \cdot 10^{-21}$	34.44	$1.7693 \cdot 10^{-20}$
10.53	$3.8168 \cdot 10^{-21}$	36.56	$1.6706 \cdot 10^{-20}$
11.84	$6.2953 \cdot 10^{-21}$	38.67	$1.5914 \cdot 10^{-20}$
13.16	$8.7738 \cdot 10^{-21}$	40.78	$1.5296 \cdot 10^{-20}$
14.47	$1.2135 \cdot 10^{-20}$	42.89	$1.4821 \cdot 10^{-20}$
15.79	$1.5230 \cdot 10^{-20}$	45.00	$1.4462 \cdot 10^{-20}$
17.11	$1.7797 \cdot 10^{-20}$	46.00	$1.4324 \cdot 10^{-20}$
18.42	$1.9773 \cdot 10^{-20}$	52.00	$1.3817 \cdot 10^{-20}$
19.74	$2.1205 \cdot 10^{-20}$	58.00	$1.3624 \cdot 10^{-20}$
21.05	$2.2160 \cdot 10^{-20}$	64.00	$1.3547 \cdot 10^{-20}$
22.37	$2.2697 \cdot 10^{-20}$	70.00	$1.3482 \cdot 10^{-20}$
23.68	$2.2872 \cdot 10^{-20}$	76.00	$1.3388 \cdot 10^{-20}$
25.00	$2.2732 \cdot 10^{-20}$	82.00	$1.3259 \cdot 10^{-20}$
26.00	$2.2445 \cdot 10^{-20}$	88.00	$1.3102 \cdot 10^{-20}$
28.11	$2.1454 \cdot 10^{-20}$	94.00	$1.2926 \cdot 10^{-20}$
30.22	$2.0177 \cdot 10^{-20}$	100.0	$1.2743 \cdot 10^{-20}$

Table 2.B.2: Calculated cross sections for neutral dissociation to CH<sub>3</sub>. Threshold energy is 7.5 eV.

$\epsilon$ (eV)	$\sigma_C$ (m <sup>2</sup> )	$\epsilon$ (eV)	$\sigma_C$ (m <sup>2</sup> )
15.79	$5.2967 \cdot 10^{-31}$	38.67	$2.9881 \cdot 10^{-22}$
17.11	$8.2093 \cdot 10^{-30}$	40.78	$3.2963 \cdot 10^{-22}$
18.42	$2.1394 \cdot 10^{-29}$	42.89	$3.5130 \cdot 10^{-22}$
19.74	$3.7055 \cdot 10^{-29}$	45.00	$3.6723 \cdot 10^{-22}$
21.05	$5.2723 \cdot 10^{-29}$	46.00	$3.7348 \cdot 10^{-22}$
22.37	$6.8390 \cdot 10^{-29}$	52.00	$4.0210 \cdot 10^{-22}$
23.68	$7.1010 \cdot 10^{-26}$	58.00	$4.2381 \cdot 10^{-22}$
25.00	$9.3899 \cdot 10^{-25}$	64.00	$4.4125 \cdot 10^{-22}$
26.00	$3.3122 \cdot 10^{-24}$	70.00	$4.5416 \cdot 10^{-22}$
28.11	$1.9703 \cdot 10^{-23}$	76.00	$4.6243 \cdot 10^{-22}$
30.22	$6.0694 \cdot 10^{-23}$	82.00	$4.6645 \cdot 10^{-22}$
32.33	$1.2475 \cdot 10^{-22}$	88.00	$4.6697 \cdot 10^{-22}$
34.44	$1.9488 \cdot 10^{-22}$	94.00	$4.6478 \cdot 10^{-22}$
36.56	$2.5467 \cdot 10^{-22}$	100.0	$4.6063 \cdot 10^{-22}$

Table 2.B.3: Calculated cross sections for neutral dissociation to C. Threshold energy is 15.5 eV.



## Chapter 3

# Comparison of Six Electron Boltzmann Solvers

Solving the electron Boltzmann equation (EBE) is necessary to obtain swarm parameters and reaction rate coefficients which are used as input for other modelling methods e.g. the fluid model. Many programs/solvers exist with the sole goal of solving the EBE. Different methods exist for solving the EBE where term-expansion and particle based are the most popular. In this work we compared the most widely available EBE solvers (`BOLSIG+`, `BOLOS`, `particle_swarm`, `METHES`, `LoKI-B`, and `MultiBolt`) on produced results, computation speed, and user-friendliness when applied to a set of model gases (analytical Maxwell, Reid ramp, and Lucas-Salee with attachment) collected from literature. For the model gases all EBE solvers stayed within 5% of each other for all swarm parameters calculated. Comparing the EBE solvers on real gases (Ar, N<sub>2</sub>, and O<sub>2</sub>) showed larger differences, especially for the ionization coefficient. Differences between the most popular EBE solver `BOLSIG+` and other solvers could reach up to 50% for the ionization coefficient. Comparisons of computation speed showed a difference of three orders of magnitude between the fastest and slowest EBE solvers when starting from exactly the same input and producing similar output.



### 3.1 Introduction

Electron swarm parameters like mobility, diffusion, ionization, and attachment coefficients are necessary input data for continuum (fluid) plasma models. These parameters, especially the mobility coefficient, can be obtained from experiment, but the parameters commonly used in plasma models are obtained from Boltzmann equation solvers. This is because it is a lot simpler to obtain swarm parameters for any gas mixture (for which cross sections are known) and electric field using a Boltzmann equation solver than designing an experiment specifically for that gas mixture and electric field strength.

The goal of this work is to compare the results obtained with the most popular Boltzmann solvers. The results will be compared among each other, but also to analytical or experimental results where possible. Besides results, also computation time and user friendliness is compared.

These solvers aim to obtain the electron distribution function. The most popular solver types are based on either a particle or a term-expansion approach. The particle based Monte Carlo Flux (MCF)[171] approach was not used in this work, but was recently improved by Vialetto *et al.*[202].

The particle based solvers evolve particles in a constant background electric field allowing for them to collide with the neutral background gas molecules according to a set of input cross sections and a collision sampling technique, where the null-collision method [91] is the most commonly used. Particles are evolved until the calculated electron swarm parameters have converged. Properties like mobility, and diffusion coefficient are calculated from the position and velocities of the particles throughout the simulation. Parameters like the ionization and attachment coefficients can be calculated either by convolution of the obtained electron energy distribution function with the relevant cross sections or by counting ionization and attachment events in the particle simulation.

The Boltzmann equation is written as [94, 206]:

$$\frac{\partial f}{\partial t} + \mathbf{v} \cdot \nabla f - \frac{e}{m_e} \mathbf{E} \cdot \nabla_{\mathbf{v}} f = C[f] \quad (3.1)$$

where  $f$  is the electron distribution function in phase space,  $\mathbf{v}$  is the velocity,

$e$  the elementary charge,  $m_e$  the electron mass,  $\mathbf{E}$  the electric field, and  $C[f]$  the collision operator which represents the rate of change of  $f$  due to collisions. The collision operator will be built-up from the input cross sections for all collisions taken into account (elastic, excitation, ionization, and attachment).

The term-expansion based solvers simplify the Boltzmann equation in several ways and for the remainder of this discussion we follow the steps in [61]. First, the electric field and collision probabilities are approximated to be spatially uniform. This simplifies the electron distribution function  $f(\mathbf{r}, \mathbf{v}, t)$  in velocity and position space. In velocity space it becomes symmetric around the electric field direction, and in position space it can vary only along the electric field direction. The electron distribution function can now be written in cylindrical coordinates ( $v$ , and  $\theta$ , with  $\theta$  the angle between the velocity and the field direction) in velocity space, one coordinate in position space, which is along the electric field direction, which we choose to be  $z$ , and time  $t$ . This procedure changes the Boltzmann equation to:

$$\frac{\partial f}{\partial t} + v \cos \theta \frac{\partial f}{\partial z} - \frac{e}{m_e} E \left( \cos \theta \frac{\partial f}{\partial v} + \frac{\sin^2 \theta}{v} \frac{\partial f}{\partial \cos \theta} \right) \quad (3.2)$$

The name “two-term” approximation comes from the method of simplifying the  $\theta$  dependence of  $f$ . This is done by expanding  $f$  using spherical harmonics (Legendre polynomials of  $\cos \theta$ ) [121]. When two terms are used in the expansion we obtain the two-term approximation. More terms can be added to get a multiterm approximation. A discussion on the validity of the two-term approximation can be found in [206]. The two-term approximation will write  $f$  as:

$$f(v, \cos \theta, z, t) = f_0(v, z, t) + f_1(v, z, t) \cos \theta \quad (3.3)$$

where  $f_0$  is the isotropic part of  $f$  and  $f_1$  an anisotropic perturbation. The two-term approximation starts to fail when inelastic collisions dominate and  $f$  becomes strongly anisotropic [61, 145].

A set of two coupled equations for  $f_0$  and  $f_1$  can now be obtained by substituting the term-expansion of eq.(3.3) into eq.(3.2). The energy-

dependence of  $f$  is now split from its dependence on time and space by assuming:

$$f_{0,1}(\epsilon, z, t) = \frac{1}{2\pi\gamma^3} F_{0,1}(\epsilon) n(z, t) \quad (3.4)$$

where  $\gamma = \sqrt{(2e/m_e)}$  and the energy distribution  $F_{0,1}$  is constant in time and space. The resulting set of equations is now simplified further by making assumptions on the temporal and spatial dependence of  $f_0$  and  $f_1$  or, after splitting off the energy dependence,  $n_e(z, t)$  the electron density.

The two assumptions that are widely used are: exponential temporal growth without space dependence, and exponential spatial growth without time dependence. These cases correspond to Pulsed Townsend experiments and Steady State Townsend experiments respectively [188]. Most calculations in this work will be done using the exponential temporal growth without space dependence assumption.

In this work we compare several available Boltzmann solvers, using the different solution methods mentioned earlier and by applying a DC electric field, for model gases (i.e. analytical Maxwell [127], Reid Ramp model [162], and Lucas-Salee model [108]) and some real gases (i.e. Ar, N<sub>2</sub>, and O<sub>2</sub>). The swarm properties obtained from these solvers for the real gases are then also compared to experimentally obtained values.

## 3.2 Boltzmann Solvers

In this section we will summarize the different Boltzmann solvers used in this comparison. The summary contains the solution method, creators, packaging method (open source, source available, or precompiled binary), date of last update, and possible papers which describe the solvers.

### 3.2.1 BOLSIG+

BOLSIG+ is a two-term approximation Boltzmann equation solver developed by Gerjan Hagelaar of the LAPLACE laboratory in Toulouse in France. The solution methods used are extensively described in Hagelaar and Pitchford [61]. A precompiled executable can be downloaded for Linux and Windows (and an older version for Mac) on the website:

<http://www.bolsig.laplace.univ-tlse.fr/>. The last version (and the version used) is dated from December 2019. This solver can also be accessed from the LXCat website [25].

### 3.2.2 BOLOS

BOLOS is a two-term approximation Boltzmann equation solver developed by Alejandro Luque of the Instituto de Astrofísica de Andalucía (IAA-CSIC). It is built upon the work of Hagelaar and Pitchford [61]. The open source Python (2 and 3) repository (GNU LGPLv2) can be found at <https://github.com/aluque/BOLOS>. The last update to the master branch was March 2018. The used version of BOLOS can be found at <https://github.com/AndyMN/BOLOS> where changes have been made to remove the assumption that inelastic cross sections were present in the input data. These changes have also been submitted as a merge-request to the original repository.

### 3.2.3 particle\_swarm

`particle_swarm` is a particle based Boltzmann equation solver developed in the Multiscale Dynamics group at Centrum Wiskunde & Informatica (CWI). It is an open source (GNU GPLv3) Fortran code with a Python (2 and 3) command-line interface and can be found at: [https://gitlab.com/MD-CWI-NL/particle\\_swarm](https://gitlab.com/MD-CWI-NL/particle_swarm). It is still in active development at the time of writing.

### 3.2.4 METHES

METHES is a particle based Boltzmann equation solver developed by Rabie *et al.* [156]. It is an open source Matlab R2014 code and can be found at <https://nl.lxcat.net/download/METHES/>. In [156] it is stated that the license is GNU GPLv3, but the code only contains what resembles a FreeBSD license with the extra condition that proper citation has to be made to [156] when reporting results. The last update to the code was July 2015.

### 3.2.5 LoKI-B

LoKI-B is a two-term approximation Boltzmann equation solver developed by Tejero A *et al.* [189]. It is an open source (GNU GPLv3) Matlab R2017b code and can be found at <https://github.com/IST-Lisbon/LoKI>. The last update to the master branch was May 2019.

### 3.2.6 MultiBolt

MultiBolt is a multiterm Boltzmann equation solver developed by Stephens [187]. It is a seemingly open source Matlab code, but no license or Matlab version have been provided. It can be found at <https://gitlab.com/LXCatThirdParty/MultiBolt>. The last update to the master branch was May 2020. The used version of MultiBolt can be found at <https://gitlab.com/AndyMN/MultiBolt> where stability fixes have been made. These fixes have been submitted as a merge-request to the original repository.

## 3.3 Methodology

### 3.3.1 Inter- and Extrapolation of Input Cross Sections

Most solvers linearly interpolate between the provided input data points. However, `particle_swarm` linearly interpolates the input data points to an equally spaced set of data points which the solver then uses for interpolation during runtime. When using an equally spaced set of data points finding the two points to use for linear interpolation becomes much more efficient.

Often times input cross sections do not span the entire energy range which you are looking at because e.g the experimental setup was not suited for it (e.g. Allan [4] who measured differential cross sections for exciting O<sub>2</sub> to an electronically and vibrationally excited state up to an energy of 18 eV where the cross section was not yet 0.) or the theoretical assumptions used were only valid in a particular energy range (e.g. Ziołkowski *et al.* [214] calculating the neutral dissociation cross section of CH<sub>4</sub> only up to 20 eV). An extrapolation scheme will have to be chosen for these circumstances. A different extrapolation scheme can produce very different swarm parameters or sometimes make the solver unable to converge. Extrapolation to an

energy outside of the input data range is different by default for many used solvers.

Among the solvers used the most commonly available extrapolation schemes were:

- Zero: Cross sections outside of the input range are fixed at 0
- Constant: Cross sections outside of the input range are fixed at the closest input data point.

Two solvers had a configuration parameter to switch extrapolation scheme: `particle_swarm` and `BOLSIG+`. The other solvers contained a hardcoded constant extrapolation scheme. `particle_swarm` can switch between the zero and constant schemes mentioned before as well as a linear extrapolation scheme. It can also have a different scheme for energies above or below the input data range. `BOLSIG+` input files contain an extrapolation flag where cross sections can be chosen to be extrapolated according to a  $\ln \epsilon/\epsilon$  (where  $\epsilon$  is the energy) decrease in cross section. This flag was turned off for this work which made `BOLSIG+` resort to a constant extrapolation scheme.

In this work we have chosen a constant extrapolation scheme since it resulted in better convergence for all solvers. This scheme uses the first input cross section for all energies below this first point and the last input cross section for all energies above the last point. To ensure that all solvers used this scheme we added 2 extra points to all cross sections at 0 eV and 10 keV with the value of the first and last input cross section respectively. In practice the effect of extrapolation scheme should be examined before relying on the results. In this work more focus was put on comparing different solvers than achieving the most physically correct swarm parameters.

### 3.3.2 Compared Swarm Parameters

As discussed in [145] bulk and flux swarm parameters are different. Bulk swarm parameters are obtained by combining the flux swarm parameters with the influence of non-conservative collisions. When comparing swarm parameters with experiments bulk swarm parameters should be used. For comparisons of results among solvers we have used flux swarm parameters.

For the diffusion coefficient we have also limited ourselves to the transverse (to the electric field) component.

The swarm parameters compared among solvers were: reduced flux mobility, reduced flux transverse diffusion coefficient, mean energy, and reduced ionization coefficient (where possible). The swarm parameters compared with experiments were: reduced bulk mobility, reduced ionization coefficient, and characteristic energy (based on the bulk transverse diffusion coefficient).

### 3.3.3 Configuration Parameters

	exp( $t$ )	Ionization equal energy	No e-e coll.	No super-elastic
BOLSIG+	✓	✓	✓	✓
BOLOS	✓	?	?	?
particle_swarm	\	✓	✓	✓
METHES	\	✓	✓	✓
LoKI-B	✓	✓	✓	✓
MultiBolt	✓	✓	?	?

Table 3.3.1: Configuration settings for the used Boltzmann solvers. ✓ means the setting was turned on in the configuration file or by default as mentioned in the code, documentation, or related publication, \ means the setting does not apply for this solver, and ? means there was no mention of this setting in the configuration file, the code, documentation, or the related publication. The property “exp( $t$ )” refers to the assumption made for the term-expansion based solvers where the electron density grows exponentially in time. “Ionization equal energy” refers to how energy of the incident electron is divided between the original electron and the ionized electron after the collision, in this case equally. “No e-e coll.” means that electron do not collide amongst themselves. They only collide with the gas molecules. “No super-elastic” means that no super-elastic collisions are taken into account.

There are several approximations and improvements that can be applied when solving the Boltzmann equation. An example of an approximation used by the term-based solvers is the choice for whether the electron density

is assumed to grow exponentially in time (written as  $\exp(t)$  in this work) or in space (written as  $\exp(z)$  in this work) [61, 145]. This is a problem-dependent choice and results will vary based on this choice. To ensure all solvers are using the same set of approximations and improvements table 3.3.1 shows the settings that are used (or not used) for all solvers compared in this work.

### 3.3.4 Convergence Criteria

Most solvers allow for the setting of a value which a convergence criterion should satisfy for the solver to stop iterating, but they mostly use difference convergence criteria. Here we discuss this shortly. The stopping value for all solvers used was  $10^{-4}$  i.e. when the convergence criterion used produces a value smaller than  $10^{-4}$  the solver stopped iterating and convergence was reached.

**MultiBolt** compares the difference between mean energies in subsequent iterations of the solvers.

**LoKI-B** compares the maximal relative difference for electron energy distribution functions between iterations.

**BOLOS** compares the L1 norm of the difference between electron energy distribution functions between iterations.

**BOLSIG+** documentation states “The convergence parameter is used in different convergence criteria on the relative change of  $f_0$  between iterations and the fractional residue of the overall energy balance.” It is not clear from the documentation which computation is done to produce a single number from the relative change of the electron energy distribution function  $f_0$ .

The particle based solvers do not have convergence criteria based on the electron energy distribution function, but based on the error of the swarm parameters. Specifically they look at if  $\frac{\sigma}{\mu} < \text{threshold}$  where  $\sigma$  is the standard deviation,  $\mu$  is the mean, and threshold is a user defined value.

**METHES** looks at the error of the drift velocity, and the diffusion coefficient. We have set the threshold to  $10^{-2}$  for both variables.

**particle\_swarm** looks at the error of the velocity squared, the drift velocity, the bulk drift velocity, the diffusion coefficient, the bulk diffusion coefficient, and the ionization coefficient. The threshold was set to:  $5 \cdot 10^{-3}$  for the velocities,  $10^{-2}$  for the diffusion coefficients, and  $5 \cdot 10^{-3}$  for the ionization coefficient.

### 3.3.5 Comparison with BOLSIG+

For almost all model gases used, the swarm parameters obtained from the different Boltzmann solvers will be compared to the results obtained from BOLSIG+. We must stress that this does not mean BOLSIG+ is seen as the most correct solver. A comparison is made with BOLSIG+ because it is the most widely known and used solver in the low-temperature plasma physics community and knowing how other solvers compare against it could serve valuable.

## 3.4 Model Gas Comparisons

Several model gases are used to test and compare the used Boltzmann solvers. Model gases offer a way to test specific features of a Boltzmann solver for instance by only containing a specific type of collision (e.g. excitation, ionization, etc.). Swarm parameters are calculated for reduced electric fields up to 1000 Td for all model gases except for the analytical Maxwell model for which we only went up to 20 Td. A gas temperature of 300 K was used for all model gases.

### 3.4.1 Maxwell Model

The Maxwell model gas is defined by having a constant momentum transfer collision frequency for which analytical solutions to transport properties exist [127]. The model is defined by taking the elastic cross section to be:

$$\sigma_m = \frac{a}{\sqrt{\epsilon}} \quad (3.5)$$

where  $\sigma_m$  is the momentum-transfer cross section in  $\text{m}^2$ ,  $\epsilon$  is the electron energy in eV, and  $a$  is a constant which was chosen to be  $6 \cdot 10^{-20} \frac{\text{m}^2}{\text{eV}}$  in this work. The momentum transfer collision frequency is then:

$$\nu_m = N\sigma_m v \quad (3.6)$$

where  $N$  is the gas number density, and  $v$  is the electron velocity. Rewriting the electron velocity as  $v = \sqrt{\frac{2e\epsilon}{\mu}}$  with  $\mu = \frac{m_e M}{m_e + M}$  the reduced mass where

$m_e$  and  $M$  are the electron and gas molecule mass respectively, and  $e$  the electron charge we can write the collision frequency  $\nu_m$  as:

$$\nu_m = N\sigma_m\sqrt{\frac{2e\epsilon}{\mu}} \quad (3.7)$$

$$\nu_m = N\frac{a}{\sqrt{\epsilon}}\sqrt{\frac{2e\epsilon}{\mu}} \quad (3.8)$$

$$\frac{\nu_m}{N} = a\sqrt{\frac{2e}{\mu}} \quad (3.9)$$

where  $\frac{\nu_m}{N}$  is now a constant collision frequency which is what defines the Maxwell model. Note that there is a divergence in the momentum-transfer cross section  $\sigma_m$  when  $\epsilon \rightarrow 0$ . For this work we calculated the cross section starting from 0.0005 eV. This value is then kept constant down to 0 eV, as discussed previously, which will no longer give the correct constant collision frequency and thus give deviations from the analytical results.

We assume the electric field to be constant and pointing along the z-axis. Analytical formulas for the transport parameters are given in [127]. In this work we do not apply a magnetic field so the analytical formulas become:

$$T_e = \frac{2}{3k_b} \left( \frac{3}{2}k_bT_g + \frac{1}{2}Mv_z^2 \right) \quad (3.10)$$

$$\bar{\epsilon} = \frac{3}{2}k_bT_e + \frac{1}{2}m_e v_z^2 \quad (3.11)$$

$$v_z = \frac{e}{m_e(\nu_m/N)} \frac{E}{N} \quad (3.12)$$

$$ND_x = ND_z = ND_y = \frac{k_bT_e}{m_e(\nu_m/N)} \quad (3.13)$$

where  $e$  is the charge of an electron,  $k_b$  is the Boltzmann constant,  $T_e$  and  $T_g$  are the electron temperature and gas temperature respectively,  $\bar{\epsilon}$  the mean energy,  $v$  the drift velocity, and  $ND$  the reduced diffusion coefficient. In this work we chose the gas molecule mass  $M = 4$  amu and  $T_g = 300$  K.

The relative difference of the mobility, the mean energy, and the transverse diffusion coefficient calculated using eq.(3.12),(3.11), and (3.13) respectively are shown in figure 3.4.1.

For all three variables at  $E/N < 1$  Td the results of each solver start deviating from the analytical result. This deviation is related to the choice of extrapolating the cross section at 0.0005 eV down to 0 eV to avoid the divergence in the cross section as  $\epsilon \rightarrow 0$  present in eq.(3.5). Additionally, at this range interpolation errors can become relevant and increasing the resolution of the energy grid can be used to reduce this effect. Note that although the relative differences start increasing as we go to lower electric fields, the absolute difference will not be relevant for practical purposes.

For  $E/N > 1$  Td both the relative difference of the mobility and of the mean energy stays within  $\pm 5\%$  for all solvers. The relative difference of the transverse diffusion coefficient is slightly larger and stays within  $\pm 10\%$  for all solvers.

### 3.4.2 Reid Ramp Model

The Reid ramp model gas [162] has been used previously in literature to test the behavior of newly developed Boltzmann equation solvers [156, 187, 189]. This model gas is defined by the following set of cross sections:

$$M = 4 \text{ amu} \quad (3.14)$$

$$\sigma_{\text{elastic}} = 6 \cdot 10^{-20} \text{ m}^2 \quad (3.15)$$

$$\sigma_{\text{inelastic}}(\epsilon) = (\epsilon - 0.2) \cdot 10^{-19} \text{ m}^2 \quad (3.16)$$

with  $M$  the molecular mass,  $N_{\text{gas}}$  and  $T$  the number density and temperature of the gas respectively,  $\sigma_{\text{elastic}}$  and  $\sigma_{\text{inelastic}}$  the elastic and inelastic cross sections respectively, and  $\epsilon$  the electron energy in eV. The cross sections were calculated starting from 0.2 eV up to 10 keV. Calculated swarm properties for all solvers and their relative difference with BOLSIG+ are shown in figure 3.4.2. For both the mean energy and the reduced flux mobility the relative difference with BOLSIG+ stayed within  $\pm 5\%$ .

A more substantial difference is visible for the reduced transverse diffusion coefficient. The relative difference with BOLSIG+ for the results of the Monte-Carlo solvers is between -20% and -30%. The term expansion based solvers stay within a couple percent of each-other. These large differences have been reported before [145, 165], but no clear explanation has been given for these large differences.

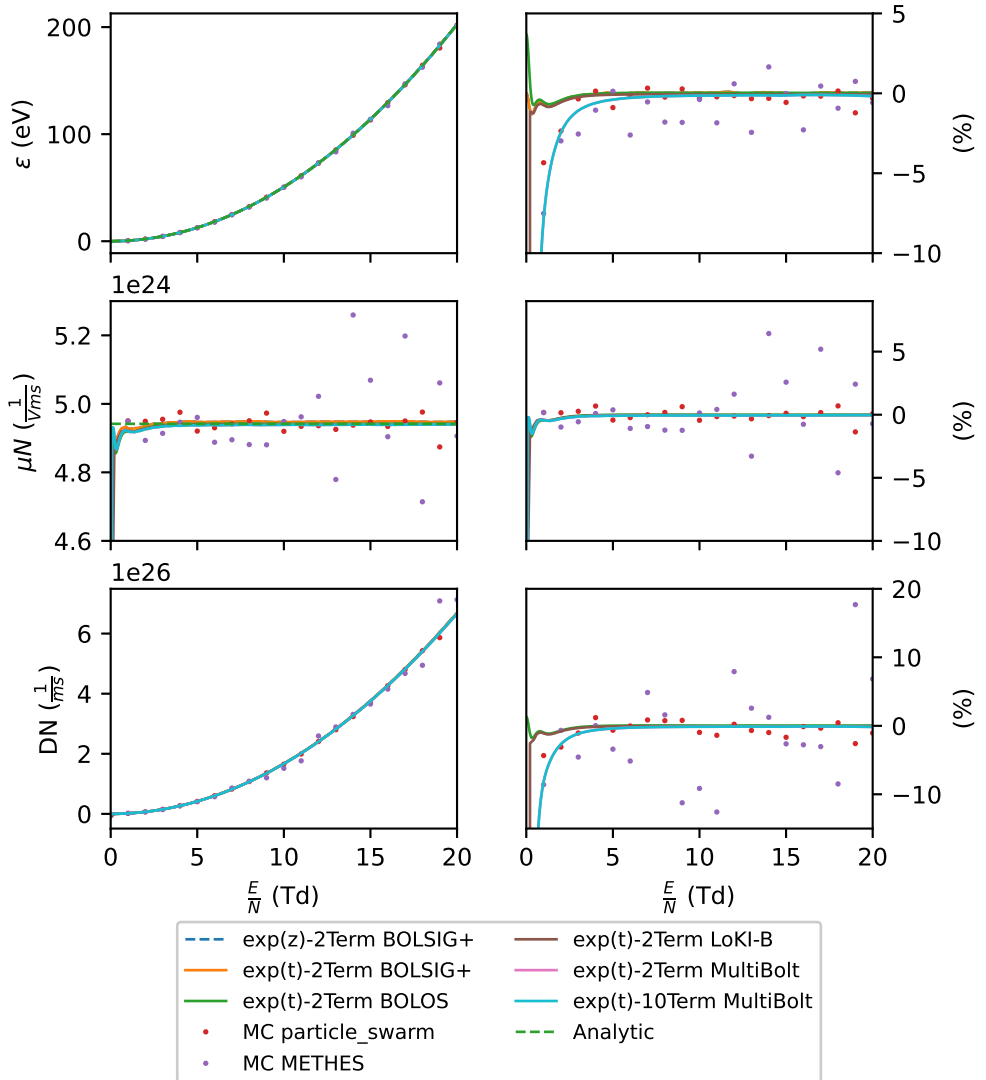


Figure 3.4.1: Swarm properties of the analytical Maxwell model. Top to bottom: mean energy, reduced flux mobility, and reduced flux transverse diffusion coefficient. Left to right: calculated value, and relative difference with analytical results

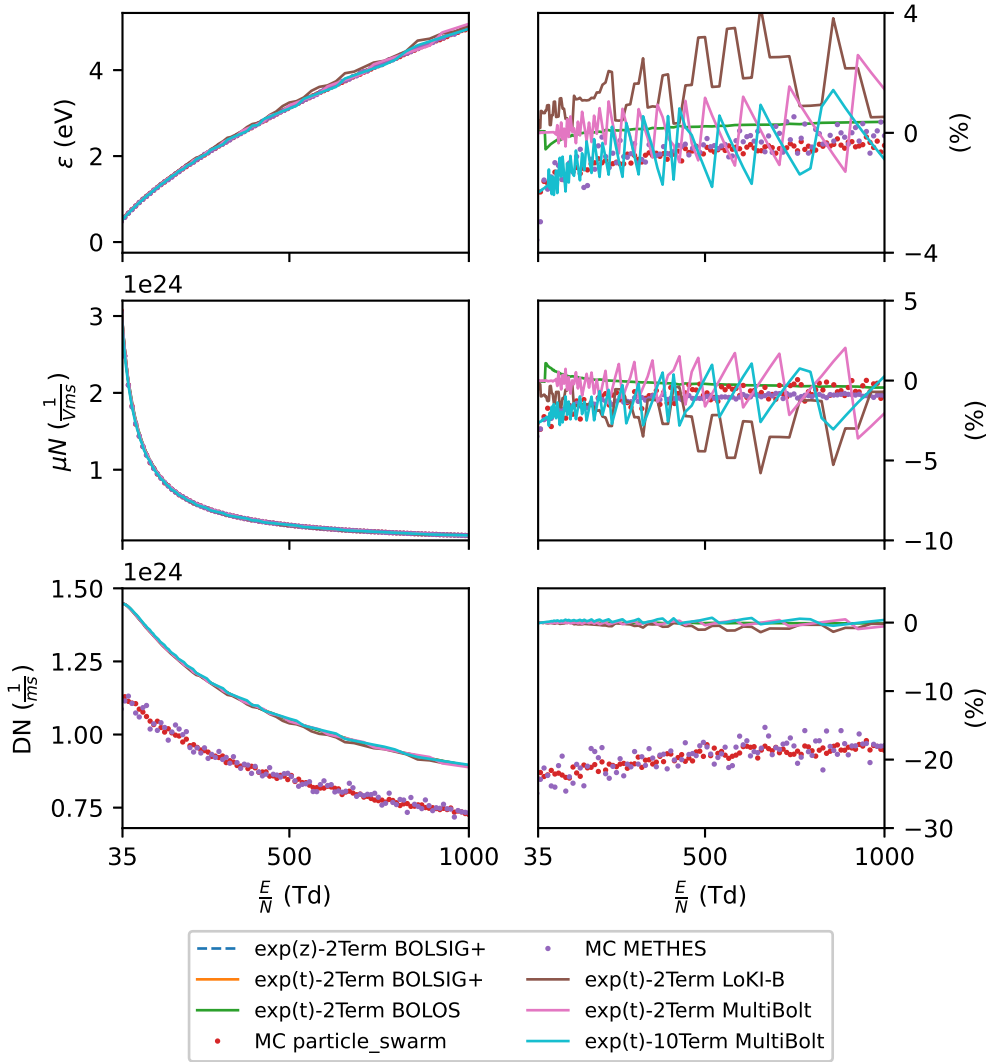


Figure 3.4.2: Swarm properties of the Reid Ramp model. Top to bottom: mean energy, reduced flux mobility, and reduced transverse diffusion coefficient. Left to right: calculated value, and relative difference with BOLSIG+. X-axis starts at 35 Td, below this some solvers had convergence issues or too large relative differences with BOLSIG+ to display.

### 3.4.3 Lucas-Salee gas

The model gas of Lucas-Salee [108] can be tuned to be conservative or not and be selective into which non-conservative process is present. This allows for testing of various aspects of a Boltzmann equation solver. The Lucas-Salee gas combined with the attachment modification of Ness and Robson [128] is given by:

$$\sigma_{mom.}(\epsilon) = 4\epsilon^{-0.5} \cdot 10^{-20} \quad (3.17)$$

$$\sigma_{exc.}(\epsilon) = 0.1(1 - F)(\epsilon - 15.6) \cdot 10^{-20} \quad (3.18)$$

$$\sigma_{ioniz.}(\epsilon) = 0.1F(\epsilon - 15.6) \cdot 10^{-20} \quad (3.19)$$

$$\sigma_{att.}(\epsilon) = a\epsilon^p \cdot 10^{-20} \quad (3.20)$$

where  $\sigma$  is the cross section in  $\text{m}^2$ ,  $\epsilon$  is the energy in eV, and  $F$ ,  $p$ , and  $a$  are parameters to tune the model to be (non-)conservative and select which process is dominant.

In the following subsections different combinations of parameters  $F$ ,  $a$ , and  $p$  will be used to tune the model to test specific parts of the Boltzmann equation solvers. The mass of the gas molecules is chosen to be  $M = 4$  amu. The cross sections were calculated starting from 0.0005 eV linearly increasing to 300 eV in 498 steps, afterwards the 0 eV and 10 keV extrapolation points were added. BOLSIG+ has a limit of 500 data-points per reaction which is the reasoning why 498 steps between 0.0005 eV and 300 eV and 2 extrapolation points were used per reaction.

#### 3.4.3.1 Non-ionizing: $F = 0$

The non-ionizing Lucas-Salee model contains elastic and excitation collisions and possibly attachment ( $a \neq 0$ ) collisions. The cross sections for both the non-attaching and attaching models are shown in figure 3.4.3. The calculated swarm parameters for the non-attaching model ( $a = 0$ ) are shown in figure 3.4.4. Attachment can be included either proportional to velocity ( $p = 0.5$ ), inversely proportional to velocity ( $p = -0.5$ ), or inversely proportional to energy ( $p = -1$ ). We observed that there is relatively very little difference between the model gas without attachment ( $a = 0$ ) and with attachment ( $a \neq 0$ ). For this reason only the swarm parameters for

the model with attachment proportional to velocity ( $p = 0.5$ ) are shown in figure 3.4.5. Increasing the attachment parameter  $a$  from 0.002 to 0.01 does not change the calculated swarm parameters considerably, but does change convergence speed (if convergence can even be obtained) drastically among solvers.

Among these non-ionizing models the calculated swarm parameters are very similar. For the mean energy and the reduced flux mobility a difference arises between the 2-term based solvers and the 10-term and Monte Carlo based solvers. For the mean energy the difference can reach -5%, and for the reduced flux mobility it can reach -10% when comparing the 10-term and Monte Carlo based solvers with BOLSIG+.

For the reduced flux transverse diffusion coefficient the results differ between the Monte Carlo based solvers and the term-expansion based solvers (even the 10-term expansion). Differences between the Monte Carlo based solver and BOLSIG+ increase with increasing electric field and can reach up to -50%.

### 3.4.3.2 Ionizing: $F = 1$

Two ionizing Lucas-Salee models were used in this work. Both contain elastic and ionizing collisions and one of them contains attachment ( $a = 0.002$ ) collisions as well. The cross sections for these two models are shown in figure 3.4.6. Calculated swarm parameters for these two models are shown in figure 3.4.7, and 3.4.8 respectively.

The results for the mean energy and the reduced flux mobility are similar to the non-ionizing models. There is a difference in results between the 2-term based solvers and the 10-term and Monte Carlo based solvers. When comparing this last group of solvers to BOLSIG+ the difference reaches -5% for the mean energy, and -10% for the reduced flux mobility. Note, in contrary to the non-ionizing models, the reduced flux mobility for the case where an exponential growth in space of the electron density is assumed deviates strongly from the cases where an exponential growth in time is assumed.

The reduced flux transverse diffusion coefficient shows, just as in the non-ionizing model, a difference of up to -50% between the Monte Carlo solvers and BOLSIG+. Contrary to the non-ionizing models the results for MultiBolt (both 2-term and 10-term) deviate from the results of the

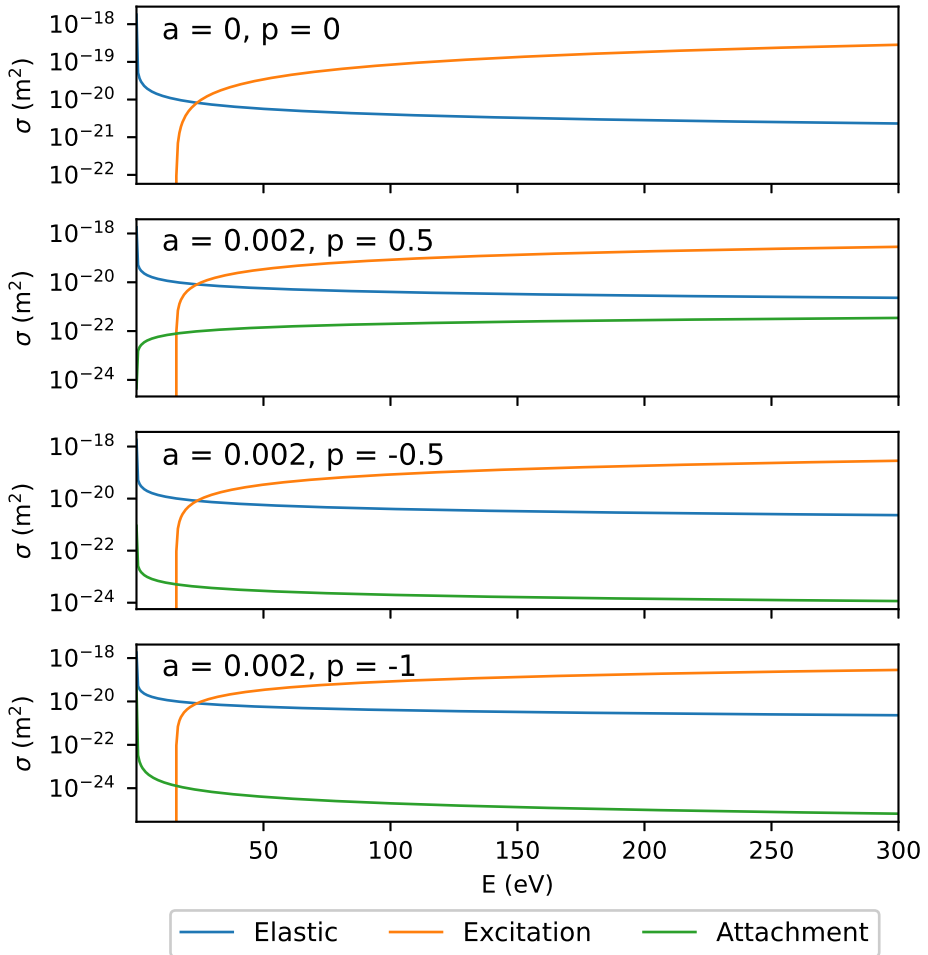


Figure 3.4.3: Cross sections for the non-ionizing ( $F = 0$ ) Lucas-Salee model gas.

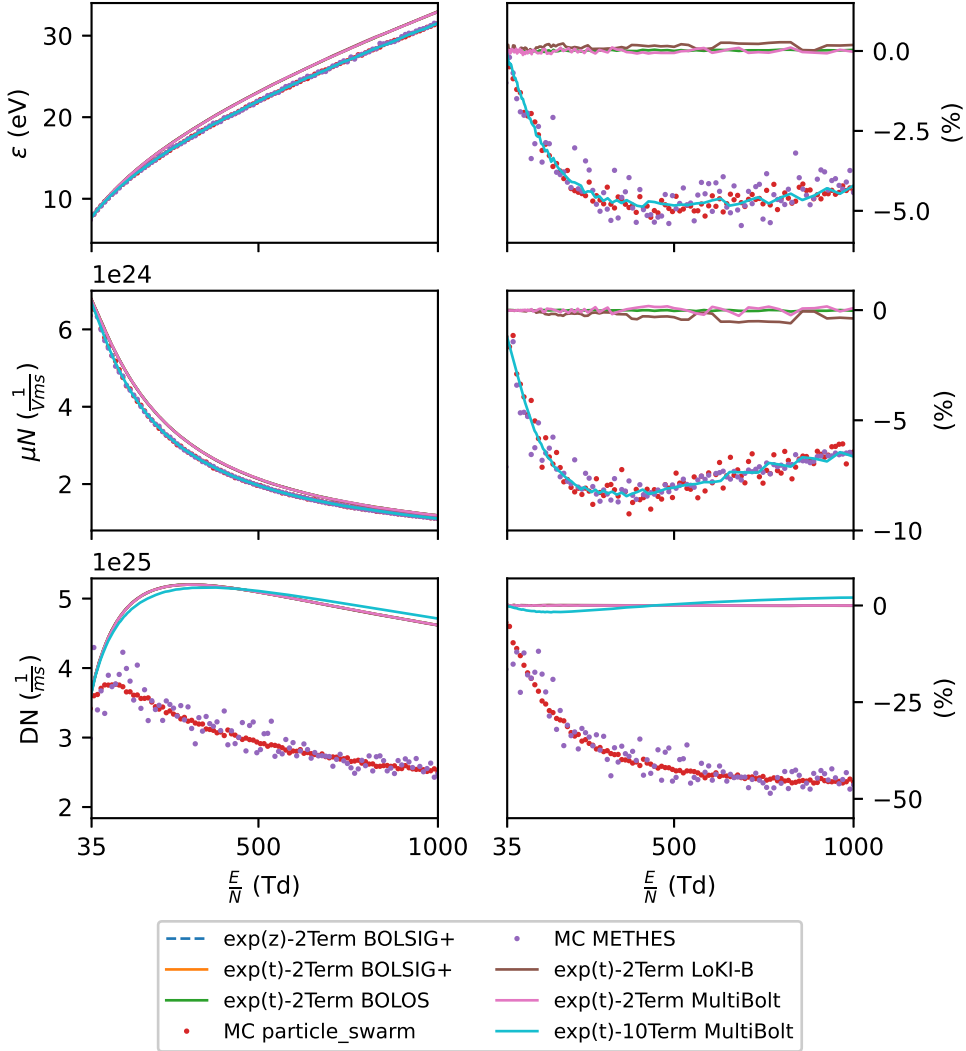


Figure 3.4.4: Swarm properties of the conservative ( $F = 0$ ,  $a = 0$ ) Lucas-Salee model. Top to bottom: mean energy, reduced flux mobility, and reduced transverse diffusion coefficient. Left to right: calculated value, and relative difference with BOLSIG+. X-axis starts at 35 Td, below this some solvers had convergence issues or too large relative differences with BOLSIG+ to display.

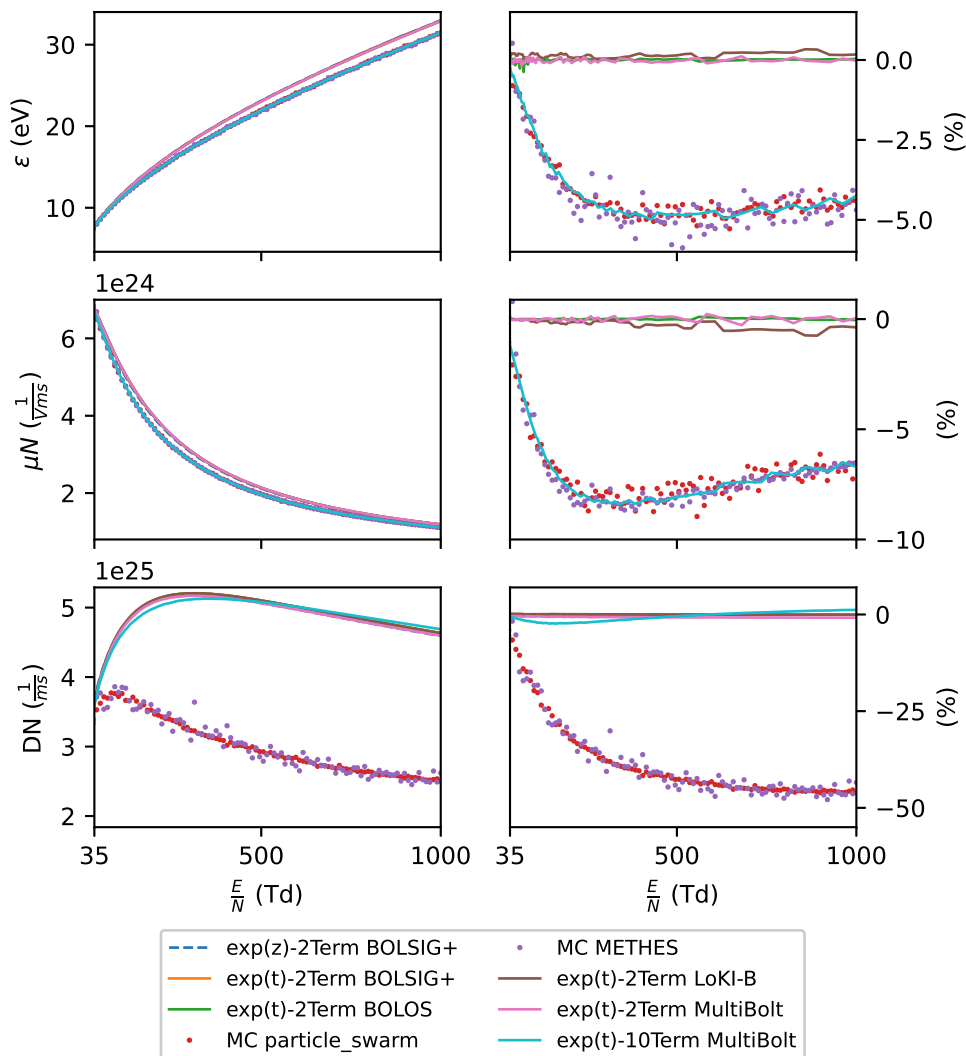


Figure 3.4.5: Swarm properties of the non-conservative attaching (proportional to velocity) ( $F = 0$ ,  $a = 0.002$ ,  $p = 0.5$ ) Lucas-Salee model. Top to bottom: mean energy, reduced flux mobility, and reduced transverse diffusion coefficient. Left to right: calculated value, and relative difference with BOLSIG+. X-axis starts at 35 Td, below this some solvers had convergence issues or too large relative differences with BOLSIG+ to display.

other 2-term solvers. Deviations reach almost 100%. It is not clear why `MultiBolt` deviates this strongly from the other solvers for this model. Surprisingly, the results diffusion coefficients of `MultiBolt` match with those of `BOLSIG+` when using the exponential spatial growth “ $\exp(z)$ ” assumption. It is unclear why this is the case.

The results for the reduced ionization coefficient are slightly different between the attaching and non-attaching model. For the non-attaching model, there is a clear difference (as seen in the mobility and mean energy) between the 2-term solvers and the Monte Carlo and 10-term based solvers. The difference reaches 5% when compared with `BOLSIG+`. For the non-attaching model the difference between the Monte Carlo solvers and the 2-term based solvers are the same except for `MultiBolt`. The 10-term and 2-term results of `MultiBolt` deviate from the Monte Carlo and other 2-term based solvers respectively. However this deviation is small (less than 1 %).

### 3.4.4 Discussion

- Analytical Maxwell model: Overall all solvers (besides `METHES`) are within 1% of the analytical results. `METHES` sometimes reaches  $\pm 10$ -20% difference. At very low fields all solvers deviate from analytical results due to inter/extrapolation errors made.
- Reid Ramp model: All solvers stay within  $\pm 4\%$  of `BOLSIG+` results for the mobility and mean energy. Monte Carlo solvers have a difference with `BOLSIG+` between -20% and -25% for the transverse diffusion coefficient.
- Non-Ionizing ( $F = 0$ ) Lucas-Salee model: 2-term solvers stay within 1% of `BOLSIG+` results for all swarm parameters. Monte Carlo solvers and 10-term `MultiBolt` solution have differences of up to -5% for the mean energy and mobility when compared to `BOLSIG+`. Monte Carlo solvers have a difference of up to -50% in the transverse diffusion coefficient when compared with `BOLSIG+`. Attachment does not have an effect on the calculated swarm parameters.
- Ionizing ( $F = 1$ ) Lucas-Salee model: All 2-term solvers stay within 1% of `BOLSIG+` results for the mean energy, mobility, transverse diffusion

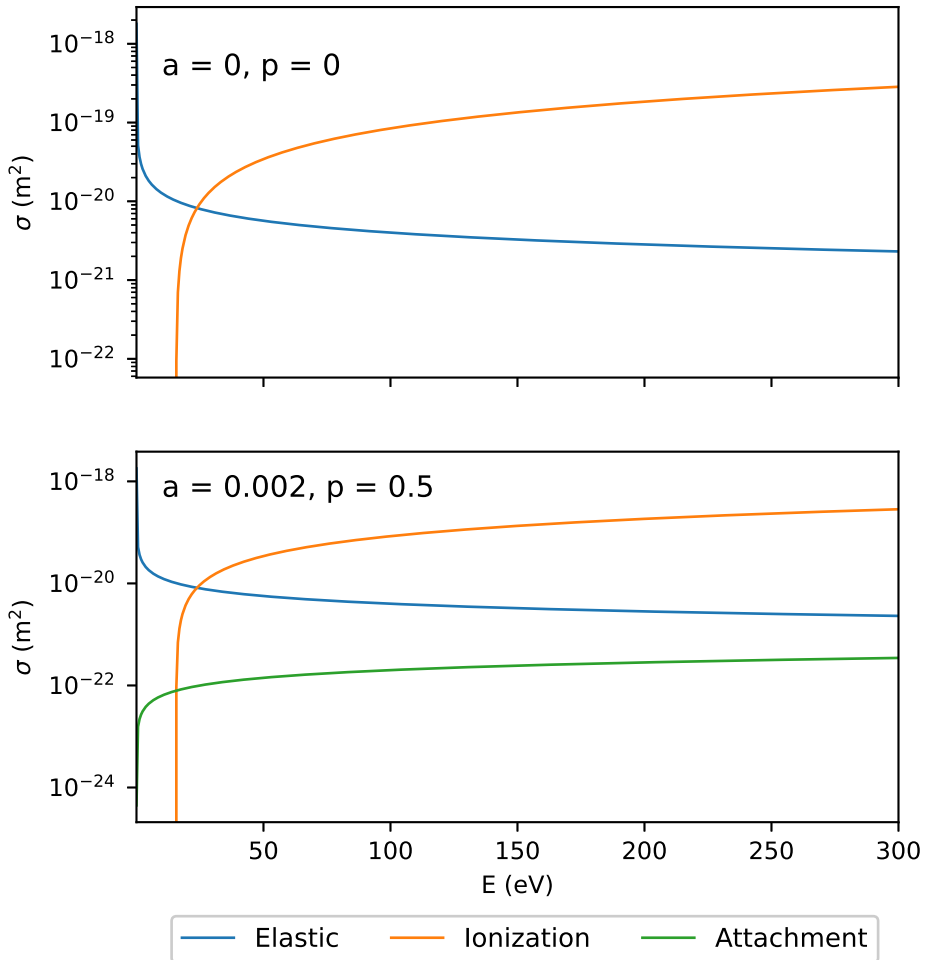


Figure 3.4.6: Cross sections for the ionizing ( $F = 1$ ) Lucas-Salee model gas.

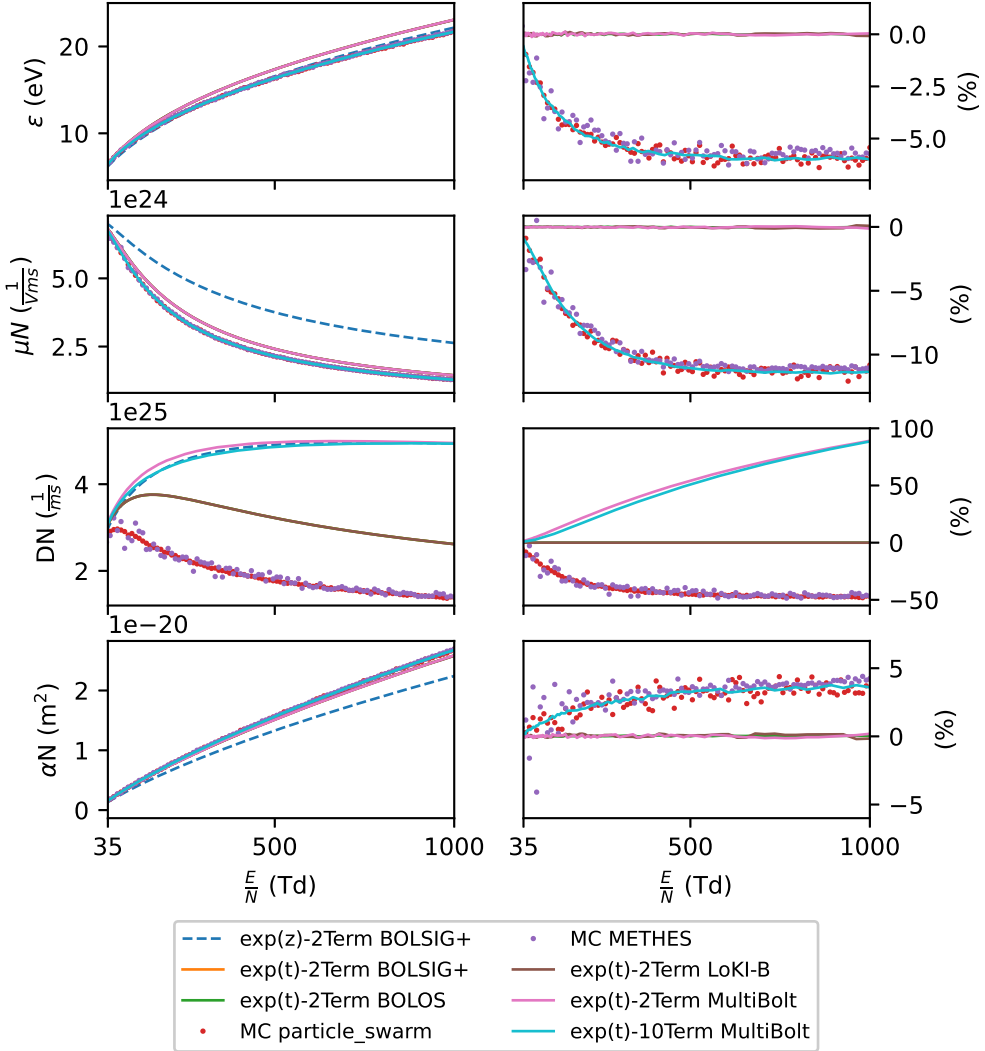


Figure 3.4.7: Swarm properties of the non-conservative ionizing ( $F = 1$ ,  $a = 0$ ) Lucas-Salee model. Top to bottom: mean energy, reduced flux mobility, and reduced transverse diffusion coefficient. Left to right: calculated value, and relative difference with **BOLSIG+**. X-axis starts at 35 Td, below this some solvers had convergence issues or too large relative differences with **BOLSIG+** to display.

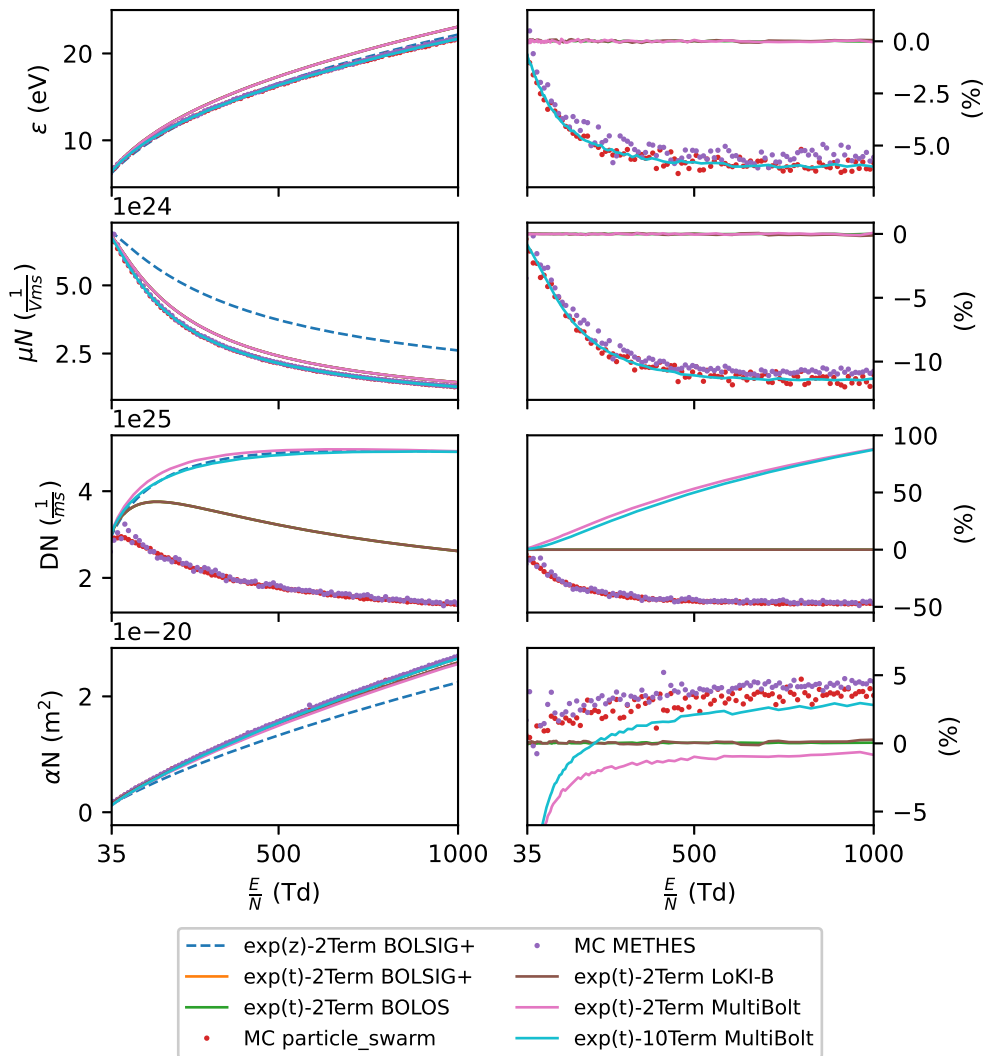


Figure 3.4.8: Swarm properties of the non-conservative ionizing and attaching (proportional to velocity) ( $F = 1$ ,  $a = 0.002$ ,  $p = 0.5$ ) Lucas-Salee model. Top to bottom: mean energy, reduced flux mobility, and reduced transverse diffusion coefficient. Left to right: calculated value, and relative difference with BOLSIG+. X-axis starts at 35 Td, below this some solvers had convergence issues or too large relative differences with BOLSIG+ to display.

coefficient, and ionization coefficient except for `MultiBolt`. Monte Carlo solvers and 10-term `MultiBolt` solution reach a difference of up to -5% for the mean energy, -10% for the mobility, and 5% for the ionization coefficient when compared with `BOLSIG+`. For the transverse diffusion coefficient `MultiBolt` (2- and 10-term) reaches a difference of up to 100%, and the Monte Carlo solvers -50%. When attachment is included the ionization coefficient calculated with 2-term and 10-term `MultiBolt` deviates a few % from the 2-term and Monte Carlo solvers respectively. Ionization seems to be treated differently in `MultiBolt` than in the other solvers.

It has been reported before [145, 165] that large differences in the reduced transverse diffusion coefficient exist when comparing a 2-term solution and a more accurate solver, however no explanation for these large differences has been given in literature. Contrary to [165] also the diffusion coefficients calculated with the 10-term solver stayed close to the 2-term results. Only the Monte Carlo solvers deviated from all other solvers.

### 3.5 Real gas comparison

In this section the results of the various Boltzmann solvers for real gases (at 300 K) are compared with experimental measurements. Since we are comparing Boltzmann solvers and solution methods it is important when choosing the input cross section data set that the data set itself was not calculated with the use of any specific Boltzmann solver or method (like a 2-term approximation). For this reason we chose data sets compiled mainly from experimentally measured or theoretically calculated cross sections.

As mentioned before, when comparing calculated swarm parameters with experimental measurements bulk swarm parameters should be used [145]. However, only the 10-term `MultiBolt` and the two Monte Carlo solvers were able to calculate bulk swarm parameters. `BOLSIG+` can also calculate bulk swarm parameters, but only if the density-gradient expansion method is used, which was not in this work. The other 2-term solvers are not able to calculate bulk swarm parameters.

### 3.5.1 Ar

In this work the BSR [22] cross section set found on LXCat [25] is used. This cross section set is calculated using the B-spline R-matrix method. This cross section set was chosen because it did not make use of the results of a Boltzmann solver to adjust any cross section.

Calculated swarm properties are shown in figure 3.5.1. For both the mean energy and the reduced flux mobility the difference between solvers is small. Differences between any solver and **BOLSIG+** stays within  $\pm 2.5\%$ .

For the reduced flux transverse diffusion coefficient we obtain 3 groups: Monte Carlo, **MultiBolt** (both 2-term and 10-term, and the other 2-term based solvers. This was observed in the ionizing Lucas-Salee model as well. Monte Carlo based solvers can deviate from the **BOLSIG+** results by up to -20%. **MultiBolt** deviates about 10% from the **BOLSIG+** results.

The reduced ionization coefficient has fairly good agreement among all solvers except for **MultiBolt**. At fields below 500 Td **MultiBolt** can deviate up to -10% from the **BOLSIG+** results. Other solvers stay within 1% of **BOLSIG+**.

Comparisons with experimental measurements are shown in figure 3.5.2. Overall there is good agreement between the calculated ionization coefficient of all solvers and the experimental values of [76, 92, 183].

For electric fields below 300 Td relatively good agreement is achieved between experimental measurements of the reduced bulk mobility of [18, 66, 93] and the Monte Carlo and 10-term solvers. The 10-term **MultiBolt** result has the largest deviation from the experimental measurements.

The characteristic energy is compared with experimental measurements of [8, 97, 117, 195]. Across the entire electric field range there is good agreement between the Monte Carlo solvers and the experimental measurements. Note the reduced spread in the results of `particle_swarm` compared to **METHES**. This can be due to stricter convergence criteria used by `particle_swarm` requiring many variables to have a small error.

### 3.5.2 N<sub>2</sub>

The cross section set used is the one reported by Kawaguchi *et al.* [81]. Calculated swarm parameters are shown in figure 3.5.3. For both the mean energy and the reduced flux mobility results from all solvers stay within

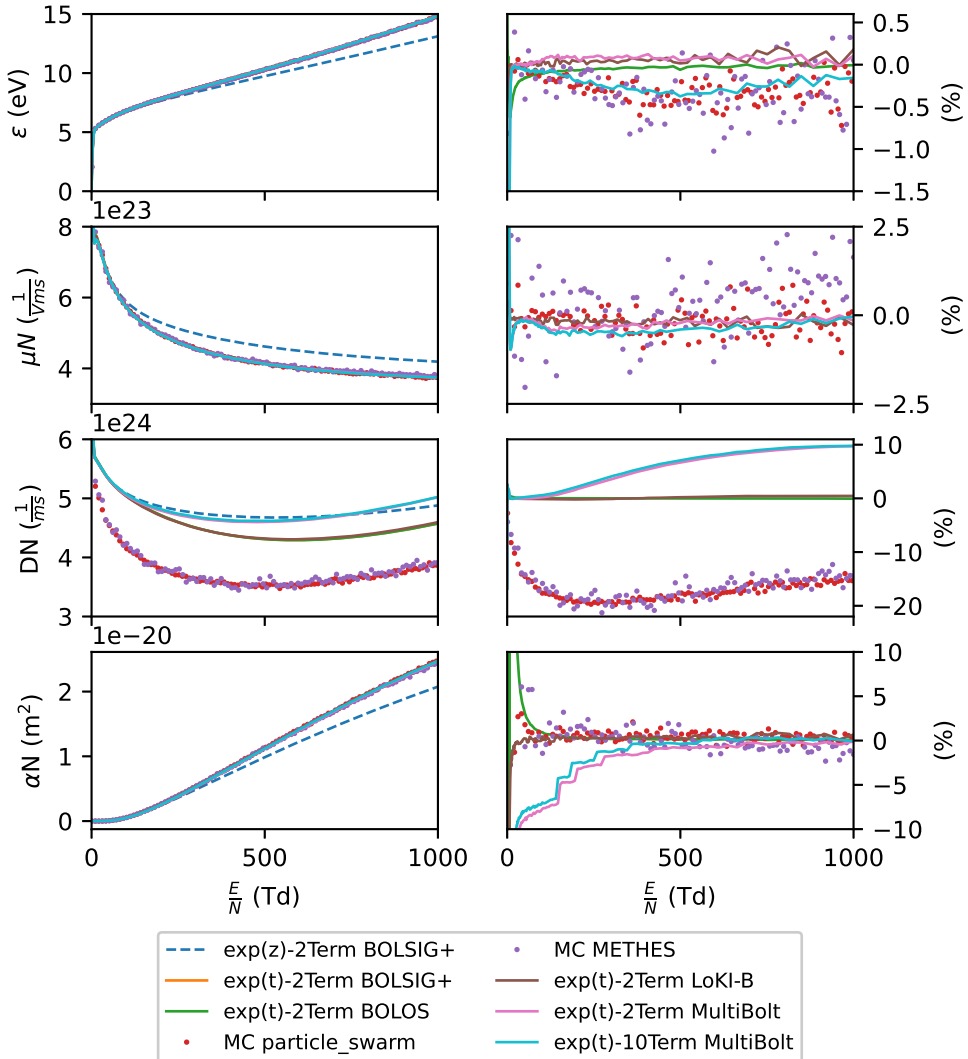


Figure 3.5.1: Swarm properties of Argon using the BSR [22] cross section set. Top to bottom: mean energy, reduced flux mobility, reduced flux transverse diffusion coefficient, and reduced ionization coefficient. Left to right: calculated value, and relative difference with BOLSIG+

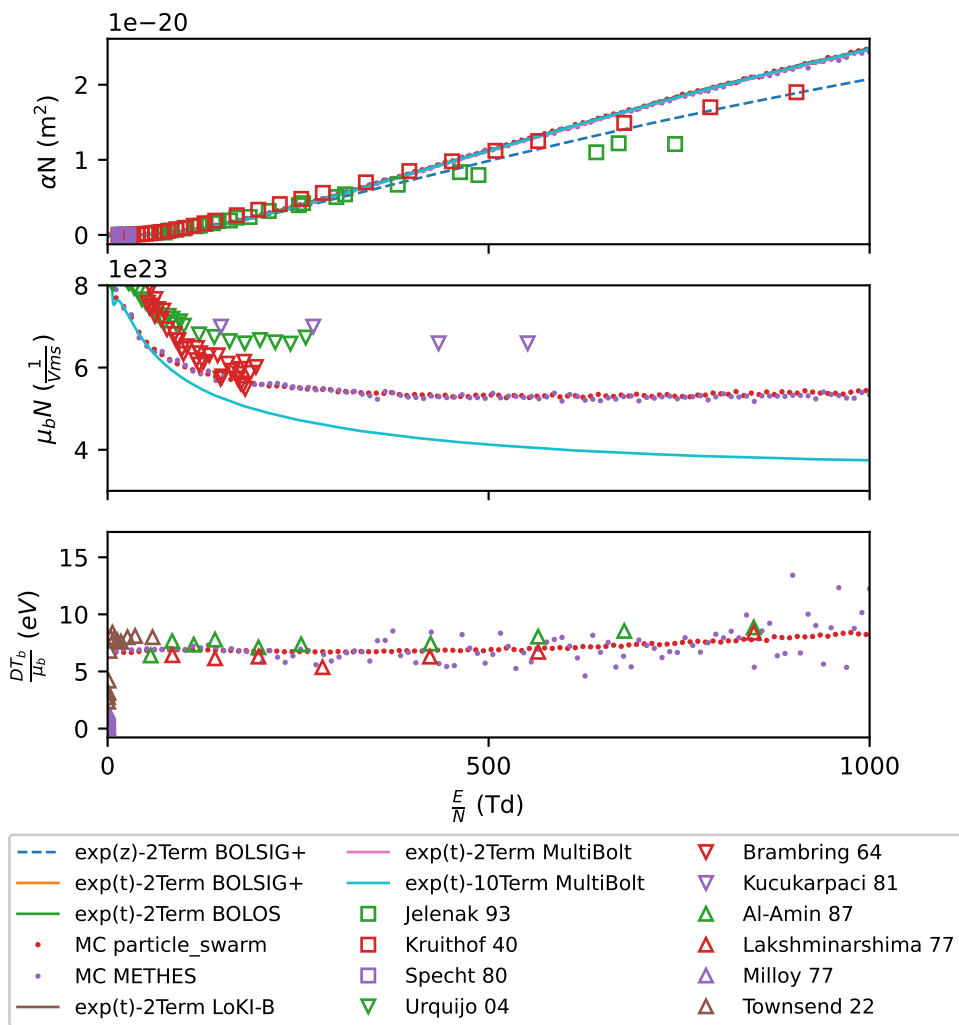


Figure 3.5.2: Bulk swarm properties of Argon using the BSR [22] cross section set compared with some experimental values. Top to bottom: reduced ionization coefficient, reduced bulk mobility, bulk transverse characteristic energy. Note: not all solvers are present in each plot even though a single legend is shown. Not all solvers can calculate bulk swarm parameters.

$\pm 5\%$  of BOLSIG+ results. Compared to Ar there is more spread among solvers, usually 1-2%.

The reduced flux transverse diffusion coefficient shows similar behaviour as with Ar and the ionizing Lucas-Salee model gas. The Monte Carlo solvers deviate from the term-expansion based solvers with differences up to -20% when compared to BOLSIG+. The MultiBolt (2-term and 10-term) solutions start to deviate from the other term-expansion based solvers around 500 Td, but still stay within 5% of BOLSIG+. LoKI-B also deviates from BOLSIG+ by about 5% across the entire electric field range.

LoKI-B deviates further from the other solvers when looking at the reduced ionization coefficient. A difference around -50% when compared to BOLSIG+ across the entire electric field range. All other solvers stay within a couple of % of the BOLSIG+ results.

Comparisons with experimental measurements are shown in figure 3.5.4. As was shown in figure 3.5.3, the reduced ionization coefficient calculated by LoKI-B deviates from all other solvers and also from the experimental measurements of [10, 11, 17, 64]. Other solvers agree relatively well with the experimental measurements.

Only the Monte Carlo solvers and the 10-term MultiBolt solver are able to calculate the reduced bulk mobility. These were compared with experimental measurements of [63, 66, 179]. Overall good agreement between calculated and experimental measurements was found.

For the transverse characteristic energy only the Monte Carlo solvers were able to calculate the required bulk parameters (bulk transverse diffusion coefficient, and bulk mobility). The results of these solvers was compared with the experimental measurements of [79, 87] and good agreement was found. Note that, just as in the Ar case, the spread of the results of `particle_swarm` is much less than that of the results of METHES.

### 3.5.3 O<sub>2</sub>

The cross section set used is from Itikawa [73, 74] retrieved from LXCat [25], but extended with the vibrational excitations from the ISTLisbon [71] database and the 3-body attachment of Phelps [138, 147]. Note, the 3-body attachment cross section was not scaled to any particular pressure.

Calculated swarm parameters are shown in figure 3.5.5. For both the mean energy and reduced flux mobility good agreement is found between

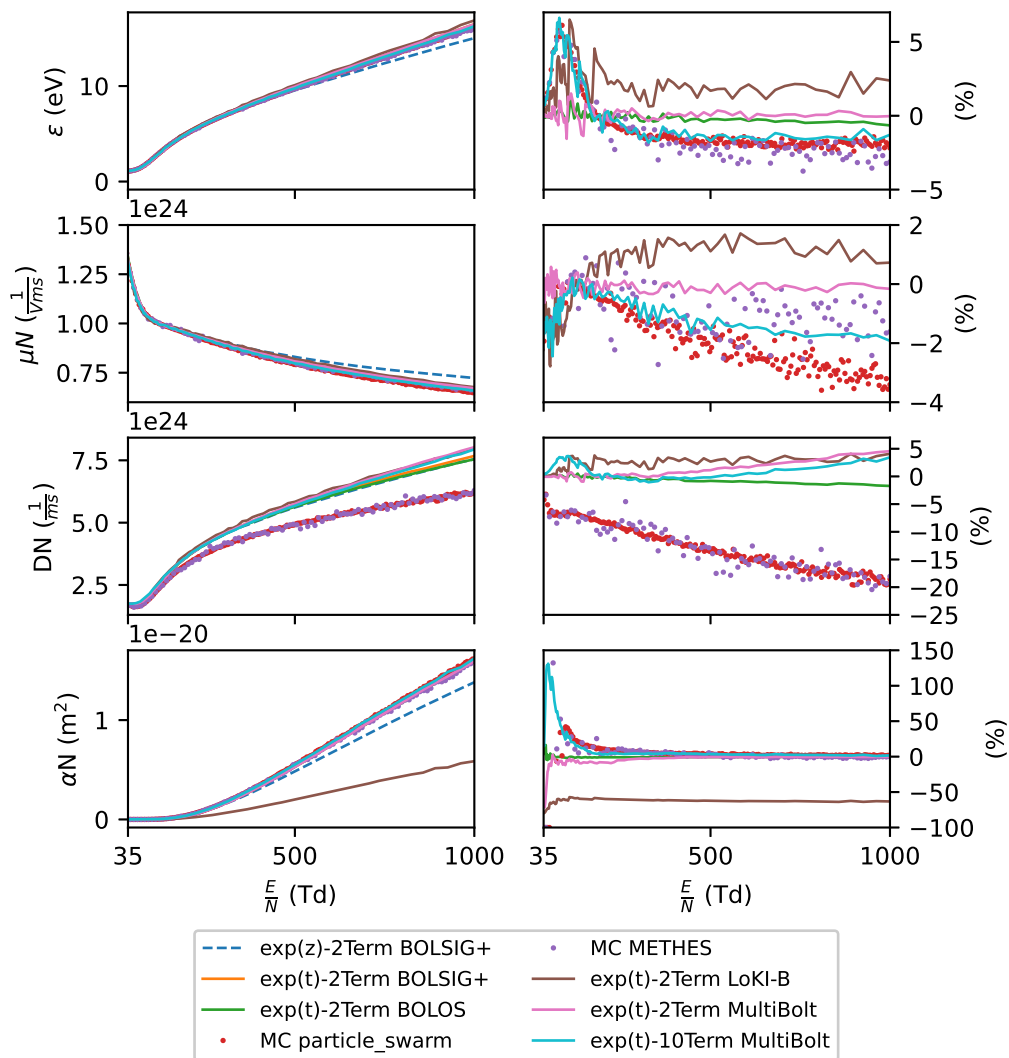


Figure 3.5.3: Swarm properties of  $N_2$  using the cross section set reported by Kawaguchi *et al.* [81]. Top to bottom: mean energy, reduced flux mobility, reduced flux transverse diffusion coefficient, and reduced ionization coefficient. Left to right: calculated value, and relative difference with BOLSIG+

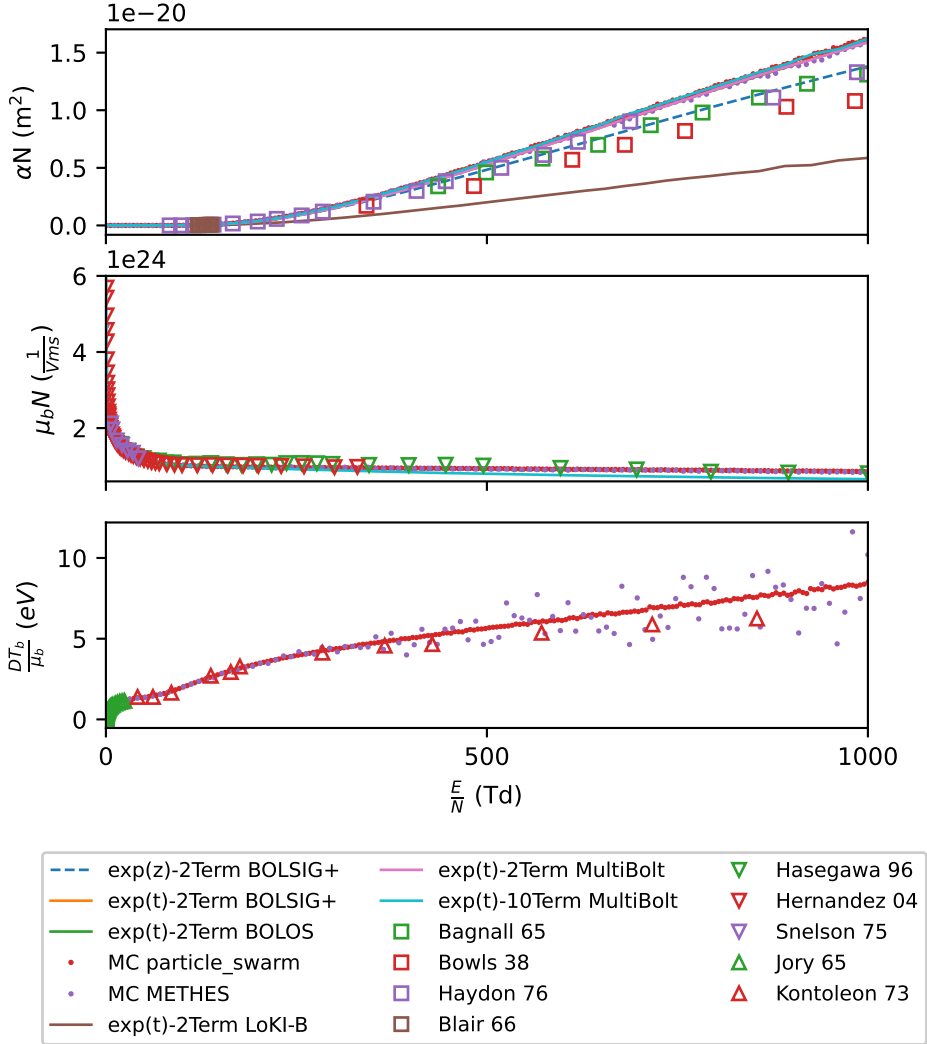


Figure 3.5.4: Bulk swarm properties of  $N_2$  using the cross section set reported by Kawaguchi *et al.* [81] compared with some experimental values. Top to bottom: reduced ionization coefficient, reduced bulk mobility, bulk transverse characteristic energy. Note: not all solvers are present in each plot even though a single legend is shown. Not all solvers can calculate bulk swarm parameters.

solvers. Differences between solvers and BOLSIG+ stay within  $\pm 2.5\%$ .

Just as in the ionizing Lucas-Salee model gas, Ar, and N<sub>2</sub> the reduced flux transverse diffusion coefficient shows `MultiBolt` (both 2-term and 10-term) deviate from the other solvers with increasing electric field. Differences with BOLSIG+ can reach up to 10%. The Monte Carlo solvers differ from the BOLSIG+ solver by up to -20%. The other 2-term based solvers stay within 1% of the BOLSIG+ results.

The reduced ionization coefficient shows a large relative difference for the `MultiBolt` (2-term and 10-term) results and the BOLSIG+ results for low electric fields, but on the absolute value plot this difference is negligible. For `LoKI-B` however the difference becomes large and reaches values of -25% when compared with BOLSIG+. This deviation of the reduced ionization coefficient for `LoKI-B` was also seen in N<sub>2</sub>. The Monte Carlo solvers and other 2-term based solvers stay within a couple % of the BOLSIG+ results.

Comparisons with experimental measurements are shown in figure 3.5.6. The reduced ionization coefficient calculated by all solvers is compared with experimental measurements of [34, 62, 154]. In the electric field range where experimental measurements exist, all solvers seem to agree with them. This includes the deviating `LoKI-B` results which only start deviating for larger electric fields.

The reduced bulk mobility of `MultiBolt` (10-term) and the Monte Carlo solvers are compared with experimental measurements of [49, 78, 104, 172]. Overall there is good agreement between the calculated and the measured values across the entire electric field range.

The transverse characteristic energy calculated by the Monte Carlo solvers was compared with the experimental measurements of [124, 161] and shown to be in good agreement for the small electric field range where experimental measurements were available.

### 3.5.4 Discussion

When comparing the solvers amongst each other for the Ar, N<sub>2</sub>, and O<sub>2</sub> gas the following observations can be made:

- The mean energy and flux mobility calculated by all solvers stays within  $\pm 5\%$  of BOLSIG+ results.

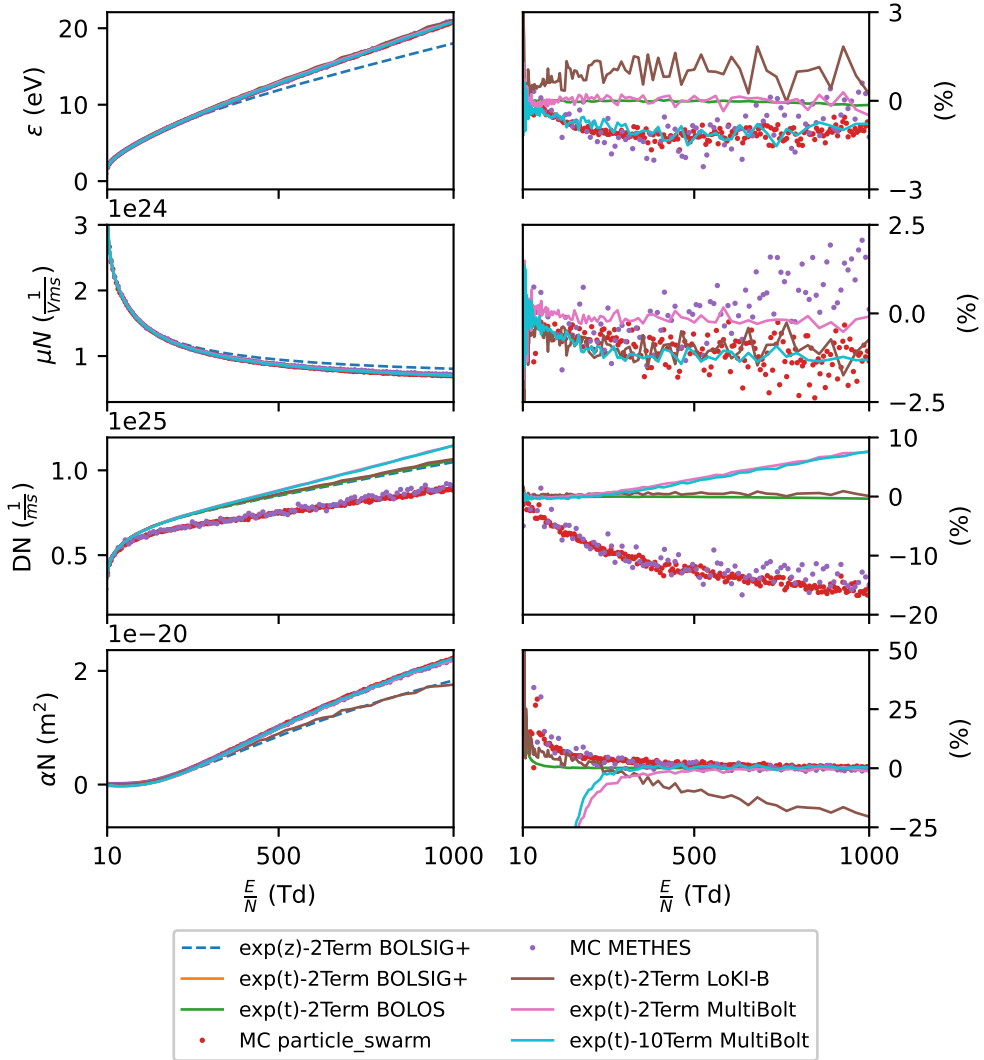


Figure 3.5.5: Swarm properties of  $O_2$  using the cross section set reported by Itikawa [73, 74] extended with the vibrational excitations from the ISTLisbon [71] database and the 3-body attachment of Phelps [138, 147]. Top to bottom: mean energy, reduced flux mobility, reduced flux transverse diffusion coefficient, and reduced ionization coefficient. Left to right: calculated value, and relative difference with BOLSIG+

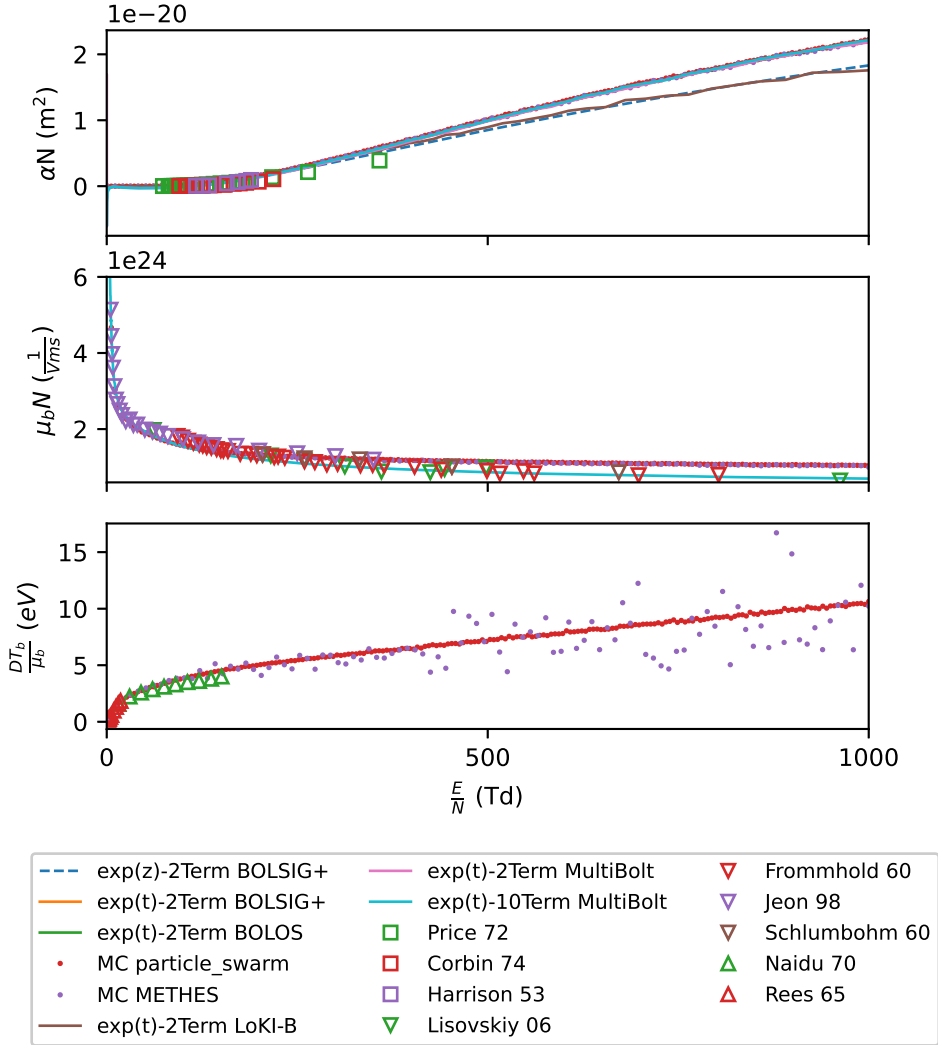


Figure 3.5.6: Bulk swarm properties of  $O_2$  using the cross section set reported by Itikawa [73, 74] extended with the vibrational excitations from the ISTLisbon [71] database and the 3-body attachment of Phelps [138, 147] compared with some experimental values. Top to bottom: reduced ionization coefficient, reduced bulk mobility, bulk transverse characteristic energy. Note: not all solvers are present in each plot even though a single legend is shown. Not all solvers can calculate bulk swarm parameters.

- The same deviation as with the ionizing Lucas-Salee model of the flux transverse diffusion coefficient from `MultiBolt` (2- and 10-term) is seen for all gases. Differences with `BOLSIG+` reach up to 10%.
- The Monte Carlo solvers have a difference in the flux transverse diffusion coefficient up to -20% when compared with `BOLSIG+`.
- Ionization coefficients for `MultiBolt` (2- and 10-term) below 100 Td can reach differences with `BOLSIG+` up to -10% for Ar, and -25% for N<sub>2</sub>. At very low fields the difference can be up to -100% for O<sub>2</sub>.
- For O<sub>2</sub> and N<sub>2</sub> `LoKI-B` produces deviating ionization coefficients across the entire electric field range. Differences around -50% for N<sub>2</sub> and up to -25% for O<sub>2</sub>.

As discussed in the model gas section, the deviations of the reduced flux transverse diffusion coefficient of more accurate solvers (multiterm and Monte Carlo) when compared to the 2-term solution have been reported before [145, 165]. No adequate explanation has been found for this discrepancy in literature.

When comparing with experiments bulk swarm parameters need to be used [145]. These are not calculated by the 2-term solvers and not all are calculated by the 10-term `MultiBolt` solver. Some observations can be made when comparing the calculated bulk swarm parameters to the experimental measurements:

- Experimental ionization coefficients match with calculated values for nearly all solvers across the entire electric field range for which experimental measurements exist. `LoKI-B` does not agree well with measurements for N<sub>2</sub>. For O<sub>2</sub> there is only a limited electric field range where the ionization coefficient is measured and for this range `LoKI-B` does match with the measurements.
- Experimentally measured bulk mobilities match well with Monte Carlo solvers and the 10-term `MultiBolt` results for N<sub>2</sub> and O<sub>2</sub>. For Ar, considerable difference exists between measurements, Monte Carlo solvers, and the 10-term `MultiBolt` results.

- For Ar, N<sub>2</sub>, and O<sub>2</sub> the experimental measurements of the transverse characteristic energy match well with the Monte Carlo solver results across the entire electric field range.

Differences in ionization coefficient when using `LoKI-B` or `MultiBolt` should be kept in mind for further research. The differences with other solvers and with experimental measurements are too large to be neglected. Especially for `LoKI-B` these differences are concerning since they are present across the entire electric field range. Why these differences exist is unclear. User error is a possibility however all other models in this work seem to work correctly and extra effort has been put into getting the current results to fall better in line with other solver results to no avail.

## 3.6 Performance

The speed of each solver depends heavily on the cross section set used and on the electric fields at which the calculations are done. To compare the solvers we use the N<sub>2</sub> cross section set of Kawaguchi used in the previous section and we calculate 100 points evenly distributed from 10 Td to 1000 Td. For the non-Matlab solvers a Python script was used to call the solver and measure the time it takes for the solver to exit. For the Matlab solvers the built-in tic-toc functions were used to measure time elapsed. The specifications of the machine on which these measurements were done are: i9-9900K CPU (3.60 GHz, 8c/16t), and 32 GB RAM.

Table 3.6.1 shows the amount of time in seconds that each solver took to solve the Boltzmann equation with previously mentioned setup. Among the 2-term solvers `BOLSIG+`, `LoKI-B`, and `BOLoS` are the fastest and the difference in time between these solvers is negligible. There is only one multi-term solver among the tested solvers and its performance is comparable to `particle_swarm` which is a Monte Carlo particle based solver. Notably, the second Monte Carlo particle based solver `METHES` performed the worst. The time required was over 17 hours. Even-though the results of `METHES` match with the other solvers its slow performance compared to the others make it not the preferred solver to use.

Solver	Time (s)
BOLSIG+ (1-8 threads)	0.71
LoKI-B	5.9
BOLOS	8.5
particle_swarm (4 threads)	226.5
MultiBolt 2-Term	350.0
particle_swarm (2 threads)	381.0
MultiBolt 10-Term	524.4
particle_swarm (1 thread)	715.0
METHES	$62 \cdot 10^3$

Table 3.6.1: Time elapsed solving for swarm parameters using the N<sub>2</sub> cross section set of Kawaguchi at 100 equidistant electric field values between 10 Td and 1000 Td.

### 3.7 User-experience

This section will list some, possibly subjective, positive and negative comments on the usage of the different solvers used in this work.

BOLSIG+ is the only term-expansion based solver which did not have any convergence issues for any model gas at any electric field value. BOLOS had most issues converging for the lower electric field values for some model gases and required careful tuning of solver parameters to get the best results. Adaptations to the BOLOS source code had to be made to be able to run the Maxwell model gas since the code assumed inelastic processes were included in the reaction set. MultiBolt has a separation between the 2-term solver and the multi-term solver. The 2-term solver is stable and overall no problems with convergence emerged. The multi-term solver did have issues converging due to matrices becoming almost singular and thus matrix inversion became an issue. The 2-term solver contained extra normalization steps to avoid almost singular matrices which were not in the multi-term solver. These steps were added in this work and were submitted as a merge request to the original MultiBolt repository. After this change convergence problems became rare.

LoKI-B requires users to adapt their LXCat formatted cross section files. All cross sections require an extra comment describing the reaction

in more detail e.g. “COMMENT: [e + M(X) → e + M(X), Elastic]” which includes electronic, vibrational, and rotational state information. Although this change is positive for scientific purposes, it can take a lot of time to add this for every reaction. Besides the extra comment line, LoKI-B also requires additional constraints on the cross section file which are not specified by the LXCat format. The LXCat format only requires 3 specific lines before the table of cross sections as a function of energy is started: Keyword indicating type of collision, Name of the target particle species, and either the ratio of electron to target mass for elastic and effective collisions or the threshold energy for excitation and ionization collisions. We found that LoKI-B also requires 3 extra lines in addition to the LXCat format and the extra comment line (example for an elastic collision): “SPECIES: e / M”, “PROCESS: e + M → e + M, Elastic”, and “PARAM.: m/M = *some ratio*”. The information in these extra lines can be found in the required LXCat lines and the additional LoKI-B comment line, but have to be added for the LoKI-B solver to run. Luckily, these extra constraints made the file still conform to the LXCat standard and thus made it usable by all other solvers, but it is still a prohibitive amount of work to go through as a user. It has to be noted that these extra lines are automatically included when retrieving data from the ISTLisbon databases [71] on the LXCat website. This will only be an issue when creating your own LXCat formatted cross section files.

The particle based solvers `METHES` and `particle_swarm` are, understandably, a lot slower to reach steady state for low electric fields compared to their term-expansion based counterparts. For this reason the particle based solvers started calculating from a reduced electric field of 1 Td instead of 0.01 Td that the term-expansion based solvers started from. The performance table in 3.6.1 shows that `METHES` has a considerably higher run-time than `particle_swarm` without offering any benefit.

Both `METHES` and `particle_swarm` use the Null collision sampling technique. A downside to this technique is that the free-flight time of a particle is determined by the maximum of the total collision frequency i.e. If the maximal collision frequency is high then a particle can only travel freely for a short amount of time before we need to check if a collision took place. Checking if a collision took place, which collision it was, and performing that collision is computationally more expensive than free-flight. Generally

the maximal total collision frequency is a single value which is obtained by summing the collision frequencies of each process across the entire energy range and taking the maximum of this summation. If at some energy the total collision frequency is sharply peaked the free-flight time of particles at all energies is reduced and the collision checking/performing parts of the code are invoked more. `METHES` comes with an algorithm which dynamically changes the maximal collision frequency used for determining the free-flight time. However, this algorithm often resulted in an infinite loop for multiple different model gases and had to be reverted to an algorithm used in a previous version of `METHES`. Because `METHES` is not hosted on a git repository these changes could not be submitted as a merge request so future users should be aware of this.

## 3.8 Conclusion

In this work a series of Boltzmann solvers were compared with each other and with experimental measurements for several model gases and real gases. The goal of this work was to test most suggested and available Boltzmann solvers and see what differences there were both in results, computation time, and user friendliness.

Overall, calculated mean energy and flux mobility for all solvers were within  $\pm 5\%$  of each other for all models and real gases used in this work. Whenever the Monte Carlo solvers produced small but noticeable differences the 10-term `MultiBolt` solver followed them showing that the 10-term `MultiBolt` solver is a viable alternative to the Monte Carlo solvers. Note it is gas-dependent if the mobility calculated using a 2-term approach is similar to a more accurate approach (multiterm or Monte Carlo). For a gas like  $\text{CF}_4$  differences of up to 30% can occur when comparing multiterm and 2-term solutions [145].

Flux transverse diffusion coefficients calculated with a Monte Carlo solver differed between -20% and 50% from the `BOLSIG+` results. These differences were reported already in earlier work [145, 165]. No explanation has been given in literature as to why this difference exists. When the application involves a plasma for which the current densities are dominated by drift (mobility) no considerable differences should be expected when using any of the solver to produce the input swarm parameters for the

model. Note that when ionization is included, the diffusion coefficients of `MultiBolt` (both 2- and 10-term) will differ from the other 2-term solvers between 5-100%. This suggests that `MultiBolt` takes into account ionization differently than the other term-expansion based solvers and that it strongly affects the calculation of the diffusion coefficient.

The ionization coefficient for the model gases for all solvers is calculated to be within  $\pm 5\%$  of each other. For Argon all solvers agree to within a couple % of each other except for `MultiBolt`. Both the 2- and 10-term `MultiBolt` results can differ from `BOLSIG+` by -10% as we go to lower electric fields. For  $N_2$  this difference can reach 100% at fields of 35 Td, and -25% for  $O_2$ . Note however that a large relative difference at low electric fields does not necessarily lead to a relevant large absolute difference. When inspecting the absolute values the difference will not be physically relevant. The story is different for `LoKI-B`, for  $N_2$  and  $O_2$  large differences arise across the entire electric field range. For  $N_2$  a difference of around -50% and for  $O_2$  up to -25% getting worse as we go to larger electric fields. This difference is also clearly visible in the absolute values and will have an effect on plasma modelling. Why this difference occurs is unclear yet.

Comparisons with experimental measurements is difficult. Bulk swarm parameters should be used when comparing to measurements [145] while all used 2-term solvers only calculate flux swarm parameters. The ionization coefficient is the only parameter that all solvers can calculate and which could be compared with experimental measurements. All calculated ionization coefficients matched well with the experimental measurements except for the ionization coefficient calculated by `LoKI-B` for  $N_2$ . For  $O_2$  the results of `LoKI-B` also deviate from the other solvers, but due to a limited electric field range where experimental measurements were taken into account it seemed to match well with the measurements.

The bulk mobility calculated by the Monte Carlo solvers and the 10-term `MultiBolt` solver matched well with the experimental measurements for  $N_2$  and  $O_2$ . For Ar, the 10-term `MultiBolt` solution does not match well with both the Monte Carlo solvers and the experimental measurements. The Monte Carlo solvers match reasonably well with the experimental measurements below about 250 Td. Not many more experimental measurements were taken into account for higher electric fields so no comment can be made on that.

### CHAPTER 3. COMPARISON OF SIX ELECTRON BOLTZMANN SOLVERS

---

The transverse characteristic energy could only be calculated by the Monte Carlo solvers. Although the 10-term `MultiBolt` solver also output a bulk transverse diffusion coefficient, its values were many orders of magnitude off the Monte Carlo solver results and looked a lot like the flux transverse diffusion coefficient. For this reason we did not take this result into account. The Monte Carlo solver results for the transverse characteristic energy match with the experimental measurements for Ar, N<sub>2</sub>, and O<sub>2</sub> for the entire electric field range where measurements were available.

From a subjective user-experience point-of-view and using the performance data from table 3.6.1 `BOLSIG+` is the preferred solver to use in most cases where the small difference of multi-term and particle based solvers is negligible. It is also the only solver among the term-expansion based solvers which had no convergence issues “out-of-the-box” for any model and real gas at any electric field value. Potential downsides to `BOLSIG+` are that it cannot be used for commercial purposes and it is closed source. The only true free and open source 2-term solver is `BOLOS` which is no longer maintained and lacks the configurability of `BOLSIG+`. For a more accurate solver the recommendation goes to `particle_swarm` since it is fast (for not too low electric fields) and it is free and open source. The Matlab codes `LoKI-B` and `MultiBolt` are indeed open source, but needing Matlab to use them is too restrictive.

## Chapter 4

# Distribution of Inception Times in Repetitive Pulsed Discharges in Synthetic Air

Knowing which processes and species are responsible for discharge inception is important for being able to speed up, delay, or completely avoid it. We study discharge inception in 500 mbar synthetic air by applying 10 ms long 17 kV pulses with a repetition frequency of 2 Hz to a pin-to-plate electrode geometry with a gap length of 6 cm. We record inception times for hundreds of pulses by measuring the time delay between the rising edge of the high-voltage pulse and the signal from a photo-multiplier tube. Three characteristic time scales for inception are observed: 1) 20 ns, 2) 25  $\mu$ s, and 3) 125  $\mu$ s. To investigate the underlying processes, we apply a low-voltage pulse in between the high-voltage pulses. These low-voltage pulses can speed up or delay discharge inception, and our results suggest that the three time scales correspond to: 1) free electrons or electron detachment from negative ions close to the electrode, 2) a process that liberates electrons from (quasi)-neutrals, and 3) the drift of an elevated density of negative ions to the ionization zone. However, each of these explanations has its caveats, which we discuss. We present a theoretical analysis of the distribution of inception times, and perform particle simulations in the experimental discharge geometry. Some of the observed phenomena can be explained by these approaches, but a surprising number of open questions remain.



This chapter is largely based on the published article:

S Mirpour *et al.* 2020 *Plasma Sources Sci. Technol.* **29** 115010

And because this was a joint work is also printed in the PhD. thesis of Dr. Shahriar Mirpour: Mirpour, S. (2021). *Lightning inception by Hydrometeors: an experimental and numerical investigation*. Eindhoven University of Technology.

The current author was responsible for all modelling results, and the majority of calculations. Writing the text was equally divided among the current author and co-author Dr. Mirpour. Interpreting results, and hypothesizing new ideas was a collective effort among all authors.

## 4.1 Introduction

The properties of streamer discharges (velocity, electric field at the tip, electron/ion densities in the body and at the tip, branching, etc.) have been widely studied, see e.g. [2, 15, 42, 122, 130, 131, 134, 176, 199]. Streamers are important in various fields like high-voltage engineering, atmospheric discharge phenomena (e.g. lightning), etc. The streamer inception voltage and the influence of the voltage rise time on this inception voltage were studied in [136, 198, 205]. [19] used time resolved optical measurements to investigate the inception of positive streamers in air. The analysis was focused on the streamer inception voltage and the reduced streamer diameter. Nevertheless, the current understanding of the complex interplay of factors governing streamer inception is still very limited. In the present work we investigate the streamer inception process in more detail.

As shown in figure 4.1.1, a positive streamer discharge can start when the electric field around a conductor or dielectric rises, free electrons move opposite to this field and travel towards positively charged tips or electrodes. When these electrons enter a region where the electron impact ionization rate is greater than the electron attachment rate they can form an avalanche. The electrons replicate rapidly due to direct impact ionization until the electron density becomes so high that space charge effects become important. The avalanche(s) can then transform into a streamer discharge. The so-called Meek criterion [113, 120] is an estimate for the number of electrons required for this avalanche-to-streamer transition.

We can identify several questions related to streamer inception: Where do the streamer-starting electrons come from? What can the inception time between an applied high-voltage and the start of the streamer discharge tell us? Are there ways to manipulate the inception of a streamer discharge without changing quantities like pressure, gas composition, applied high-voltage? Answers to these questions can be useful in high-voltage engineering applications where the inception of streamer discharges is unwanted or better control over the streamer development is needed. Somewhat related is a more poorly understood fundamental question [41, 144]: How does lightning initiate inside thunderstorms when the background electric field is below breakdown? A big difference with lightning inception and repetitive pulse discharge inception is that lightning inception is not a repetitive

process. Nevertheless, answering the posed questions in a lab setting with a repetitive pulse is a first step towards better understanding of the lightning inception process.

Streamer-starting electrons can be provided by a cosmic ray ionization event, by radioactivity from surrounding material, by gas specific electron sources, and by charges in the gap leftover from previous discharges. For  $\text{N}_2/\text{O}_2$ -mixtures, processes like detachment from  $\text{O}_2^-$  and  $\text{O}^-$  [95, 107, 140], can provide electrons to start a streamer discharge. [101] investigated how the time between two high-voltage (HV) pulses influences positive streamer inception and propagation. It was found that for short times between two HV pulses positive streamers starting on the second pulse would follow the paths of the streamers developed during the first pulse. The general physical mechanism is understood, but the mechanism that provides electrons for these second-pulse streamers is not clear yet.

The time delay between applying an HV pulse to an electrode and the inception of a streamer discharge was investigated by [205]. They split the streamer inception time into two components: the time to reach the inception voltage, and a statistical time delay due to the random nature of having an electron in the right circumstances to trigger a discharge. They conclude that the density and lifetime of  $\text{O}_2^-$  are the two main factors that determine the statistical delay, and that the statistical delay using a positive lightning impulse voltage follows a Rayleigh distribution.

[47] investigated the voltage recovery rate in spark gaps. They developed a repetitive nanosecond pulse source and found that by applying a +1 kV DC bias between two high voltage pulses to their trigger electrode they could reduce the effect of residual electrons in the discharge gap. This reduction increased the voltage recovery rate of the pulse source. Moreover, they showed that a higher DC bias voltage does not change the voltage recovery rate because of the shielding effect around the electrode. [211] investigated the influence of memory effect agents on the streamer evolution in a nanosecond repetitive discharge. They showed that by applying a superimposed DC voltage bias the number of pulses required to get breakdown is reduced. This is further reduced by increasing the DC bias until a minimum is reached. They stated that at high HV repetition frequency the electrons are attracted towards the anode by a positive DC bias. At low repetition frequency, they showed that the number of pulses before break-

down decreases. Also, they observed that the inception moment is delayed under a negative DC voltage bias.

In this work, we have taken these prior investigations as a basis for new advanced experiments and numerical models. These will give a more detailed insight into the relevant mechanisms and species involved in the inception of repetitively pulsed discharges in synthetic air. We experimentally studied the statistical distribution of the inception time ( $t_{\text{inc}}$ ) and how this distribution can be manipulated. We have detected three distinct peaks in the distribution of  $t_{\text{inc}}$  which implies three different processes for triggering a discharge in the experiment.

We also found that the histogram of inception times  $t_{\text{inc}}$  could be manipulated by applying a low-voltage (LV) pulse between two HV pulses. This LV pulse influenced the residual charged species in the discharge gap. This method allowed further investigations of the processes responsible for each peak in the  $t_{\text{inc}}$  histogram. We investigate possible sources of the three peaks: free electrons or quickly detached electrons from negative ions, Penning ionization, and drift of negative ions to the ionization zone.

A particle model for the electrons with Monte-Carlo based collision sampling (MCC) was used to further substantiate the arguments made for the sources of each peak in the  $t_{\text{inc}}$  histogram. The particle model is described in [190] except that in the current investigation of the avalanche phase, the electric field does not change in time. We have also tracked  $\text{O}_2^-$  as particles drifting in the electric field and eventually detaching electrons.

This paper is organized as follows: In section 2 we describe the experimental setup, applied conditions, and diagnostic methods. Section 3 discusses estimates of initial conditions for the simulation model. Section 4 explains the simulation model. Section 5 shows the results and discussion of the baseline experiment and different variations of the LV pulse parameters (polarity, width, and time between it and the HV pulse). Finally, in section 6 we summarize the paper and list the open questions.

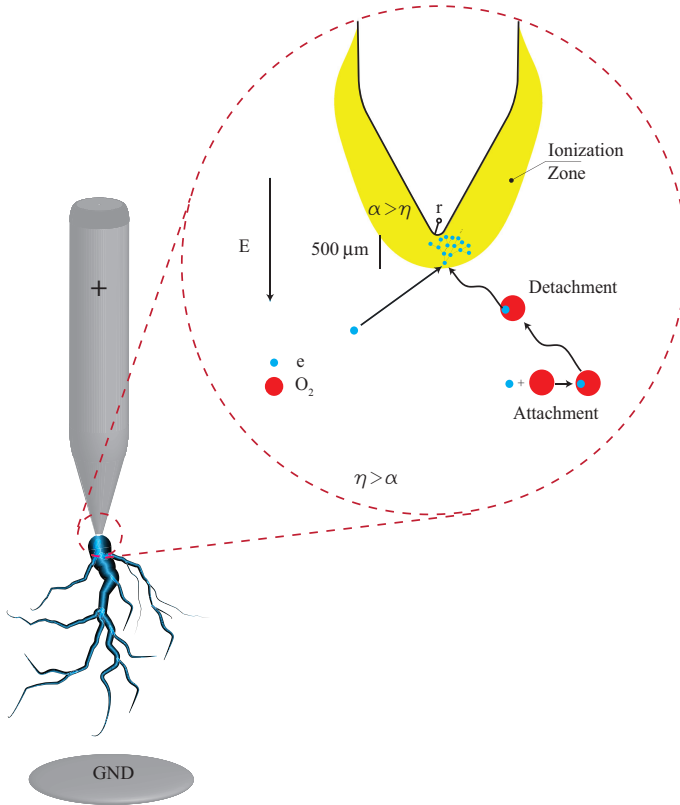


Figure 4.1.1: The inception process in which a free electron or an electron detached from a negative ion can enter the ionization zone and trigger the inception process (not to scale,  $r = 100 \mu\text{m}$ ).  $\alpha$  and  $\eta$  represent the ionization and attachment coefficient respectively.

## 4.2 Experimental Setup

### 4.2.1 Experimental conditions

All experiments in this study are performed with a point-to-plane electrode geometry (shown in figure 4.2.1) in which the electrodes are separated by a distance of 60 mm. The powered electrode, anode (with a tip radius of about 100  $\mu\text{m}$ ), is connected to the HV circuit which consists of an HV solid state push-pull switch (Behlke HTS 301-10-GSM) and a 200 pF capacitor. This produces voltage pulses with amplitudes of 17 kV, pulse widths of 10 ms, and rise times of about 40 ns. The pulses were applied with a repetition rate of 2 Hz. We chose this frequency to have a shorter acquisition time. The background pressure level in the vessel was 1 mbar and the working pressure was 500 mbar. Synthetic air (80%  $\text{N}_2$  + 20%  $\text{O}_2$ ) with less than 1 ppm impurity was used. The humidity level outside of the vessel was measured at around 47%. During the entire experimental period the vessel was kept closed. We have not seen any noticeable changes in the tip curvature and the obtained results were well reproducible.

To study how residual charges influence the streamer inception, in most experiments we applied an LV pulse between each two HV pulses. This was possible via a second custom-built push-pull switch which can apply a bias to the negative side of the HV switch. With that, we were able to make a bias with variable voltage ( $V_b$ ), width ( $t_{\text{LV-dur}}$ ), and time before the HV pulse ( $t_{\text{LV-sep}}$ ). In the case of  $t_{\text{LV-sep}} = 0$ , the LV pulse attaches to the HV pulse. The applied  $V_b$  was always plus or minus 300 V.

### 4.2.2 Measuring inception time $t_{\text{inc}}$

A photo-multiplier tube (PMT, Hamamatsu H6779-04) was placed behind a window of the vessel to capture photons produced by the discharge around the anode tip. The PMT has a response time of less than 1 ns and can measure the photons emitted in the inception process. The output signal was collected by a 12 bit HD 6104 Teledyne Lecroy oscilloscope with a maximum sample rate of 50 MS/s. Such a measurement was generally done for 600 cycles per setting. We consistently observed only one inception for each 10 ms HV pulse. From these results we established for each cycle the temporal delay between the moment the HV pulse reaches 10% of its

maximum and the moment that the PMT reaches 10% of its maximum, which would indicate streamer inception. We call this temporal delay the inception time  $t_{\text{inc}}$  and have indicated it in figure 4.2.2. The estimated total error in  $t_{\text{inc}}$  is less than 5 ns. Next, a histogram of the  $t_{\text{inc}}$  values was made. For histograms with logarithmic bins we used a binning function which divided the data into 700 bins in a logarithmic scale starting from 10 ns to the logarithm of the maximum of the  $t_{\text{inc}}$  (with the MATLAB function of `logspace(log10(0.01), log10(max(data)), 700)`), and for the linear bin histogram (figure 4.5.5) we divided the data into 100 bins. Note that for low-time bins the histogram is sparsely filled due to the limitation of the oscilloscope memory in long-acquisition windows. This results in a coarser effective bin spacing for these conditions.

### 4.2.3 ICCD imaging of streamers

An intensified CCD (ICCD, Andor Technology iStar) with nanosecond gate and a Nikkor UV 105 mm lens f/4.5 was used to image the discharges. The images presented in figure 4.2.1c-e are rendered in a false-colour scale for clarity.

The criterion used for detecting streamer inception is the moment when the PMT shows a peak which is three times higher than the average background noise. Note that the very first few pulses after starting the experiment were not included in the measurements to avoid any start-up effects. We found that in all cases exactly one discharge inception event per HV cycle was observed. This means that the discharge inception probability was 100% for all experiments done. The criterion for streamer inception detection was tested using the ICCD camera. In all cases, we found that whenever the PMT detected streamer inception, the ICCD images also showed a developed streamer. The images also show that most of the streamers reach the grounded electrode (see below).

Every time an experimental parameter was varied (pressure, applied voltage, pulse duration, etc.) the system was evacuated to a background pressure of about 1 mbar and then refilled with synthetic air. This procedure removed any species produced by preceding experiments.

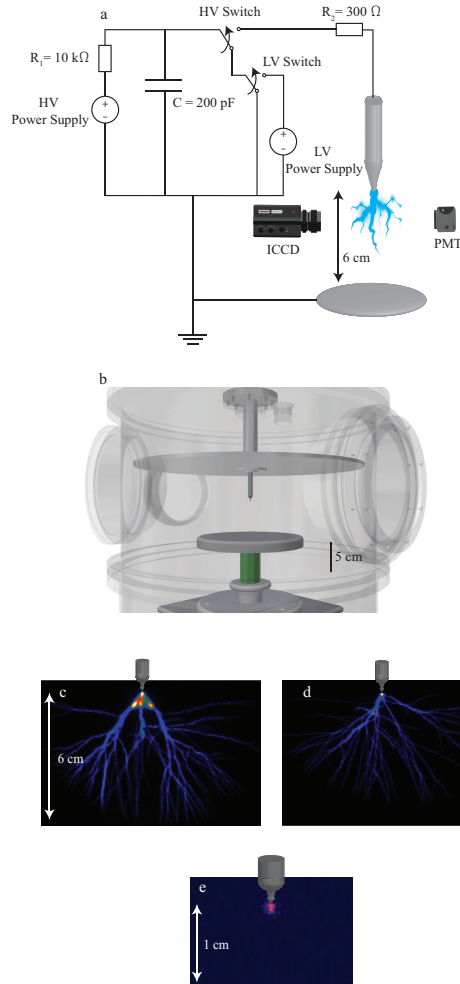


Figure 4.2.1: a) Schematic view of experimental setup with HV power supply connected to the anode (not to scale), b) schematic of experimental vessel. The large disc above the anode tip is a teflon disc to separate the high-voltage from the top of the vessel. c-e) Discharges in 500 mbar synthetic air with HV amplitude of 17 kV and repetition rate of 2 Hz. c) without applying LV pulse, d) with applying positive LV pulse  $t_{LV-sep} = 0$  and  $t_{LV-dur} = 50$  ms. The gate time of the camera is  $10 \mu\text{s}$ . e) Glow observed after a streamer burst, the glow lasts for the remaining duration of the HV pulse.

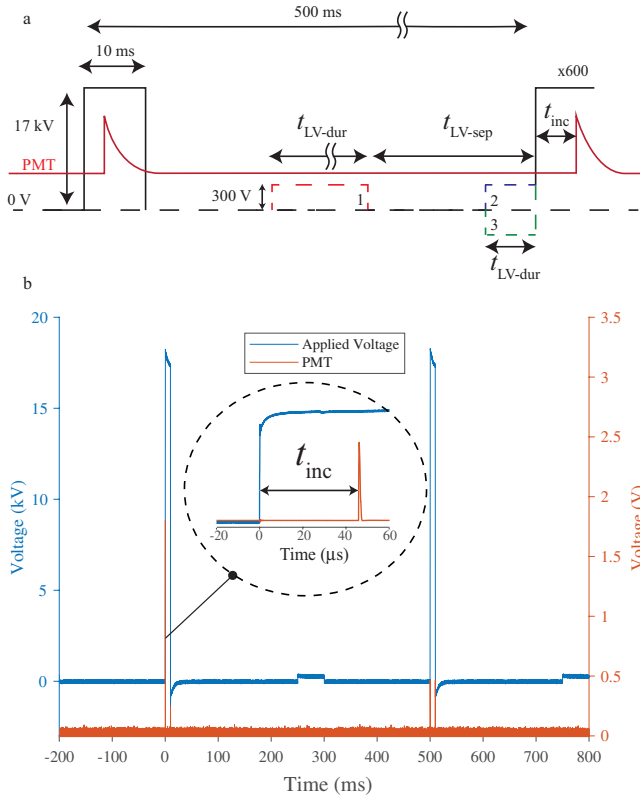


Figure 4.2.2: a) Scheme of applied HV pulse with three different LV pulse configurations: 1. Positive LV pulse between two HV pulses (red) 2. Positive LV pulse attached to the HV pulse (blue) and 3. Negative LV pulse attached to the HV pulse (green). b) Typical applied HV and LV voltage with PMT signal output.

### 4.3 Estimate of initial conditions

Figure 4.2.1c-d shows ICCD images of streamers with and without applying an LV pulse. The inception cloud, which has been introduced in [19], is smaller when an LV pulse with  $t_{LV-sep} = 0$  and  $t_{LV-dur} = 50$  ms is applied before the HV pulse. Note that later we will discuss that after the application of such a positive 50 ms LV pulse (see figure 4.5.3e) most discharges occur during the rise-time of the HV pulse, i.e., within the first inception peak (to be defined later). Based on these observations, we may conclude that the negative ions which accumulate around the anode during the LV pulse initiate the discharge faster and hence the inception cloud breaks up already during the rise-time of the HV pulse, and hence stays smaller, as the maximal radius is given by voltage over break-down field [19]. A more comprehensive explanation will be given in the coming section. Except for this observation, no significant differences in streamer propagation and branching were found in the streamer images with or without application of a LV pulse. There were also no differences observed between the images of streamers initiated in the first, second, and third peak.

After the streamer burst we observed a DC glow (figure 4.2.1e), often called Hermstein glow [36], which lasts during the remaining duration of the HV pulse and uniformly covered the powered electrode tip. The DC glow contains negative charges, screens the local electric field near the electrode tip, and prevents the onset of a new streamer [52]. Generally, the DC glow together with the streamer channel leave ions and excited species behind which can play a significant role in the emergence of streamers during the next HV pulse.

Here we estimate the density and distribution of the ions left behind by a streamer channel at the beginning of the next HV pulse. Electrons are not taken into account in this estimation (and future simulations) since they will attach very quickly after they have been produced (see also figure 4.4.4). At ground level the majority of background ionization is produced by radioactive decay [139], mainly by radon which produces alpha particles which in turn create electron-ion pairs by disintegration. This process can produce a background ionization level of  $10^3$ – $10^4$   $\text{cm}^{-3}$  (predominantly in the form of positive and negative ions). Since we perform our experiments in a metallic vessel which stops alpha particles after tens of  $\mu\text{m}$ , the back-

ground ionization due to radon decay inside the experimental vessel will be substantially lower. Cosmic ray ionization events can still occur inside the metallic vessel, but for the free electrons to have an effect on the discharge inception, before they become attached, they would need to be present in the small ionization zone around the HV pin electrode (yellow zone in figure 4.2.2) at the moment the HV pulse is turned on (or before the attachment time on the order of ns).

Following the arguments in [208], the ion density changes due to diffusion and recombination

$$\partial_t n_i = D_{ion} \cdot \nabla^2 n_i - k_{rec} \cdot n_i^2 \quad (4.1)$$

where  $n_i$  denotes the density of both positive and negative ions, and net charges and electric fields are neglected.  $D_{ion} = 0.1 \frac{\text{cm}^2}{\text{s}}$  and  $k_{req} = 2.6 \cdot 10^{-6} \frac{\text{cm}^3}{\text{s}}$  are diffusion coefficient and recombination rate at 500 mbar in air, respectively [208]. Note that we assumed that the positive and negative ion densities are equal. It is possible that there may be a small or local imbalance in charged species densities which would be able to severely affect the recombination rate. The initial condition for this equation consists of a Gaussian streamer channel centered around  $r = 0$  with  $n_i = n_{\text{channel}} \cdot e^{-r^2/R^2}$  with  $n_{\text{channel}} = 10^{14} \text{ cm}^{-3}$  and  $R = 0.3 \text{ mm}$ , and an initial background ionization of  $0.1 \text{ cm}^{-3}$ . These values are derived from an actual streamer observed by an ICCD camera and described in [208]. Fig. 4.3.1 shows this estimated initial ion density after the end of the HV pulse as  $t = 0$  and its temporal evolution under diffusion and recombination until the next HV pulse at  $t = 0.5 \text{ s}$ . Within these 0.5 s between the pulses, the ionization density decreases to about  $10^5 \text{ cm}^{-3}$  on the streamer axis and the spatial profile becomes wider due to diffusion. The ionization density stays approximately constant up to a radius of 0.5 cm. (We remark that we used  $\partial_r n_i = 0$  as a boundary condition at  $r = 1.5 \text{ cm}$ , which imitates the next streamer channel being at 3 cm distance.)

The calculated initial ion density of  $10^5 \text{ cm}^{-3}$  is several orders of magnitude larger than the largest initial  $\text{O}_2^-$ -ion density of  $10 \text{ cm}^{-3}$  used in the simulations presented in this paper. The results for these simulations are shown in figure 4.5.6c and will be discussed in a later section. The main point to be discussed here is that if a density of  $10 \text{ cm}^{-3}$  (or larger) is used as an initial homogeneous  $\text{O}_2^-$ -ion density, all inception times  $t_{inc}$  are

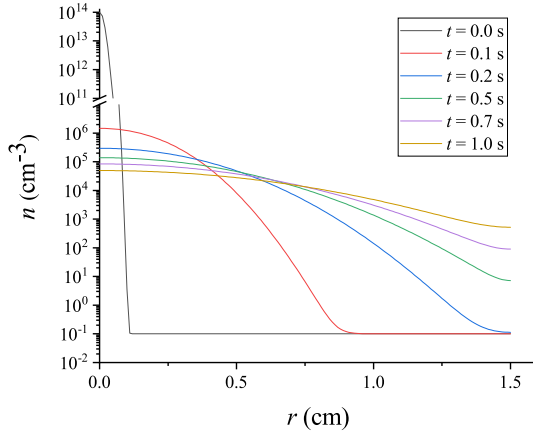


Figure 4.3.1: Ionization density  $n_i$  as a function of radius  $r$  for different times  $t$  after the streamer discharge, as described in the text.

smaller than  $1 \mu\text{s}$  which does not match with experiments.

A possible explanation for this discrepancy is the formation of  $\text{O}_3^-$  and  $\text{NO}_3^-$ . [151] has shown that already after 10 ms of diffusive expansion of a streamer channel in air at atmospheric pressure the main negative ions are  $\text{O}_3^-$  and  $\text{NO}_3^-$  with other ions like  $\text{O}_2^-$  having a substantially lower contribution to the total negative ion density.  $\text{O}_3^-$  and  $\text{NO}_3^-$  have an electron bonding energy 4 and 7 times higher than  $\text{O}_2^-$  respectively. This means that detachment from these negative ions does not occur as easily as from  $\text{O}_2^-$ .

$\text{O}_3^-$  and  $\text{NO}_3^-$  will serve as an effective electron sink. The result is that when the next HV pulse is applied, only a small fraction of negative ions (mainly the  $\text{O}_2^-$  ions) will be able to detach an electron which can initiate the discharge. Further chemical modelling is needed to investigate this in the future.

## 4.4 Simulation Model

### 4.4.1 Particle model

We have developed a particle model to simulate the inception behavior. In this model, electrons and negative oxygen ions ( $\text{O}_2^-$ ) are tracked as particles

Elastic	$e^- + N_2 \rightarrow e^- + N_2$ (*) $e^- + O_2 \rightarrow e^- + O_2$ (*)
Ionization	$e^- + N_2 \rightarrow 2e^- + N_2^+$ $e^- + N_2 \rightarrow 2e^- + N^+ + N$ $e^- + N_2 \rightarrow 3e^- + N^{2+} + N$ $e^- + O_2 \rightarrow 2e^- + O_2^+$ $e^- + O_2 \rightarrow 2e^- + O^+ + O$ $e^- + O_2 \rightarrow 3e^- + O^{2+} + O$
Attachment	$e^- + O_2 + O_2 \rightarrow O_2^- + O_2$ ( $\diamond$ ) $e^- + O_2 \rightarrow O^- + O$
Excitation	$e^- + O_2 \rightarrow$ ( $\star$ ) $e^- + N_2 \rightarrow$ ( $\star$ )
Photo-Ionization ( $\ddagger$ )	1) $e^- + N_2 \rightarrow e^- + N_2^*$ 2) $N_2^* \rightarrow N_2 + \gamma$ 3) $\gamma + O_2 \rightarrow e^- + O_2^+$
Detachment ( $\Delta$ )	$O_2^- + M \rightarrow O_2 + e^- + M$

Table 4.4.1: Reactions included in the particle model with  $M = N_2$  or  $O_2$ . Cross sections were taken from the Itikawa database [72–74]. ( $\diamond$ ) 3-body attachment was taken from the Phelps database [147] and was only taken into account for the case where  $O_2$  is the third body. According to reaction rates for 3-body attachment reported in [89] the 3-body attachment with  $O_2$  as third body is almost 50 times higher than with  $N_2$  as the third body. (\*) Elastic momentum transfer cross sections were taken from the Itikawa database to use as elastic scattering cross sections. Since the particle model only has isotropic elastic scattering this is a valid approximation to make. ( $\star$ ) All excitation reactions for  $N_2$  and  $O_2$  which were listed in the Itikawa database [74] were taken into account; listing them here would clutter the reaction list. ( $\ddagger$ ) Photo-ionization was included using a stochastic version of Zheleznyak’s model [213], as was done before in [29] and [190]. ( $\Delta$ ) The detachment reaction rate was taken from [140].

moving through a constant background of  $N_2$  and  $O_2$  molecules under the influence of the local electric field. Table 4.4.1 shows the plasma-chemical reactions included in the model; they include electron impact ionization, electron attachment and detachment and photo-ionization.

The electrons were moved with a 3D particle model using a Monte-Carlo based collision sampling (MCC) technique, as described in [190], to take collisions with the neutral background gas into account. A Velocity Verlet scheme was used to advance the electrons. The axisymmetric electric field was kept static throughout the simulations. This field was interpolated to the particle positions by converting the Cartesian particle coordinates  $(x, y, z)$  to  $(r, z)$  coordinates.

The availability of cross sections for  $O_2^-$  collisions with neutral gas molecules is limited. The motion of these ions was therefore modeled by using a mobility coefficient  $\mu$ . Their drift velocity is then given by  $\mathbf{v} = -\mu\mathbf{E}$ , where  $\mathbf{E}$  is the electric field at the location of the  $O_2^-$  ion. This drift approximation was deemed acceptable since the  $O_2^-$  ions only serve as an electron source through detachment.

The mobility of  $O_2^-$  as a function of the reduced electric field was taken from the VIEHLAND database [203]. This mobility is reported for air at STP conditions and was scaled to a pressure of 500 mbar using  $\mu = \mu_{STP} \frac{N_{STP}}{N}$ , with  $\mu$  and  $\mu_{STP}$  the mobility at 500 mbar and at 1 bar respectively, and  $N$  and  $N_{STP}$  the number density of the gas at 500 mbar and at 1 bar respectively. This tabulated database was linearly interpolated to obtain mobilities corresponding to electric fields which are not explicitly included in the database.

Experimentally measured detachment rates were fitted by [140] to obtain the following approximation for the electron detachment rate from  $O_2^-$ :  $r = N_{gas} k_0 \exp \frac{-\Delta\epsilon}{\theta}$ . Here,  $N_{gas}$  is the number density of the gas, and  $k_0 = (1.22 \pm 0.07) 10^{-11} \text{ cm}^3 \text{ s}^{-1}$  and  $\Delta\epsilon = 0.78 \pm 0.03 \text{ eV}$  are the fit parameters used for the Arrhenius approximation. Furthermore,  $\theta$  is the effective ion temperature calculated as  $\theta = \frac{\pi}{2} m_{ion} v_{ion}^2 + k_B T_{gas}$  where  $m_{ion}$  and  $v_{ion}$  are the mass and velocity of the ion respectively,  $k_B$  is Boltzmann's constant and  $T_{gas}$  is the temperature of the gas. The detachment rate is used as a collision frequency for the  $O_2^-$ -ions so that the null collision method can be used to stochastically determine if a detachment reaction takes places in a given timestep for a given  $O_2^-$ -ion.

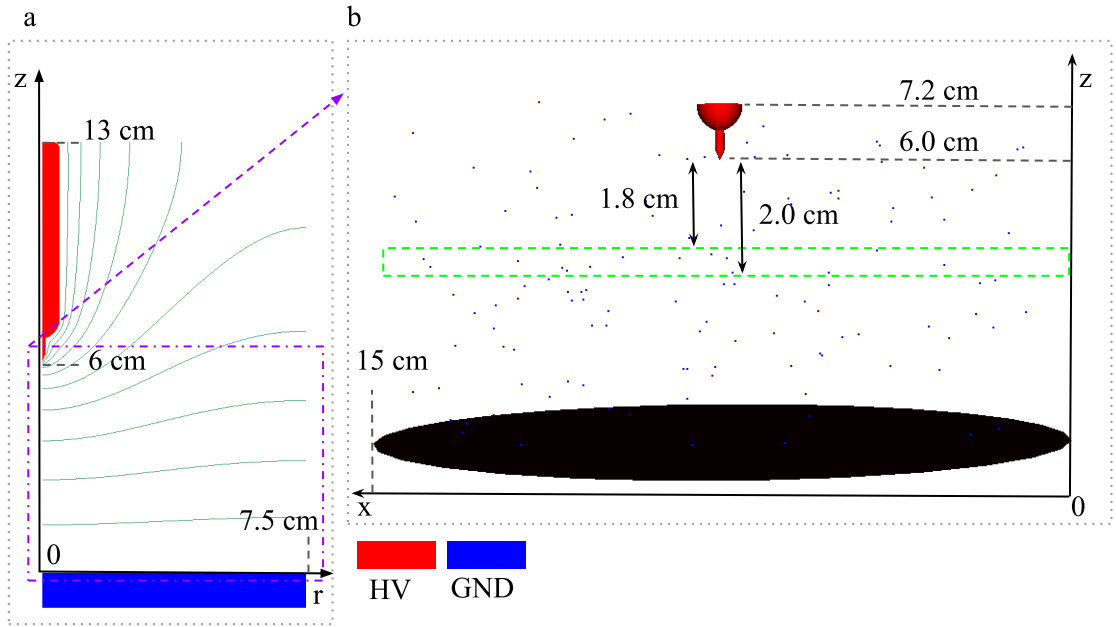


Figure 4.4.1: The computational domain for a) the electric field computation with COMSOL (included are scalar potential contour lines), and b) the particle model. The COMSOL domain uses cylindrical coordinates while the particle model uses 3D cartesian coordinates in a box of  $15 \times 15 \times 7.2 \text{ cm}^3$ . The coloured spheres in b) represent  $\text{O}_2^-$  ions placed homogeneously in the simulation box (in this particular figure a density of  $0.1 \text{ cm}^{-3}$  was used which equals 128 ions). The green highlighted area represents the position where an inhomogeneous distribution of  $\text{O}_2^-$ -ions was placed in some simulations to obtain the histograms in figure 4.5.6d.

### 4.4.2 Electric field

The electrode geometry, shown in figure 4.4.1a, was drawn in a CAD program according to the dimensions of the experimentally used electrode. To calculate the electric field distribution, this CAD drawn electrode geometry was imported into COMSOL [33] where the cylindrical symmetry of the problem was used. The boundary conditions for the scalar potential  $\phi$  were set to:  $\frac{\partial\phi}{\partial r}|_{r=0} = 0$ ,  $\frac{\partial\phi}{\partial r}|_{r=7.5\text{ cm}} = 0$ ,  $\frac{\partial\phi}{\partial z}|_{z=13\text{ cm}} = 0$ ,  $\phi|_{z=0} = 0$ , and  $\phi|_{\text{pin}} = V$  (where  $V$  is the applied voltage to the pin electrode). The rise time of the experimentally used voltage source was not taken into account in the simulations. Since we only have negative ions as initial condition in section 3 the rise time of tens of ns would not have a substantial effect. In choosing these boundary conditions we neglected the influence of the teflon disc above the needle electrode at  $z = 13\text{ cm}$ . Because the teflon disc is so far away from the discharge region and the dielectric constant of teflon is only around 2, we can assume that it would not influence the discharge considerably. The reduced electric field on the axis of the discharge gap is shown in figure 4.4.2, for the case of an applied voltage of 300 V (the LV pulse) and of 17 kV (the HV pulse).

This electric field was imported into the particle model and assumed to remain constant in time during the inception phase, i.e., space-charge effects as they occur later in the streamer phase are neglected. The simulation domain is shown in figure 4.4.1b; it is a cube of  $15 \times 15 \times 7.2\text{ cm}^3$  which completely covers the 15 cm diameter grounded electrode and the full discharge gap.

### 4.4.3 Inception time $t_{\text{inc}}$

In the experiments, the inception time  $t_{\text{inc}}$  was measured as the time from the application of the high voltage pulse until the time of light emission from the discharge. In the simulations, the presence of  $10^6$  electrons was used to determine the moment of inception, as was also done in previous inception simulations [167]. We assume the presence of  $10^6$  electrons indicates rapid and continued discharge growth, due to additional electron avalanches caused by photo-ionization.

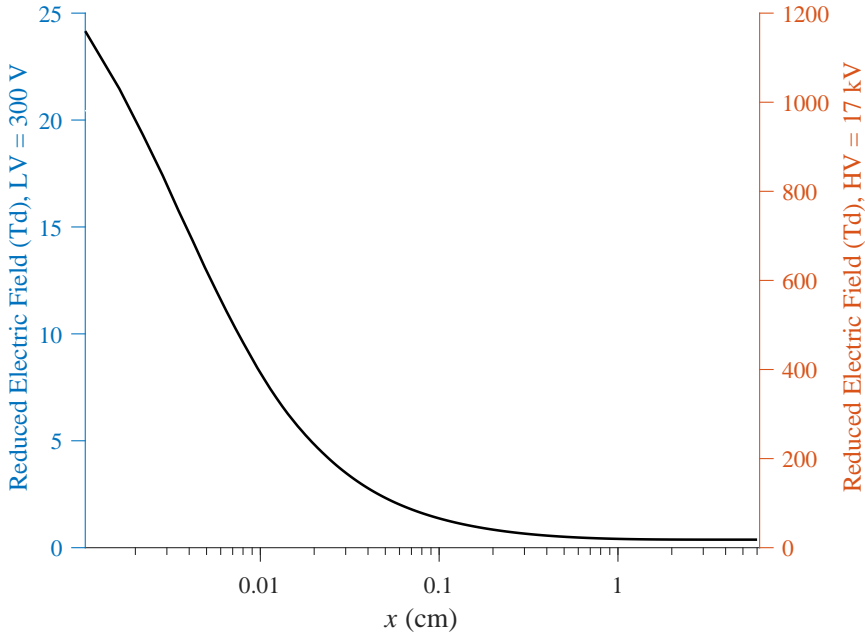


Figure 4.4.2: The reduced electric field  $E/N$  (where  $N$  is the gas number density) in Townsend on the axis of the gap for 500 mbar synthetic air at 300 K. Blue (left) y-axis shows the values for an applied potential of 300 V, red (right) y-axis shows the values for an applied potential of 17 kV. The maximum reduced electric field at the tip of the pin electrode ( $x = 0$ ) was 24 Td for 300 V applied and close to 1200 Td for 17 kV applied. The bottom grounded electrode is at  $x = 6$  cm.

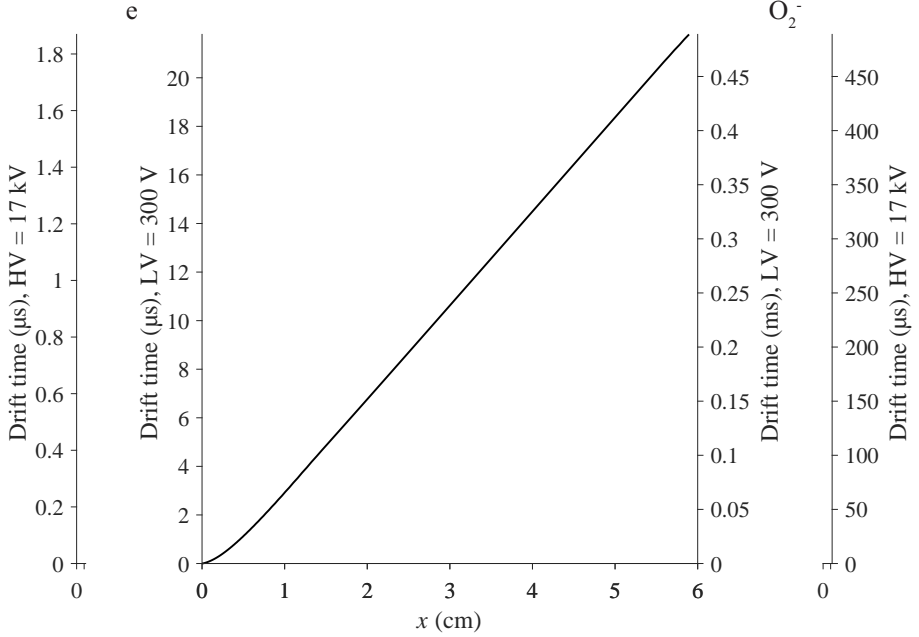


Figure 4.4.3: Drift time on the axis of symmetry of an electron (left) or an  $\text{O}_2^-$  ion (right) from a distance  $x$  to the pointed electrode at  $x = 0$  when a voltage of 300 V (inner y-axis) or 17 kV (outer y-axis) is applied across the gap. Calculated using (4.2). Only a single line is drawn because the different mobilities and voltages only change the slope of the drift time curves which can be reflected in the y-axis scale.

#### 4.4.4 Drift and reaction times

To guide the interpretation of the experimental results, we here discuss relevant drift and reaction times.

Figure 4.4.3 shows the drift time  $t_{\text{drift}}(x)$  of electrons and  $\text{O}_2^-$  ions from a distance  $x$  to the pointed electrode at  $x = 0$  on the axis of symmetry. It is calculated as

$$t_{\text{drift}}(x) = \int_0^x \frac{1}{\mu(E)E(x')} dx', \quad (4.2)$$

where  $\mu$  is the mobility of the respective species, and  $E(x)$  the electric field

on the axis, see figure 4.4.2. The two axes on the left of Figure 4.4.3 show the drift time of electrons either in the high voltage (HV) of 17 kV or in the low voltage (LV) of 300 V, and the two axes on the right show the same for  $O_2^-$  ions, in the inverse order of LV and HV. To cross the gap of 6 cm on the axis of symmetry, electrons need around  $1.8 \mu s$  under HV conditions and  $20 \mu s$  under LV conditions, and  $O_2^-$  ions need around  $490 \mu s$  (HV) and  $27.5 \text{ ms}$  (LV).

The charged species do not only drift in the field, but they also react, and characteristic times for electrons as a function of reduced electric field are plotted in Figure 4.4.4, namely the attachment time, the detachment time and the impact ionization time as a function of the reduced electric field. The breakdown field is indicated as well; for higher fields electron avalanches grow.

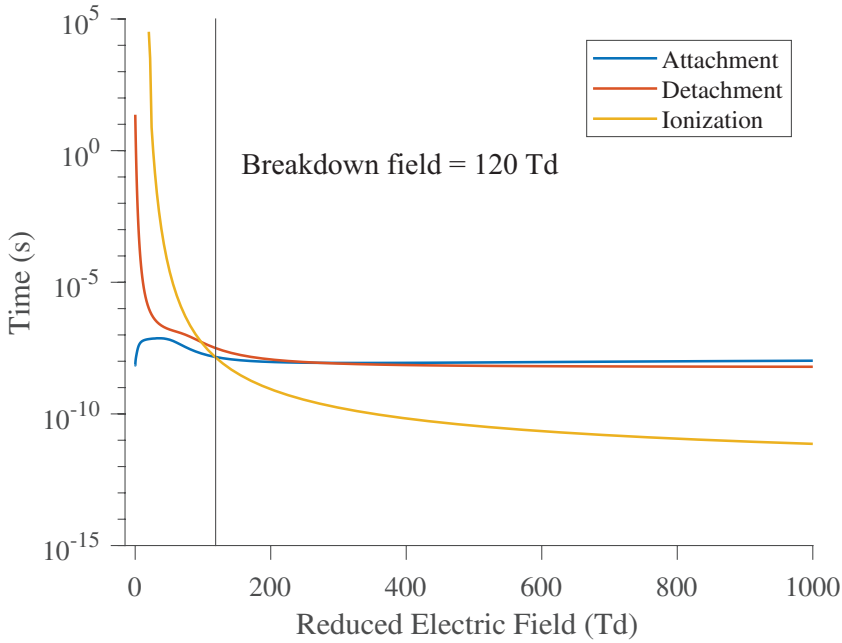


Figure 4.4.4: Attachment, detachment and ionization time of electrons in an 80/20  $\text{N}_2/\text{O}_2$  mixture at 500 mbar. The detachment time from  $\text{O}_2^-$  was calculated from formulas given in [140]. The attachment and ionization time was calculated from cross sections of Itikawa [72–74] and for the 3-body attachment from Phelps [147] which were input into BOLSIG+ [13, 61] to calculate reaction rates.

## 4.5 Results and Discussion

### 4.5.1 Baseline Experiment

In our baseline experiment, we applied HV pulses of 17 kV with a duration of 10 ms to artificial air at 500 mbar, and we repeated this 6000 times with a repetition frequency of 2 Hz. The histogram of inception times  $t_{\text{inc}}$  is displayed in figure 4.5.1a on a logarithmic scale for the time, where the size of the time bins is scaled as  $\log t$ . The histogram shows that there are three distinct peaks in this distribution, namely at around 20 ns, 25  $\mu\text{s}$ , and 125  $\mu\text{s}$ . The aim of the paper is to study the conditions for these three peaks to form and to understand their physical nature as far as possible — though puzzles remain.

It is clear that a discharge starts from an impact ionization avalanche of electrons in the high field zone near the pin electrode. And our simulations confirm that one initial electron in this region can start sufficient electron multiplication to start a discharge, at least when it is initially near the symmetry axis of the set-up. So the relevant question is: where do these initial electrons come from, when and how many? And the fact that there are three distinct inception time peaks suggests, that there might be three distinct sources for these electrons.

In a first step, we have checked whether there is any temporal correlation between discharges of the three different peaks. Figure 4.5.1b shows the  $t_{\text{inc}}$  histogram for the discharges immediately before a discharge with a  $t_{\text{inc}}$  in the first peak, and panels c and d show the same for the second and third peak. We see that the histograms in figure 4.5.1b-d all retain the same structure as the baseline figure 4.5.1a, up to differences due to the different total number of discharges. This means that the inception times  $t_{\text{inc}}$  for two consecutive discharges are uncorrelated.

### 4.5.2 Baseline theory

Before embarking into a more detailed discussion of the experiments, let us first state what we expect in the simplest case: a homogeneous distribution either of electrons or of  $\text{O}_2^-$  ions.

Let us assume in a first step that electron reactions like impact ionization or attachment as well as electron diffusion can be neglected. In this

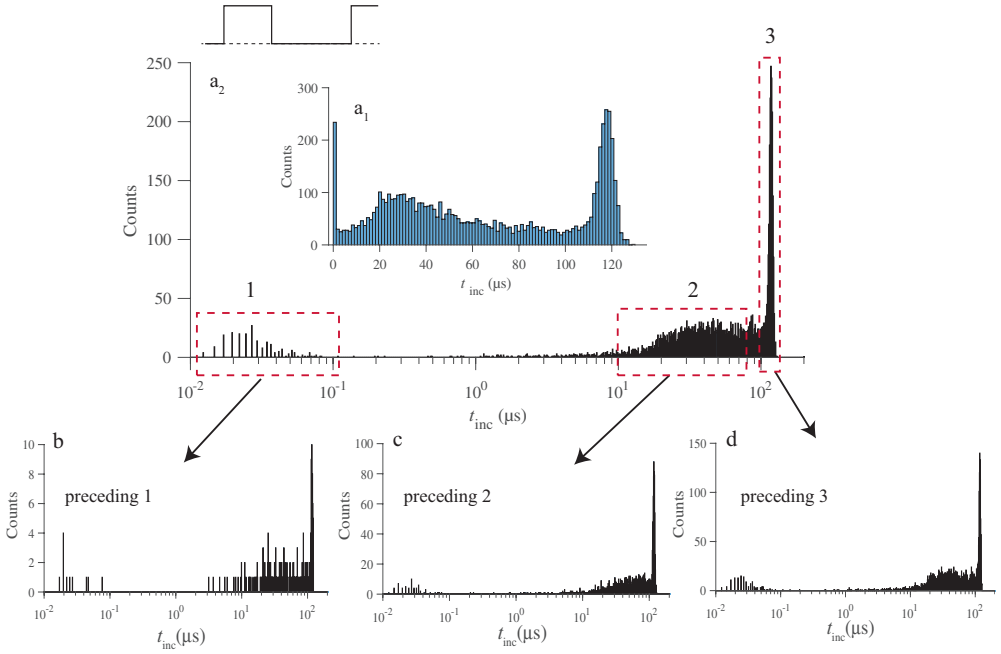


Figure 4.5.1: Histogram of discharge inception times  $t_{\text{inc}}$  with  $a_1$ ) linear and  $a_2$ ) logarithmic bins for 6000 discharges in the baseline experiment. For the logarithmic plot the bin size scales with  $\log t$ , but note that for the smallest timescales most bins are empty due to sparse oscilloscope sampling. The graph in the upper left corner of panel a) indicates the voltage wave form, a sequence of high voltage pulses. The graphs in the second row show the histogram of  $t_{\text{inc}}$  for the pulse preceding b) the first peak, c) the second peak, and d) the third peak. The contribution of the first, second, and third peak is 3.4%, 60.9%, and 31.8%, respectively. Note that the second peak is not covering all of the data between the first and the third peak.

case the electron flux  $\mathbf{j}$  in an electric field  $\mathbf{E}$  is  $\mathbf{j} = \mu_e(E)\mathbf{E} n_e$  where  $n_e$  is the electron density. We can neglect space charge effects on the inception process itself because space charge densities of such magnitudes that they have a significant effect on the electric field contradict with the observed stochastic behaviour of the inception delay. If the mobility  $\mu_e$  does not depend on the electric field, and if there are no space charges  $\nabla \cdot \mathbf{E} = 0$ , then a homogeneous electron density will stay homogeneous while drifting in the field, as

$$\partial_t n_e = -\nabla \cdot \mathbf{j} = -\nabla \cdot (\mu_e \mathbf{E} n_e) = 0, \quad (4.3)$$

according to the conservation law of electrons and to the assumptions above. This means that at any moment in time the same flux of electrons passes at any point in space, independently of the precise electric field configuration. In particular, the electron flux arriving at the high field zone near the electrode is constant in time.

As shown in 4.A, the probability density of inception can then be approximated by

$$f(t) = N/t_{\max} (1 - t/t_{\max})^{N-1}, \quad (4.4)$$

where  $N$  denotes the initial number of electrons (or  $\text{O}_2^-$  ions) equally distributed in some volume around the electrode and  $t_{\max}$  is the maximal drift time of these particles towards the electrode. As discussed in 4.A, equation (4.4) depends to a good approximation on the ratio  $N/t_{\max}$ , which can be interpreted as the number of particles reaching the electrode per unit time. Figure 4.5.2 illustrates the dependence of equation (4.4) on  $N$  and  $t_{\max}$ . In all cases, the probability of inception decreases with time, but this happens more rapidly for larger values of  $N/t_{\max}$ . The mean inception time given by equation (4.4) is  $t_{\max}/(N + 1)$ ; this time scale decreases approximately like the inverse of  $N/t_{\max}$ .

The above analysis applies to both electrons and  $\text{O}_2^-$  ions, but with a longer time scale for  $\text{O}_2^-$  ions due to their smaller mobility. These ions will drift in the field until they reach the high field zone, where they detach an electron that can start an avalanche and a discharge. In the experiments, we expect to have mostly negative ions at the beginning of the HV pulse, since the time scale for electron attachment in the absence of an electric field is on the order of 10 ns, see figure 4.4.4.

Comparing the analytical estimate for the histogram of inception times  $t_{\text{inc}}$  in figure 4.5.2 with the experimentally observed histogram in figure

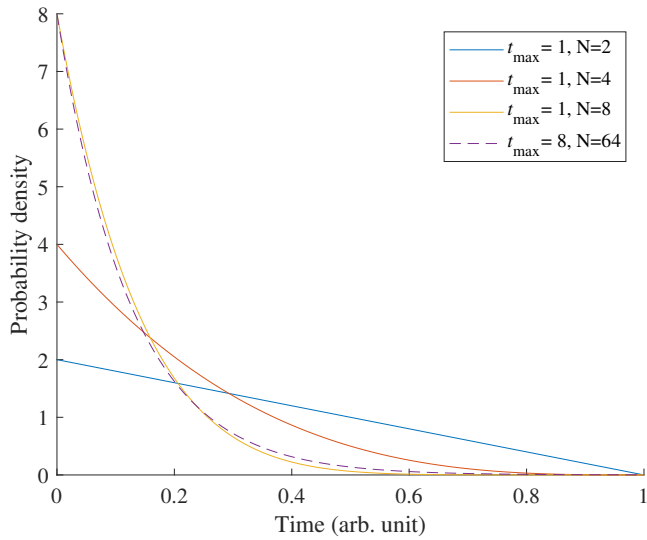


Figure 4.5.2: Analytic estimate of the inception probability versus time as given by equation (4.4).  $N$  represents the initial number of particles and  $t_{\max}$  their maximal drift time to the electrode, see the text for details. Note that the inception probability depends, to a good approximation, on the ratio  $N/t_{\max}$ . Surprisingly, our experimental results do not resemble the curves shown here.

4.5.1 we see that there is a strong deviation from the analytical estimate, with three peaks in the distribution rather than one continuous decrease. Therefore at least one of the assumptions above must be wrong. This could for example happen when:

- There is more than one species involved.
- The species are initially not homogeneously distributed.
- Attachment or ionization reactions cannot be neglected along the path of the charged species or there is another reaction liberating or binding free electrons under specific conditions.
- There are space charge effects, hence  $\nabla \cdot \mathbf{E} \neq 0$ .
- The mobility of the species is strongly field dependent.

In the following sections we will discuss each peak in the distribution of inception times, and how and why they deviate from the analytical estimate above.

### 4.5.3 The first peak

In the inception time histogram, shown in figure 4.5.1a with a statistics over 6000 discharges, the first peak occurs between 10 ns and 100 ns which is several orders of magnitude earlier and shorter than the two other peaks. The first peak accounts for about 3.4% of all inception events.

There are essentially two possible sources for this early peak: either free electrons are already available when the HV pulse starts, or there are particles, e.g.,  $\text{O}_2^-$  ions, that rapidly release electrons at that moment.

Electrons are quite unlikely to be present at the beginning of the HV pulse, since according to figure 4.4.4 they attach to oxygen on a timescale of 10 to 100 ns for electric fields well below the breakdown value. Therefore electrons produced during a previous HV pulse will attach between the pulses. It is reasonable to assume that free electrons already present in the gap when an HV pulse is applied were not produced by a previous discharge, but by rare events like cosmic rays or radioactive decay of materials present in the lab.

$O_2^-$ -ions could be a source of free electrons as figure 4.4.4 shows that a detachment time smaller than 100 ns occurs for a reduced electric field larger than 120 Td. Figure 4.4.2 shows that this reduced electric field is found for distances smaller than 0.06 cm from the pin electrode when a potential of 17 kV is applied. This shows that ions very close to the pin electrode can detach an electron sufficiently rapidly to produce the first peak. The region of space extending to a distance of 0.06 cm will be called the active zone for the rest of the discussion of the first peak. The following discussion will assume  $O_2^-$ -ions to be the main contributor to the discharges belonging to the first peak (in principle any detaching negative ion can contribute to the discharge inception, but for our experimental conditions  $O_2^-$  will be the most prevalent [140]).

#### 4.5.3.1 Hypothesis: electrons detaching from $O_2^-$ in the active zone as the source of the first peak

To test whether  $O_2^-$ -ions were present before an HV pulse, we applied a positive LV pulse of 300 V with a duration of  $t_{LV-dur} = 1$  ms or longer and immediately before the HV pulse ( $t_{LV-sep} = 0$ ). The goal was to pull all negative ions in the gap towards the pin electrode during the LV pulse without triggering a discharge.

The histogram of inception times for 600 repetitions of the pulse experiment is shown in figure 4.5.3b; it shows that the first peak is removed. The removal of the first peak can be explained in the following manner: As  $O_2^-$ -ions are drawn closer to the electrode at a certain point they will be too close to the surface of the electrode for a detached electron to produce a large enough avalanche to initiate a discharge.

A new question arises when we follow this reasoning: Why wouldn't  $O_2^-$  coming from further in the discharge gap 'replace' the  $O_2^-$  that are now pulled too close to the pin electrode and thus keep the first peak unchanged? This can only happen if the density of  $O_2^-$ -ions is higher in the active zone than in the region of space from which  $O_2^-$ -ions could travel towards this active zone during the LV pulse. It remains unsolved as to what would cause such a difference in  $O_2^-$  density. A possible source of a higher density of  $O_2^-$  ions close to the pin electrode could be the continuous glow discharge observed after a discharge has been triggered but before the HV pulse is turned off. This glow discharge has been discussed in section 3.

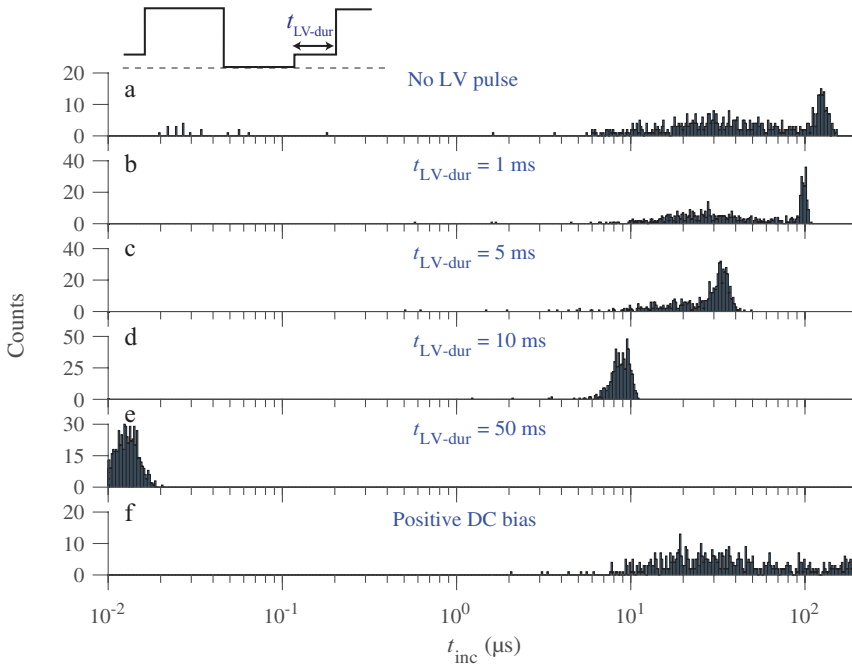


Figure 4.5.3: Histograms of discharge inception time  $t_{\text{inc}}$  for 600 discharges produced a) for no LV pulse and by applying a 300 V pulse for  $t_{\text{LV-dur}} =$  b) 1, c) 5, d) 10, and e) 50 ms, f) a DC bias before a 17 kV pulse of 10 ms with a repetition frequency of 2 Hz.

Figure 4.5.4 shows the effects that a -300 V LV pulse has on the  $t_{\text{inc}}$  histogram. For any duration  $t_{\text{LV-dur}}$  (1 ms, 5 ms, 10 ms, 50 ms, and DC) of the LV pulse,  $\text{O}_2^-$  should drift out of the active zone according to the calculated drift times in figure 4.4.3. This would mean that the first peak should not be present anymore in the  $t_{\text{inc}}$  histogram or be shifted to higher  $t_{\text{inc}}$  accounting for the drift time of  $\text{O}_2^-$ -ions. Figure 4.5.4b-f shows that the first peak remains present for times below 100 ns, just as without an LV pulse.

A possible explanation is that the electric field off-axis of the discharge gap is much lower which would keep at least some  $\text{O}_2^-$ -ions in the active zone during a negative LV pulse. This is a reasonable explanation for the short LV pulses ( $t_{\text{LV-sep}} \leq 10$  ms), but should still not be able to explain the results for  $t_{\text{LV-sep}} = 50$  ms or negative DC.

Another explanation can be the emission of electrons from the electrode due to impact/absorption of the positive ions. The kinetic energy of the positive ions will be much lower than the work function of the electrode, but if the positive ions are in a more energetic state (increased internal energy) then a surface reaction might occur which emits an electron.

## 4.5.4 The second peak

### 4.5.4.1 Experimental evaluation

The second peak in the inception time histogram in figure 4.5.1 occurs around  $25 \mu\text{s}$ . We re-plot this data in figure 4.5.5a in a linear scale to better investigate this source of discharge inception. The results of applying a positive or negative LV pulse, with different  $t_{\text{LV-dur}}$ , before the HV pulse ( $t_{\text{LV-sep}} = 0$ ) are plotted on a linear scale in figure 4.5.5b-f.

We see in figure 4.5.5b-f that the second peak does not shift significantly to lower or higher  $t_{\text{inc}}$ . The first and third peak shift substantially more and, in figure 4.5.5d, the shifted third peak 'eats up' part of the second peak. These results suggest that the source of the second peak is not measurably influenced by the electric field produced by the LV pulse.

For one set of 600 discharges we decreased the repetition frequency of the HV pulses to 0.2 Hz to investigate its effects on the second peak. Figure 4.5.9a shows the effect that this repetition frequency change had on  $t_{\text{inc}}$ . We see that decreasing the repetition frequency causes the first and third

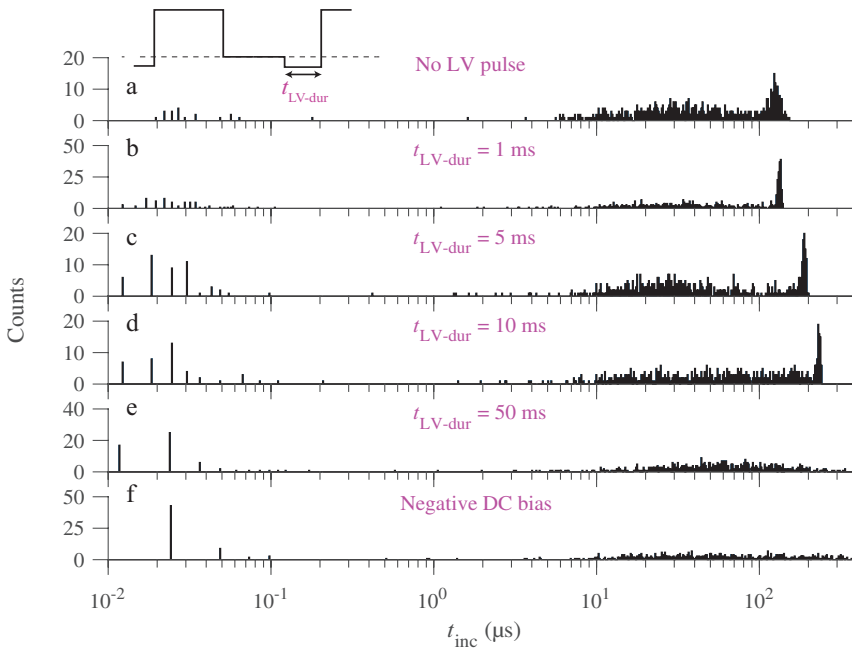


Figure 4.5.4: Histograms of discharge inception time  $t_{\text{inc}}$  for 600 discharges produced by applying a  $-300\text{ V}$  pulse for  $t_{\text{LV-dur}} =$  b) 1, c) 5, d) 10, and e) 50 ms, for a) no LV pulse and f) a DC bias before a  $17\text{ kV}$  pulse of  $10\text{ ms}$  with a repetition frequency of  $2\text{ Hz}$ . Note: The y-axis of each histogram is different which can give the impression that the first peak strongly changes in height depending on  $t_{\text{LV-dur}}$  which it does not.

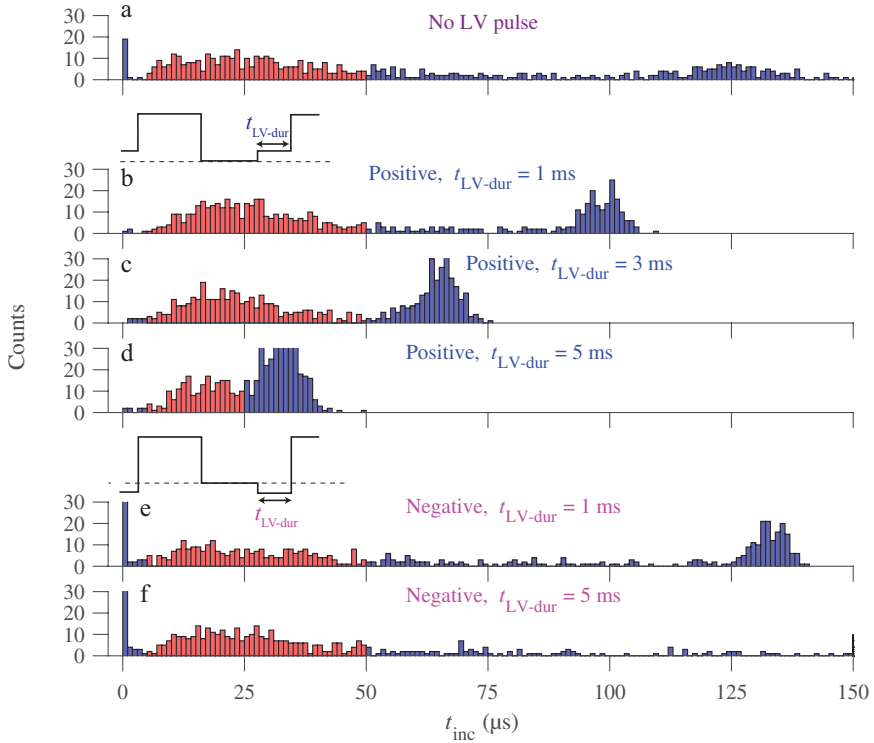


Figure 4.5.5: Characterization of second peak (red bars) after applying positive (b-d) and negative (e-f) LV pulses with 300 V amplitude and varying  $t_{LV-dur}$ . Note: The peaks of this histogram are clipped at 30 counts. This figure is mainly to show relative shifts of the second peak to the other peaks. For absolute counts refer to figure 4.5.3 and 4.5.4.

peak to completely disappear while keeping the second peak intact. The source of the second peak seems to be able to live for at least 5 seconds without an applied electric field.

We would also like to remark that we had to open up the vessel once for maintenance. When we closed the vessel and pumped the pressure down to 500 mbar, the second peak was completely removed from the  $t_{\text{inc}}$  histogram. After pumping the vessel down for a week we measured the  $t_{\text{inc}}$  histogram again and found the histogram as in figure 4.5.1 again. We think that by opening the vessel we allowed  $\text{H}_2\text{O}$  to enter the vessel. From [106] we know that  $\text{H}_2\text{O}$  is an effective quencher of excited  $\text{O}_2$  and  $\text{N}_2$  states which could correspond with the removal of the second peak. Since  $\text{H}_2\text{O}$  is not easily pumped out of the vessel we required a week to obtain the original synthetic air composition of 80%  $\text{N}_2$  and 20%  $\text{O}_2$ .

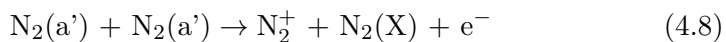
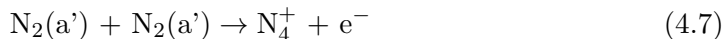
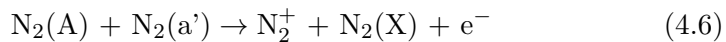
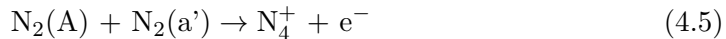
In the following section we will discuss several hypotheses which could explain the different experimental observations about the source of the second peak (No measurable effect of an LV pulse, only peak which remains when the repetition frequency is reduced to 0.2 Hz, and removal of only this peak when the vessel was briefly opened).

#### 4.5.4.2 Hypothesis

The first peak has been argued in the previous section to be caused by discharge inception by free electrons or  $\text{O}_2^-$  already present in the discharge gap when the HV pulse is applied (or created shortly thereafter).

Since the first peak is influenced strongly by applying an LV pulse before the HV pulse and the second peak is not, we think it is likely that the second peak is caused by electron creation processes involving only neutral species.

One hypothesis would be the production of electrons due to Penning ionization. We worked in an  $\text{N}_2/\text{O}_2$  gas mixture so we can identify various Penning ionization reactions from literature [59]:



However, the lifetime of the excited states  $N_2(A)$  and  $N_2(a')$  are determined by quenching reactions with  $O_2$  as shown in [24]. At a pressure of 500 mbar these quenching reactions will have a timescale on the order of 10 to 100 ns. Taking these quenching reactions into account we can assume that the density of  $N_2(A)$  and  $N_2(a')$  will be very low after the hundreds of ms that the HV pulse was off and thus cannot explain the second peak.

Another possible explanation for the second peak could be that there are quasi-neutral patches of charged species which, due to their space charge effects, cannot be pulled apart by the field created by the LV pulse (or DC), but the large charge densities required for this are not consistent with the observed stochastic inception behaviour.

## 4.5.5 The third peak

### 4.5.5.1 Source of Electrons

The third peak in the baseline experiment occurs around 125  $\mu$ s. The histogram obtained when we applied a 300 V pulse for 1 ms before the HV pulse, shown in figure 4.5.3b, shows that the third peak shifted to lower  $t_{inc}$ . This shift can mean one of two things: either the source of electrons shifts closer to the electrode, or the process to produce an electron is sped up.

Theoretical results obtained by assuming that the third peak is caused by a source of electrons which can move due to the application of an LV pulse match well with the experimental observations. For this reason the following analysis will start from this assumption.

### 4.5.5.2 Hypothesis: Drift time of $O_2^-$ as the characteristic time of the third peak

Assuming that the inception time for the third peak is caused by the drift time of a negative ion (e.g.  $O_2^-$ ) we can calculate whether the shift of the third peak, when applying a positive LV pulse, corresponds to the movement of negative ions during the positive voltage pulse. In the following calculations the drift of the negative ions is calculated directly on the axis of the pin electrode. The electric field will be slightly different off-axis and so results will change when ions are allowed to drift off-axis.

Without a positive LV pulse the third peak occurs at 122.8  $\mu\text{s}$ . We assume that this is the average drift time of an  $\text{O}_2^-$ -ion to get to the HV pin electrode. In principle it is sufficient for the negative ions to travel to the ionization zone, but for calculation purposes it is easier to take the HV pin electrode as endpoint. We therefore find the distance  $\Delta x$  from the HV electrode at which the negative ions start by applying equation 4.2, where  $t_{\text{inc}}$  is the average inception time of 122.8  $\mu\text{s}$ ,  $E(x)$  is the applied electric field between the electrodes (on the axis), and  $\mu_I(E(x))$  is the  $\text{O}_2^-$ -ion mobility at 500 mbar at position  $x$ . We obtain  $\Delta x = 1.73$  cm. This means that if the inception time of 122.8  $\mu\text{s}$  of the third peak is caused by the drift time of negative ions to the HV electrode, they would need to have started at a distance of 1.73 cm from the pin electrode.

When we applied a positive LV pulse with  $t_{\text{LV-dur}} = 1$  ms and  $t_{\text{LV-sep}} = 0$ , the third peak shifted to 98.3  $\mu\text{s}$ . Performing the same calculation as before, we find that the negative ions started at a distance of 1.45 cm from the HV pin electrode. Indicating that during the LV pulse the negative ions moved 0.28 cm towards the pin electrode.

Now we can calculate the distance that an  $\text{O}_2^-$ -ion would travel during this LV pulse. Starting from a position of 1.73 cm from the pin electrode the  $\text{O}_2^-$ -ion will drift for a time  $t_{\text{LV-dur}}$  in the field of the LV pulse. In this case  $t_{\text{LV-dur}} = 1$  ms and using Eq.(4.2) we find  $\Delta x = 0.20$  cm.

We see that the difference in travel distance (1.73 cm - 1.45 cm = 0.28 cm) of the negative ions for the experiments with and without this positive LV pulse corresponds to the distance  $\text{O}_2^-$ -ions can travel during this LV pulse (0.20 cm). These calculations suggest that  $\text{O}_2^-$ -ions cause the third peak and that the values of  $t_{\text{inc}}$  correspond to the average drift time of the  $\text{O}_2^-$ -ions to the HV pin electrode.

A comparison of the shift of the third peak caused by the application of a positive LV pulse with various  $t_{\text{LV-dur}}$  and the distance negative ions can travel during this LV pulse is given in table 4.5.1. In this table we can observe that for  $t_{\text{LV-dur}} = 10$  ms the  $\text{O}_2^-$ -ions should have already reached the pin electrode, but their starting position seems to still be 0.3 cm from the pin electrode. A possible explanation is that the electric field of the LV pulse is not the only force in the gap. Space charge effects could reduce the distance that the negative ions can drift in the field of the LV pulse.

We also applied a negative LV pulse with various  $t_{\text{LV-dur}}$  and  $t_{\text{LV-sep}}$

$t_{LV-dur}$ (ms)	$t_{inc}$ ( $\mu$ s)	$\Delta t_{inc}$ ( $\mu$ s)	$x_{start}$ (cm)	$\Delta x_{start}$ (cm)	$\Delta x_{LV}$ (cm)
Positive LV					
0	122.8		1.73		
1	98.3	24.5	1.45	0.28	0.20
5	32.52	90.28	0.66	1.07	1.04
10	9.1	113.7	0.3	1.43	>1.73
Negative LV					
0	122.8		1.73		
1	132.3	-9.5	1.84	-0.11	-0.2
5	184.6	-61.8	2.45	-0.72	-1.03
10	228.3	-105.5	2.95	-1.22	-2.02

Table 4.5.1: Table with experimentally observed shifts ( $\Delta t_{inc}$ ) of the third peak in the  $t_{inc}$  histograms shown in figure 4.5.4 when applying an LV pulse with variable  $t_{LV-dur}$ . If the  $t_{inc}$  of the third peak corresponds to the drift time of  $O_2^-$ -ions then  $x_{start}$  would be the average starting position of the  $O_2^-$ -ions. The shift in starting position due to the LV pulse is represented by  $\Delta x_{start}$ . The distance that  $O_2^-$  can travel during the LV pulse is calculated using Eq.(4.2) and represented here as  $\Delta x_{LV}$ .

= 0. Figure 4.5.4e shows the histogram obtained from these experiments. We can see that the third peak is now shifted to higher  $t_{inc}$ . Table 4.5.1 shows the experimental and calculated shifts of the third peak for different  $t_{LV-dur}$ . We can see that the calculated shifts match pretty well with the experimentally observed shifts. The presented results seem to agree with the idea that the third peak is mainly caused by the drift of negative ions, likely to be  $O_2^-$ -ions.

Note that there is a sharp drop after the third peak of around 125  $\mu$ s. An interpretation could be that up to a distance of around 1.7 cm there are sufficient negative ions to have a near unity probability of inception. The results should not be interpreted as if there are no ions after this distance of 1.7 cm, they simply do not get a chance to be the cause of inception.

### 4.5.5.3 Producing the Third Peak

Here, we discuss how the third peak appears in linear and log scaled histograms of  $t_{\text{inc}}$  obtained from particle simulations with different initial conditions. The goal is to understand what the initial conditions of the particle simulations have to be to obtain a comparable result to experiment. Homogeneous ion densities of  $0.1 \text{ cm}^{-3}$  to  $10 \text{ cm}^{-3}$  were used as initial conditions. Only  $\text{O}_2^-$ -ions were placed since from figure 4.4.4 we can see that most electrons should have attached already during the 490 ms HV pulse off-time. A fourth particle simulation was done where a homogeneous ion density of  $10 \text{ cm}^{-3}$  was placed together with an extra patch of ions at a distance of around 1.9 cm from the pin electrode as shown as the green rectangle in figure 4.4.1. This extra patch of ions contained 3 times as many ions as in the rest of the domain (124 in the domain, 354 in the extra patch). Each initial condition was run 600 times to obtain statistics on  $t_{\text{inc}}$  from the simulation results. An initial homogeneous distribution of  $0.1 \text{ cm}^{-3}$   $\text{O}_2^-$  resulted in a probability of inception within 1 ms of 91%, all other initial conditions had a 100% inception chance.

We can see in all initially homogeneous cases that the experimentally observed peak around  $125 \mu\text{s}$  is absent from the linear scaled histograms shown in figure 4.5.6a-c.

The log scaled histogram shown in figure 4.5.6a<sub>2</sub> contains a peak  $> 125 \mu\text{s}$  which would naively be matched with the third peak observed in figure 4.5.1. A property of the log scaled histogram is that the bins on the x-axis increase in size as we move along the x-axis. This property causes a peak to show up in log scaled histograms fairly easily. However, note that in the experimental observations of the third peak, it is also visible on a linear scale.

For these simulations there was only one assumption which was that the initial ion density was distributed homogeneously. Since we are investigating the discharge inception for repetitive pulses it is possible that the initial density for the next pulse is not homogeneously distributed. Figure 4.2.1c shows a typical discharge during one of the HV pulses. We can see that it is not unreasonable to assume an initial inhomogeneous distribution of ions as we move away from the HV pin electrode.

Figure 4.5.6d shows the histograms of  $t_{\text{inc}}$  for the simulations with an extra patch of  $\text{O}_2^-$ -ions placed between 1.8 cm and 2.0 cm from the pin

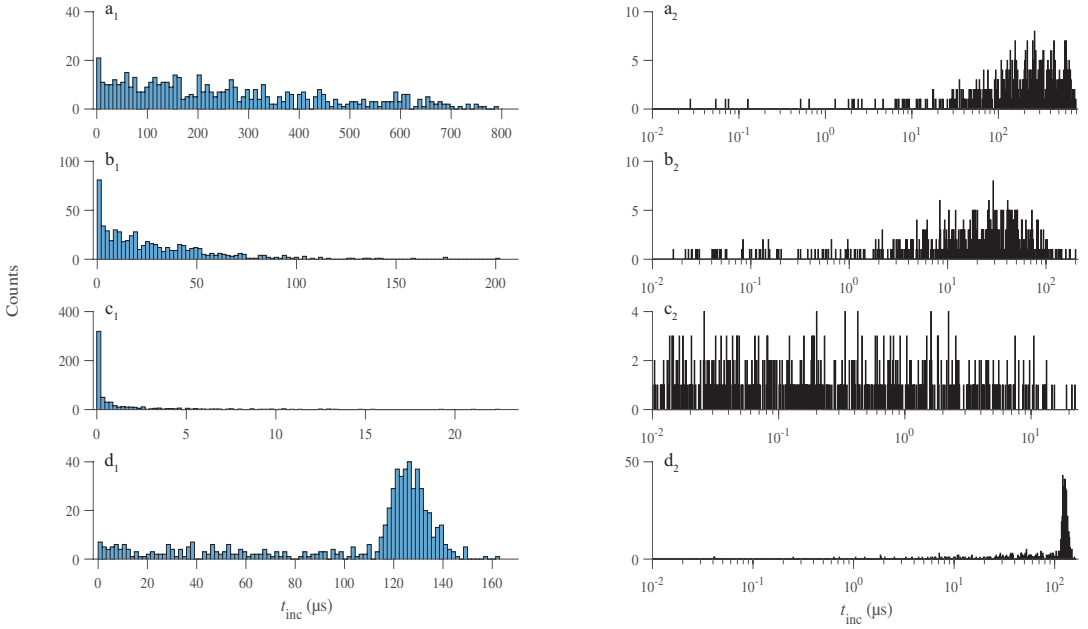


Figure 4.5.6: Histograms of  $t_{\text{inc}}$  from particle simulations with a sample size of 600. Histograms on the same row depict the same simulation results but left side is linear and right side is logarithmic. The initial homogeneous density of  $\text{O}_2^-$ -ions were: a)  $0.1 \text{ cm}^{-3}$  ( $N = 124$ ), b)  $1 \text{ cm}^{-3}$  ( $N = 1238$ ), c)  $10 \text{ cm}^{-3}$  ( $N = 12364$ ), and d)  $0.1 \text{ cm}^{-3}$  ( $N = 124$ ) with an extra patch of  $\text{O}_2^-$ -ions ( $N = 354$ ) placed between 1.8 cm and 2.0 cm from the pin electrode (green highlighted area in figure 4.4.1). All simulations have an inception probability of 1 except for a) which has an inception probability of 0.92.

electrode. Due to this inhomogeneous distribution of  $O_2^-$ -ions we can see in these histograms that a peak is not only present in the logarithmic scale but also in the linear histogram.

From these results it seems that some inhomogeneity in the spatial distribution of  $O_2^-$ -ions is needed to produce the experimentally observed third peak in the histogram of  $t_{inc}$ .

#### 4.5.5.4 Increasing duration between LV and HV pulse

In this section we investigate the influence of increasing the time between the LV pulse and the next HV pulse. We apply an LV pulse of 300 V for a duration of 50 ms at  $t_{LV-sep}$  ms before the next HV pulse i.e. if  $t_{LV-sep} = 0$  ms then the LV pulse is attached to the next HV pulse which is the same situation as shown in figure 4.5.3e. An LV pulse duration of 50 ms was chosen because this is a sufficient time to pull all negative ions in the discharge gap towards the HV pin electrode.

Figure 4.5.7 shows a collection of histograms of  $t_{inc}$  for different values of  $t_{LV-sep}$ . We see that for small values of  $t_{LV-sep}$  (5 - 10 ms, figure 4.5.7b-c) a peak is moving from small  $t_{inc}$  to higher  $t_{inc}$  and for high values of  $t_{LV-sep}$  (150 - 250 ms, figure 4.5.7e-f) the histogram resembles the baseline experiment histogram (figure 4.5.7a). We can make sense of this behavior by noting that the 50 ms LV pulse of 300 V not only pulled all negative ions towards the HV pin electrode, but also pushed positive ions away from it. When the applied potential is now turned off, the separation of these charged species can create an electric field which pulls the charged species back towards their starting position.

If  $t_{LV-sep}$  is not long enough (5 - 10 ms, figure 4.5.7b-c) we see that the negative ions did not have enough time to return back to their starting position and are still relatively close to the HV pin electrode. Because they are still close to the HV pin electrode they can trigger a discharge quickly ( $\mu$ s) after the application of the HV pulse. If  $t_{LV-sep}$  is long enough (150 - 250 ms, figure 4.5.7e-f) we can see that the charged species were able to return back to their starting position since the histograms now resemble the baseline experiment (figure 4.5.7a).

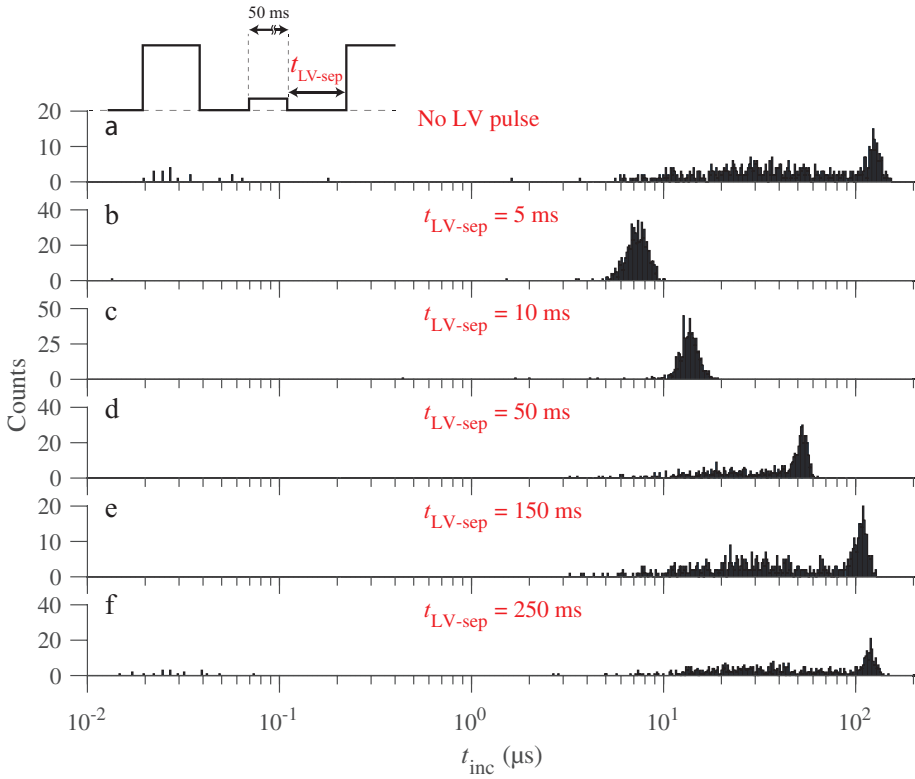


Figure 4.5.7: Histograms of discharge inception time  $t_{\text{inc}}$  for 600 discharges produced by applying a 300 V pulse for 50 ms and  $t_{\text{LV-sep}} =$  b) 5, c) 10, d) 50, e) 150, f) 250 ms before a 17 kV pulse of 10 ms with a repetition frequency of 2 Hz.

#### 4.5.5 Increasing LV Pulse Duration

In this section we investigate the influence of high values of  $t_{LV-dur}$  ( $\geq 50$  ms) for the same voltage configuration as for the experiment in figure 4.5.3. Figure 4.5.3 and figure 4.5.8 show that for  $t_{LV-dur}$  up to 50 ms the third peak moves to the left (the discharge starts faster). For higher values of  $t_{LV-dur}$ , the third peak disappears and the second peak seems to re-emerge.

When  $t_{LV-dur} = 50$  ms, the negative ions can gather around the HV pin electrode. When an HV pulse is then applied, right after this LV pulse, the negative ions no longer have to travel towards the HV pin electrode. The only process that needs to happen to trigger a discharge is the detachment of an electron from the negative ion which can then start the discharge.

Increasing  $t_{LV-dur}$  keeps the negative ions against the pin electrode for a longer time. During this time the negative ions can neutralize [200]. Inception becomes slower as  $t_{LV-dur}$  increases since more negative ions are neutralized. The result of applying any positive LV pulse is that negative charges are being removed from the discharge gap. For the LV pulse applied in this work: the free electrons need  $t_{LV-dur} \geq 1$  ms, and the negative ions need  $t_{LV-dur} \geq 50$  ms.

If the LV pulse is on during the entire time between two HV pulses (positive DC bias), we see in figure 4.5.8f that the third peak is almost completely removed. The counts that are still present around the third peak timescale (125  $\mu$ s) could still be caused by leftover negative ions, but they can also be due to the long tail of the second peak. The height of the second peak remains relatively unchanged from the base experiment (4.5.8a).

#### 4.5.6 Streamer inception under different conditions

The experiments described above show that in a specific condition, 17 kV HV amplitude with a repetition frequency of 2 Hz and a working pressure of 500 mbar, an electron which initiates a streamer can originate from three different sources. The question that we now need to address is whether these conclusions are generic or only valid for these specific experiment conditions. Hence, we repeated some of the experiments for combinations of a different repetition frequency (0.2 Hz), pressure (250 and 750 mbar),

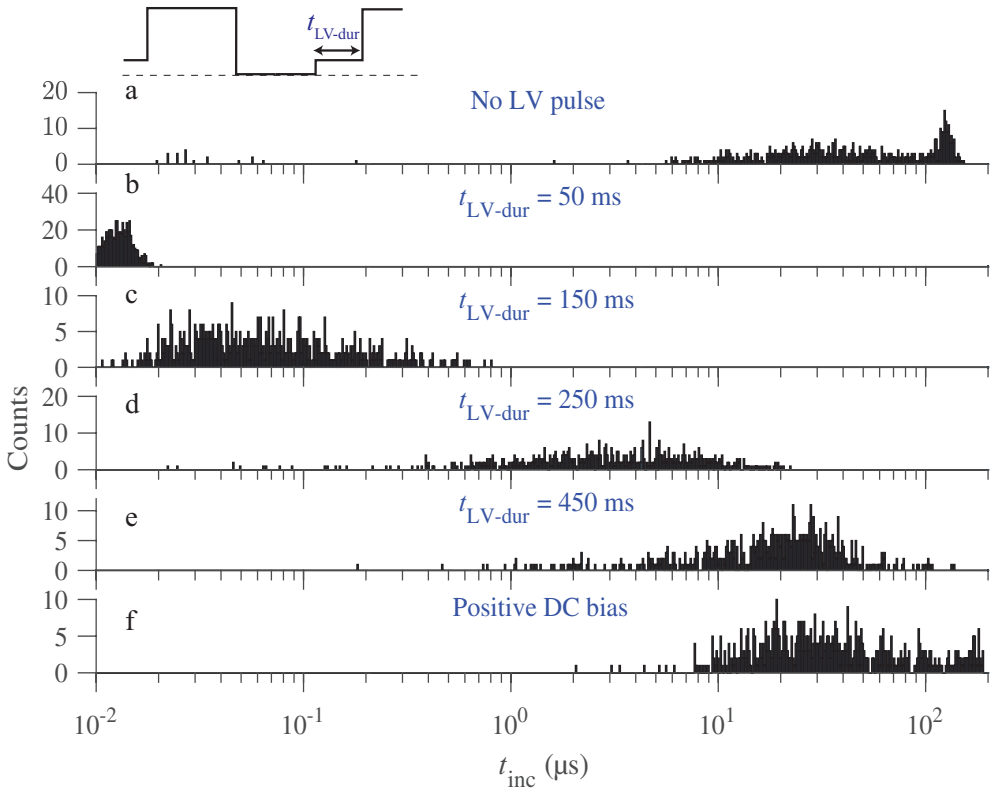


Figure 4.5.8: Histograms of discharge inception time  $t_{\text{inc}}$  for 600 discharges produced by applying a 300 V pulse for  $t_{\text{LV-dur}} =$  b) 50, c) 150, d) 250, and e) 450 ms, for a) no LV pulse and f) a DC bias before a 17 kV pulse of 10 ms with a repetition frequency of 2 Hz.

and voltage (12 kV) to see whether the observations still hold.

Figure 4.5.9a shows that for a repetition frequency of 0.2 Hz only one peak is present in the  $t_{\text{inc}}$  histogram. The sources for the first and third peak in figure 4.5.1 do not seem to play a role when the repetition frequency is decreased. This may be due to the increased time between HV pulses where no electric field is applied across the gap. During this time ion recombination processes can remove the detaching negative ion species. This again indicates that the source of the second peaks has a long lifetime.

Figure 4.5.9b shows the  $t_{\text{inc}}$  histogram for an increased pressure of 750 mbar. We observed similar peaks as in the baseline experiment (figure 4.5.1), but the third peak shifted to higher  $t_{\text{inc}}$ . The drift time of ions will scale inversely with the pressure which can explain the shift of the third peak to higher  $t_{\text{inc}}$  for a higher pressure. When the pressure is lowered to 250 mbar we see that most inception takes place at  $t_{\text{inc}} < 0.1 \mu\text{s}$ . It does not seem reasonable to attribute this shift of  $t_{\text{inc}}$  from 125  $\mu\text{s}$  to 0.1  $\mu\text{s}$  due to a halving of the pressure. The attachment time would also not be decreased enough to allow for free electrons to exist when an HV pulse is applied and thus triggering a fast inception of the discharge. A possible explanation is that the detaching negative ions are not converted to  $\text{O}_3^-$  (stable) or neutralized through recombination reactions as quickly. This would result in more detaching negative ions to remain from the previous discharge. The density of detaching negative ions would increase over time (also in the ionization zone) which will increase the chance of fast discharge inception.

When a lower HV (12 kV) is applied (still higher than the inception voltage, probability of inception = 100%), the first peak seems to have almost disappeared, as shown in figures 4.5.9c and d. This may be caused by the smaller ionization zone around the pin electrode which would reduce the chance of having a detaching negative ion in this zone when an HV pulse is applied. This would reduce the occurrences of fast discharge inception (first peak).

In summary, any change in experimental setup which would change the density and distribution of species in the streamer channel will have an effect on the  $t_{\text{inc}}$  histogram. Parameters that can be changed and will have an influence are: gap distance, applied voltage, gas pressure, repetition frequency, etc.

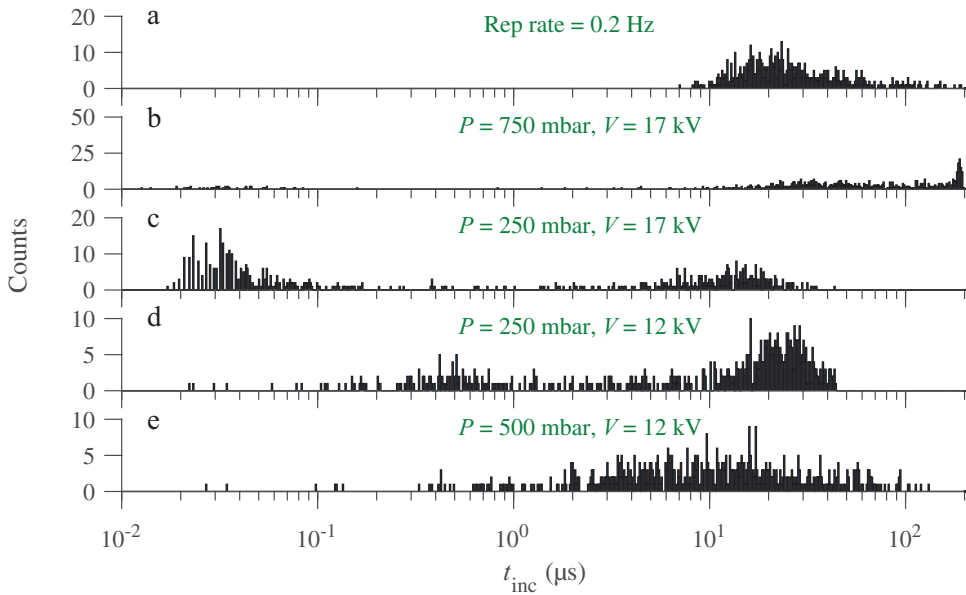


Figure 4.5.9: Histograms of discharge inception time  $t_{\text{inc}}$  for 600 discharges with a different experimental setup than the rest of the experiments. a) A repetition frequency of 0.2 Hz instead of 2 Hz, b) A pressure of 750 mbar instead of 500 mbar, c) A pressure of 250 mbar instead of 500 mbar, d) A pressure of 250 mbar and HV of 12 kV instead of 500 mbar and 17 kV, e) an HV of 12 kV instead of 17 kV.

## 4.6 Summary and open questions

We investigated the inception process of repetitive pulsed discharges by measuring the distribution of discharge inception times  $t_{\text{inc}}$  after the start of the HV pulse. We applied 17 kV pulses of 10 ms duration with a repetition frequency of 2 Hz to 500 mbar synthetic air and produced a histogram of inception times  $t_{\text{inc}}$ , which shows three distinct peaks. By applying LV pulses between the HV pulses, these peaks could be shifted in time or changed in magnitude. We provide theoretical arguments and numerical calculations aimed at identifying different electron producing processes that would explain each peak. However, open questions remain.

We start with two theoretical considerations.

First, in section 4.5.2 it is argued that a single uniformly distributed electron source would create only one early peak, with an initial increase related to the voltage rise time or to the electron detachment time from an oxygen ion, and then with a continuous decay of the inception probability in time. So the different peaks suggest different physical mechanisms.

Second, after a streamer discharge in synthetic air, electrons attach to oxygen molecules on a time scale of 10 to 100 ns between the HV pulses, and the negative oxygen ions can rapidly detach electrons and start a discharge in the high field zone near the electrode during the next HV pulse. We estimate the  $\text{O}_2^-$  density in a decaying streamer channel as  $10^5 \text{ cm}^{-3}$  at the beginning of the next HV pulse. This number is based on the assumption of fast electron attachment to form  $\text{O}_2^-$ , and on diffusion and recombination of positive and negative ions. However, to reach inception times comparable to experiment, the  $\text{O}_2^-$  density needs to be as low as  $10 \text{ cm}^{-3}$ , i.e., 4 orders of magnitude smaller. A possible explanation is that more plasma chemistry has to be added, in particular, that further ion conversion takes place to form the ozone ion  $\text{O}_3^-$  and  $\text{NO}_3^-$ . These ions are rather stable, and therefore an effective electron sink. This question needs further investigation in the future.

Concerning the physical processes causing the distinct peaks, we find that the first and the third peak are susceptible to LV pulses, consistent with the drift of negative oxygen ions; in the high field zone near the electrode these ions can detach an electron and create an ionization avalanche. However, to form these two peaks, the ions need to be quite inhomogeneously

distributed. The first peak would be caused by a large ion concentration in the high field zone near the electrode (possibly due to the glow during most of the previous HV pulse), and the third peak would be caused by another large ion concentration starting at a distance of about 1.5 cm from the electrode. However, to create the well separated peaks, the two regions with high ion density would need to be clearly separated by a region with very low ion density. It is not clear how such a concentration profile would arise.

The second peak does not shift in time with an LV pulse, which suggests that this electron source is electrically neutral. A continuous, field independent electron source due to Penning ionization could be an explanation, but the lifetime of the Penning ionizing species  $N_2(A)$  and  $N_2(a')$  are determined by quenching reactions with  $O_2$  and these have timescales on the order of 10 to 100 ns which makes Penning ionization an unlikely hypothesis. Another explanation could be the presence of quasi-neutral ion patches which cannot be separated by an LV pulse due to space charge effects. The negative ions in these patches can drift in the HV field towards the pin electrode and initiate a discharge by detaching an electron. It is not clear yet if such quasi-neutral patches would be created by a discharge.

Applying a negative LV pulse did not remove the first peak which we argument to be caused by negative ions close to the pin electrode. Secondary emission from the electrode could happen due to impact of positive ions, but in the electric field of the LV pulse the kinetic energy of these ions would be much lower than the work function of the electrode material. Other secondary emission reactions will need to be investigated in the future to understand this observation better.

The open questions which arose from this research are listed as follows:

1. If the first peak is caused by detaching  $O_2^-$ -ions, why can it be removed by applying a positive LV pulse?  $O_2^-$ -ions from further away in the gap should move towards the pin electrode.
2. If the first peak is caused by detaching  $O_2^-$ -ions, why can it not be removed by applying a negative LV pulse (or even a negative DC bias)?
3. What causes the second peak? It seems to not be influenced by any LV pulse applied. It is the only peak present when the repetition

frequency is decreased to 0.2 Hz. It accounts for 61% of the discharge inceptions.

4. Simulations show that the third peak can be produced by an inhomogeneous  $O_2^-$ -ion distribution. What causes this spatial inhomogeneity?

# Appendix

## 4.A Analytic estimate for inception probability

In this appendix, we derive an analytic estimate for the probability of inception when only drift is taken into account; effects due to reactions, diffusion or space charge are neglected.

Suppose that a single  $\text{O}_2^-$  ion or electron is present in the discharge vessel, with a spatially homogeneous probability distribution. For simplicity, we assume that inception occurs when this particle reaches the HV electrode (for the  $\text{O}_2^-$  ion, an electron would be liberated through detachment in the high field around the electrode). The probability of inception is then equal to the probability that the particle has reached the HV electrode in a time  $t$ , which we denote by  $F_1(t)$ .

As discussed in section 4.5.2, we can assume the particle flux (or its probabilistic equivalent) to be constant in time until boundary effects due to the finite vessel size become relevant. The underlying assumptions are that the field is divergence-free, that the mobility is constant, and that the initial density is homogeneous. If the flux is constant, then we have  $F_1(t) \propto t$ . If we assume that any particle reaches the HV electrode within a time  $t_{\max}$ , then we can write

$$F_1(t) = t/t_{\max}, \quad (4.9)$$

in other words, the inception probability linearly increases with time from zero to one. If there are  $N$  initial particles, the probability of inception  $F(t)$  is one minus the probability that inception did not occur

$$F(t) = 1 - (1 - F_1(t))^N,$$

so that the probability density of inception  $f(t)$  is

$$f(t) \equiv \partial_t F(t) = N(1 - F(t))^{N-1} \frac{dF(t)}{dt}.$$

Plugging in equation (4.9), the result is

$$f(t) = N/t_{\max}(1 - t/t_{\max})^{N-1}. \quad (4.10)$$

For large  $N$  and  $t/t_{\max} \ll 1$ , this can be approximated by  $f(t) \approx k(1 - kt)$ , where  $k = N/t_{\max}$ . To a good approximation, the dependence on  $k$  instead of  $N$  and  $t_{\max}$  individually also holds at later times. This means that the specific values used for  $N$  and  $t_{\max}$  are not important, only their ratio. One could for example consider a volume around the electrode containing  $N \gg 1$  initial particles, and let  $t_{\max}$  denote the maximal drift times of these particles to the electrode.

## Chapter 5

# Simulations of Repetitive Pulsed Streamer Discharges in Synthetic Air

Streamer experiments often use a repetitive voltage pulse. It has been observed that when the repetition frequency is high enough, streamers will be influenced by the leftovers of the streamers produced during the previous voltage pulses. In this work we simulate positive streamers with a 2D-axisymmetric model in synthetic air (80/20 N<sub>2</sub>/O<sub>2</sub>) at 80 mbar in a discharge gap of 15 cm (electrode tip radius of 0.4 mm) with a double voltage pulse where the linear rise and fall time was 40 ns, a constant voltage of 20 kV was applied for 200 ns, and the time between the two pulses was 0.5, 1, 5, 10, or 20  $\mu$ s. We used a plasma-chemical reaction set with over 400 reactions to model the temporal and spatial variation of plasma species during the voltage pulses and during the time between voltage pulses. Experiments in similar conditions, but at 133 mbar, a voltage of 13 kV over a 10 cm gap and an electrode tip radius of 0.015 mm, report a “continuation time” of 500 ns for the second voltage pulse to produce a streamer starting at the end of the streamer of the first voltage pulse. Exact experimental conditions could not be used due to resulting in prohibitively long simulation times. In this work we have found a continuation time between 5 and 10  $\mu$ s at the lower pressure of 80 mbar. These two continuation times do not easily scale to the same experimental result with pressure largely due to differences in electric field distribution produced by differences in electrode geometry. Additionally, we have resolved the reaction rate

*CHAPTER 5. SIMULATIONS OF REPETITIVE PULSED  
STREAMER DISCHARGES IN SYNTHETIC AIR*

---

of each reaction individually for different segments of the streamer (head, channel, back/electrode). These reaction rates are shown and discussed axially for each segment of the streamer separately. When there is no applied voltage, initially the positive ion conversion reactions are dominant in the streamer channel. These reactions mainly convert  $O_2^+$  into  $O_4^+$  and back. After some time the dominant reactions become negative ion conversion reactions which convert  $O_2^-$  into  $O_4^-$  and back. Finally, we have included a model for gas flow and heating to investigate the effects of repetitive voltage pulses on the gas dynamics. The temperature increase was mainly found close to the electrode, 1 cm away from the electrode the temperature remained at 300 K. Close to the electrode the maximal temperature after two voltage pulses was 330 K. Overall, heating up to 30 K was shown to have negligible influence on the streamer dynamics and reaction rates.



The text and implementation on gas heating and dynamics was done by Hemaditya Malla.

---

## 5.1 Introduction

Streamers are space-charge dominated and growing filamentary gas discharges [134] which have numerous applications, such as in plasma medicine [48, 57, 98, 201], plasma agriculture [159], and in the production of specific chemical species like ozone [65, 83]. They also occur in high voltage circuit-breakers. In nature they occur as streamer coronas ahead of lightning leaders and as tens of kilometers tall sprite discharges in the thin atmosphere high above thunderstorms.

Previous experimental and modelling studies have shown that the streamer evolution is influenced by excited and charged species including electrons and by gas density variations present on their propagation path. These species and density modifications can e.g., be present due to an ionizing laser [133], a radioactive admixture [132], or previous discharges [101, 129]. In particular, in experiments and applications streamers are commonly produced with a repetitively pulsed voltage source [101, 118, 129], to keep up the production of excited and ionized species, and also to overcome the inception problems of the very first streamer. Typical pulse repetition frequencies range from Hz to MHz in a gap on the scale of cm to m [85] between electrodes.

The effect of pulse repetition on positive streamers in nitrogen oxygen mixtures was studied systematically in double pulse experiments by Nijdam *et al.* [129], and by Yuan Li *et al.* [101]. They have investigated the effect of the time between two voltage pulses on the formation and propagation of the second streamer in different gas compositions including synthetic air (80:20 N<sub>2</sub>:O<sub>2</sub>). Nijdam *et al.* [129] have identified 6 distinct formation or propagation behaviors for the second streamer that depend on the time between the two voltage pulses. If the time between pulses is sufficiently short, the streamer continues to propagate during the second pulse where it stopped at the end of the first pulse. The maximum time between two voltage pulses for which this happens was called the continuation time. For longer times, the second streamer first propagates through the pre-ionized area inside the first streamer. In [129] a 0D-model for the plasma chemistry in the first streamer and during the interpulse time was presented, and the continuation time in different nitrogen oxygen mixtures was predicted, in good agreement with the experiments.

However, the 0D model is a large simplification, and the following questions arise: Are minimum electron density and conductivity values required for the entire streamer channel, or should they be present in a region around the electrode or at the tip of the first streamer? What species are present along the first streamer (head and body) and are they relevant for streamer continuation? Why do the second streamers seemingly initiate faster?

In this work we will try to answer these questions using a 2D axisymmetric streamer fluid model of a double pulse experiment in synthetic air at 80 mbar in which the time between pulses is varied and the formation and propagation of the second streamer is investigated. The gap length is 15 cm and the voltage 20 kV, so the average applied field is about 60% of the breakdown value (which is 113 Td or 2.26 kV/cm at 80 mbar). The chemistry set used includes around 400 different reactions and gives us a detailed view on which species are present where and at which times; it is much more detailed on the chemistry than the ZDPlaskin model used in [129]. The effect of the heating of the first streamer channel on the guiding of the second streamer is also investigated as this was a possible (minor) contributing effect according to [129].

## 5.2 Model

### 5.2.1 Equations

The simulations are done with the afivo-streamer code [194]. A recent addition to the afivo-streamer code is the inclusion of rod or conical shaped electrodes. The potential on the contour of the electrode was implemented by modifying the multigrid methods in [192] using a level-set function [137]. This addition to the code was first used in a comparison between experiment and simulation by Li *et al.*[100].

We solve the classical fluid model for streamers in a 2D axisymmetric coordinate system  $(r, z)$ . The continuity equation for the electron density  $n_e$  is

$$\frac{\partial n_e}{\partial t} = \nabla \cdot (\mu \mathbf{E} n_e + D \nabla n_e) + S_e + S_\gamma, \quad (5.1)$$

and for the ion and neutral densities  $n_i$  (numbered by  $i = 1, \dots, n$ ):

$$\frac{\partial n_i}{\partial t} = S_i. \quad (5.2)$$

Here  $\mu$  is the electron mobility coefficient,  $D$  the diffusion coefficient,  $\mathbf{E}$  the electric field, and  $S_{e,i}$  the sources (and sinks) of each species which are determined by the reaction set used. Electrons and  $\text{O}_2^+$  also have a photo-ionization source  $S_\gamma$  implemented as discussed in [212]. Homogeneous Neumann boundary conditions are used for electrons at all domain boundaries:

$$\frac{\partial n_e}{\partial r} \Big|_{r=0,R} = 0, \quad (5.3)$$

$$\frac{\partial n_e}{\partial z} \Big|_{z=0,L} = 0, \quad (5.4)$$

with  $R$  and  $L$  the maximal lengths in the radial and axial direction respectively.

This set of equations is coupled to the Poisson equation:

$$\Delta\phi = -\frac{e(n_+ - n_- - n_e)}{\epsilon_0} \quad (5.5)$$

$$\mathbf{E} = -\nabla\phi \quad (5.6)$$

where  $\phi$  is the electrostatic potential,  $n_+$  and  $n_-$  the total number density of all positive and negative charged ion species respectively, and  $\epsilon_0$  the vacuum permittivity. The following boundary conditions were used:

$$\frac{\partial\phi}{\partial r} \Big|_{r=0,R} = 0 \quad (5.7)$$

$$\phi \Big|_{z=0} = 0 \quad (5.8)$$

$$\phi \Big|_{\text{electrode}} = V \quad (5.9)$$

where  $V$  is the fixed applied potential on the upper electrode. A cylindrical electrode with semispherical cap protrudes from the upper planar electrode, as shown in figure 5.2.1.

Neutral	$N_2, O_2, N, O, NO, NO_2, NO_3, N_2O$
Positive	$N_2^+, N_2O_2^+, N_2O^+, N_3^+, N_3O^+, N_4^+, N^+,$ $N^{2+}, NO_2^+, NO_3^+, NO^+, NO^+ \cdot N_2, NO^+ \cdot NO,$ $NO^+ \cdot O_2, NON_2^+, O_2^+, O_2^+ \cdot N_2, O_4^+, O^+, O^{2+}$
Negative	$e^-, N_2O^-, NO_2^-, NO_3^-, NO^-, O_2^-, O_3^-, O_4^-,$ $O^-$

Table 5.2.1: Ground state species which were included in the discharge model.

## 5.2.2 Geometry

The geometry of the model is shown in figure 5.2.1. A cylindrical coordinate system was used with a maximum radial (R) and axial (L) dimension of 16 cm. The tip radius  $r_{tip}$  was 0.4 mm. The gap distance  $d_{gap}$  was 15 cm. Exact experimental conditions of [129] could not be used in the model within this work since the combination of a sharp electrode (tip radius of 15  $\mu\text{m}$ ) and a relatively large domain of  $(10\text{ cm})^2$  within the 2D-axisymmetric model results in a prohibitively long computation time when simulations of up to 20  $\mu\text{s}$  were necessary.

## 5.2.3 Reaction Set

The reaction set included electron scattering cross-sections for  $N_2$  from Kawaguchi *et al.* [81] and for  $O_2$  from Itikawa [73, 74]. The cross-sections for  $O_2$  were appended by the three-body attachment cross-section of Pack and Phelps [138, 147]. To improve the matching of calculated swarm parameters to experimental measurements, the vibrational excitation cross-sections for  $O_2$  were taken from the ISTLisbon database [71] on LXCat [110].

Plasma-chemical reactions are mainly taken from Kossyi [89] where all reactions with ground state molecules as input were digitized [39] and used in the present work. The reactions in this set were appended (and sometimes replaced) by the reactions of Pancheshnyi [140] and Aleksandrov and Bazelyan [3]. In total 411 reactions were included, reactions which are referenced within the results of this work are shown in table 5.2.2. The species which are included are shown in table 5.2.1.

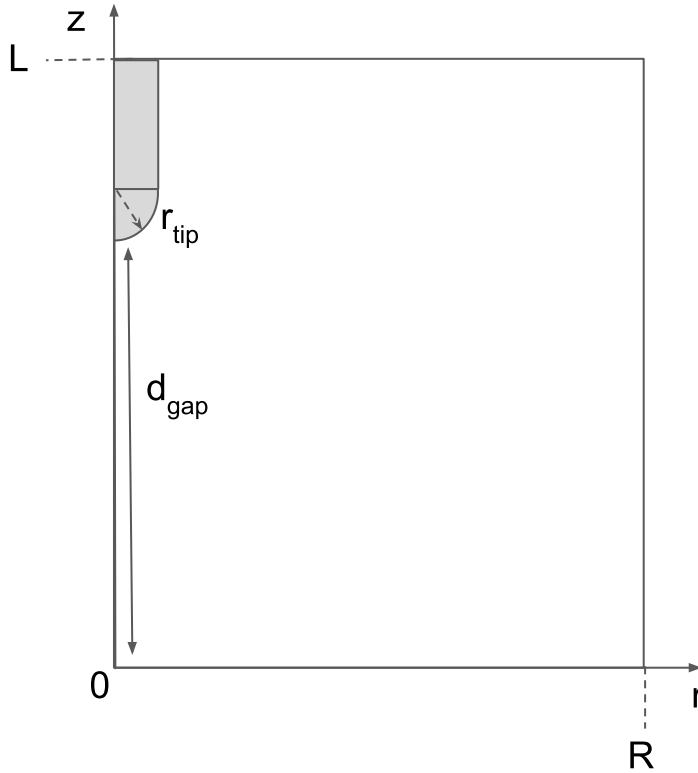


Figure 5.2.1: The axi-symmetric geometry used in the simulations. Dimensions are:  $R = L = 16$  cm,  $r_{\text{tip}} = 0.4$  mm,  $d_{\text{gap}} = 15$  cm. The plane at  $z = L$  and the cylinder mark the high voltage electrode ( $\phi = V$ ), while the bottom plate at  $z = 0$  is grounded ( $\phi = 0$ ).

CHAPTER 5. SIMULATIONS OF REPETITIVE PULSED  
STREAMER DISCHARGES IN SYNTHETIC AIR

---

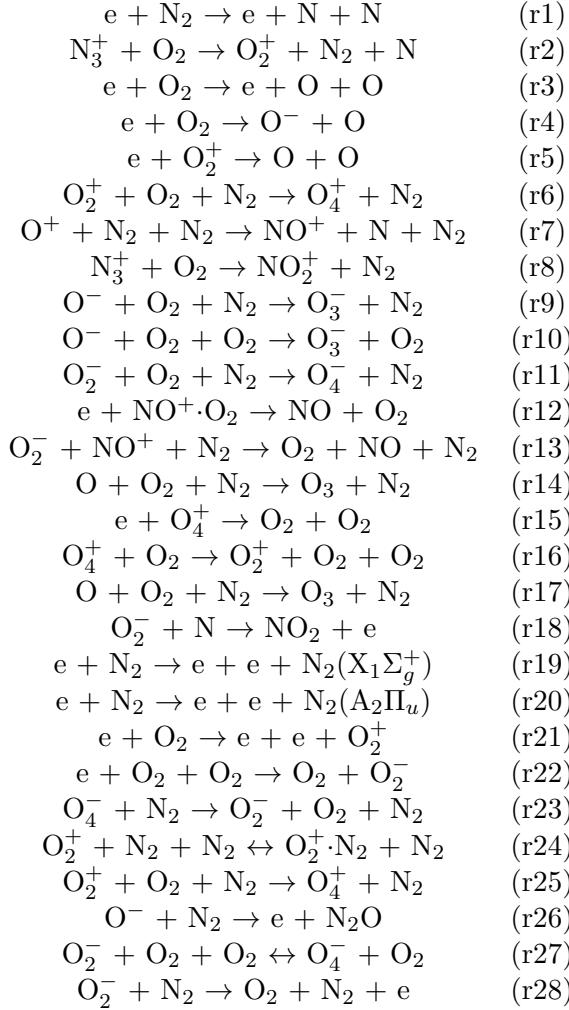


Table 5.2.2: Selection of reactions which are referenced throughout this work

## 5.2.4 Simulation conditions

### 5.2.4.1 Gas.

We used artificial air which consists of 80% N<sub>2</sub> and 20% O<sub>2</sub>. As lower gas pressures allow easier experimental access, the double pulse experiments are performed at pressures in the range of 100 mbar. In particular, as we want to compare in the future with yet unpublished experiments from the group of S. Nijdam, we used a pressure of 80 mbar. The initial temperature was 300 K.

As an initial condition, we used a neutral (electrons and N<sub>2</sub><sup>+</sup>) background ionization density of 1e11 m<sup>-3</sup>. This density was used previously by Xiaoran Li *et al.* [100] where experimental measurements and simulations were compared and found matching within 20%.

### 5.2.4.2 Applied Voltage.

We applied a voltage with a shape shown in figure 5.2.2. The voltage shape is defined by a voltage  $V_{\text{appl}}$ , which was 20 kV in all simulations, and 3 timescales:  $\Delta t_{\text{rise,fall}}$  (the rise and fall time of the pulse),  $\Delta t_{\text{const}}$  (time at constant  $V$ ), and  $\Delta t_{\text{inter}}$  (the time between pulses).  $\Delta t_{\text{rise,fall}}$  was chosen to be 40 ns, and  $\Delta t_{\text{const}}$  was set to 200 ns. These timings were chosen because they are achievable in a lab environment, but still relatively short to be able to simulate. Faster  $\Delta t_{\text{rise,fall}}$  or shorter  $\Delta t_{\text{const}}$  becomes a challenge for experiments.  $\Delta t_{\text{inter}}$  was varied from 500 ns to 20  $\mu\text{s}$ .

The applied average background field of 20 kV/15 cm is about 60% of the breakdown field (113 Td) in 80 mbar artificial air at 300 K.

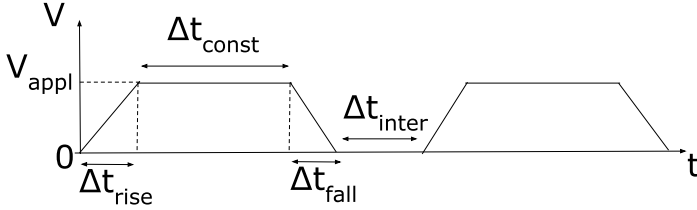


Figure 5.2.2: The voltage shape  $V(t)$  with two pulses as a function of time  $t$ : In each pulse the voltage rises linearly from 0 to  $V_{appl} = 20$  kV within  $\Delta t_{rise} = 40$  ns, stays constant for a time interval  $\Delta t_{const} = 400$  ns, and falls linearly to 0 within  $\Delta t_{fall} = 40$  ns. The time interval  $\Delta t_{inter}$  between the two pulses varies and takes the values 0.5, 1, 5, 10 and 20  $\mu$ s in different simulations.

### 5.3 Results and Discussion

We study streamer development as a function of the interpulse time  $\Delta t_{inter}$  between two consecutive voltage pulses. Properties of the streamer will be compared at two different sets of time: right after the first and before the second voltage pulse i.e. the interpulse time, and at the end of the constant voltage time of the first and second voltage pulse. However, for the cases where  $\Delta t_{inter} = 0.5 \mu$ s and  $1 \mu$ s the streamers produced by the second voltage pulse are fast enough to reach the bottom side of the simulation domain before the end of the constant voltage time of the second voltage pulse. For these cases we took the time at which the length is equal to that of the simulation with  $\Delta t_{inter} = 5 \mu$ s at the end of the constant voltage time of the first pulse.

Figures 5.3.1 and 5.3.2 show the electron density (top) and electric field (bottom) at different times during the applied voltage pulses for  $\Delta t_{inter} = 0.5 \mu$ s and  $20 \mu$ s respectively. The third pane of figure 5.3.1 shows the electric field of the streamer after the first voltage pulse. The last pane of figure 5.3.1 shows the electric field of the streamer after the second voltage pulse. We can see that for  $\Delta t_{inter} \approx 0.5 \mu$ s the streamer can completely bridge the gap. This shows that for a relatively short  $\Delta t_{inter}$  the streamer channel produced in the first voltage pulse can be restored and the second

CHAPTER 5. SIMULATIONS OF REPETITIVE PULSED  
STREAMER DISCHARGES IN SYNTHETIC AIR

---

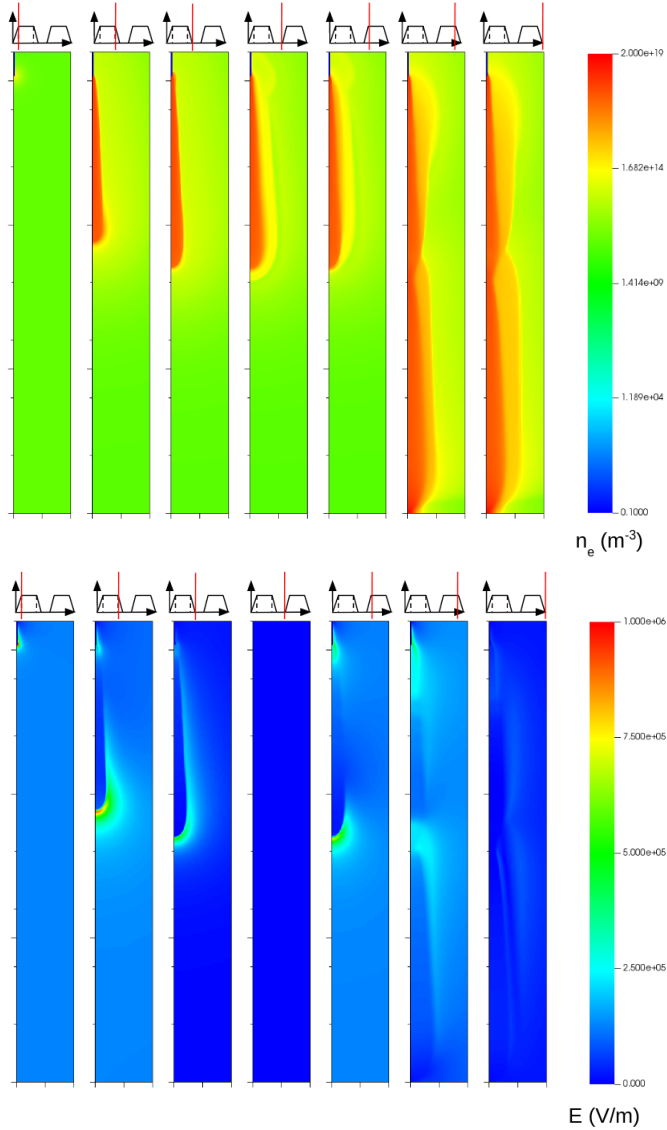


Figure 5.3.1: Electron density (top) and electric field (bottom) at the times when the voltage shape changes (as indicated at the very top), for the case when the voltage is off for a short time interval  $\Delta t_{\text{inter}} = 0.5 \mu\text{s}$  between the voltage pulses.

CHAPTER 5. SIMULATIONS OF REPETITIVE PULSED  
STREAMER DISCHARGES IN SYNTHETIC AIR

---

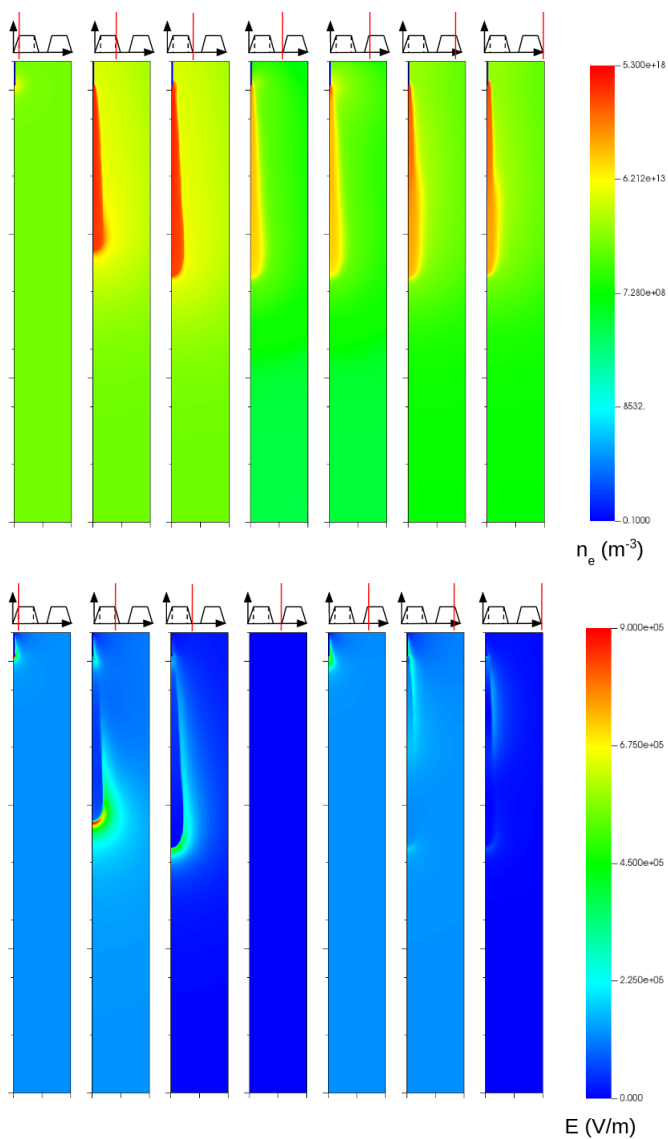


Figure 5.3.2: The same plots as in Fig. 5.3.1, but now for the long time interval  $\Delta t_{\text{inter}} = 20 \mu\text{s}$  between the voltage pulses.

voltage pulse can simply continue the streamer that was developed in the first voltage pulse.

For  $\Delta t_{\text{inter}} \approx 5 \mu\text{s}$  the second voltage pulse produces a streamer that continues from the streamer produced in the first voltage pulse, but the streamer cannot grow as far as for a smaller  $\Delta t_{\text{inter}}$ . For larger  $\Delta t_{\text{inter}}$  like 10-20  $\mu\text{s}$  the second voltage pulse fails to develop the streamer channel further as can be seen in figure 5.3.2. In the next subsections we will investigate properties like velocity, conductivity of the streamer channel, dominant species, and the dominant reactions to try and explain the differences seen in streamer development for double pulse (and by extension multiple-pulse) streamer experiments.

### 5.3.1 Velocity

The velocity of the streamers is calculated using the axial position of the maximal electric field. Figure 5.3.3 shows the velocity of the streamers for the first and second voltage pulse, including  $\Delta t_{\text{inter}}$ . The velocities for the cases where  $\Delta t_{\text{inter}} = 10\text{-}20 \mu\text{s}$  are not shown since the streamer does not develop further during the second voltage pulse as seen in figure 5.3.2. It is possible that for a longer second voltage pulse a new streamer would develop again, but this has not been tested.

We can see that for  $\Delta t_{\text{inter}} = 0.5$  and  $1 \mu\text{s}$  the streamer produced by the second voltage pulse is able to more or less continue from the velocity that the first pulse streamer had. The situation changes when  $\Delta t_{\text{inter}}$  is increased to  $5 \mu\text{s}$ . The streamer propagates a shorter amount of time and propagates slower. The streamer propagates a shorter amount of time because it takes a longer portion of the second voltage pulse to restore the streamer channel produced by the first voltage pulse to a state where a streamer can develop from it.

### 5.3.2 Conductivity of the Channel

The conductivity of the streamer channel is calculated as  $\sigma_e = en_e\mu_e$  where  $e$  is the electron charge in C,  $n_e$  is the electron number density in  $m^{-3}$ , and  $\mu_e$  is the electron mobility. Since we do not take into account ion motion the only contribution to the conductivity is the mobility of the electrons.

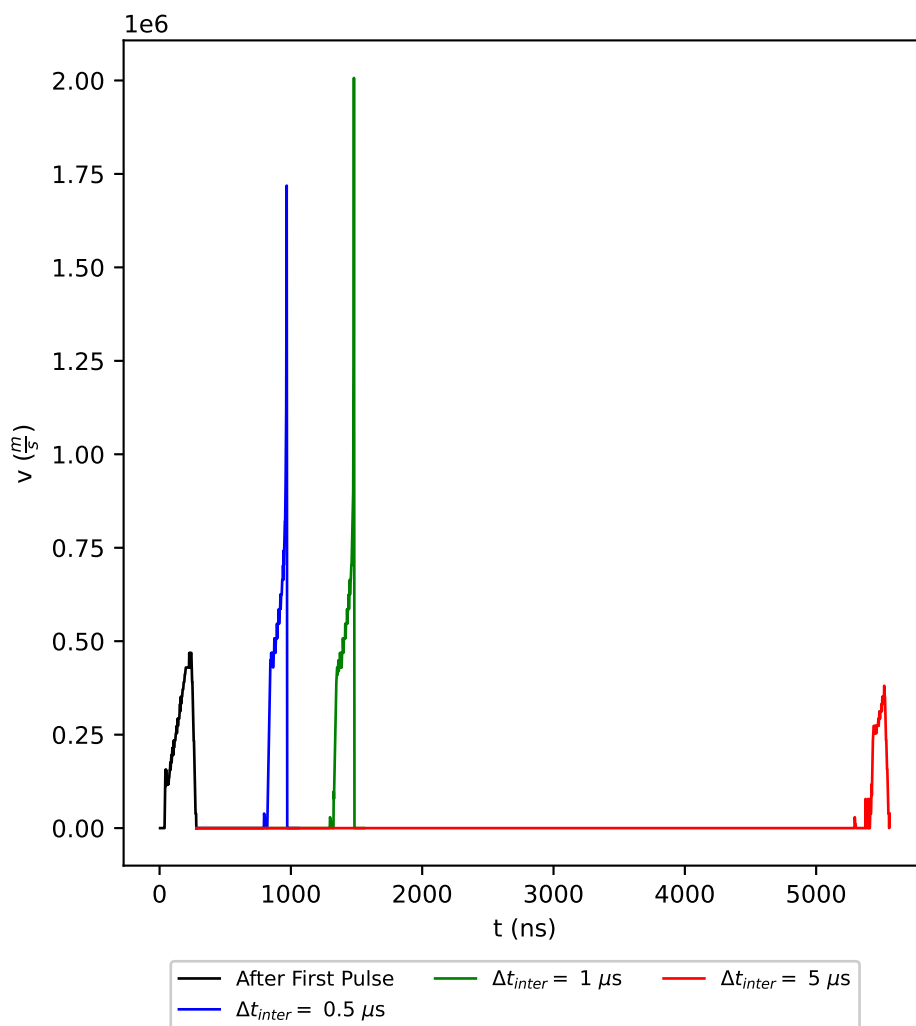


Figure 5.3.3: Velocities of the first and second pulse streamer for  $\Delta t_{inter} = 0.5 \mu\text{s}$ ,  $1 \mu\text{s}$ , and  $5 \mu\text{s}$ .

### 5.3.2.1 Interpulse time

The conductivity right after the first pulse and at the start of the second pulse for various  $\Delta t_{\text{inter}}$  is shown in figure 5.3.4a. We see that for some time after the first voltage pulse (when there is no applied voltage) the conductivity increases in the channel. Figure 5.3.4c shows the electric field inside the streamer channel. We see that the electric field decreases rapidly (several orders of magnitude within the channel) when the first voltage pulse has passed. This rapid decrease of the electric field is accompanied by a rapid increase in electron mobility. On the other hand we can see that the electron density, shown in figure 5.3.4b, does not decrease that fast initially. The decrease of the electron density between voltage pulses is mainly due to the three-body attachment reaction (r22). The combination of a fast increase in electron mobility after the first voltage pulse and an initial slow decrease of the electron density results in an initial increase in conductivity of the streamer channel up until around  $5 \mu\text{s}$  after the first voltage pulse occurred.

### 5.3.2.2 End of Constant Voltage Interval

Conductivities within the voltage pulse after different  $\Delta t_{\text{inter}}$ , shown in figure 5.3.5a, were compared. We can see that the conductivity within the first voltage pulse is very similar to the conductivity of the streamers in the second voltage pulse when  $\Delta t_{\text{inter}} \leq 5 \mu\text{s}$ . However, the conductivity of the first pulse streamer has reduced already for  $\Delta t_{\text{inter}} = 5 \mu\text{s}$  as was also visible in figure 5.3.4a. This reduction in conductivity is due to electrons getting attached due to three-body attachment during  $\Delta t_{\text{inter}}$ . For  $\Delta t_{\text{inter}} \geq 10 \mu\text{s}$  the channel has lost too much conductivity/electrons to propagate again on the second voltage pulse.

The maximal electric fields for the second pulse streamers (if one developed) are nearly equal to that of the first pulse streamer. The electric fields within the streamer channel are slightly lower for the second pulse streamer with  $\Delta t_{\text{inter}} = 5 \mu\text{s}$  than for shorter  $\Delta t_{\text{inter}}$  resulting in a slightly higher mobility inside the second pulse streamer.

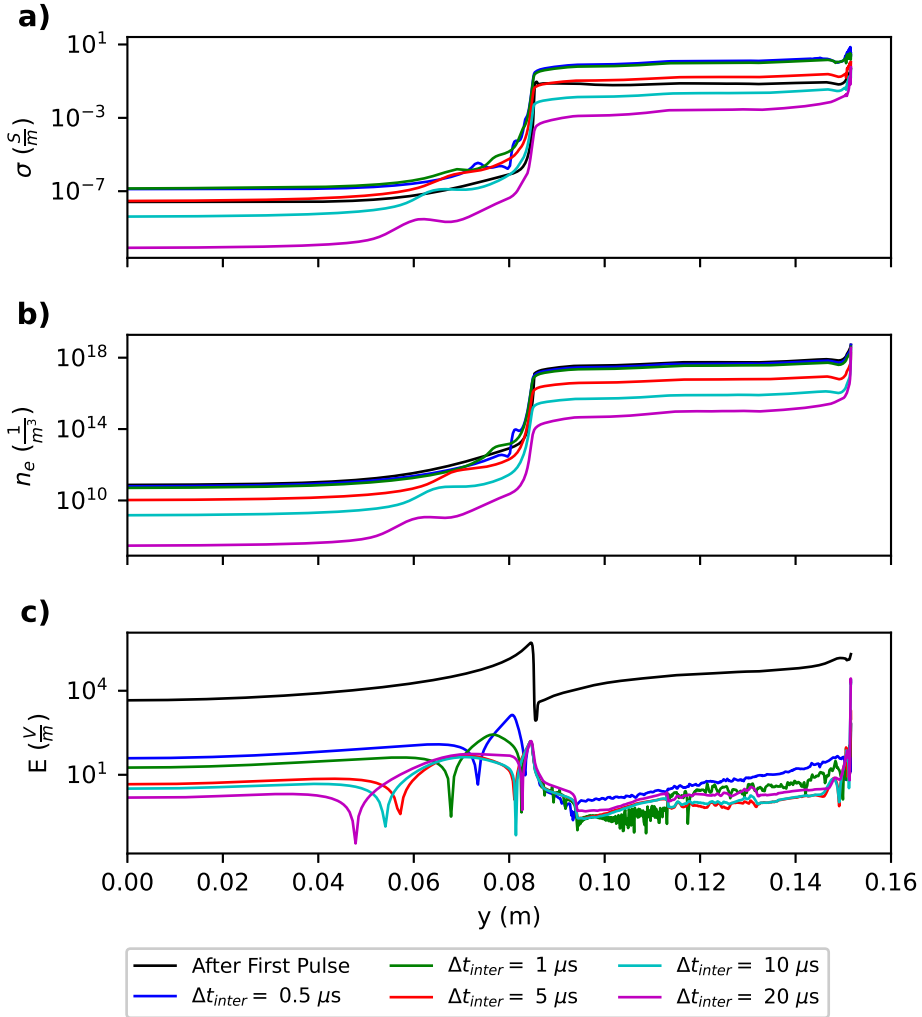


Figure 5.3.4: The conductivity (top), the electron density (middle), and the electric field (bottom) on the streamer axis right after the first voltage pulse and immediately before the second pulse, i.e. the interpulse time  $\Delta t_{inter}$  later. Note that the streamer propagates towards the left.

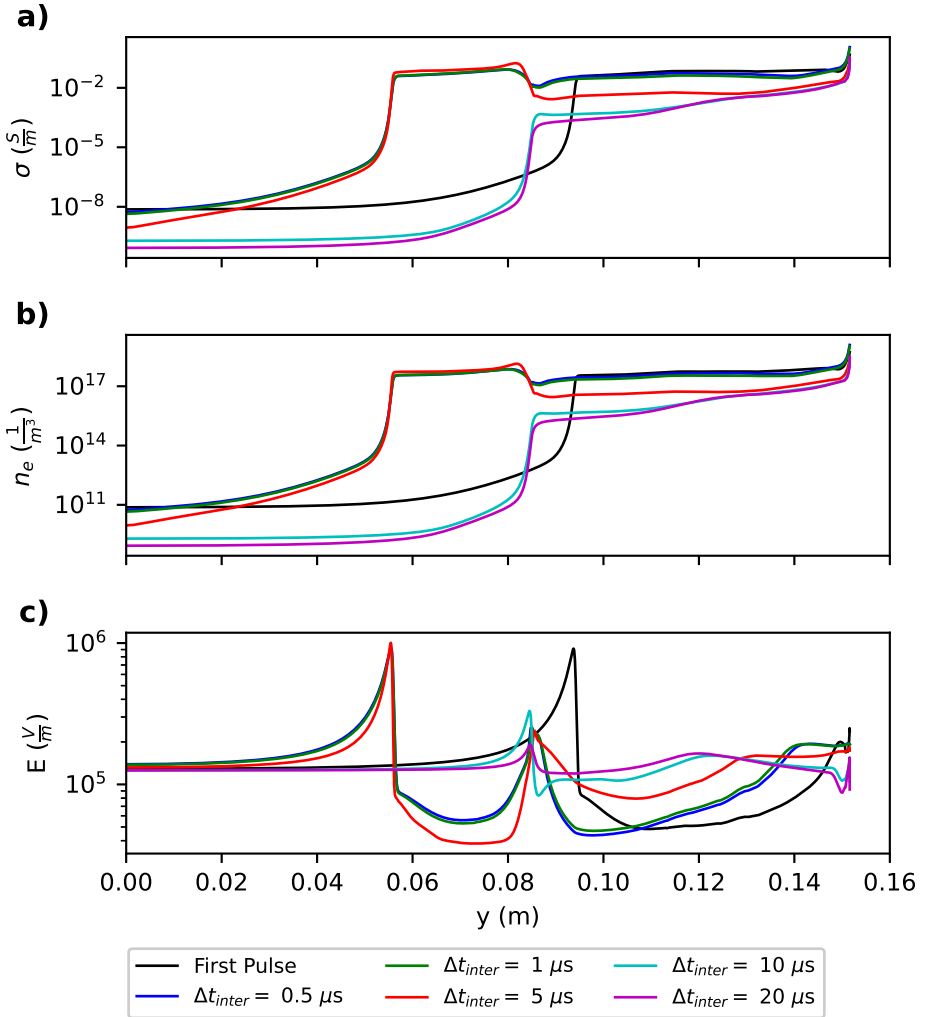


Figure 5.3.5: The conductivity (top), the electron density (middle), and the electric field (bottom) on the streamer axis at the end of the constant voltage interval. Note that the streamer propagates towards the left.

### 5.3.3 Dominant Species

#### 5.3.3.1 Interpulse time

Right after the first voltage pulse passed the species which showed the highest densities were the rotationally and vibrationally excited  $N_2$  as shown in figure 5.3.6a. However, among the reactions included these were states which did not participate in any other reactions, once they were created there was no way to lose/convert them. Even though cross sections for de-excitations exist [81], the simulation uses reaction rates derived from BOLSIG+ [14, 61]. Since these excited states did not exist initially BOLSIG+ did not output a reaction rate for the deexcitation reactions which is why they were not included in the simulation. The only thing we can say from figure 5.3.6a is that the vibrationally and rotationally excited states can be created in high volumes, but we cannot state that they remain throughout the discharge lifetime.

Removing the vibrationally and rotationally excited states from consideration for the highest densities species we get figure 5.3.6b. Besides the electronically excited states we observe that atomic N and O have considerable densities. Atomic N is produced in the streamer head and back predominantly by the dissociation reaction (r1) and in the streamer channel by the positive-ion conversion reaction (r2). Atomic O is produced in the streamer head and back predominantly by the dissociation reaction (r3) and also the dissociative attachment reaction (r4). In the streamer channel the electron-positive-ion recombination reaction (r5) is mainly responsible for atomic O.

If we also ignore the electronically excited species and atomic N and O we get figure 5.3.6c. The most abundant charged species are (non surprisingly) products of ionization (electrons,  $O_2^+$ , and various states of  $N_2^+$ ). Among the top 10 charged species we also find products of attachment ( $O^-$  and  $O_2^-$ ) and  $O_4^+$ ,  $NO^+$ , and  $NO_2^+$  which are predominantly created by the reactions: (r6), (r7), and (r8) respectively.

After 1  $\mu s$  we can see differences in the top species as shown in figure 5.3.7b. Electron density is reducing while  $O_2^-$  density is increasing due to three-body attachment. We can also see that  $O_3^-$  joined the top 10 while  $NO_2^+$  is no longer in the list.  $O_3^-$  is mainly produced by the reactions: (r9) and (r10).

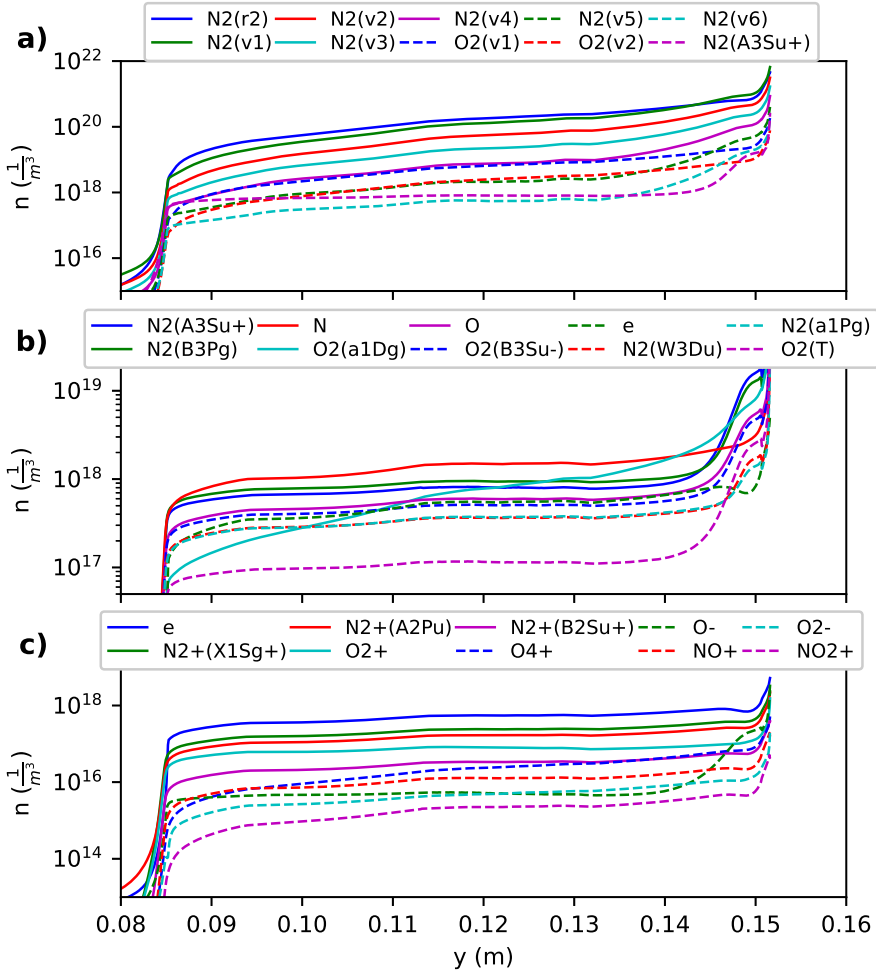


Figure 5.3.6: Species densities on the axis right after the first voltage pulse. a) The 10 species with the highest densities; they are vibrationally excited states of  $\text{N}_2$  and  $\text{O}_2$  and one electronically excited state, b) the 10 species with the highest densities, excluding vibrationally and rotationally excited states; these are electronically excited states,  $\text{N}$  and  $\text{O}$  radicals and electrons, and c) the 10 species with the highest densities, excluding vibrationally, rotationally or electronically excited states and  $\text{N}$  and  $\text{O}$  radicals; here finally various ions are seen.

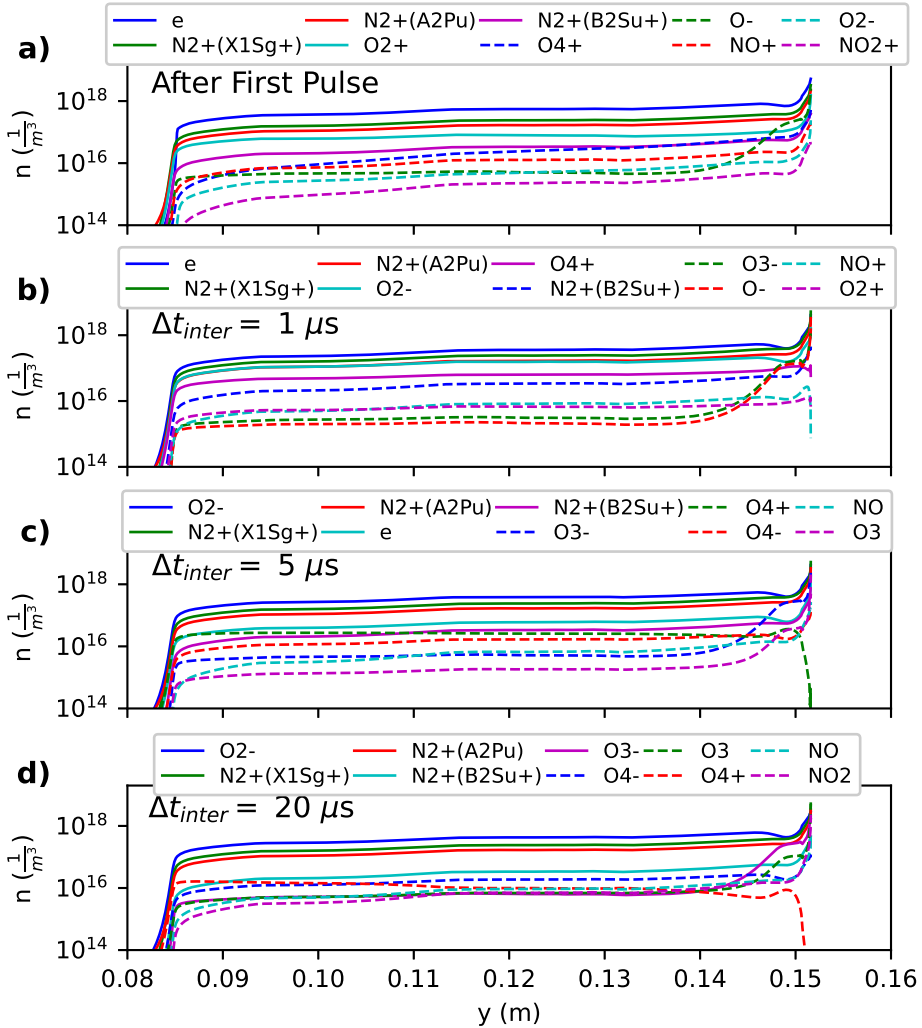


Figure 5.3.7: Species densities on the axis: a) right after the voltage pulse, b) - d) after the interpulse time  $\Delta t_{inter} = 1, 5,$  and  $20\mu\text{s}$  excluding vibrationally, rotationally or electronically excited states and N and O radicals.

After 5  $\mu\text{s}$ , shown in figure 5.3.7c,  $\text{O}_2^-$  has overtaken the electrons as more electrons are lost to three-body attachment. The species  $\text{O}^-$ ,  $\text{NO}^+$ , and  $\text{O}_2^+$  are no longer in the top 10 and are replaced by  $\text{O}_4^-$ ,  $\text{NO}$ , and  $\text{O}_3$  which were mainly produced through the reactions: (r11), (r12) and (r13), and (r14) respectively.

After 20  $\mu\text{s}$ , shown in figure 5.3.7d, electrons are no longer in the top 10 species while  $\text{O}_2^-$  is the dominant species. This is caused by three-body attachment. A reduction in  $\text{O}_4^+$  can also be seen which was mainly caused by the reaction (r15) and also (r16).  $\text{O}_3$  is still increasing due to the reaction (r17). Because  $\text{O}_2^-$  is increasing so is  $\text{NO}_2$  through the detachment reaction (r18).

### 5.3.3.2 End of Constant Voltage Interval

Figure 5.3.8 shows the dominant species ignoring vibrationally, rotationally, and neutral electronically excited states and atomic N and O for the first and second voltage pulse at the end of the constant voltage interval  $\Delta t_{\text{const}}$ . As expected, for the cases where a streamer developed during the voltage pulse (first pulse and second pulse for  $\Delta t_{\text{inter}} \leq 5 \mu\text{s}$ ) the dominant species in the streamer head are products of ionization (electrons, various  $\text{N}_2^+$  states, and  $\text{O}_2^+$ ).

Figure 5.3.8b and c show cases where a streamer developed on the second voltage pulse starting from the end of the streamer of the first voltage pulse. We can see that for the  $\Delta t_{\text{inter}} = 1 \mu\text{s}$  electrons are still dominant in the remaining channel of the first streamer since there was not enough time for three-body attachment to  $\text{O}_2$  to reduce it yet. For  $\Delta t_{\text{inter}} = 5 \mu\text{s}$  we see that three-body attachment had enough time to strongly reduce the density of electrons and convert them into  $\text{O}_2^-$  which are now the dominant species in the remainder of the first pulse streamer channel.

Figure 5.3.8d shows what was already seen in figure 5.3.7d. Because of the large  $\Delta t_{\text{inter}}$  a too large quantity of electrons became attached to  $\text{O}_2$  through three-body attachment resulting in no streamer being developed on the second voltage pulse.

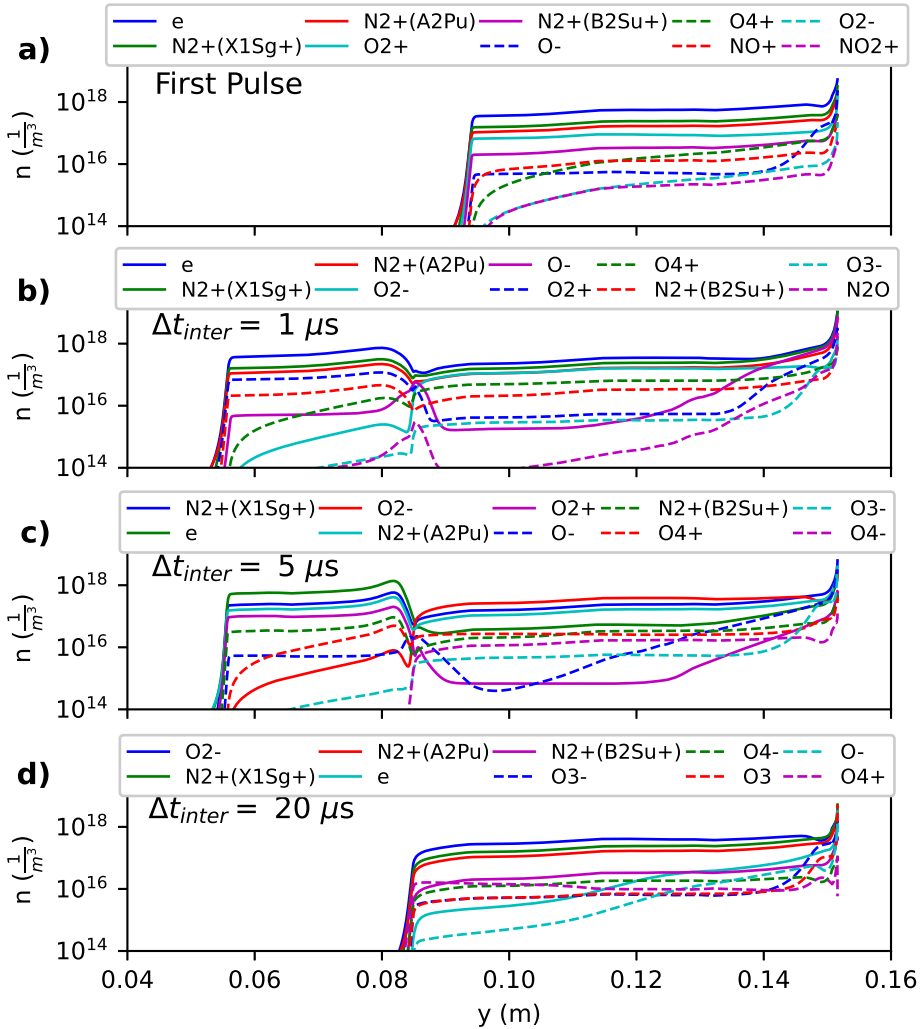


Figure 5.3.8: Species densities on the axis at the end of the constant voltage interval  $\Delta t_{\text{const}}$  of: a) the first pulse, b) - d) the second pulse after the interpulse time  $\Delta t_{\text{inter}} = 1, 5,$  and  $20 \mu\text{s}$  excluding vibrationally, rotationally or electronically excited states and N and O radicals.

### 5.3.4 Dominant Reactions

Investigating which reactions dominate where and when can provide valuable information for deciding which reactions to take into account for future modelling efforts. This section will be split in sections related to the streamer head, channel, and back where each region is analysed as  $\Delta t_{\text{inter}}$  varies.

#### 5.3.4.1 Interpulse time

**Streamer Head** Right after the first voltage pulse there is still a high electric field in the streamer head as shown in figure 5.3.4c for this reason the dominant reactions in the streamer head (figure 5.3.9a) will be the three main ionization reactions: (r19), (r20), and (r21). The dissociative attachment reaction (r4) plays a smaller, but still substantial role.

After  $1 \mu\text{s}$  the electric field (figure 5.3.4c) has already reduced several orders of magnitude. The dominant reaction (figure 5.3.9b) in the streamer head is the three-body attachment (r22).

For longer times after the first voltage pulse the three-body attachment reaction gets overtaken by two negative ion conversion reactions: (r11) and (r23). Figure 5.3.9c shows the top reactions in the streamer head at  $20 \mu\text{s}$  after the first voltage pulse, but results are similar even already after  $5 \mu\text{s}$ .

**Streamer Channel** Figure 5.3.10a shows the dominant reactions in the streamer channel right after the first voltage pulse. We see that the dominant reactions are positive-ion conversion reactions like (r24), and (r25). Since the electric field is much lower in the channel (due to screening) ionization and dissociative attachment reactions do not play a considerable role as compared to in the streamer head.

As is the case in the streamer head, after  $1 \mu\text{s}$  after the first voltage pulse the dominant reaction in the streamer channel is three-body attachment as shown in figure 5.3.10b. Other notable reactions are the negative-ion conversion reactions (r11) and (r23) and the electron-positive-ion recombination reaction (r15).

For longer times after the first voltage pulse, the dominant reactions inside the streamer channel are the same as those in the streamer head as shown in figure 5.3.10c. The negative-ion conversion reactions (r11) and

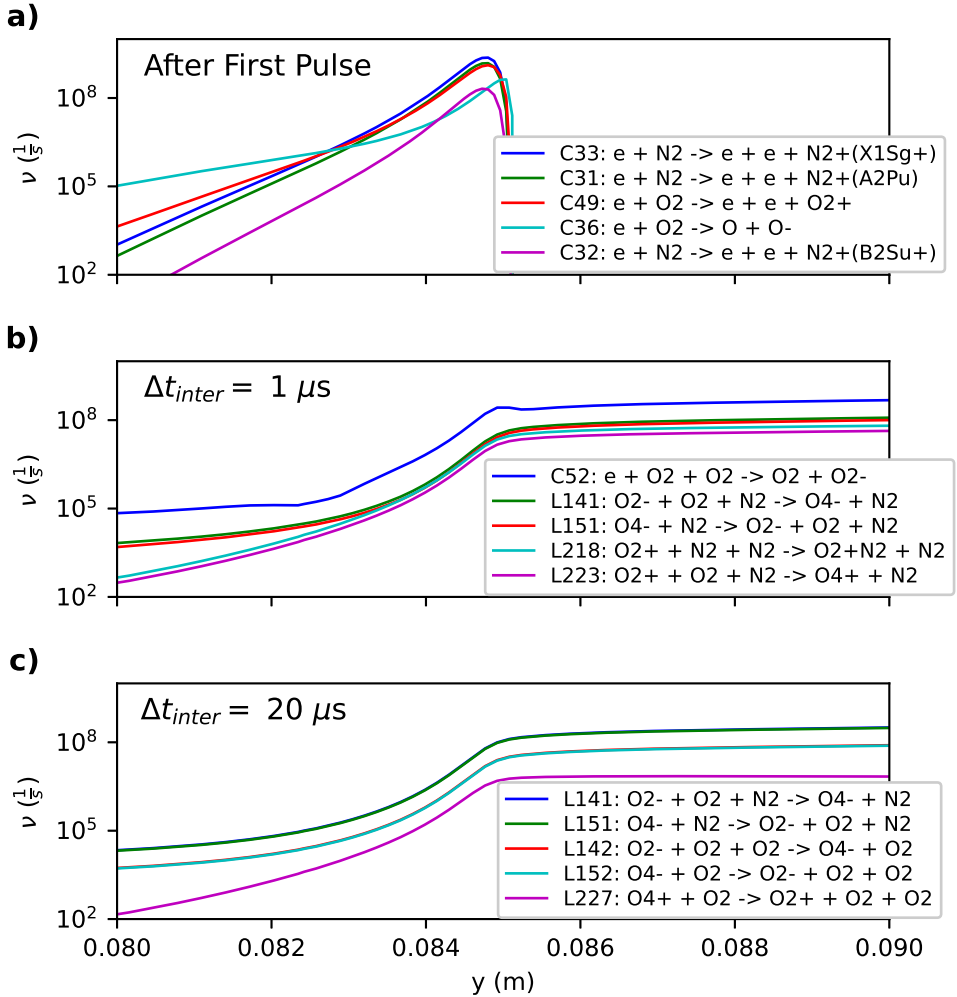


Figure 5.3.9: Axial profiles of the reaction frequencies of the most dominant reactions in the streamer head: a) right after the first pulse, b) after waiting  $1 \mu s$ , and c) after waiting  $20 \mu s$ . The streamer propagates to  $y = 0$ .

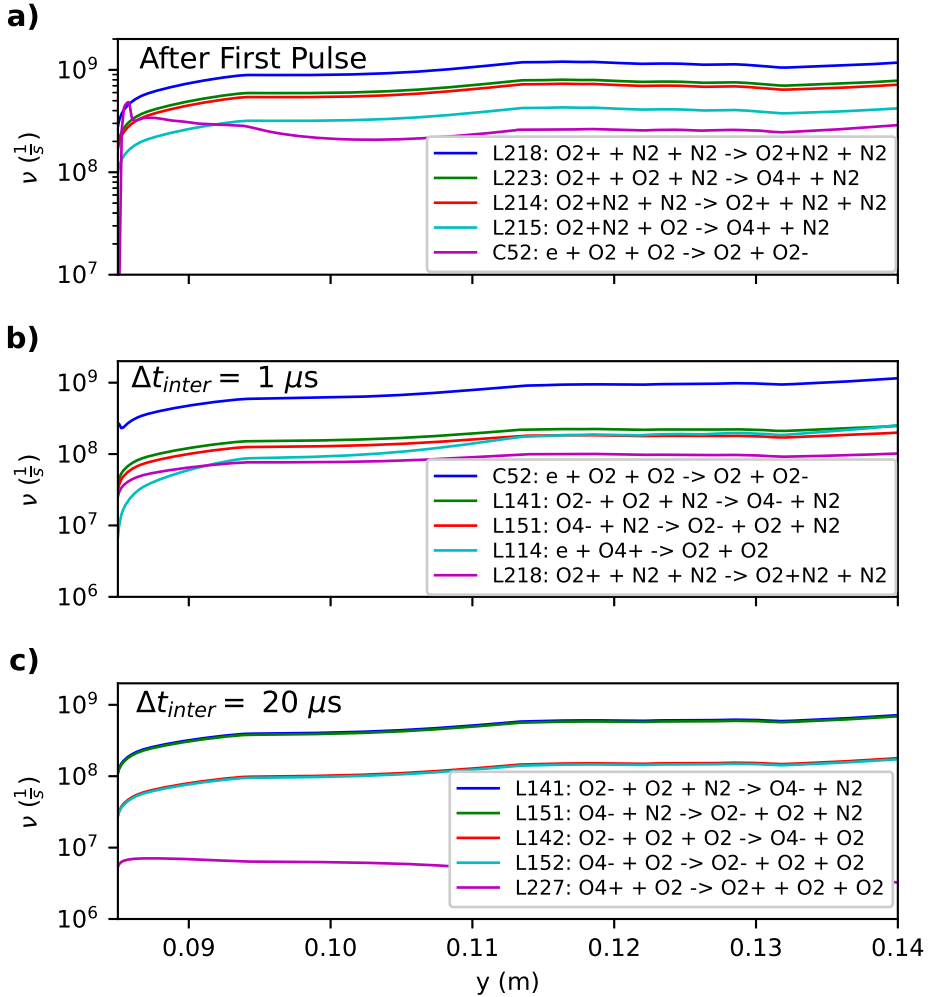


Figure 5.3.10: Axial profiles of the reaction frequencies of the most dominant reactions in the streamer channel: a) right after the first pulse, b) after waiting  $1 \mu s$ , and c) after waiting  $20 \mu s$ . The streamer propagates to  $y = 0$ .

(r23) are the most dominant since  $O_2^-$  is the most dominant species due to three-body attachment.

**Streamer Back/Near Electrode** Since electrons are flowing towards the electrode tip, the electron density is high in that area resulting in a high electric field similar to that at the streamer head. Figure 5.3.11a shows a zoomed in view at the electrode of the reactions with the highest contribution. Very close to the electrode we see that the dissociative attachment (r4) and detachment (r26) reactions belong to the dominant reactions. The same pairs of positive-ion conversion reactions as in the streamer channel continue to be important reactions.

At  $1 \mu s$  after the first voltage pulse figure 5.3.11b shows that we can find the same dominant reaction as in the streamer head namely the three-body attachment reaction to  $O_2$ . However, the negative-ion conversion reaction (r9) becomes almost just as important very close to the electrode.

$20 \mu s$  after the first voltage pulse the dominant reactions (shown in figure 5.3.11c) are the negative-ion conversion reactions (r27), (r11), and (r23). However, since the density of electrons is so high very close to the electrode, three-body attachment to  $O_2$  remains an important reaction.

#### 5.3.4.2 End of Constant Voltage Interval

**Streamer Head** The four most dominant reactions in the streamer head are the same for the streamer produced by the first voltage pulse and the streamer produced by the second voltage pulse for  $\Delta t_{inter} = 5 \mu s$  as shown in figure 5.3.12a and b. Figure 5.3.12c shows that the dominant reaction in the streamer head for  $\Delta t_{inter} = 20 \mu s$  is the detachment reaction (r28) this due to the density of  $O_2^-$  being so high. The other dominant reactions in this region are all negative-ion conversion reactions converting  $O_2^-$  to  $O_4^-$  and back.

**Streamer Channel** As in the streamer head, the dominant reaction in the streamer channel are the same for the first pulse streamer as for the second pulse streamer (if one was produced), as shown in figure 5.3.13a and

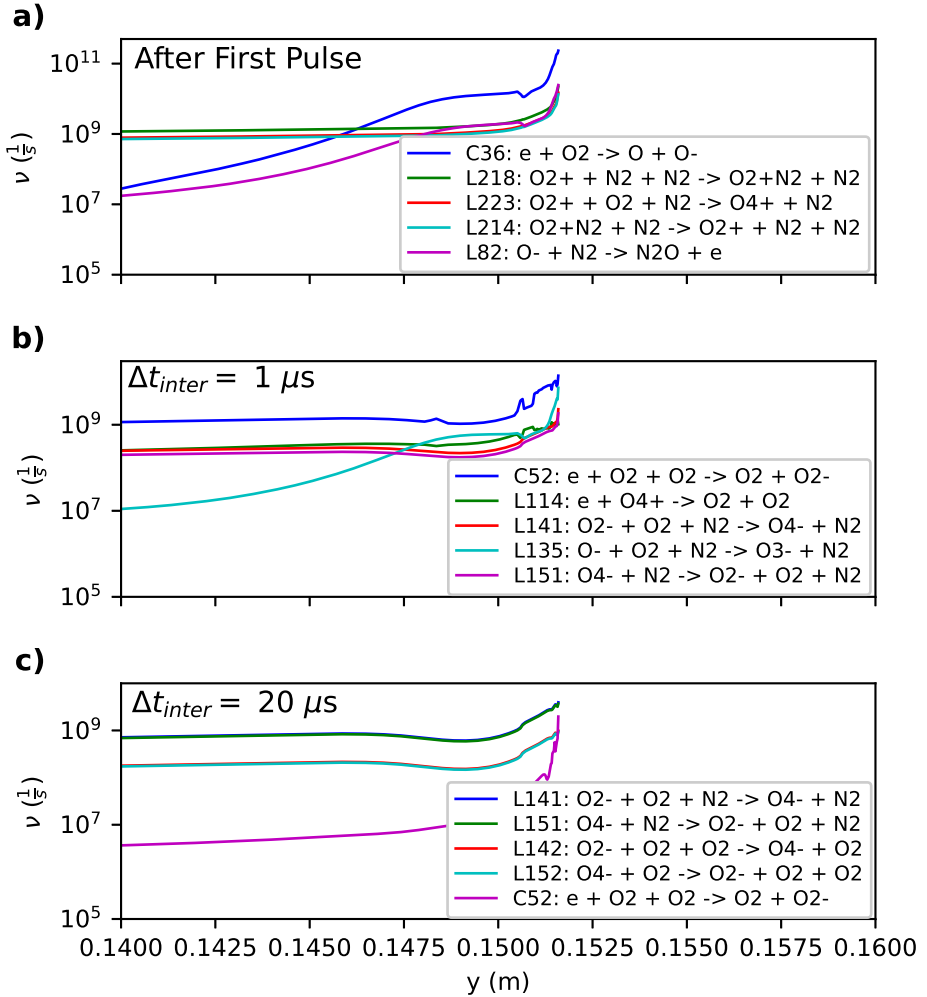


Figure 5.3.11: Axial profiles of the reaction frequencies of the most dominant reactions at the back of the streamer/near electrode: a) right after the first pulse, b) after waiting  $1 \mu s$ , and c) after waiting  $20 \mu s$ . The streamer propagates to  $y = 0$ .

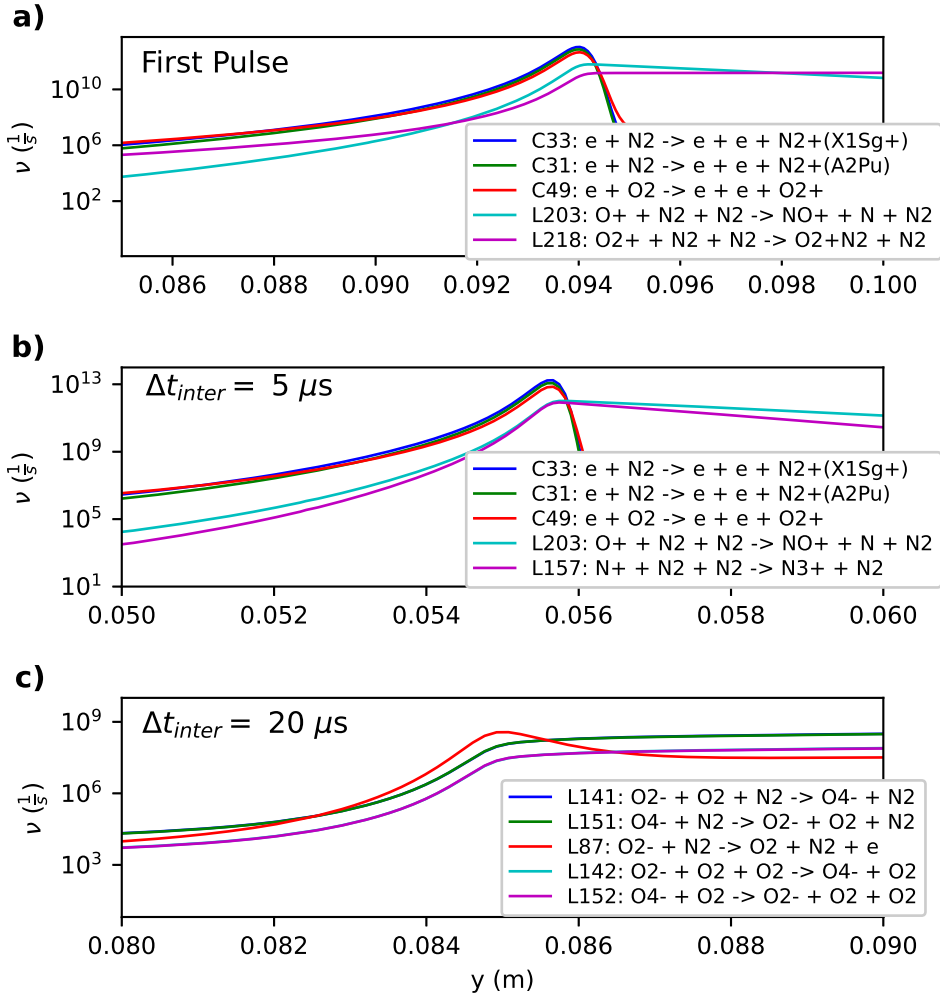


Figure 5.3.12: Axial profiles of the reaction frequencies of the most dominant reactions in the streamer head at pre-fall times for: a) the first pulse, b) after waiting  $5 \mu s$ , and c) after waiting  $20 \mu s$ . The streamer propagates to  $y = 0$ .

b. The main reactions in the channel are positive-ion conversion reactions and the three-body attachment reaction to  $O_2$ . For  $\Delta t_{\text{inter}} = 20 \mu\text{s}$ , as shown in figure 5.3.13c, the dominant reactions are negative-ion conversion reactions between  $O_2^-$  and  $O_4^-$  since the channel has existed for a longer period of time and most electrons have been attached already and thus a high density of  $O_2^-$  is present. We can also see the dissociative attachment of  $O_2$  becoming dominant the further to the back of the channel we look. This is due to the proximity to the electrode where the electric field is higher than in the channel as can be seen in figure 5.3.5c.

**Streamer Back/Near Electrode** The back of the streamer is taken as either near the electrode or at the point where the second pulse streamer started from (i.e. the end point of the first pulse streamer). The dominant reactions near the electrode for the first pulse streamer and at the back of the second pulse streamer for  $\Delta t_{\text{inter}} = 1 \mu\text{s}$  are shown in figure 5.3.14a and b. The dominant reactions between these two cases are similar, mostly positive-ion conversion of  $O_2^+$  and  $O_4^+$ . However, near the electrode for the first pulse streamer the ionization of  $O_2$  belongs to the most dominant reactions while at the back of the second pulse streamer this is not the case. The ionization of  $O_2$  requires a higher electron energy (electric field) than is present in this area. Figure 5.3.5c shows that the electric field is lower in this region than close to the electrode resulting in this difference in dominant reactions.

Due to the abundance of  $O_2^-$  in the streamer for  $\Delta t_{\text{inter}} = 20 \mu\text{s}$  the negative-ion conversion reactions belong to the most important reactions even near the electrode. Due to the high electric field near the electrode the dissociative attachment reaction to  $O_2$  has the highest frequency in that region. Due to this reaction producing  $O^-$  the detachment reaction (r26) also has a high frequency close to the electrode.

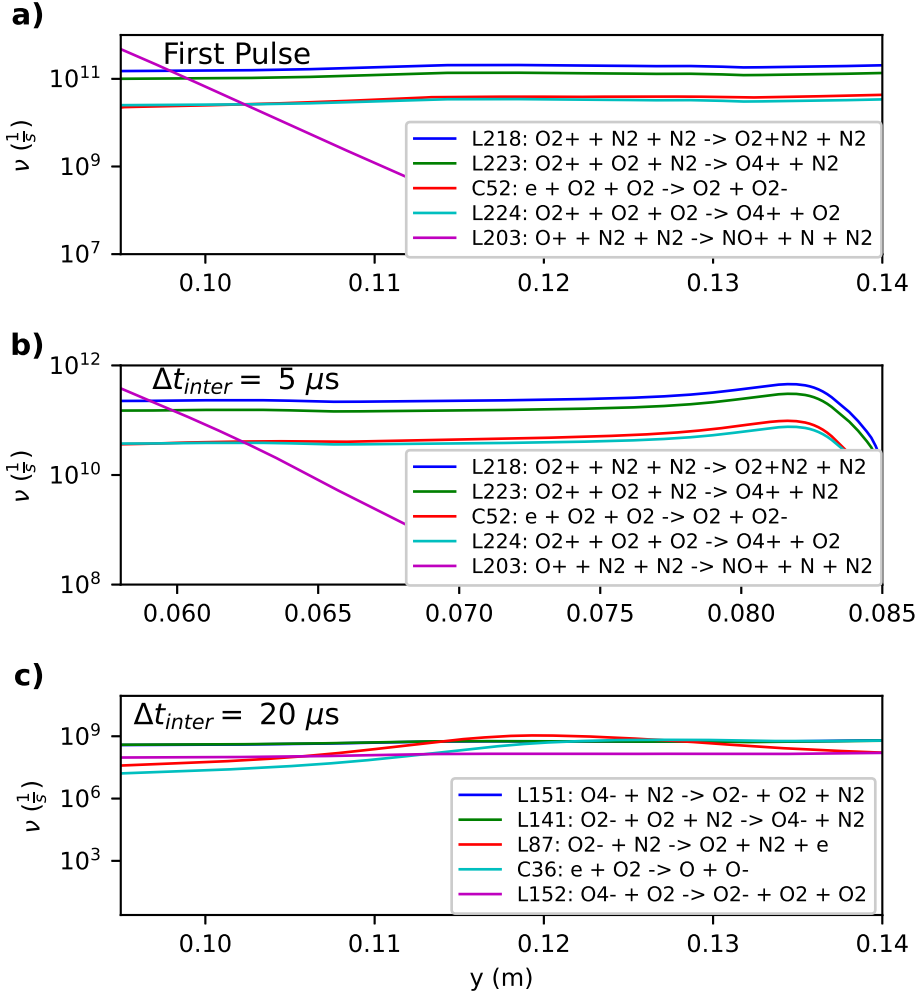


Figure 5.3.13: Axial profiles of the reaction frequencies of the most dominant reactions in the streamer channel at pre-fall times for: a) the first pulse, b) after waiting 5  $\mu s$ , and c) after waiting 20  $\mu s$ . The streamer propagates to  $y = 0$ .

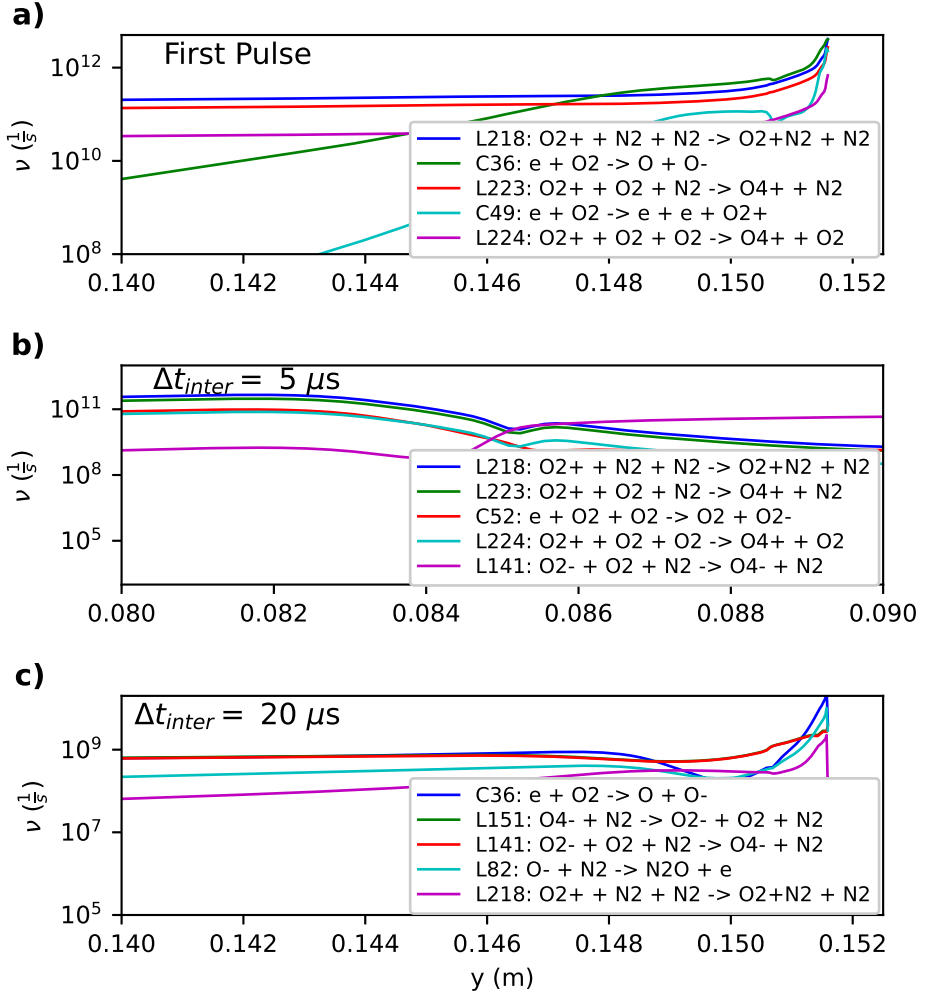


Figure 5.3.14: Axial profiles of the reaction frequencies of the most dominant reactions at the back of the streamer/near electrode at pre-fall times for: a) the first pulse, b) after waiting 5  $\mu s$ , and c) after waiting 20  $\mu s$ . The streamer propagates to  $y = 0$ .

## 5.4 Gas Heating and Dynamics

Previous results were obtained by running the model described in 5.2.1 without including the gas dynamics i.e. gas temperature and density/pressure were constant. In this section we will discuss the additional equations that have to be solved to take into account the gas heating and dynamics and we discuss the results obtained when including them in the simulations.

### 5.4.1 Equations

In order to simulate the effect of gas heating on the discharge, we need to model the evolution of the gas properties (pressure, temperature, velocity). The discharge produces charged particles which get accelerated by the present electric field. The collision between the accelerated charged particles and the neutral gas molecules can happen through one of two ways:

- **Elastic:** Momentum is transferred between the accelerated charged particles and the neutral gas molecules. In this work super-elastic collisions are not taken into account. The gas molecules will gain kinetic energy which directly contributes to the gas temperature. If there is a net charge density and an electric field, the momentum transfer from negatively and positively charged particles to the gas molecules will be unbalanced and generate the so-called 'corona wind' [30, 197].
- **Inelastic:** Kinetic energy of the charged particles is transferred to the neutral gas molecule resulting in the production of a different species through ionization, attachment, dissociation or excitation. This energy might eventually relax to thermal equilibrium, but only after a characteristic relaxation time.

We solve the Euler equations for gas dynamics with discharge dynamics coupled in as source terms.

$$\frac{\partial \rho}{\partial t} + \nabla \cdot (\rho \mathbf{u}) = 0, \quad (5.10a)$$

$$\frac{\partial (\rho u_r)}{\partial t} + \nabla \cdot (\rho u_r \mathbf{u}) + \frac{\partial p}{\partial r} = e(n_+ - n_e - n_-)E_r, \quad (5.10b)$$

$$\frac{\partial(\rho u_z)}{\partial t} + \nabla \cdot (\rho u_z \mathbf{u}) + \frac{\partial p}{\partial z} = e(n_+ - n_e - n_-)E_z, \quad (5.10c)$$

$$\frac{\partial \mathcal{E}}{\partial t} + \nabla \cdot ((\mathcal{E} + p)\mathbf{u}) = S_{\mathcal{E}}, \quad (5.10d)$$

where  $\rho$  is the density,  $\mathbf{u} = [u_r, u_z]$  is the velocity,  $p$  is the gas pressure, and  $\mathcal{E}$  is the energy density. The energy density  $\mathcal{E}$  is the sum of the internal thermal energy density and the kinetic energy density of the neutral gas; it is given by

$$\mathcal{E} = \frac{p}{\gamma - 1} + \frac{1}{2}\rho(u_r^2 + u_z^2). \quad (5.11)$$

In equations 5.10b and 5.10c, the expression on the right hand side is the momentum transfer source term and  $S_{\mathcal{E}}$  in equation 5.10d is the energy transfer source term. We use the following boundary conditions for all domain boundaries:

$$\frac{\partial \rho}{\partial r} = 0, \quad \frac{\partial \rho}{\partial z} = 0 \quad (5.12a)$$

$$\frac{\partial \rho u_r}{\partial r} = 0, \quad \frac{\partial \rho u_r}{\partial z} = 0 \quad (5.12b)$$

$$\frac{\partial \rho u_z}{\partial r} = 0, \quad \frac{\partial \rho u_z}{\partial z} = 0 \quad (5.12c)$$

$$\frac{\partial \mathcal{E}}{\partial r} = 0, \quad \frac{\partial \mathcal{E}}{\partial z} = 0 \quad (5.12d)$$

In general, we would also have to take into account the gas velocity  $\mathbf{u}$  when solving the drift-diffusion equations (5.1) and (5.2), because the charged particles move relative to the gas. The current density term for the electrons would then become  $(\mu \mathbf{E} n_e + D \nabla n_e - \mathbf{u} n_e)$ . The ion equations (5.2) would then become  $\frac{\partial n_i}{\partial t} = -\nabla \cdot (\mathbf{u} n_i) + S_i$ . These additions to the equations evolving the charged-particle densities were not done in this work, but will be done when preparing this work for a publication. We did not see a large gas velocity within this work, so the effect of gas velocity on the charged particle species would be minimal.

### 5.4.2 Gas heating model

In this section we explain the exact modelling of the energy transfer source term  $S_{\mathcal{E}}$  used in equation 5.10d in the previous section. The model we use has been used in [1, 30, 197, 210].

The power density dissipated in the discharge is given by

$$P = P_{elec} + P_{ion} = \mathbf{j}_e \cdot \mathbf{E} + \mathbf{j}_i \cdot \mathbf{E}, \quad (5.13)$$

where  $\mathbf{j}_e = e\mu_e n_e \mathbf{E}$  is the current density due to the electrons and  $\mathbf{j}_i$  is the current density due to the ions. Since the ion mobilities are much lower than the electron densities, and their densities are comparable, we neglect  $P_{ion}$ .

The deposited energy is distributed over various processes occurring in the discharge, and it might be thermalized after a characteristic time. A detailed description is given in [210]. In our chemistry model (given in detail in section 5.2.3), we consider effective-momentum, ionization, attachment, rotational, electronic excitation, and vibrational excitation processes of nitrogen and oxygen molecules. The fraction of discharge energy that goes into each of these processes for a given reduced electric field  $E/N$  can be computed using BOLSIG+ [14, 61], and these fractions are plotted in Figure 5.4.1. Below we denote these fractions by  $\eta_i$  (for ionization processes),  $\eta_{e-m}$  (for effective-momentum collisions),  $\eta_r$  (for rotational-excitation processes),  $\eta_a$  (for attachment processes),  $\eta_{e-e}$  (for electronic-excitation processes),  $\eta_{v-e}$  (for vibrational excitation processes).

Based on the work of Popov [152], 30% of the energy dissipated in electronic excitation instantaneously. The energy dissipated in the vibrational excitations relaxes into gas heating over a characteristic time scale, denoted by  $\tau_{VT}$ . The mathematical model for gas heating based on the processes above is

$$S\mathcal{E} = (\eta_{e-m} + \eta_r + \eta_a + \eta_i + 0.3\eta_{e-e})P + P_{VT}, \quad (5.14)$$

where  $P_{VT}$  is the slow heat release due to vibrational-translational relaxation and is modeled as

$$\frac{\partial P_{VT}}{\partial t} = \frac{1}{\tau_{VT}} (\eta_{v-e}P - P_{VT}). \quad (5.15)$$

We solve this differential equation along with the drift-diffusion equations, and the Euler equations for gas dynamics. The value of  $\tau_{VT}$  as  $20\mu s$  was used in [1][197] [30] for atmospheric discharge conditions. Furthermore, they report that varying  $\tau_{VT}$  between  $2 - 20\mu s$  did not change the results much. In [174], expressions for  $\tau_{VT}$  in air and nitrogen were given. These expressions scale inversely with pressure (thus also with  $N$ ). However,

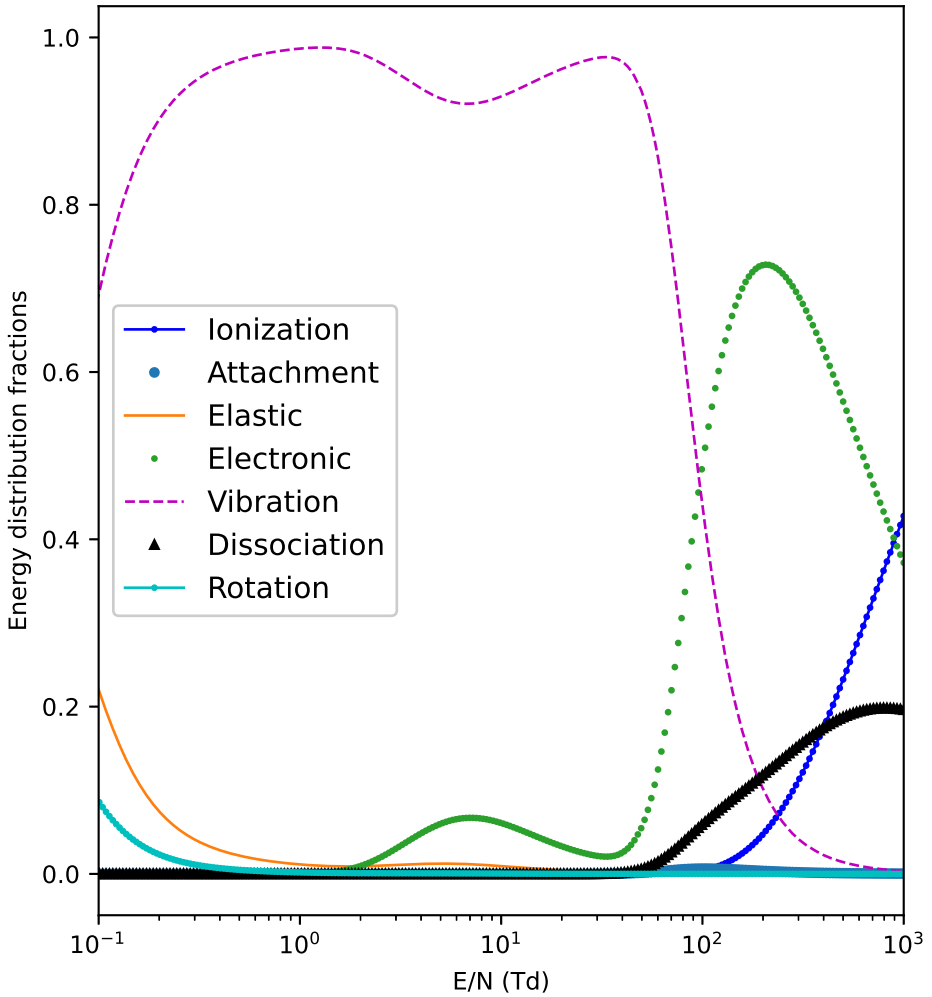


Figure 5.4.1: Energy distribution fractions of various chemical processes vs. electric field. These fractions are computed using BOLSIG+ [14, 61].

there is some uncertainty in the applicability of these expressions to the conditions used in this paper. As a simplifying assumption, we take  $\tau_{VT}$  to be  $20\mu s$  at 1 bar and scale it to  $250\mu s$  for the 80 mbar.

### 5.4.3 Gas Temperature, and Density

The biggest change in gas temperature occurs near the electrode as shown in figure 5.4.2a. Right after the first pulse the gas temperature near the electrode increased to 308 K. Waiting  $0.5\mu s$ , without applying a new voltage pulse, we see that the temperature has increased slightly to 310 K. This gas temperature increase after the voltage pulse is due to the slow heat release due to vibrational-translational relaxation as modeled by eq.(5.15). Waiting for a longer time before applying a new voltage lets the gas temperature reduce back to the temperature right after the first voltage pulse.

Figure 5.4.2b shows the temperature near the electrode at the end of the constant voltage interval of the second voltage pulse. Applying the second voltage pulse after waiting  $0.5-1\mu s$  makes the gas temperature increase to around 330 K from around 305 K that it was during the first voltage pulse. Waiting  $5\mu s$  between voltage pulses increased the temperature only to about 310 K. The increase in gas temperature in the second voltage pulse is almost negligible when waiting for longer times between voltage pulses.

Notice how the temperature increase drops very sharply when looking further from the electrode. At about 1 cm away from the electrode there is practically no difference in gas temperature no matter how much time there was between voltage pulses.

The gas number density, shown in figure 5.4.3, decreases near the electrode maximally by a few %. This decrease is visible between the voltage pulses and during the second voltage pulses at the end of the constant voltage interval (figure 5.4.3a and b respectively). This relatively small change in gas number density has nearly no effect on reaction frequencies or any other relevant aspect of the simulated discharges in this work.

Nijdam [129] noted a guiding effect of the first pulse streamers on the second pulse streamer for  $5\mu s < \Delta t_{inter} < 1 ms$ . They suggested, although with much doubt, that an increase in gas temperature could cause the pressure and thus gas density to decrease in the first pulse streamer channel

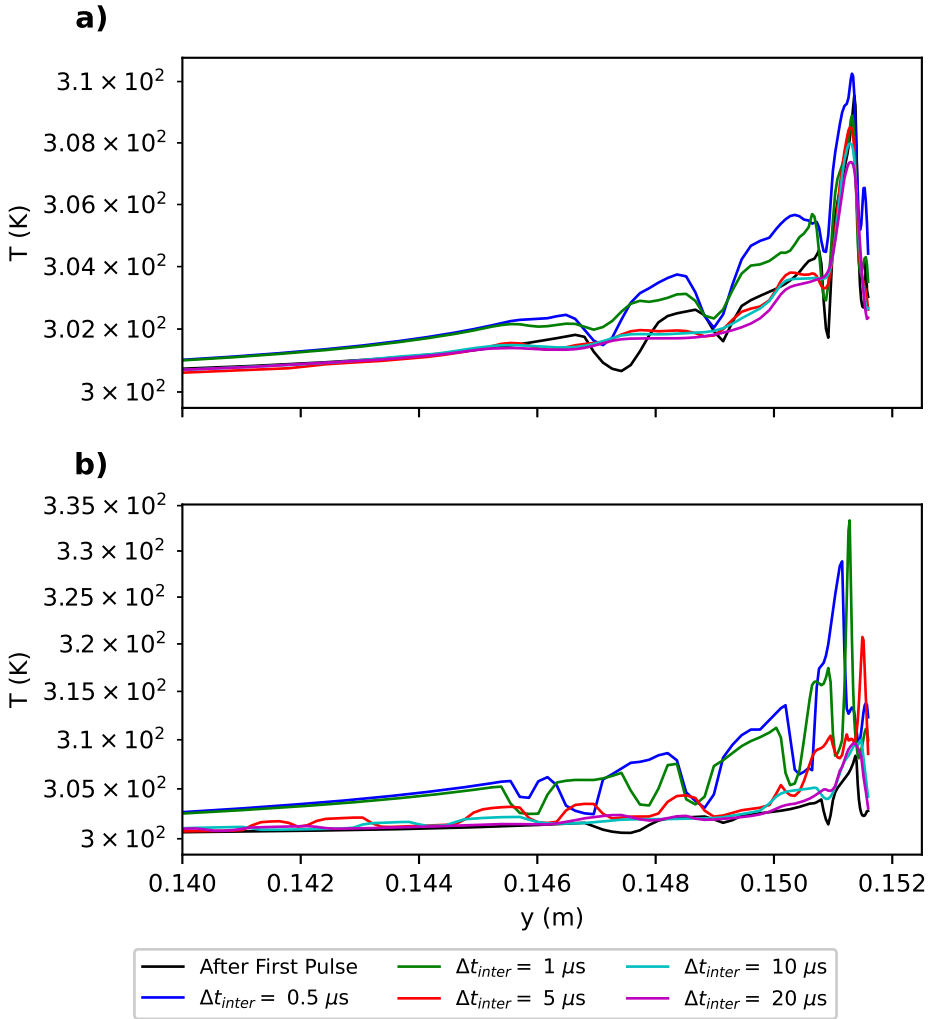


Figure 5.4.2: Gas temperature on the axis near the electrode: a) after the interpulse times, and b) at the end of the constant voltage interval

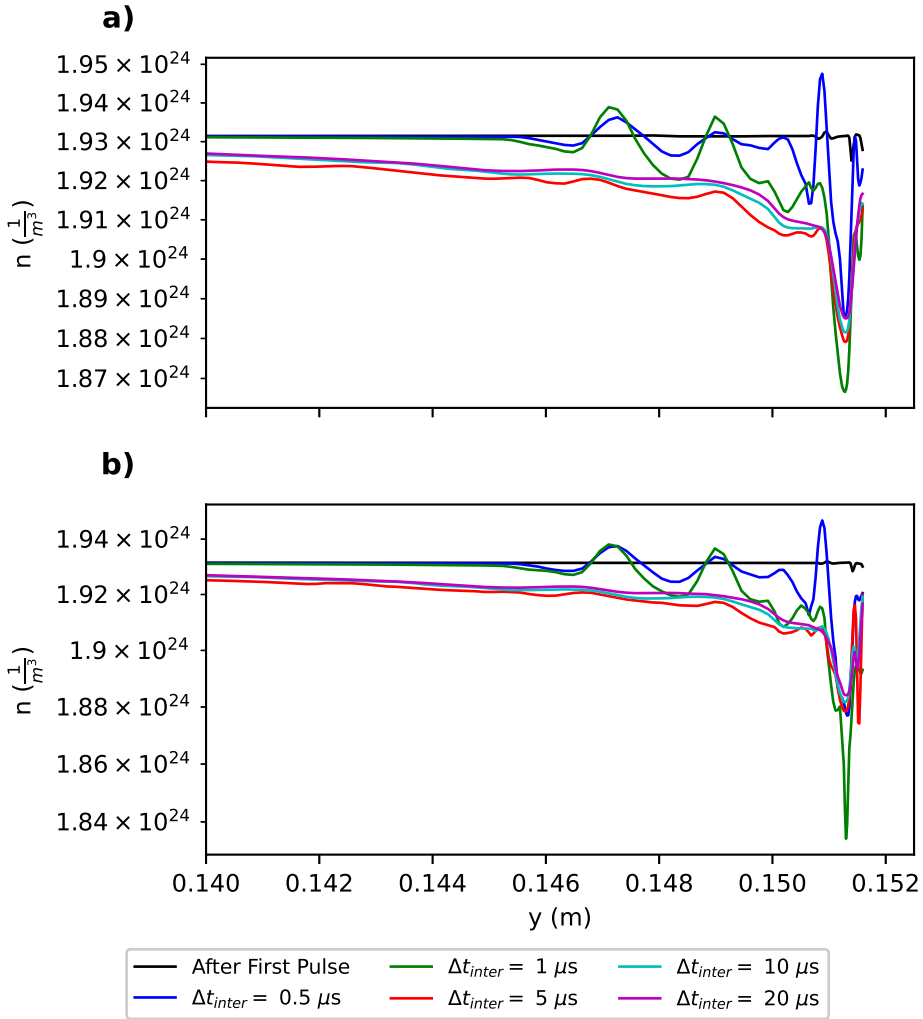


Figure 5.4.3: Gas number density on the axis near the electrode: a) after the interpulse times, and b) at the end of the constant voltage interval.

which serves as the guiding effect for the second pulse streamers. Here we see, for comparable conditions, that after  $5\ \mu\text{s}$  the heating of the gas and the decrease in gas number density is fairly negligible so, as stated in Nijdam [129], this guiding effect is probably minor/negligible. However, keep in mind that in this work there were exactly two voltage pulses while in an experiment there could be many pulses after each other with only  $\Delta t_{\text{inter}}$  separating them. In these cases the temperature increase could accumulate and the effects on the discharge become noticeable. Nijdam [129] employed a repetition frequency of  $0.7\ \text{Hz}$  so we do not expect the heating to accumulate in that experiment due to the long time between sets of two voltage pulses.

## 5.5 Conclusion

In this work we have investigated streamer continuation in a double pulse setup in  $80\ \text{mbar}$  artificial air (i.e., in an  $80:20$  mixture of  $\text{N}_2/\text{O}_2$ ). The time between the two voltage pulses was varied. Besides streamer continuation a large plasma-chemical reaction set was used to investigate which reactions were most important at which point in time and region of the streamer.

Nijdam *et al.* [129] found, in particular, a continuation time of  $500\ \text{ns}$  in their experiments in  $133\ \text{mbar}$  artificial air; after an interpulse time larger than the continuation time, the streamer during the second pulse would not continue the path of the first pulse streamer, because too much conductivity is lost between the voltage pulses. In our simulations in  $80\ \text{mbar}$  artificial air, the continuation time was between  $5$  and  $10\ \mu\text{s}$ . They do not easily scale with pressure to the experimental observations in [129], but it should be taken into account

- that the field distribution varied between the rod-plane setup of the experiment and the protrusion-plane set-up of the simulation, and
- that the design of the simulation was guided by another, yet unpublished experiment from Sander Nijdam's group.

The investigation will be continued in the future.

Looking at which reactions are important when and where we see a common trend. When the electric field is high e.g. at the streamer head or near the electrode when the voltage is applied ionization reactions with  $\text{N}_2$  and  $\text{O}_2$  as well as dissociative attachment to  $\text{O}_2$  are dominant. In the

streamer channel, where the electric field is lower, initially positive ion conversion reactions are dominant. These are reactions converting  $O_2^+$  into  $O_4^+$  or  $O_2^+ \cdot N_2$  and back. Waiting for a longer time after the voltage has been turned off (i.e. for much lower electric fields inside the channel) the dominant reactions become the negative ion conversion reactions. These reactions convert  $O_2^-$  to  $O_4^-$  and back. Negative ion conversion reactions become dominant at a later time/lower electric field because a large fraction of electrons undergo three-body attachment to  $O_2^-$ . Since there are no reactions (among the dominant ones) to remove  $O_2^-$ , these negative ion conversion reactions stay among the most dominant ones over time.

When looking at the dominant species we found a large density of rotationally, vibrationally, and neutral electronically excited  $N_2$  and  $O_2$ . Reactions which have these excited states as input should therefore be included in detailed plasma-chemical modelling input reaction sets. The reaction set used in the present work only contained quenching reactions for the  $N_2(C_3\Pi_u)$  state. Further work is needed to include more reactions using these excited states.

Finally we extended the model to include gas flow and heating. We found that in the current setup the gas heating (and other gas dynamics effects) is mainly localized around the electrode. At a distance of 1 cm from the electrode the gas temperature was practically the same as without gas heating. The heating that occurred around the electrode was also fairly low reaching about 330 K at the hottest point. Barely any effect of the gas dynamics is noticed on any relevant aspect of the discharge (velocity, reaction frequencies, dominant species, etc.).

# Chapter 6

## Conclusions and Outlook

In this thesis we have worked on topics within discharge modelling ranging from the most fundamental input (cross sections) to simulating long time behaviour of plasma species within a repetitive pulsed streamer discharge. In this section we will summarize each topic and highlight the main results obtained throughout the PhD. Afterwards we will offer the author's perspective on possible future research questions on these topics.

### 6.1 Chapter 2: Neutral Dissociation Cross Sections of CH<sub>4</sub>

Streamers in CH<sub>4</sub> are investigated for their application in, among other things, plasma-assisted combustion [185, 186]. As previously mentioned, cross sections are the most important input data for any streamer modelling endeavour. The two most important/complete cross section sets were: the IST-Lisbon set[6], and the set gathered by Song *et al.*[180].

The IST-Lisbon set is a swarm derived set. As discussed in section 1.1.4, swarm derived sets use the solution of a particular electron Boltzmann solver and compare the calculated electron swarm parameters with those measured in experiments. Cross sections are adjusted in a systematic way to make the calculated and the experimentally measured electron swarm parameters agree. The average electron dynamics will be correctly incorpo-

rated within the model (through the use of swarm parameters, cf. section 1.3.3). The problem is that rates of different collision types might be incorrect due to the non-uniqueness of a cross section set which can produce electron swarm parameters matching to experiment. When resolving different collision types (as in the particle model discussed in section 1.3.2) being able to produce the correct rates of different types of excitations, ionizations etc. becomes important.

The Song cross section set is obtained through extensive review of experimentally measured and theoretically calculated cross sections. Throughout that review comparisons of solutions of a particular electron Boltzmann solver to experimentally measured swarm parameters were not made. The downside of such a set, and this set in particular, is that when experimental measurements of a process are not available, or deemed too inaccurate, that process will not be included. This can have large effects both on the average plasma behaviour (swarm parameters) and on the microscopic behaviour as modelled using a particle model. The Song cross section set produced a much larger ionization coefficient (up to a factor 10) than was experimentally measured. This had large effects on any modelling effort and this set was therefore not recommended.

In this thesis the major missing processes from the Song cross section set were identified. Cross sections for these processes were calculated using a method that was not based on the output of any particular electron Boltzmann solver. The important processes missing from the Song cross section set were neutral dissociation reactions e.g.  $e + \text{CH}_4 \rightarrow e + \text{H} + \text{CH}_3$ . These neutral dissociation reactions are an important electron energy sink. When these are included, electron energies will generally be lower resulting in a lower incidence of ionizing collisions and thus in a lower ionization coefficient. In this thesis we have added these neutral dissociation reactions with the calculated cross sections to the Song cross section set resulting in swarm parameters (especially the ionization coefficient) which match those measured in experiment. This extended Song cross section set was submitted to the LXCat project [25] and will be available as the “Song-Bouwman”-database (named after my co-author Dennis Bouwman).

The text within chapter 2 and accompanying publication was mainly written by Dennis Bouwman. The majority of calculations of cross sections, and comparisons of resulting swarm parameters with experiment were done by the current author.

## 6.2 Chapter 3: Extensive Comparison of Available Electron Boltzmann Solvers

As discussed in section 1.3.1, solving the electron Boltzmann equation is necessary to obtain swarm parameters which are used in e.g. fluid models (as discussed in section 1.3.3). Over the years, different researchers have developed their own software to be able to solve this equation. These solvers can differ in many ways: approximations used, programming language, open/closed source, computation speed, stability, and user friendliness. In this thesis we have extensively compared the most widely known and easily available solvers. Included solvers were ones using the “two-term approximation” i.e. BOLSIG+ [13], LoKI-B [189], and BOLOS [12], using the “multi-term approximation” i.e. MultiBolt [187], and using a particle model based approach i.e. METHES [156], and `particle_swarm` [142].

These solvers were compared using an extensive set of model gases designed to test individual aspects of a solver. These model gases differ by the type of collisions included e.g. only elastic resulting in a model that can be solved for analytically, including either ionization or attachment to test the solver with non-particle-conserving reactions, etc. This collection of model gases should serve as a set of test cases that all new solvers should run and report their results on. A set of agreed upon tests and accompanying results are necessary to increase confidence in the results produced by researchers using different solvers.

Results of the solvers were compared to those of BOLSIG+ since it is the most widely used solver and comparing to it can be beneficial to the wider plasma modelling community. Overall all solvers produce flux coefficients to within 5% of each other for the model gases. Whenever deviations occurred for the more accurate particle based solvers, the MultiBolt solver using a 10-term approximation followed it closely. Also for the real gases

(Ar, N<sub>2</sub>, and O<sub>2</sub>) results mostly stayed within 10% of each except for the LoKI-B solver where ionization coefficients could differ by up to 50%. The reason for this deviation was not found. Although the likely culprit is user error, an extensive set of model gases were compared as well with LoKI-B and no significant differences were found. This shows that the solver was either correctly used and has some error or there is a non-user-friendly configuration that had to be used for real gases which was not necessary for the model gases.

Eventhough most solvers did not differ significantly from each other on a physics results basis, there were large differences on other fronts like computation time. For the same input cross sections (N<sub>2</sub>) and electric field values (100 points between 10 Td and 1000 Td), the computation time of these solvers spanned several orders of magnitude. BOLSIG+ was the fastest clocking in at 1.5 s while METHES was the slowest at 62·10<sup>3</sup> s.

After comparing this collection of solvers a suggestion was made to the reader on which solvers to use. When solutions from a two-term approximation is accurate enough BOLSIG+ is the suggested solver to use (which it already is in the discharge modelling community). For a more accurate solver we suggest the particle based solver `particle_swarm`, as long as the electric fields are not too low since then particle based solvers take a long time to converge to a solution.

Some solvers were completely open source so that fixes, improvements, or suggestions could be made to the source code. The author has submitted improvements to BOLOS, and fixes to METHES. These additions are not yet accepted into the main source code.

### **6.3 Chapter 4: Investigation of Streamer Inception in Air**

In this thesis we have investigated where the streamer initiating electrons in air come from. Experimental measurements of the time between the onset of the voltage pulse and the inception of a streamer were made. The inception of a streamer was measured by using a photomultiplier tube (PMT)

and recording at which time the signal of the PMT rose above the background level. Displaying these inception times in a histogram produced three distinct peaks i.e. three “preferential” times at which the streamer initiates. To gain further insight into this streamer inception behaviour, a low voltage pulse (not able to trigger a discharge) was prepended to the streamer-initiating high voltage pulse. This low voltage pulse could be adjusted in three ways: the polarity, the length in time, and the time separating it from the high voltage pulse.

These experimental measurements and techniques were combined with modelling results to give reasonable explanations for some of the experimental observations. The modelling was done using a particle model (see 1.3.2) where only the discharge inception was simulated, and not the entire discharge development. By changing the position and species of the charged particles within the model we found candidate species and processes causing some of the peaks observed in the experimentally measured histogram of inception times.

The first peak was in the nanosecond range and could be removed by applying a positive low voltage pulse. These observations led us to the conjecture that this peak was caused by negative ions already present in the high field region around the electrode. At the voltage onset these negative ions can detach an electron which is able to trigger streamer inception quickly thereafter. A particle simulation including multiple voltage pulses (and streamer development) where both ions and electrons are simulated could substantiate this idea further.

The cause of the second peak (around  $25 \mu\text{s}$ ) remains a mystery. This peak did not shift or change due to the application of any polarity or length of low voltage pulse. For these reasons the source of these inception times seems to be electrically neutral. Initially we postulated that this was caused by Penning ionization of electronically excited nitrogen molecules, but the quenching reactions with oxygen molecules have timescales on the order of 10 to 100 ns which makes this unlikely to be a considerable effect around  $25 \mu\text{s}$ . The final hypothesis we landed on was the presence of quasi-neutral ion patches which could not be separated by a low voltage pulse, though

this hypothesis has not been elaborated. At the onset of the high voltage pulse the negative ions could drift towards the high field region around the electrode and detachment would provide the streamer-initiating free electrons.

The third peak (around  $120 \mu\text{s}$ ) was susceptible to the low voltage pulse in the same way as the first peak was. This led us to believe that the third peak was also due to negative ions which had to drift from further in the gap towards the high field region around the electrode. A puzzling observation was that for the first and third peak to be as separated as they are there has to be a region of considerably lower ion density between the region around the electrode (cause of first peak) and the region from which the ions have to drift (cause of third peak). If there was no such difference then the first and third peak would not have a clear gap between them. We did not find a clear explanation to what would cause this ion density gap.

Additionally, with the knowledge of what species trigger streamer inception and the addition of a low voltage pulse we were able to delay or speed-up streamer inception which can be beneficial to practical applications and other types of streamer experiments.

All experimental work was done by my co-author Dr. Shahriar Mirpour. All simulations and the majority of calculations were done by the current author. Interpretation of results, hypothesizing new ideas, and writing the text was a collective effort.

## 6.4 Chapter 5: Repetitive Pulsed Streamer Discharges in Air

In this thesis we have investigated positive streamer development when a repetitive voltage pulse is applied. The time between voltage pulses (i.e. the interpulse time) determines which species remain in the discharge gap by the previous streamer and thus the influence of the previous streamer on subsequent streamers. This was investigated for positive streamers in 80 mbar synthetic air (80/20  $\text{N}_2/\text{O}_2$ ) in a 2D axi-symmetric fluid model with a discharge gap of 15 cm and a double voltage pulse where each volt-

age pulse had a linear rise- and falltime of 40 ns, a constant voltage of 20 kV for 200 ns, and an interpulse time of 0.5, 1, 5, 10, or 20  $\mu$ s.

Experimental investigations on the influence of the interpulse time on streamer continuation (i.e. where the streamer produced by the voltage pulse starts from the end of the streamer produced by the previous voltage pulse) found a minimal “continuation time”. Experiments at 133 mbar synthetic air with a discharge gap of 10 cm and a maximum voltage of 13 kV found the continuation to be around 500 ns. In this thesis, we have found the continuation time to be between 5 and 10  $\mu$ s. It is not yet clear what brings about this difference. The continuation time does not easily scale with pressure towards the experimental measurement. However, an important difference between the electrode geometry in simulation and experiment should be kept in mind. For experiment there was a rod-plane geometry while simulation had a protrusion-plane geometry. This will result in a different electric field distribution. Further investigation is necessary to understand this difference in continuation time.

We have included over 400 plasma-chemical reactions to investigate which reactions dominate in which region of the streamer and at which time within the double voltage pulse. Non surprisingly, when the electric field is high (at the streamer head and the electrode during the constant voltage interval) the ionization reactions with  $N_2$  and  $O_2$ , and the dissociative attachment to  $O_2$  were dominant. Within the streamer channel, where the electric field is lower, initially the positive-ion conversion reactions converting  $O_2^+$  into  $O_4^+$  and back were dominant. As we move into the interpulse region (i.e. no voltage applied), the negative-ion conversion reactions converting  $O_2^-$  into  $O_4^-$  become dominant. These negative-ion conversion reactions remain dominant until the next voltage pulse is applied.

Additionally, we included a model for gas heating to investigate how repetitive voltage pulses (and thus discharges) increase the temperature of the gas. We found that for a double voltage pulse in our model, the gas heating was mainly observable close to the electrode. Already at 1 cm distance from the electrode there was practically no heating. The amount of heating was also limited, for a short interpulse time the maximal heating observed was

30 K. This temperature increase had negligible effects on reaction rates and minimal effects on other included gas dynamics e.g. small expansion of the discharge.

## 6.5 Outlook

In this section we will discuss possible future avenues of research based on the topics presented in this thesis.

### 6.5.1 Discharge Inception

As shown in the work in chapter 4 on discharge inception in air understanding which species cause discharge inception can help us in creating methods to speed up or delay the inception. This proved difficult for the synthetic air which was used in the current work. However, often times discharges are produced in ambient air i.e. humid air. The effects of water on discharge inception are largely unknown. Unpublished experimental measurements done in humid air show very different inception behaviour than in synthetic air. The properties of discharges in humid air should be better investigated since this is often the environment in which discharges for applications are produced (e.g. plasma-agriculture, and plasma-medicine). Also for CO<sub>2</sub> there still remain open questions as to what species/processes are responsible for discharge inception. Experimental measurements of the distribution of inception times by Mirpour *et al.* [119] show a complex difference in inception time behaviour when applying a positive or negative prepulse. Understanding discharge inception in CO<sub>2</sub> could be beneficial for high voltage circuit breakers where CO<sub>2</sub> is looked at as a replacement for SF<sub>6</sub>.

### 6.5.2 Repetitive Pulses

The work in chapter 5 showed a discrepancy between the streamer continuation time as measured in experiment and as calculated in simulation. It is as of yet unclear how this difference arose. Even though the pressure in experiment and in simulation differed by almost a factor two, the continuation times differed by a factor 10-20. This difference shows that results cannot simply be scaled by pressure. The difference in electrode

geometry between experiment and simulation produces a different electric field distribution which is a big contributor to the differences in results between experiment and simulation. Future research into the continuation time should try to match the simulation electrode geometry as closely as possible to that of experiment since the electric field distribution is an important factor when comparing experiment and simulation.

In this thesis, reactions using excited species were not taken into account. This resulted in some excited species to be among the most dominant species in the simulation. This could paint the wrong picture since there are no reactions which take these species out of the simulation. Future simulations should include reactions which use the dominant excited species found in the work of chapter 5.

### **6.5.3 Boltzmann Solvers and Other Scientific Software**

Throughout the thesis many different scientific codes were used, but they do not come without their own sets of issues. Software development includes not only writing seemingly working code, but also writing documentation, writing tests, cleaning up existing code, etc. Because researchers are under high time pressure to publish new results and because they usually have a very limited (in time) contract the majority of these ‘auxiliary’ software development tasks will not be undertaken since they cost a lot of time and they do not provide new scientific results. The problem that occurs is that multiple research groups will develop their own piece of software to solve the same equations, but no quality standard is maintained and no tests are in place in the software to maintain confidence in each other’s scientific results. The field needs a community effort to define a set of test cases (going from easy and fundamental to more specialized for the application at hand) that each research group’s software should adhere to. Additionally these test cases should be run on every change of the code and the results should be either continuously updated on a website for all to see or added in some way to the publication where the software was used.

To go more in detail on the last points of previous paragraph I will present a list of things that should be taken into account during software development to increase productivity and confidence in the software:

- Use a code formatter: These are programs that take a file with code and rewrite them (purely visually) into a predefined style. This ensures consistency throughout the codebase which is otherwise hard to accomplish when working with multiple people on one codebase. This can be run by the developers themselves before sharing the code or as part of the continuous integration process (discussed in a later point). Examples of this are: `Prettier` [153] (for Javascript), and `clang-format` [31] for C, C++, and Java.
- Write tests: Software tests increase confidence and reliability of the software. Software testing is a field on its own so I will present a short summary. There are two types of tests: unit, and functional. Unit tests will test individual pieces of the code (usually functions or a class). Functional tests will actually ‘do’ something e.g. run a simulation or calculation of which the results are known. These will use many different parts of the code and see if they work correctly together. “Unit tests tell a developer the code is doing things right. Functional tests tell a developer the code is doing the right things.”.

It is tempting to quickly create a format and some files in which co-developers should write their unit tests. I advise strongly to use an already existing unit testing framework. Not only will this make writing unit tests easier (and thus more tests will be written), but also running the tests will be better integrated into the development process. Common unit testing frameworks are: `Catch2` [26], `Google Test` [56], and `Boost.Test` [16] for C++, and `Robot` framework [164], and `PyUnit` [155] for Python. At the bare minimum every bug encountered should be turned into a unit test. Preferably, every function should have several unit tests.

Functional tests will usually also be written using the aforementioned testing frameworks, but the scope of a functional test is much wider. An example of a functional test would be: The ionization coefficient calculated using my new Boltzmann equation solver class and this specific set of input data should be  $x$ . Where  $x$  is known before the test is run.

- Use a version control system (VCS): In short, VCS will keep track of any changes happened to the code and who made it. It will allow you to revert back to a previous version of the code in case of breaking bugs, or quickly get an overview of new additions to the code since you have last worked on it. A common VCS is `git` [53] which can be run locally, but for a collaboration this is usually used in conjunction with an online platform like GitHub [54] or GitLab [55].

A crucial aspect of a VCS is that changes to the code i.e. ‘commits’ are small and described clearly. A change to several functions with a description of ‘some fixes’ is not good. An example of a good commit is when a clear goal is achieved and only those pieces of code necessary to achieve that goal are altered e.g. ‘Add timestep config variable’, ‘Fix bug xyz’, ‘Add LXCat-file reader class’. This is an often overlooked aspect of VCS within academia and should be stressed more within software developing research groups.

- Choose a clear VCS workflow: A VCS will bring more annoyance and time waste to a project if there is no sane workflow in place. If the majority of the developer or project maintainer’s time is spent resolving conflicts between the changes of several developers or if results of one researcher change drastically (in a bad way) when using the “updated” version of the code there are problems. A VCS workflow helps streamline the process of adding new features to the code and can offer moments of commenting and reviewing bigger changes to the code before they are actually added. A great summary of common workflows can be found at [9]. Some workflows will fit a situation better than others, but the most important point is that a clear choice is made and developers stick to it.
- Use a continuous integration (CI) tool: CI allows to automate a vast variety of things that can happen after new code is added to the codebase. Usually these will be things as building the codebase into an executable and running tests. Arguably the most popular tool for this is Jenkins [77], but nowadays VCS sites like GitHub and GitLab have their own implementation of CI tools. At a minimum, whenever new code is added to the main codebase the code should be built from

scratch on a fresh system and unit tests should be run. Preferably, every night/week all functional tests are run depending on runtime. If the software is to be used by people outside of your own research group the software should be built and tested for different operating systems and compilers.

- Write documentation: This is a self-explanatory point which everybody agrees with, but hardly anyone does. At a minimum, there should be clear descriptions of what each function does and what the input and output parameters are/represent. This should be annotated within the source code, but should preferably also exist outside of the code on an external website or document. The most common tool to produce documentation from source code annotations is Doxygen [40]. An extension that is more user focused is the inclusion of small tutorials or completely explained examples to help the user get familiar with the code and how to use it properly.

In academia there is a high turnover of researchers within research groups e.g. PhD. students, and PostDocs. These researchers also become software developers when working on modelling projects. Every researcher will have their own programming skill level and style. If every researcher just adds what they want however they want to the code, the codebase will quickly turn into a big mess that nobody really understands i.e. spaghetti code [182]. This will decrease the confidence in the results produced by this codebase. Thinking about and implementing the previously mentioned items can drastically improve confidence in any software that we develop.

During the COVID-19 pandemic we have seen governments base their course of actions on the recommendations and results of experts and we have seen misinformation and doubt spread faster than ever before with sometimes dire consequences. Maybe someday our software has to produce results to guide government actions so let us take software development serious. Because this is a topic that I feel strongly about let me close with the following: Let us, as a community, make it acceptable to spend considerable time on work that makes our software more stable, reliable, and user-friendly instead of only chasing and producing new publishable results.

# Bibliography

- [1] A Agnihotri, W Hundsdorfer, and U Ebert. ‘Modeling heat dominated electric breakdown in air, with adaptivity to electron or ion time scales’. Plasma Sources Science and Technology 26.9 (2017), p. 095003 (cit. on pp. 177, 178).
- [2] Hidenori Akiyama. ‘Streamer discharges in liquids and their applications’. IEEE Transactions on Dielectrics and Electrical Insulation 7.5 (2000), pp. 646–653 (cit. on p. 99).
- [3] N L Aleksandrov and E M Bazelyan. ‘Ionization processes in spark discharge plasmas’. Plasma Sources Science and Technology 8.2 (Jan. 1999), pp. 285–294. DOI: 10.1088/0963-0252/8/2/309 (cit. on p. 150).
- [4] M Allan. ‘Experimental differential cross sections for the electron impact excitation of the  $a^1\Delta_g$ ,  $b^1\Sigma_g^+$ , and the 6 eV states of  $O_2$ ’. Journal of Physics B: Atomic, Molecular and Optical Physics 28.19 (Oct. 1995), pp. 4329–4345. DOI: 10.1088/0953-4075/28/19/018 (cit. on p. 62).
- [5] Michael Allan. ‘Improved techniques of measuring accurate electron - molecule cross sections near threshold and over a large angular range’. AIP Conference Proceedings 901.1 (Apr. 2007), pp. 107–116. ISSN: 0094-243X. DOI: 10.1063/1.2727361 (cit. on p. 27).
- [6] L. L. Alves. ‘The IST-LISBON database on LXCat’. J. Phys.: Conf. Ser. 565 (Dec. 2014), p. 012007. ISSN: 1742-6596.

## BIBLIOGRAPHY

---

- DOI: 10.1088/1742-6596/565/1/012007 (cit. on pp. 6, 18, 26, 27, 29–32, 36, 38, 39, 185).
- [7] S. A. J. Al-Amin, H. N. Kucukarpaci, and J. Lucas. ‘Electron swarm parameters in oxygen and methane’. *J. Phys. D: Appl. Phys.* 18.9 (Sept. 1985), pp. 1781–1794. ISSN: 0022-3727. DOI: 10.1088/0022-3727/18/9/009 (cit. on p. 38).
- [8] S. A. J. Al-Amin and J. Lucas. ‘Time of flight measurements of the ratio of radial diffusion coefficient and mobility for electron swarms in helium, argon, neon and krypton at high E/N’. *J. Phys. D: Appl. Phys.* 20.12 (Dec. 1987), pp. 1590–1595. ISSN: 0022-3727. DOI: 10.1088/0022-3727/20/12/007 (cit. on p. 81).
- [9] Atlassian: git workflows. URL: <https://www.atlassian.com/git/tutorials/comparing-workflows> (cit. on p. 195).
- [10] F. T. Bagnall and S. C. Haydon. ‘Pre-breakdown Ionization in Molecular Nitrogen in E x B Fields’. *Aust. J. Phys.* 18.3 (1965), pp. 227–236. ISSN: 1446-5582. DOI: 10.1071/ph650227 (cit. on p. 84).
- [11] D. T. A. Blair. ‘The use of alpha-particle irradiation in ionization coefficient measurements in gases’. *Br. J. Appl. Phys.* 17.8 (Aug. 1966), pp. 1051–1060. ISSN: 0508-3443. DOI: 10.1088/0508-3443/17/8/313 (cit. on p. 84).
- [12] BOLOS: Two-Term Electron Boltzmann Solver. URL: <https://github.com/aluque/bolos> (cit. on p. 187).
- [13] BOLSIG+ (Linux). Mar. 2016. URL: <http://www.bolsig.laplace.univ-tlse.fr/> (cit. on pp. 117, 187).
- [14] BOLSIG+ (Linux). Dec. 2019. URL: <http://www.bolsig.laplace.univ-tlse.fr/> (cit. on pp. 162, 178, 179).
- [15] Z Bonaventura, A Bourdon, S Celestin, and V P Pasko. ‘Electric field determination in streamer discharges in air at atmospheric pressure’. *Plasma Sources Science and Technology* 20.3 (Apr. 2011), p. 035012. ISSN: 1361-6595. DOI: 10.1088/0963-0252/20/3/035012 (cit. on p. 99).

- [16] Boost.Test. URL: [https://www.boost.org/doc/libs/1\\_78\\_0/libs/test/doc/html/index.html](https://www.boost.org/doc/libs/1_78_0/libs/test/doc/html/index.html) (cit. on p. 194).
- [17] W. E. Bowls. ‘The Effect of Cathode Material on the Second Townsend Coefficient for Ionization by Collision in Pure and Contaminated N<sub>2</sub> Gas’. Phys. Rev. 53.4 (Feb. 1938), pp. 293–301. DOI: 10.1103/PhysRev.53.293 (cit. on p. 84).
- [18] Jörg Brambring. ‘Driftgeschwindigkeit von Elektronen in Argon’. Z. Physik 179.5 (Oct. 1964), pp. 539–543. ISSN: 0044-3328. DOI: 10.1007/BF01380827 (cit. on p. 81).
- [19] T.M.P. Briels, E.M. van Veldhuizen, and U. Ebert. ‘Time Resolved Measurements of Streamer Inception in Air’. IEEE Trans. Plasma Sci. 36.4 (Aug. 2008), pp. 908–909. DOI: 10.1109/TPS.2008.920223 (cit. on pp. 99, 107).
- [20] Will J. Brigg, Jonathan Tennyson, and Martin Plummer. ‘R-matrix calculations of low-energy electron collisions with methane’. J. Phys. B: At. Mol. Opt. Phys. 47.18 (Sept. 2014), p. 185203. ISSN: 0953-4075. DOI: 10.1088/0953-4075/47/18/185203 (cit. on pp. 6, 45).
- [21] William L. Briggs, Van Emden Henson, and Steve F. McCormick. A Multigrid Tutorial (2<sup>nd</sup> Ed.) Philadelphia, PA, USA, 2000. ISBN: 0-89871-462-1 (cit. on p. 17).
- [22] BSR database. Aug. 2021. URL: [www.lxcat.net](http://www.lxcat.net) (cit. on pp. 81–83).
- [23] Stephen J. Buckman, Michael J. Brunger, and Kurunathan Ratnavelu. ‘Atomic Scattering Data and Their Evaluation: Strategies for Obtaining Complete Cross-Section Sets for Electron Collision Processes’. Fusion Science and Technology 63.3 (May 2013), pp. 385–391. ISSN: 1536-1055. DOI: 10.13182/FST13-A16446 (cit. on p. 26).
- [24] M. Capitelli, C. M. Ferreira, B. F. Gordiets, and A. I. Osipov. Plasma Kinetics in Atmospheric Gases. Springer Series on Atomic, Optical, and Plasma Physics. Berlin Heidelberg, 2000. ISBN: 978-3-540-67416-0. DOI: 10.1007/978-3-662-04158-1 (cit. on p. 129).

## BIBLIOGRAPHY

---

- [25] Emile Carbone, Wouter Graef, Gerjan Hagelaar, Daan Boer, Matthew Hopkins, Jacob Stephens, Benjamin T. Yee, Sergey Pancheshnyi, Jan van Dijk, Leanne Pitchford, and on Team. ‘Data Needs for Modeling Low-Temperature Non-Equilibrium Plasmas: The LXCat Project, History, Perspectives and a Tutorial’. *Atoms* 9.1 (2021), p. 16. ISSN: 2218-2004. DOI: 10.3390/atoms9010016 (cit. on pp. 46, 61, 81, 84, 186).
- [26] Catch2. URL: <https://github.com/catchorg/Catch2> (cit. on p. 194).
- [27] Carlo Cercignani. ‘The boltzmann equation’. In: The Boltzmann equation and its applications. 1988, pp. 40–103 (cit. on p. 11).
- [28] L. M. Chanin, A. V. Phelps, and M. A. Biondi. ‘Measurements of the Attachment of Low-Energy Electrons to Oxygen Molecules’. *Phys. Rev.* 128.1 (Oct. 1962), pp. 219–230. DOI: 10.1103/PhysRev.128.219 (cit. on p. 3).
- [29] Olivier Arnaud Chanrion and Torsten Neubert. ‘A PIC-MCC code for simulation of streamer propagation in air’. *Journal of Computational Physics* 15.15 (2008), pp. 7222–7245. ISSN: 0021-9991. DOI: 10.1016/j.jcp.2008.04.016 (cit. on p. 110).
- [30] She Chen, Kelin Li, and Sander Nijdam. ‘Transition mechanism of negative DC corona modes in atmospheric air: from Trichel pulses to pulseless glow’. *Plasma Sources Science and Technology* 28.5 (2019), p. 055017 (cit. on pp. 176–178).
- [31] Clang Format. URL: <https://clang.llvm.org/docs/ClangFormat.html> (cit. on p. 194).
- [32] L. W. Cochran and D. W. Forester. ‘Diffusion of Slow Electrons in Gases’. *Phys. Rev.* 126.5 (June 1962), pp. 1785–1788. DOI: 10.1103/PhysRev.126.1785 (cit. on p. 38).
- [33] COMSOL Multiphysics® v. 5.4. URL: [www.comsol.com](http://www.comsol.com). (cit. on p. 113).
- [34] R. J. Corbin and Lothar Frommhold. ‘Electron avalanches in oxygen and in mixtures of O<sub>2</sub> and H<sub>2</sub>: Determination of the first Townsend coefficient  $\alpha$ ’. *Phys. Rev. A* 10.6 (Dec. 1974), pp. 2273–2279. DOI: 10.1103/PhysRevA.10.2273 (cit. on p. 87).

- [35] T. L. Cottrell and Isobel C. Walker. ‘Drift velocities of slow electrons in polyatomic gases’. Trans. Faraday Soc. 61.0 (Jan. 1965), pp. 1585–1593. ISSN: 0014-7672. DOI: 10.1039/TF9656101585 (cit. on p. 38).
- [36] J Cross and J Beattie. ‘Positive glow corona in quasi-uniform fields’. Canadian Electrical Engineering Journal 5.3 (1980), pp. 22–32 (cit. on p. 107).
- [37] D. K. Davies, L. E. Kline, and W. E. Bies. ‘Measurements of swarm parameters and derived electron collision cross sections in methane’. Journal of Applied Physics 65.9 (May 1989), pp. 3311–3323. ISSN: 0021-8979. DOI: 10.1063/1.342642 (cit. on p. 38).
- [38] Luc Devroye. ‘Non-Uniform Random Variate Generation’. In: Non-Uniform Random Variate Generation. 1986, pp. 27–39 (cit. on p. 14).
- [39] Digitized reaction rates. URL: <https://gitlab.com/MD-CWI-NL/chemistry-data> (cit. on p. 150).
- [40] Doxygen. URL: <https://www.doxygen.nl/index.html> (cit. on p. 196).
- [41] Anna Dubinova, Casper Rutjes, Ute Ebert, Stijn Buitink, Olaf Scholten, and Gia Thi Ngoc Trinh. ‘Prediction of Lightning Inception by Large Ice Particles and Extensive Air Showers’. Physical Review Letters 115.1 (June 2015). ISSN: 0031-9007, 1079-7114. DOI: 10.1103/PhysRevLett.115.015002 (cit. on p. 99).
- [42] Ute Ebert, Sander Nijdam, Chao Li, Alejandro Luque, Tanja Briels, and Eddie van Veldhuizen. ‘Review of recent results on streamer discharges and discussion of their relevance for sprites and lightning’. Journal of Geophysical Research: Space Physics 115.A7 (2010) (cit. on p. 99).
- [43] M. T. Elford, S. J. Buckman, and M. Brunger. ‘6.3 Elastic momentum transfer cross sections’. In: Interactions of Photons and Electrons with Molecules. Ed. by Y. Itikawa. Vol. 17C. Berlin/Heidelberg, 2003, pp. 6085–6117. ISBN: 978-3-540-44338-4. DOI: 10.1007/10874891\_6 (cit. on p. 27).

## BIBLIOGRAPHY

---

- [44] Daniel A. Erwin and Joseph A. Kunc. ‘Dissociation and ionization of the methane molecule by nonrelativistic electrons including the near threshold region’. Journal of Applied Physics 103.6 (Mar. 2008), p. 064906. ISSN: 0021-8979. DOI: 10.1063/1.2891694 (cit. on pp. 27, 28, 31–35, 39).
- [45] Daniel A. Erwin and Joseph A. Kunc. ‘Electron-impact dissociation of the methane molecule into neutral fragments’. Phys. Rev. A 72.5 (Nov. 2005), p. 052719. DOI: 10.1103/PhysRevA.72.052719 (cit. on pp. 27, 28, 31–33, 39).
- [46] Kamil Fedus and Grzegorz P. Karwasz. ‘Ramsauer-Townsend minimum in methane — modified effective range analysis’. Eur. Phys. J. D 68.4 (Apr. 2014), p. 93. ISSN: 1434-6079. DOI: 10.1140/epjd/e2014-40738-x (cit. on p. 27).
- [47] Tao Fengbo, Zhang Qiaogen, Gao Bo, Wang Hu, and Li Zhou. ‘A repetitive nanosecond pulse source for generation of large volume streamer discharge’. Plasma Science and Technology 10.5 (2008), p. 588 (cit. on p. 100).
- [48] Gregory Fridman, Gary Friedman, Alexander Gutsol, Anatoly B. Shekhter, Victor N. Vasilets, and Alexander Fridman. ‘Applied Plasma Medicine’. Plasma Processes and Polymers 5.6 (2008), pp. 503–533. DOI: <https://doi.org/10.1002/ppap.200700154> (cit. on pp. 11, 147).
- [49] L. Frommhold. ‘Über verzögerte Elektronen in Elektronenlawinen, insbesondere in Sauerstoff und Luft, durch Bildung und Zerfall negativer Ionen (O-)’. Fortschritte der Physik 12.11 (1964), pp. 597–642. ISSN: 1521-3978. DOI: 10.1002/prop.19640121102 (cit. on p. 87).
- [50] L. S. Frost and A. V. Phelps. ‘Rotational Excitation and Momentum Transfer Cross Sections for Electrons in H<sub>2</sub> and N<sub>2</sub> from Transport Coefficients’. Phys. Rev. 127.5 (Sept. 1962), pp. 1621–1633. DOI: 10.1103/PhysRev.127.1621 (cit. on p. 38).
- [51] A. Gadoum and D. Benyoucef. ‘Set of the Electron Collision Cross Sections for Methane Molecule’. IEEE Transactions on Plasma Science 47.3 (Mar. 2019),

- pp. 1505–1513. ISSN: 1939-9375. DOI: 10.1109/TPS.2018.2885610 (cit. on p. 27).
- [52] Trinh N Giao and Jan B Jordan. ‘Modes of corona discharges in air’. IEEE Transactions on Power Apparatus and Systems 5 (1968), pp. 1207–1215 (cit. on p. 107).
- [53] git. URL: <https://git-scm.com/> (cit. on p. 195).
- [54] GitHub. URL: <https://github.com/> (cit. on p. 195).
- [55] GitLab. URL: <https://gitlab.com/> (cit. on p. 195).
- [56] Google Test. URL: <https://github.com/google/googletest> (cit. on p. 194).
- [57] David B. Graves. ‘Low temperature plasma biomedicine: A tutorial review’. Physics of Plasmas 21.8 (Aug. 2014), p. 080901. ISSN: 1070-664X. DOI: 10.1063/1.4892534 (cit. on pp. 11, 147).
- [58] G. K. Grubert, M. M. Becker, and D. Loffhagen. ‘Why the local-mean-energy approximation should be used in hydrodynamic plasma descriptions instead of the local-field approximation’. Phys Rev E Stat Nonlin Soft Matter Phys 80.3 Pt 2 (Sept. 2009), p. 036405. ISSN: 1550-2376. DOI: 10.1103/PhysRevE.80.036405 (cit. on p. 17).
- [59] V Guerra and J Loureiro. ‘Electron and heavy particle kinetics in a low-pressure nitrogen glow discharge’. Plasma Sources Sci. Technol. 6.3 (Aug. 1997), pp. 361–372. DOI: 10.1088/0963-0252/6/3/013 (cit. on pp. 3, 128).
- [60] Scott Habershon, David E. Manolopoulos, Thomas E. Markland, and Thomas F. Miller. ‘Ring-Polymer Molecular Dynamics: Quantum Effects in Chemical Dynamics from Classical Trajectories in an Extended Phase Space’. Annu. Rev. Phys. Chem. 64.1 (Apr. 2013), pp. 387–413. ISSN: 0066-426X. DOI: 10.1146/annurev-physchem-040412-110122 (cit. on p. 46).

## BIBLIOGRAPHY

---

- [61] G. J. M. Hagelaar and L. C. Pitchford. ‘Solving the Boltzmann equation to obtain electron transport coefficients and rate coefficients for fluid models’. Plasma Sources Sci. Technol. 14.4 (Oct. 2005), pp. 722–733. ISSN: 0963-0252. DOI: 10.1088/0963-0252/14/4/011 (cit. on pp. 11, 59–61, 65, 117, 162, 178, 179).
- [62] Melvin A. Harrison and Ronald Geballe. ‘Simultaneous Measurement of Ionization and Attachment Coefficients’. Phys. Rev. 91.1 (July 1953), pp. 1–7. DOI: 10.1103/PhysRev.91.1 (cit. on p. 87).
- [63] H. Hasegawa, H. Date, M. Shimosuma, K. Yoshida, and H. Tagashira. ‘The drift velocity and longitudinal diffusion coefficient of electrons in nitrogen and carbon dioxide from 20 to 1000 Td’. J. Phys. D: Appl. Phys. 29.10 (Oct. 1996), pp. 2664–2667. ISSN: 0022-3727. DOI: 10.1088/0022-3727/29/10/018 (cit. on p. 84).
- [64] S Haydon and Owen Williams. ‘Combined spatial and temporal studies of ionization growth in nitrogen’. Journal of Physics D: Applied Physics 9 (Jan. 2001), p. 523. DOI: 10.1088/0022-3727/9/3/018 (cit. on p. 84).
- [65] E J M van Heesch, G J J Winands, and A J M Pemen. ‘Evaluation of pulsed streamer corona experiments to determine the O<sup>\*</sup>-radical yield’. Journal of Physics D: Applied Physics 41.23 (Nov. 2008), p. 234015. DOI: 10.1088/0022-3727/41/23/234015 (cit. on pp. 11, 147).
- [66] J. L. Hernández-Ávila, E. Basurto, and J. de Urquijo. ‘Electron transport and ionization in CHF<sub>3</sub>–Ar and CHF<sub>3</sub>–N<sub>2</sub>gas mixtures’. J. Phys. D: Appl. Phys. 37.22 (Oct. 2004), pp. 3088–3092. ISSN: 0022-3727. DOI: 10.1088/0022-3727/37/22/005 (cit. on pp. 81, 84).
- [67] A. E. D. Heylen. ‘Ionization coefficients and sparking voltages from methane to butane’. International Journal of Electronics 39.6 (Dec. 1975), pp. 653–660. ISSN: 0020-7217. DOI: 10.1080/00207217508920532 (cit. on p. 38).

- [68] R. W. Hockney and J. W. Eastwood. Computer Simulation Using Particles. 1988. DOI: <https://doi.org/10.1201/9780367806934> (cit. on pp. 12, 14, 15).
- [69] L. D. Horton. ‘Atomic and molecular data needs for fusion research’. Phys. Scr. T65 (Jan. 1996), pp. 175–178. ISSN: 1402-4896. DOI: 10.1088/0031-8949/1996/T65/025 (cit. on p. 25).
- [70] S. R. Hunter, J. G. Carter, and L. G. Christophorou. ‘Electron transport measurements in methane using an improved pulsed Townsend technique’. Journal of Applied Physics 60.1 (July 1986), pp. 24–35. ISSN: 0021-8979. DOI: 10.1063/1.337690 (cit. on p. 38).
- [71] IST-Lisbon database. Aug. 2021. URL: [www.lxcat.net](http://www.lxcat.net) (cit. on pp. 84, 88, 89, 93, 150).
- [72] Yukikazu Itikawa. ‘Cross Sections for Electron Collisions with Nitrogen Molecules’. Journal of Physical and Chemical Reference Data 35.1 (Dec. 2005), pp. 31–53. ISSN: 0047-2689. DOI: 10.1063/1.1937426 (cit. on pp. 2, 110, 117).
- [73] Yukikazu Itikawa. ‘Cross Sections for Electron Collisions with Oxygen Molecules’. Journal of Physical and Chemical Reference Data 38.1 (Mar. 2009), pp. 1–20. ISSN: 0047-2689. DOI: 10.1063/1.3025886 (cit. on pp. 2, 3, 84, 88, 89, 110, 117, 150).
- [74] Itikawa database. May 2020. URL: [www.lxcat.net](http://www.lxcat.net) (cit. on pp. 84, 88, 89, 110, 117, 150).
- [75] R. K. Janev and D. Reiter. ‘Collision processes of CH<sub>y</sub> and CH<sub>y</sub>+ hydrocarbons with plasma electrons and protons’. Physics of Plasmas 9.9 (Aug. 2002), pp. 4071–4081. ISSN: 1070-664X. DOI: 10.1063/1.1500735 (cit. on pp. 28, 33).
- [76] Z. M. Jelenak, Z. B. Velikić, J. V. Božin, Z. Lj Petrović, and B. M. Jelenković. ‘Electronic excitation of the 750- and 811-nm lines of argon’. Phys. Rev. E 47.5 (May 1993), pp. 3566–3573. DOI: 10.1103/PhysRevE.47.3566 (cit. on p. 81).
- [77] Jenkins. URL: <https://www.jenkins.io/> (cit. on p. 195).

- [78] Byoung-Hoon Jeon and Yoshiharu Nakamura. ‘Measurement of drift velocity and longitudinal diffusion coefficient of electrons in pure oxygen and in oxygen-argon mixtures’. *J. Phys. D: Appl. Phys.* 31.17 (Sept. 1998), pp. 2145–2150. ISSN: 0022-3727. DOI: 10.1088/0022-3727/31/17/011 (cit. on p. 87).
- [79] R. L. Jory. ‘Transport Coefficients for Low Energy Electrons in Crossed Electric and Magnetic Fields’. *Aust. J. Phys.* 18.3 (1965), pp. 237–256. ISSN: 1446-5582. DOI: 10.1071/ph650237 (cit. on p. 84).
- [80] Mutsukazu Kamo, Yoichiro Sato, Seiichiro Matsumoto, and Nobuo Setaka. ‘Diamond synthesis from gas phase in microwave plasma’. *Journal of Crystal Growth* 62.3 (Aug. 1983), pp. 642–644. ISSN: 0022-0248. DOI: 10.1016/0022-0248(83)90411-6 (cit. on p. 25).
- [81] S. Kawaguchi, K. Takahashi, and K. Satoh. ‘Electron collision cross section set for N<sub>2</sub> and electron transport in N<sub>2</sub>, N<sub>2</sub>/He, and N<sub>2</sub>/Ar’. *Plasma Sources Sci. Technol.* 30.3 (Mar. 2021), p. 035010. ISSN: 0963-0252. DOI: 10.1088/1361-6595/abe1d4 (cit. on pp. 81, 85, 86, 150, 162).
- [82] H. C. Kim, F. Iza, S. S. Yang, M. Radmilović-Radjenović, and J. K. Lee. ‘Particle and fluid simulations of low-temperature plasma discharges: benchmarks and kinetic effects’. *J. Phys. D: Appl. Phys.* 38.19 (Sept. 2005), R283. ISSN: 0022-3727. DOI: 10.1088/0022-3727/38/19/R01 (cit. on p. 17).
- [83] Hyun-Ha Kim. ‘Nonthermal Plasma Processing for Air-Pollution Control: A Historical Review, Current Issues, and Future Prospects’. *Plasma Processes and Polymers* 1.2 (2004), pp. 91–110. ISSN: 1612-8869. DOI: 10.1002/ppap.200400028 (cit. on p. 147).
- [84] Tobias G. Klämpfl, Georg Isbary, Tetsuji Shimizu, Yang-Fang Li, Julia L. Zimmermann, Wilhelm Stolz, Jürgen Schlegel, Gregor E. Morfill, and Hans-Ulrich Schmidt. ‘Cold Atmospheric Air Plasma Sterilization against Spores and Other Microorganisms of Clinical Interest’. *Applied and Environmental Microbiology* 78.15 (2012), pp. 5077–5082. DOI: 10.1128/AEM.00583-12 (cit. on p. 11).

- [85] P O Kochkin, C V Nguyen, A P J van Deursen, and U Ebert. ‘Experimental study of hard x-rays emitted from metre-scale positive discharges in air’. Journal of Physics D: Applied Physics 45.42 (Oct. 2012), p. 425202. DOI: 10.1088/0022-3727/45/42/425202 (cit. on pp. 8, 147).
- [86] Christoph Köhn, Saša Dujko, Olivier Chanrion, and Torsten Neubert. ‘Streamer propagation in the atmosphere of Titan and other N<sub>2</sub>:CH<sub>4</sub> mixtures compared to N<sub>2</sub>:O<sub>2</sub> mixtures’. Icarus 333 (2019), pp. 294–305. ISSN: 0019-1035. DOI: <https://doi.org/10.1016/j.icarus.2019.05.036> (cit. on p. 25).
- [87] N. Kontoleon, J. Lucas, and L. E. Virr. ‘Electron swarm parameters in nitrogen’. J. Phys. D: Appl. Phys. 6.10 (June 1973), pp. 1237–1246. ISSN: 0022-3727. DOI: 10.1088/0022-3727/6/10/308 (cit. on p. 84).
- [88] I. Korolov, M. Vass, and Z. Donkó. ‘Scanning drift tube measurements of electron transport parameters in different gases: argon, synthetic air, methane and deuterium’. J. Phys. D: Appl. Phys. 49.41 (Sept. 2016), p. 415203. ISSN: 0022-3727. DOI: 10.1088/0022-3727/49/41/415203 (cit. on p. 5).
- [89] I A Kossyi, A Yu Kostinsky, A A Matveyev, and V P Silakov. ‘Kinetic scheme of the non-equilibrium discharge in nitrogen-oxygen mixtures’. Plasma Sources Sci. Technol. 1.3 (Aug. 1992), pp. 207–220. ISSN: 0963-0252, 1361-6595. DOI: 10.1088/0963-0252/1/3/011 (cit. on pp. 4, 110, 150).
- [90] Marios Kotsonis. ‘Diagnostics for characterisation of plasma actuators’. Measurement Science and Technology 26.9 (Aug. 2015), p. 092001. DOI: 10.1088/0957-0233/26/9/092001 (cit. on p. 11).
- [91] Katsuhisa Koura. ‘Null-collision technique in the direct-simulation Monte Carlo method’. The Physics of Fluids 29.11 (Nov. 1986), pp. 3509–3511. ISSN: 0031-9171. DOI: 10.1063/1.865826 (cit. on pp. 13, 58).
- [92] A. A. Kruithof. ‘Townsend’s ionization coefficients for neon, argon, krypton and xenon’. Physica 7.6 (June 1940), pp. 519–540. ISSN: 0031-8914. DOI: 10.1016/S0031-8914(40)90043-X (cit. on p. 81).

## BIBLIOGRAPHY

---

- [93] H. N. Kucukarpaci and J. Lucas. ‘Electron swarm parameters in argon and krypton’. *J. Phys. D: Appl. Phys.* 14.11 (Nov. 1981), pp. 2001–2014. ISSN: 0022-3727. DOI: 10.1088/0022-3727/14/11/008 (cit. on p. 81).
- [94] Kailash Kumar, HR Skullerud, and RE Robson. ‘Kinetic Theory of Charged Particle Swarms in Neutral Gases’. *Aust. J. Phys.* 33.2 (1980), pp. 343–448. URL: <https://doi.org/10.1071/PH800343B> (cit. on p. 58).
- [95] EE Kunhardt and Y Tzeng. ‘Development of an electron avalanche and its transition into streamers’. *Physical Review A* 38.3 (1988), p. 1410 (cit. on p. 100).
- [96] M. Kurachi and Y. Nakamura. *Proc. of 13th Symposium on Ion Sources and Ion-Assisted Technology* (1990) (cit. on p. 27).
- [97] C. S. Lakshminarasimha and J. Lucas. ‘The ratio of radial diffusion coefficient to mobility for electrons in helium, argon, air, methane and nitric oxide’. *J. Phys. D: Appl. Phys.* 10.3 (Feb. 1977), pp. 313–321. ISSN: 0022-3727. DOI: 10.1088/0022-3727/10/3/011 (cit. on pp. 38, 81).
- [98] Mounir Laroussi. ‘From Killing Bacteria to Destroying Cancer Cells: 20 Years of Plasma Medicine’. *Plasma Processes and Polymers* 11.12 (2014), pp. 1138–1141. DOI: <https://doi.org/10.1002/ppap.201400152> (cit. on pp. 11, 147).
- [99] Sergey B Leonov, Igor V Adamovich, and Victor R Soloviev. ‘Dynamics of near-surface electric discharges and mechanisms of their interaction with the airflow’. *Plasma Sources Science and Technology* 25.6 (Nov. 2016), p. 063001. DOI: 10.1088/0963-0252/25/6/063001 (cit. on p. 11).
- [100] Xiaoran Li, Siebe Dijcks, Sander Nijdam, Anbang Sun, Ute Ebert, and Jannis Teunissen. ‘Comparing simulations and experiments of positive streamers in air: steps toward model validation’. *Plasma Sources Science and Technology* 30.9 (Sept. 2021), p. 095002. DOI: 10.1088/1361-6595/ac1b36 (cit. on pp. 148, 153).

- [101] Yuan Li, Eddie M Van Veldhuizen, Guan-Jun Zhang, Ute Ebert, and Sander Nijdam. ‘Positive double-pulse streamers: how pulse-to-pulse delay influences initiation and propagation of subsequent discharges’. Plasma Sources Science and Technology 27.12 (2018), p. 125003 (cit. on pp. 20, 100, 147).
- [102] S. L. Lin, R. E. Robson, and E. A. Mason. ‘Moment theory of electron drift and diffusion in neutral gases in an electrostatic field’. J. Chem. Phys. 71.8 (Oct. 1979), pp. 3483–3498. ISSN: 0021-9606. DOI: 10.1063/1.438738 (cit. on p. 38).
- [103] B. G. Lindsay and M. A. Mangan. ‘5.1 Ionization’. In: Interactions of Photons and Electrons with Molecules. Ed. by Y. Itikawa. Vol. 17C. Berlin/Heidelberg, 2003, pp. 5001–5077. ISBN: 978-3-540-44338-4. DOI: 10.1007/10874891\_2 (cit. on pp. 27, 34).
- [104] V. Lisovskiy, J.-P. Booth, K. Landry, D. Douai, V. Cassagne, and V. Yegorenkov. ‘Electron drift velocity in N<sub>2</sub>O in strong electric fields determined from rf breakdown curves’. J. Phys. D: Appl. Phys. 39.9 (Apr. 2006), pp. 1866–1871. ISSN: 0022-3727. DOI: 10.1088/0022-3727/39/9/022 (cit. on p. 87).
- [105] Leonard B. Loeb and Arthur F. Kip. ‘Electrical Discharges in Air at Atmospheric Pressure The Nature of the Positive and Negative Point-to-Plane Coronas and the Mechanism of Spark Propagation’. Journal of Applied Physics 10.3 (Mar. 1939), pp. 142–160. ISSN: 0021-8979. DOI: 10.1063/1.1707290 (cit. on p. 6).
- [106] JJ Lowke. ‘The initiation of lightning in thunderclouds: The possible influence of metastable nitrogen and oxygen molecules in initiating lightning streamers’. Journal of Geophysical Research: Atmospheres 120.8 (2015), pp. 3183–3190 (cit. on p. 128).
- [107] JJ Lowke. ‘Theory of electrical breakdown in air-the role of metastable oxygen molecules’. Journal of Physics D: Applied Physics 25.2 (1992), p. 202 (cit. on p. 100).

## BIBLIOGRAPHY

---

- [108] J Lucas and H T Saelee. ‘A comparison of a Monte Carlo simulation and the Boltzmann solution for electron swarm motion in gases’. J. Phys. D: Appl. Phys. 8.6 (Apr. 1975), pp. 640–650. ISSN: 0022-3727, 1361-6463. DOI: 10.1088/0022-3727/8/6/007 (cit. on pp. 60, 71).
- [109] Alejandro Luque, Valeria Ratushnaya, and Ute Ebert. ‘Positive and negative streamers in ambient air: modelling evolution and velocities’. J. Phys. D: Appl. Phys. 41.23 (Nov. 2008), p. 234005. ISSN: 0022-3727. DOI: 10.1088/0022-3727/41/23/234005 (cit. on pp. 8, 10).
- [110] LXCat. URL: [www.lxcat.net](http://www.lxcat.net) (cit. on p. 150).
- [111] C. Makochekanwa, K. Oguri, R. Suzuki, T. Ishihara, M. Hoshino, M. Kimura, and H. Tanaka. ‘Experimental observation of neutral radical formation from CH<sub>4</sub> by electron impact in the threshold region’. Phys. Rev. A 74.4 (Oct. 2006), p. 042704. DOI: 10.1103/PhysRevA.74.042704 (cit. on pp. 29–33, 35).
- [112] F. Manders, P. C. M. Christianen, and J. C. Maan. ‘Propagation of a streamer discharge in a magnetic field’. J. Phys. D: Appl. Phys. 41.23 (Nov. 2008), p. 234006. ISSN: 0022-3727. DOI: 10.1088/0022-3727/41/23/234006 (cit. on p. 17).
- [113] J. M. Meek. ‘A Theory of Spark Discharge’. Phys. Rev. 57.8 (Apr. 1940), pp. 722–728. DOI: 10.1103/PhysRev.57.722 (cit. on pp. 6, 99).
- [114] Charles E. Melton and P. S. Rudolph. ‘Radiolysis of Methane in a Wide-Range Radiolysis Source of a Mass Spectrometer. I. Individual and Total Cross Sections for the Production of Positive Ions, Negative Ions, and Free Radicals by Electrons’. J. Chem. Phys. 47.5 (Sept. 1967), pp. 1771–1774. ISSN: 0021-9606. DOI: 10.1063/1.1712163 (cit. on pp. 29, 30, 36).
- [115] William H. Miller. ‘Theory of Penning Ionization. I. Atoms’. The Journal of Chemical Physics 52.7 (1970), pp. 3563–3572. DOI: 10.1063/1.1673523 (cit. on p. 3).

- [116] P. G. Millican and I. C. Walker. ‘Electron swarm characteristic energies ( $Dr/\mu$ ) in methane, perdeuteromethane, silane, perdeuteriosilane, phosphine and hydrogen sulphide at low  $E/N$ ’. J. Phys. D: Appl. Phys. 20.2 (Feb. 1987), pp. 193–196. ISSN: 0022-3727. DOI: 10.1088/0022-3727/20/2/007 (cit. on p. 38).
- [117] H. B. Milloy and R. W. Crompton. ‘The Ratio of the Lateral Diffusion Coefficient to Mobility for Electrons in Argon at 294 K’. Aust. J. Phys. 30.1 (1977), pp. 51–60. ISSN: 1446-5582. DOI: 10.1071/ph770051 (cit. on p. 81).
- [118] S Mirpour, A Martinez, J Teunissen, U Ebert, and S Nijdam. ‘Distribution of inception times in repetitive pulsed discharges in synthetic air’. Plasma Sources Science and Technology 29.11 (Nov. 2020), p. 115010. DOI: 10.1088/1361-6595/abb614 (cit. on p. 147).
- [119] Shahriar Mirpour and Sander Nijdam. Investigating CO<sub>2</sub> streamer inception in repetitive pulsed discharges. 2021. arXiv: 2107.10088 [physics.plasm-ph] (cit. on p. 192).
- [120] Carolynne Montijn and Ute Ebert. ‘Diffusion correction to the Raether–Meek criterion for the avalanche-to-streamer transition’. Journal of Physics D: Applied Physics 39.14 (2006), p. 2979 (cit. on p. 99).
- [121] W. Morgan. ‘Electron Collision Data for Plasma Chemistry Modeling’. Advances in Atomic Molecular and Optical Physics - ADVAN ATOM MOL OPT 43 (Dec. 2000), pp. 79–110. DOI: 10.1016/S1049-250X(08)60122-6 (cit. on p. 59).
- [122] R Morrow and JJ Lowke. ‘Streamer propagation in air’. Journal of Physics D: Applied Physics 30.4 (1997), p. 614 (cit. on p. 99).
- [123] Safa Motlagh and John H. Moore. ‘Cross sections for radicals from electron impact on methane and fluoroalkanes’. J. Chem. Phys. 109.2 (June 1998), pp. 432–438. ISSN: 0021-9606. DOI: 10.1063/1.476580 (cit. on pp. 28–33).

## BIBLIOGRAPHY

---

- [124] M. S. Naidu and A. N. Prasad. ‘Mobility, diffusion and attachment of electrons in oxygen’. *J. Phys. D: Appl. Phys.* 3.6 (June 1970), pp. 957–964. ISSN: 0022-3727. DOI: 10.1088/0022-3727/3/6/317 (cit. on p. 87).
- [125] Tohru Nakano, Hirotaka Toyoda Hirotaka Toyoda, and Hideo Sugai Hideo Sugai. ‘Electron-Impact Dissociation of Methane into CH<sub>3</sub> and CH<sub>2</sub> Radicals I. Relative Cross Sections’. *Jpn. J. Appl. Phys.* 30.11R (Nov. 1991), p. 2908. ISSN: 1347-4065. DOI: 10.1143/JJAP.30.2908 (cit. on pp. 29–33, 35, 36, 50–52).
- [126] Tohru Nakano, Hirotaka Toyoda Hirotaka Toyoda, and Hideo Sugai Hideo Sugai. ‘Electron-Impact Dissociation of Methane into CH<sub>3</sub> and CH<sub>2</sub> Radicals II. Absolute Cross Sections’. *Jpn. J. Appl. Phys.* 30.11R (Nov. 1991), p. 2912. ISSN: 1347-4065. DOI: 10.1143/JJAP.30.2912 (cit. on pp. 5, 29–33, 35, 36, 50–52).
- [127] K. F. Ness. ‘Multi-term solution of the Boltzmann equation for electron swarms in crossed electric and magnetic fields’. *J. Phys. D: Appl. Phys.* 27.9 (Sept. 1994), pp. 1848–1861. ISSN: 0022-3727. DOI: 10.1088/0022-3727/27/9/007 (cit. on pp. 60, 66, 67).
- [128] K. F. Ness and R. E. Robson. ‘Velocity distribution function and transport coefficients of electron swarms in gases. II. Moment equations and applications’. *Phys. Rev. A* 34.3 (Sept. 1986), pp. 2185–2209. ISSN: 0556-2791. DOI: 10.1103/PhysRevA.34.2185 (cit. on p. 71).
- [129] S Nijdam, E Takahashi, A H Markosyan, and U Ebert. ‘Investigation of positive streamers by double-pulse experiments, effects of repetition rate and gas mixture’. *Plasma Sources Sci. Technol.* 23.2 (Mar. 2014), p. 025008. DOI: 10.1088/0963-0252/23/2/025008 (cit. on pp. 20, 147, 148, 150, 180, 183).
- [130] S Nijdam, J Teunissen, E Takahashi, and U Ebert. ‘The role of free electrons in the guiding of positive streamers’. *Plasma Sources Science and Technology* 25.4 (May 2016), p. 044001. ISSN: 1361-6595. DOI: 10.1088/0963-0252/25/4/044001 (cit. on pp. 10, 99).

- [131] S Nijdam, F M J H van de Wetering, R Blanc, E M van Veldhuizen, and U Ebert. ‘Probing photo-ionization: experiments on positive streamers in pure gases and mixtures’. Journal of Physics D: Applied Physics 43.14 (Mar. 2010), p. 145204. ISSN: 1361-6463. DOI: 10.1088/0022-3727/43/14/145204 (cit. on p. 99).
- [132] S Nijdam, G Wormeester, E M van Veldhuizen, and U Ebert. ‘Probing background ionization: positive streamers with varying pulse repetition rate and with a radioactive admixture’. Journal of Physics D: Applied Physics 44.45 (Oct. 2011), p. 455201. DOI: 10.1088/0022-3727/44/45/455201 (cit. on pp. 10, 147).
- [133] S. Nijdam, E. Takahashi, J. Teunissen, and U. Ebert. ‘Streamer discharges can move perpendicularly to the electric field’. New J. Phys. 16.10 (Oct. 2014), p. 103038. ISSN: 1367-2630. DOI: 10.1088/1367-2630/16/10/103038 (cit. on pp. 10, 147).
- [134] Sander Nijdam, Jannis Teunissen, and Ute Ebert. ‘The physics of streamer discharge phenomena’. Plasma Sources Sci. Technol. 29.10 (Nov. 2020), p. 103001. ISSN: 0963-0252. DOI: 10.1088/1361-6595/abaa05 (cit. on pp. 1, 8, 13, 17, 99, 147).
- [135] Tomohiro Nozaki and Ken Okazaki. ‘Non-thermal plasma catalysis of methane: Principles, energy efficiency, and applications’. Catalysis Today. Recent Advances in Plasma and Catalysis (ISPCEM 2012) 211 (Aug. 2013), pp. 29–38. ISSN: 0920-5861. DOI: 10.1016/j.cattod.2013.04.002 (cit. on p. 25).
- [136] Daisuke Okano. ‘Time-lag properties of corona streamer discharges between impulse sphere and dc needle electrodes under atmospheric air conditions’. Review of Scientific Instruments 84.2 (2013), p. 024702 (cit. on p. 99).
- [137] Stanley Osher and James A Sethian. ‘Fronts propagating with curvature-dependent speed: Algorithms based on Hamilton-Jacobi formulations’. Journal of Computational Physics 79.1 (1988), pp. 12–49. ISSN: 0021-9991. DOI: [https://doi.org/10.1016/0021-9991\(88\)90002-2](https://doi.org/10.1016/0021-9991(88)90002-2) (cit. on p. 148).

## BIBLIOGRAPHY

---

- [138] J. L. Pack and A. V. Phelps. ‘Electron Attachment and Detachment. I. Pure O<sub>2</sub> at Low Energy’. J. Chem. Phys. 44.5 (Mar. 1966), pp. 1870–1883. ISSN: 0021-9606. DOI: 10.1063/1.1726956 (cit. on pp. 3, 84, 88, 89, 150).
- [139] S. Pancheshnyi. ‘Role of electronegative gas admixtures in streamer start, propagation and branching phenomena’. Plasma Sources Sci. Technol. 14.4 (Aug. 2005), pp. 645–653. ISSN: 0963-0252. DOI: 10.1088/0963-0252/14/4/002 (cit. on p. 107).
- [140] Sergey Pancheshnyi. ‘Effective ionization rate in nitrogen–oxygen mixtures’. Journal of Physics D: Applied Physics 46.15 (2013), p. 155201 (cit. on pp. 100, 110, 111, 117, 123, 150).
- [141] Sergey Pancheshnyi. ‘Photoionization produced by low-current discharges in O<sub>2</sub>, air, N<sub>2</sub>, and CO<sub>2</sub>’. Plasma Sources Science and Technology 24.1 (Dec. 2014), p. 015023. DOI: 10.1088/0963-0252/24/1/015023 (cit. on p. 10).
- [142] particle\_swarm Boltzmann Solver. URL: [https://gitlab.com/MD-CWI-NL/particle\\_swarm/-/tree/9b7e181f5098a40267cad6ed714e9552f1c32cd](https://gitlab.com/MD-CWI-NL/particle_swarm/-/tree/9b7e181f5098a40267cad6ed714e9552f1c32cd) (cit. on pp. 38, 42, 187).
- [143] J. Perrin, J. P. M. Schmitt, G. de Rosny, B. Drevillon, J. Huc, and A. Lloret. ‘Dissociation cross sections of silane and disilane by electron impact’. Chemical Physics 73.3 (Dec. 1982), pp. 383–394. ISSN: 0301-0104. DOI: 10.1016/0301-0104(82)85177-X (cit. on pp. 49, 51).
- [144] Danyal Petersen, Matthew Bailey, William H Beasley, and John Hallett. ‘A brief review of the problem of lightning initiation and a hypothesis of initial lightning leader formation’. Journal of Geophysical Research: Atmospheres 113.D17 (2008) (cit. on p. 99).
- [145] Z. Lj Petrović, S. Dujko, D. Marić, G. Malović, Ž Nikitović, O. Šašić, J. Jovanović, V. Stojanović, and M. Radmilović-Radenović. ‘Measurement and interpretation of swarm parameters and their application in plasma modelling’. J. Phys. D: Appl. Phys. 42.19 (Sept. 2009), p. 194002. ISSN:

- 0022-3727. DOI: 10.1088/0022-3727/42/19/194002 (cit. on pp. 5, 59, 63, 65, 68, 80, 90, 94, 95).
- [146] Z. Lj Petrović, M. Šuvakov, Z. Nikitović, S. Dujko, O. Šaić, J. Jovanović, G. Malović, and V. Stojanović. ‘Kinetic phenomena in charged particle transport in gases, swarm parameters and cross section data’. *Plasma Sources Science and Technology* 16.1 (2007). ISSN: 09630252. DOI: 10.1088/0963-0252/16/1/S01 (cit. on pp. 6, 26, 45).
- [147] Phelps database. May 2020. URL: [www.lxcat.net](http://www.lxcat.net) (cit. on pp. 84, 88, 89, 110, 117, 150).
- [148] L. C. Pitchford, L. L. Alves, K. Bartschat, S. F. Biagi, M. C. Bordage, A. V. Phelps, C. M. Ferreira, G. J. M. Hagelaar, W. L. Morgan, S. Pancheshnyi, V. Puech, A. Stauffer, and O. Zatsarinny. ‘Comparisons of sets of electron–neutral scattering cross sections and swarm parameters in noble gases: I. Argon’. *J. Phys. D: Appl. Phys.* 46.33 (Aug. 2013), p. 334001. ISSN: 0022-3727. DOI: 10.1088/0022-3727/46/33/334001 (cit. on p. 25).
- [149] W. J. Pollock. ‘Momentum transfer and vibrational cross-sections in non-polar gases’. *Trans. Faraday Soc.* 64.0 (Jan. 1968), pp. 2919–2926. ISSN: 0014-7672. DOI: 10.1039/TF9686402919 (cit. on p. 38).
- [150] N A Popov. ‘Kinetics of plasma-assisted combustion: effect of non-equilibrium excitation on the ignition and oxidation of combustible mixtures’. *Plasma Sources Science and Technology* 25.4 (May 2016), p. 043002. DOI: 10.1088/0963-0252/25/4/043002 (cit. on pp. 11, 18).
- [151] N. A. Popov. ‘Evolution of the negative ion composition in the afterglow of a streamer discharge in air’. *Plasma Phys. Rep.* 36.9 (Sept. 2010), pp. 812–818. ISSN: 1063-780X, 1562-6938. DOI: 10.1134/S1063780X10090084 (cit. on p. 109).
- [152] NA Popov. ‘Fast gas heating in a nitrogen–oxygen discharge plasma: I. Kinetic mechanism’. *Journal of Physics D: Applied Physics* 44.28 (2011), p. 285201 (cit. on p. 178).
-

## BIBLIOGRAPHY

---

- [153] Prettier. URL: <https://prettier.io/> (cit. on p. 194).
- [154] D. A. Price, J. Lucas, and J. L. Moruzzi. ‘Ionization in oxygen-hydrogen mixtures’. J. Phys. D: Appl. Phys. 5.7 (July 1972), pp. 1249–1259. ISSN: 0022-3727. DOI: 10.1088/0022-3727/5/7/309 (cit. on p. 87).
- [155] PyUnit. URL: <https://wiki.python.org/moin/PyUnit> (cit. on p. 194).
- [156] M. Rabie and C. M. Franck. ‘METHES: A Monte Carlo collision code for the simulation of electron transport in low temperature plasmas’. Computer Physics Communications 203 (June 2016), pp. 268–277. ISSN: 0010-4655. DOI: 10.1016/j.cpc.2016.02.022 (cit. on pp. 61, 68, 187).
- [157] H. Raether. ‘Die Entwicklung der Elektronenlawine in den Funkenkanal’. Z. Physik 112.7 (July 1939), pp. 464–489. ISSN: 0044-3328. DOI: 10.1007/BF01340229 (cit. on p. 7).
- [158] I. U. P. Raizer. Gas discharge physics. Berlin; New York, 1997. ISBN: 978-3-540-19462-0 978-3-642-64760-4 (cit. on pp. 1, 7).
- [159] Pietro Ranieri, Nicholas Sponcel, Jon Kizer, Marcela Rojas-Pierce, Ricardo Hernández, Luciano Gatiboni, Amy Grunden, and Katharina Stapelmann. ‘Plasma agriculture: Review from the perspective of the plant and its ecosystem’. Plasma Processes and Polymers 18.1 (2021), p. 2000162. DOI: <https://doi.org/10.1002/ppap.202000162> (cit. on p. 147).
- [160] Prashant Rawat, Vaibhav S. Prabhudesai, M. A. Rahman, N. Bhargava Ram, and E. Krishnakumar. ‘Absolute cross sections for dissociative electron attachment to NH<sub>3</sub> and CH<sub>4</sub>’. International Journal of Mass Spectrometry. Electron-induced atomic and molecular processes: A special issue honoring Eugen Illenberger on his 65th birthday 277.1 (Nov. 2008), pp. 96–102. ISSN: 1387-3806. DOI: 10.1016/j.ijms.2008.05.015 (cit. on p. 27).
- [161] J. A. Rees. ‘The Behaviour of Free and Attached Electrons in Oxygen’. Aust. J. Phys. 18.1 (1965), pp. 41–58. ISSN: 1446-5582. DOI: 10.1071/ph650041 (cit. on p. 87).

- [162] Ivan D. Reid. ‘An Investigation of the Accuracy of Numerical Solutions of Boltzmann’s Equation for Electron Swarms in Gases with Large Inelastic Cross Sections’. Aust. J. Phys. 32.3 (1979), pp. 231–254. ISSN: 1446-5582. DOI: 10.1071/ph790231 (cit. on pp. 60, 68).
- [163] D. Reiter and R. K. Janev. ‘Hydrocarbon Collision Cross Sections for Magnetic Fusion: The Methane, Ethane and Propane Families’. Contributions to Plasma Physics 50.10 (2010), pp. 986–1013. ISSN: 1521-3986. DOI: <https://doi.org/10.1002/ctpp.201000090> (cit. on p. 28).
- [164] Robot Framework. URL: <https://robotframework.org/> (cit. on p. 194).
- [165] R. E. Robson and K. F. Ness. ‘Velocity distribution function and transport coefficients of electron swarms in gases: Spherical-harmonics decomposition of Boltzmann’s equation’. Phys. Rev. A 33.3 (Mar. 1986), pp. 2068–2077. DOI: 10.1103/PhysRevA.33.2068 (cit. on pp. 68, 80, 90, 94).
- [166] Ankit Rohatgi. Webplotdigitizer: Version 4.4. 2020. URL: <https://automeris.io/WebPlotDigitizer> (cit. on p. 49).
- [167] Casper Rutjes. ‘Modeling high energy atmospheric physics and lightning inception’. PhD thesis. Department of Applied Physics, Mar. 2018. ISBN: 978-94-028-0965-7 (cit. on p. 113).
- [168] T. Sakae, S. Sumiyoshi, E. Murakami, Y. Matsumoto, K. Ishibashi, and A. Katase. ‘Scattering of electrons by CH<sub>4</sub>, CF<sub>4</sub> and SF<sub>6</sub> in the 75-700 eV range’. J. Phys. B: At. Mol. Opt. Phys. 22.9 (May 1989), pp. 1385–1394. ISSN: 0953-4075. DOI: 10.1088/0953-4075/22/9/011 (cit. on p. 27).
- [169] A. Salabas, G. Gousset, and L. L. Alves. ‘Two-dimensional fluid modelling of charged particle transport in radio-frequency capacitively coupled discharges’. Plasma Sources Sci. Technol. 11.4 (Oct. 2002), pp. 448–465. ISSN: 0963-0252. DOI: 10.1088/0963-0252/11/4/312 (cit. on p. 38).

## BIBLIOGRAPHY

---

- [170] O. Šašić, G. Malović, A. Strinić, Z. Nikitović, and Z. Lj Petrović. ‘Excitation coefficients and cross-sections for electron swarms in methane’. New Journal of Physics 6 (2004), pp. 1–11. ISSN: 13672630. DOI: 10.1088/1367-2630/6/1/074 (cit. on pp. 29, 36, 37).
- [171] G Schaefer and P Hui. ‘The Monte Carlo flux method’. Journal of Computational Physics 89.1 (July 1990), pp. 1–30. ISSN: 0021-9991. DOI: 10.1016/0021-9991(90)90114-G (cit. on p. 58).
- [172] H. Schlumbohm. Proc. 4th Int. Conference on Ioniz. Phenomena in Gases (Sweden) (Aug. 1959) (cit. on p. 87).
- [173] R. W. Schunk. ‘Mathematical structure of transport equations for multispecies flows’. Reviews of Geophysics 15.4 (1977), pp. 429–445. ISSN: 1944-9208. DOI: 10.1029/RG015i004p00429 (cit. on p. 16).
- [174] Daniel I Sebacher and Robert W Guy. Vibrational relaxation in expanding N<sub>2</sub> and air. Tech. rep. 1974. URL: <https://ntrs.nasa.gov/citations/19740023649> (cit. on p. 178).
- [175] Alan A. Sebastian and J. M. Wadehra. ‘Time-dependent behaviour of electron transport in methane-argon mixtures’. Journal of Physics D: Applied Physics 38.10 (2005), pp. 1577–1587. ISSN: 00223727. DOI: 10.1088/0022-3727/38/10/013 (cit. on p. 45).
- [176] A Shashurin, M N Shneider, and M Keidar. ‘Measurements of streamer head potential and conductivity of streamer column in cold nonequilibrium atmospheric plasmas’. Plasma Sources Science and Technology 21.3 (Apr. 2012), p. 034006. ISSN: 1361-6595. DOI: 10.1088/0963-0252/21/3/034006 (cit. on p. 99).
- [177] M. Shimozuma and H. Tagashira. ‘Measurement of the ionisation coefficients in nitrogen and methane mixtures’. J. Phys. D: Appl. Phys. 14.10 (Oct. 1981), pp. 1783–1789. ISSN: 0022-3727. DOI: 10.1088/0022-3727/14/10/012 (cit. on p. 38).

- [178] T. Shirai, T. Tabata, H. Tawara, and Y. Itikawa. ‘Analytic cross sections for electron collisions with hydrocarbons: CH<sub>4</sub>, C<sub>2</sub>H<sub>6</sub>, C<sub>2</sub>H<sub>4</sub>, C<sub>2</sub>H<sub>2</sub>, C<sub>3</sub>H<sub>8</sub>, and C<sub>3</sub>H<sub>6</sub>’. Atomic Data and Nuclear Data Tables 80.2 (2002), pp. 147–204. ISSN: 0092-640X. DOI: <https://doi.org/10.1006/adnd.2001.0878> (cit. on pp. 34, 47–49, 51).
- [179] R. A. Snelson. ‘Measurements of the longitudinal diffusion coefficient and the drift velocity for electron swarms in hydrogen and nitrogen using a time-of-flight technique’. Proceedings of the Institution of Electrical Engineers 122.3 (Mar. 1975), pp. 333–336. ISSN: 2053-7891. DOI: 10.1049/piee.1975.0092 (cit. on p. 84).
- [180] Mi-Young Song, Jung-Sik Yoon, Hyuck Cho, Yukikazu Itikawa, Grzegorz P. Karwasz, Viatcheslav Kokoouline, Yoshiharu Nakamura, and Jonathan Tennyson. ‘Cross Sections for Electron Collisions with Methane’. Journal of Physical and Chemical Reference Data 44.2 (May 2015), p. 023101. ISSN: 0047-2689. DOI: 10.1063/1.4918630 (cit. on pp. 18, 27–29, 34, 38, 39, 44, 45, 47–50, 185).
- [181] Mi-Young Song, Jung-Sik Yoon, Hyuck Cho, Grzegorz P. Karwasz, Viatcheslav Kokoouline, Yoshiharu Nakamura, and Jonathan Tennyson. ‘“Recommended” cross sections for electron collisions with molecules’. Eur. Phys. J. D 74.3 (Mar. 2020), p. 60. ISSN: 1434-6079. DOI: 10.1140/epjd/e2020-100543-6 (cit. on pp. 26, 29, 49).
- [182] Spaghetti Code. URL: <https://www.bmc.com/blogs/spaghetti-code/> (cit. on p. 196).
- [183] L. T. Specht, S. A. Lawton, and T. A. DeTemple. ‘Electron ionization and excitation coefficients for argon, krypton, and xenon in the low E/N region’. Journal of Applied Physics 51.1 (Jan. 1980), pp. 166–170. ISSN: 0021-8979. DOI: 10.1063/1.327395 (cit. on p. 81).
- [184] S M Starikovskaia. ‘Plasma-assisted ignition and combustion: nanosecond discharges and development of kinetic mechanisms’.

## BIBLIOGRAPHY

---

- Journal of Physics D: Applied Physics 47.35 (Aug. 2014), p. 353001. DOI: 10.1088/0022-3727/47/35/353001 (cit. on pp. 11, 18).
- [185] S. M. Starikovskaia. ‘Plasma assisted ignition and combustion’. J. Phys. D: Appl. Phys. 39.16 (Aug. 2006), R265–R299. ISSN: 0022-3727. DOI: 10.1088/0022-3727/39/16/R01 (cit. on pp. 25, 185).
- [186] Andrey Starikovskiy and Nickolay Aleksandrov. ‘Plasma-assisted ignition and combustion’. Progress in Energy and Combustion Science 39.1 (Feb. 2013), pp. 61–110. ISSN: 0360-1285. DOI: 10.1016/j.pecs.2012.05.003 (cit. on pp. 25, 185).
- [187] J. Stephens. ‘A multi-term Boltzmann equation benchmark of electron-argon cross-sections for use in low temperature plasma models’. J. Phys. D: Appl. Phys. 51.12 (Mar. 2018), p. 125203. ISSN: 0022-3727. DOI: 10.1088/1361-6463/aaaf8b (cit. on pp. 62, 68, 187).
- [188] H. Tagashira, Y. Sakai, and S. Sakamoto. ‘The development of electron avalanches in argon at high E/N values. II. Boltzmann equation analysis’. J. Phys. D: Appl. Phys. 10.7 (May 1977), pp. 1051–1063. ISSN: 0022-3727. DOI: 10.1088/0022-3727/10/7/011 (cit. on p. 60).
- [189] A. Tejero-del-Caz, V. Guerra, D. Gonçalves, M. Lino da Silva, L. Marques, N. Pinhão, C. D. Pintassilgo, and L. L. Alves. ‘The LisbOn KInetics Boltzmann solver’. Plasma Sources Sci. Technol. 28.4 (Apr. 2019), p. 043001. ISSN: 0963-0252. DOI: 10.1088/1361-6595/ab0537 (cit. on pp. 62, 68, 187).
- [190] Jannis Teunissen and Ute Ebert. ‘3D PIC-MCC simulations of discharge inception around a sharp anode in nitrogen/oxygen mixtures’. Plasma Sources Sci. Technol. 25.4 (Aug. 2016), p. 044005. DOI: 10.1088/0963-0252/25/4/044005 (cit. on pp. 13, 101, 110, 111).
- [191] Jannis Teunissen and Ute Ebert. ‘3D PIC-MCC simulations of discharge inception around a sharp anode in nitrogen/oxygen mixtures’. Plasma Sources Science and Technology 25.4 (2016).

- ISSN: 13616595. DOI: 10.1088/0963-0252/25/4/044005 (cit. on pp. 14, 38, 42).
- [192] Jannis Teunissen and Ute Ebert. ‘Afivo: A Framework for Quadtree/Octree AMR with Shared-Memory Parallelization and Geometric Multigrid Methods’. Computer Physics Communications 233 (Dec. 2018), pp. 156–166. ISSN: 0010-4655. DOI: 10.1016/j.cpc.2018.06.018 (cit. on pp. 18, 148).
- [193] Jannis Teunissen and Ute Ebert. ‘Controlling the Weights of Simulation Particles: Adaptive Particle Management Using k-d Trees’. Journal of Computational Physics 259 (Feb. 2014), pp. 318–330. ISSN: 0021-9991. DOI: 10.1016/j.jcp.2013.12.005 (cit. on p. 15).
- [194] Jannis Teunissen and Ute Ebert. ‘Simulating streamer discharges in 3D with the parallel adaptive Afivo framework’. Journal of Physics D: Applied Physics 50.47 (Oct. 2017), p. 474001. DOI: 10.1088/1361-6463/aa8faf (cit. on p. 148).
- [195] J.S. Townsend and V.A. Bailey. ‘LXX. The motion of electrons in argon’. Lond.Edinb.Dubl.Phil.Mag. 43.255 (Mar. 1922), pp. 593–600. ISSN: 1941-5982. DOI: 10.1080/14786442208633916 (cit. on p. 81).
- [196] S. Trajmar and J.W. McConkey. ‘Benchmark Measurements of Cross Sections for Electron Collisions: Analysis of Scattered Electrons’. In: Cross Section Data. Ed. by Mitio Inokuti. Vol. 33. Advances In Atomic, Molecular, and Optical Physics. 1994, pp. 63–96. DOI: [https://doi.org/10.1016/S1049-250X\(08\)60033-6](https://doi.org/10.1016/S1049-250X(08)60033-6) (cit. on p. 26).
- [197] Th Unfer and JP Boeuf. ‘Modelling of a nanosecond surface discharge actuator’. Journal of physics D: applied physics 42.19 (2009), p. 194017 (cit. on pp. 176–178).
- [198] EM Van Veldhuizen and WR Rutgers. ‘Inception behaviour of pulsed positive corona in several gases’. Journal of Physics D: Applied Physics 36.21 (2003), p. 2692 (cit. on p. 99).

## BIBLIOGRAPHY

---

- [199] EM Van Veldhuizen and WR Rutgers. ‘Pulsed positive corona streamer propagation and branching’. Journal of Physics D: Applied Physics 35.17 (2002), p. 2169 (cit. on p. 99).
- [200] L. J. Varnerin. ‘Neutralization of Ions and Ionization of Atoms Near Metal Surfaces’. Phys. Rev. 91 (4 Aug. 1953), pp. 859–863. DOI: 10.1103/PhysRev.91.859 (cit. on p. 136).
- [201] Ruben Verloy, Angela Privat-Maldonado, Evelien Smits, and Annemie Bogaerts. ‘Cold Atmospheric Plasma Treatment for Pancreatic Cancer—The Importance of Pancreatic Stellate Cells’. Cancers 12.10 (Sept. 2020), p. 2782. ISSN: 2072-6694. DOI: 10.3390/cancers12102782 (cit. on p. 147).
- [202] L. Vialetto, S. Longo, and P. Diomede. ‘Benchmark calculations for electron velocity distribution function obtained with Monte Carlo Flux simulations’. Plasma Sources Sci. Technol. 28.11 (Nov. 2019), p. 115015. ISSN: 0963-0252. DOI: 10.1088/1361-6595/ab4b95 (cit. on p. 58).
- [203] VIEHLAND database. Nov. 2019. URL: [www.lxcat.net](http://www.lxcat.net) (cit. on p. 111).
- [204] M. Vranic, T. Grismayer, J.L. Martins, R.A. Fonseca, and L.O. Silva. ‘Particle Merging Algorithm for PIC Codes’. Computer Physics Communications 191 (June 2015), pp. 65–73. ISSN: 00104655. DOI: 10.1016/j.cpc.2015.01.020 (cit. on p. 15).
- [205] Zezhong Wang and Yinan Geng. ‘Study on the streamer inception characteristics under positive lightning impulse voltage’. AIP Advances 7.11 (2017), p. 115115 (cit. on pp. 99, 100).
- [206] R D White, R E Robson, B Schmidt, and Michael A Morrison. ‘Is the classical two-term approximation of electron kinetic theory satisfactory for swarms and plasmas?’ Journal of Physics D: Applied Physics 36.24 (Nov. 2003), pp. 3125–3131. DOI: 10.1088/0022-3727/36/24/006 (cit. on pp. 58, 59).

- [207] Harold F. Winters. ‘Dissociation of methane by electron impact’. J. Chem. Phys. 63.8 (Oct. 1975), pp. 3462–3466. ISSN: 0021-9606. DOI: 10.1063/1.431783 (cit. on pp. 33, 34, 49–51).
- [208] G Wormeester, S Pancheshnyi, A Luque, S Nijdam, and U Ebert. ‘Probing Photo-Ionization: Simulations of Positive Streamers in Varying N<sub>2</sub>:O<sub>2</sub>-Mixtures’. J. Phys. D: Appl. Phys. 43.50 (Dec. 2010), p. 505201. ISSN: 1361-6463. DOI: 10.1088/0022-3727/43/50/505201 (cit. on p. 108).
- [209] Yoav Yair, Yukihiro Takahashi, Roy Yaniv, Ute Ebert, and Yukihiro Goto. ‘A study of the possibility of sprites in the atmospheres of other planets’. Journal of Geophysical Research: Planets 114.E9 (2009). ISSN: 2156-2202. DOI: <https://doi.org/10.1029/2008JE003311> (cit. on p. 25).
- [210] J Zhang, AH Markosyan, M Seeger, EM van Veldhuizen, EJM Van Heesch, and U Ebert. ‘Numerical and experimental investigation of dielectric recovery in supercritical N<sub>2</sub>’. Plasma Sources Science and Technology 24.2 (2015), p. 025008. DOI: 10.1088/0963-0252/24/2/025008 (cit. on pp. 177, 178).
- [211] Zheng Zhao and Jiangtao Li. ‘Integrated effect on evolution of streamer dynamics under long-term repetitive sub-microsecond pulses in high-pressure nitrogen’. Plasma Sources Science and Technology (2019) (cit. on p. 100).
- [212] M. B. Zhelezniak, A. Kh. Mnatsakanian, and S. V. Sizykh. ‘Photoionization of nitrogen and oxygen mixtures by radiation from a gas discharge’. High Temperature Science 20.3 (Nov. 1982), pp. 357–362 (cit. on p. 149).
- [213] M. B. Zheleznyak and A. Kh. Mnatsakanyan. ‘Photoionization of nitrogen and oxygen mixtures by radiation from a gas discharge’. Teplofizika Vysokikh Temperatur 20.3 (1982), pp. 423–428 (cit. on pp. 2, 9, 110).
- [214] Marcin Ziółkowski, Anna Vikár, Maricris Lodriguito Mayes, Ákos Bencsura, György Lendvay, and George C. Schatz. ‘Modeling the electron-impact dissociation of methane’. J. Chem. Phys.

*BIBLIOGRAPHY*

---

137.22 (July 2012), 22A510. ISSN: 0021-9606. DOI:  
10.1063/1.4733706 (cit. on pp. 6, 29, 31–33, 35, 45, 62).

# Curriculum Vitae

Andy Martinez Nieto was born on the 4<sup>th</sup> of November 1993 in Antwerp, Belgium. After completing his secondary education in at Xaverius College, Borgerhout, Belgium, he received a bachelor's degree (cum laude) and a master's degree (magna cum laude) in Physics at the University of Antwerp. From 2017, he started a PhD. project in the Multiscale Dynamics group of Centrum Wiskunde & Informatica (CWI), Amsterdam under supervision of Ute Ebert. The results of this PhD. project are presented in this thesis.

## List of publications

1. D. Bouwman, A. Martinez, B. J. Braams, and U. Ebert, Neutral dissociation of methane by electron impact and a complete and consistent cross section set. *Plasma Sources Sci. Technol.* **30** 075012 2021
2. S. Mirpour, A. Martinez, J. Teunissen, U. Ebert, and S. Nijdam, Distribution of inception times in repetitive pulsed discharges in synthetic air. *Plasma Sources Sci. Technol.* **29** 115010 2020
3. A. Martinez, J. Teunissen, and U. Ebert, Comparison of Electron Boltzmann Solvers. [in preparation, based on chapter 3 of this thesis]
4. A. Martinez, H. Malla, J. Teunissen, and U. Ebert, Simulations of Repetitive Pulsed Streamer Discharges in Synthetic Air. [in preparation, based on chapter 5 of this thesis]